Nonlinear modeling of frame members for rapid infrastructure assessment

by

Claudio Matias Perez

A dissertation submitted in partial satisfaction of the
requirements for the degree of
Doctor of Philosophy
in
Structural Engineering
in the
Graduate Division
of the
University of California, Berkeley

Committee in charge:

Professor Filippos Filippou, Co-chair
Professor Khalid Mosalam, Co-chair
Professor Sanjay Govindjee
Professor Panayiotis Papadopoulos

Spring 2026

Nonlinear modeling of frame members for rapid infrastructure assessment

Abstract

Nonlinear modeling of frame members for rapid infrastructure assessment

by

Claudio Matias Perez

Doctor of Philosophy in Structural Engineering

University of California, Berkeley

Professor Filippos Filippou, Co-chair

Professor Khalid Mosalam, Co-chair

This dissertation develops computational methods for the nonlinear modeling of frame members and their use in rapid infrastructure assessment following extreme events.

The work is motivated by the need to convert recorded structural motions into quantitative assessments of condition at the speed and scale required for regional operations. In this setting, physics-based assessment requires beam and column models that can represent geometric nonlinearity and multiaxial inelastic material response, without sacrificing the efficiency of one-dimensional frame analysis. At the same time, data-driven assessment requires a computational framework in which recorded motions, system identification procedures, structural simulation, and model calibration may operate within a common workflow.

In Part I, a general framework is developed for the constitutive modeling of beam sections with cross-sectional warping. The framework is formulated in the setting of geometrically exact beam theory with an arbitrary number of global warping fields and remains applicable to linearizations of that model, including classical Timoshenko beam theory. Enhanced section strains are introduced with amplitudes determined locally at each cross section, thereby improving the three-dimensional strain field used for multiaxial constitutive integration while preserving the standard one-dimensional equilibrium equations. The proposed section models may therefore be used with existing beam finite element implementations without modification of the element state determination procedure. Two specializations are developed. For members for which warping boundary effects are insignificant, the framework yields warping-free section models that recover Saint–Venant continuum solutions in the elastic regime, including Poisson-coupled in-plane warping effects, and are compatible with classical six-field beam elements. For restrained torsion, one torsional warping field is retained globally and an additional correction is resolved locally, yielding a seven-field beam theory that restores pointwise equilibrium in the elastic regime and rectifies the equilibrium defect of standard single-field torsion-warping theory. The resulting formulations are organized for finite element implementation through a separation of frame, section, and material models. Numerical studies verify exact agreement with Saint–Venant solutions in the elastic

regime and demonstrate improved response in shear-dominated inelastic problems, restrained torsion, evaluation of the Wagner term, and finite-deformation benchmarks.

In Part II, a framework is developed for operational structural health monitoring that integrates physics-based simulation and data-driven inference within a common assessment environment. The framework is implemented in BRACE^2, developed in collaboration with the California Department of Transportation to deliver post-earthquake assessments for instrumented highway bridges in California. Structural assessment is organized around five abstractions, Assets, Events, Predictors, Metrics, and Evaluations, and realized through a four-layer architecture separating presentation, orchestration, domain, and infrastructure concerns. This organization permits heterogeneous predictors to operate through a common event-evaluation workflow, reduces their outputs to a shared metric representation with explicit provenance, and assembles those metrics into actionable reports for closure and inspection decisions. A second contribution of Part II is a compositional formulation for computing analytic gradients of finite element responses. In this formulation, a host-level parameterization constructs the solver parameters required by the analysis kernel, kernel-level direct differentiation furnishes derivatives with respect to those parameters, and full sensitivities with respect to the original modeling variables are recovered by the chain rule. The resulting construction supports model updating, reliability analysis, and integration with automatic-differentiation toolchains employed in machine learning.

These developments furnish a computational environment in which recorded motions, nonlinear structural simulation, differentiable calibration, and operational decision-making are brought into a single workflow for rapid infrastructure assessment. Following a pilot deployment covering 22 bridges, an implementation of the proposed framework is being advanced toward operational use by approximately forty engineers of the California Department of Transportation, with coverage extending across the state highway network.

A mis abuelos, por su amor abnegado.

Contents

Acknowledgments

My gratitude to my advisors, Professors Filip C. Filippou and Khalid M. Mosalam, cannot be overstated. Their guidance, encouragement, and sustained support throughout my doctoral studies have gone far beyond what I could reasonably have asked of them, and I am deeply grateful for the care and confidence they have shown me.

I also thank Professors Sanjay Govindjee and Panayiotis Papadopoulos, who served on the dissertation committee. I am also indebted to them, to my advisors, and to Professor James Casey, for courses whose depth and careful craftsmanship had a lasting influence on my education at Berkeley.

I would like to thank Frank McKenna for countless discussions, from which I benefited far more than he did, and for his patience with code written during my early attempts to program.

I am grateful to my friends and colleagues for many enjoyable discussions. John Vouvakis Manousakis for his friendship and for generously sharing his gift for pristine programming. Xuan for many insightful discussions arising from his work in the trenches of fracture mechanics, and for the late nights spent trying to program what at first seemed impossible. Nima Khodadadi for the thoughtfulness and many valuable conversations.

I would also like to thank M. Scott and David McCallen for their generosity with their time and for their willingness to discuss questions that helped advance this work. Thanks are also due to all who have contributed to the OpenSees code base.

I owe more than I can say to Chrystal. Her patience, encouragement, and support have been unending.

Finally, I thank my family for their relentless encouragement.

Financial support for this research was provided in part by the California Department of Transportation (Caltrans) under Task Order 001 of the PEER Bridge Program, Agreement 65A0774, to the Pacific Earthquake Engineering Research (PEER) Center for the Bridge Rapid Assessment Center for Extreme Events (BRACE2) project. This support is gratefully acknowledged.

Chapter 1

Overview

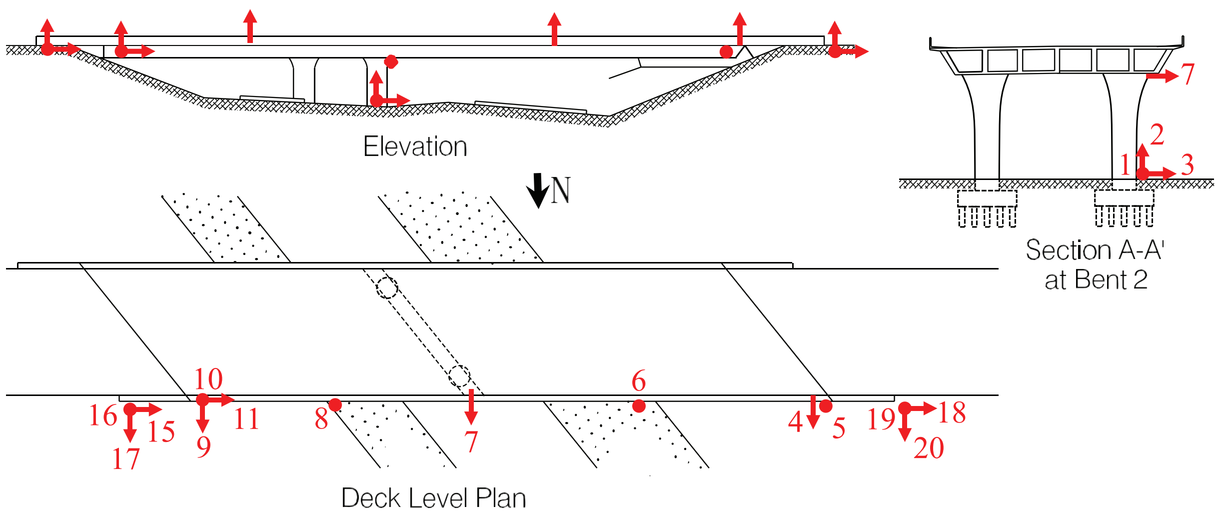

Figure 1.1: Instrumentation of a highway bridge.

1.1 Background

Effective structural assessment requires both accurate physical simulations, and data-driven analysis procedures. In both contexts, sensors on a structure may be regarded as providing input or output signals (Figure 1.1).

1.1.1 Structural Simulation

Physical simulations typically involve a finite element analysis of a structural model subjected to loads that represent the input signals of an event. The response quantities resulting from such a simulation are processed into a label that identifies the predicted condition of the structure. This condition may be evaluated at discrete points in the structure (local evaluation), discrete members (member evaluation), or for the structure as a whole (global evaluation). Localized condition labels may be extrapolated to produce global labels.

Two labeling approaches are distinguished. Capacity approaches evaluate the state of the structure at each step in the simulation and assign labels by association with monotonic response data. For example, a member capacity evaluation may compare resultant moments in beam elements for a column at each point in time against experimental or simulated monotonic load tests. A local capacity evaluation compares point-wise stress or strain at each step against monotonic material tests. Capacity approaches are convenient because monotonic capacity data is often available. However, these approaches are incapable of accounting for hysteretic behavior (Zhou & Kunnath, 2022).

Damage approaches account for hysteretic behavior by associating a damage model to response quantities of interest. A damage model is generally formulated in terms of internal state variables that evolve under cyclic loading and represent stiffness degradation, strength deterioration, residual deformation, or cumulative energy dissipation. These formulations improve physical fidelity under earthquake loading, but require additional calibration data and introduce model uncertainty that is inherent in the specification of model parameters.

In these approaches, the accurate representation of shear response remains a central limitation (Zhou & Kunnath, 2022). The literature identifies several open problems that motivate the present work.

- Le Corvec (2012) identified modular treatment of the Wagner term with full axial torsion interaction as an unresolved issue in nonlinear beam formulations.
- Le Corvec (2012) also identified a need for efficient mixed shear deformable elements capable of representing finite deformations.
- Zhou and Kunnath (2022) noted a need for finite element formulations that represent shear response accurately and efficiently in the condition assessment of non-ductile bridge columns.
- Zhou and Kunnath (2022) further highlighted the need for strain based labeling procedures for columns with arbitrary cross section.

1.1.2 Data-Driven Assessment

Data-driven assessment treats a bridge as a dynamical system inferred from measurements rather than from a fully specified finite element model. Given accelerometer records, identification procedures estimate quantities such as modal frequencies, damping ratios, mode shapes, and reduced state-space parameters. These identified quantities define a baseline representation of normal behavior and can be updated as new events are recorded.

Two identification settings are commonly encountered. When support motion and structural response are both available, input-output procedures estimate transfer characteristics directly from event records. When only the structural response is available, output-only procedures infer dynamic properties from ambient or event-induced vibration under stochastic excitation assumptions. In either setting, condition indicators are constructed from temporal changes in the identified parameters, the residual prediction error, or the derived health metrics, which are calibrated against historical behavior (Chern et al., 2025).

The principal challenge is that parameter changes from data-driven methods are not generally directly attributable to damage (Farrar & Worden, 2007). A practical way to reduce this ambiguity is to couple the system identification process with simulation-based inference.

In this cooperative setting, identification methods provide target response descriptors such as modal properties, transfer characteristics, and selected response histories, while physics-based simulation provides mechanistic constraints for interpretation. Analytic gradients of simulated responses with respect to model parameters then enable the efficient calibration of the simulation model to the identified targets through gradient-based optimization and uncertainty analysis, while avoiding the cost and numerical fragility of finite-difference approximations. This feedback loop lets data-driven procedures refine simulation models which in turn stabilize data-driven indicators.

1.2 Organization

The presentation is organized in two parts.

Part I of this dissertation develops a class of beam models and their finite element implementation that addresses the requirements established in Section 1.1.1 for structural simulation. A detailed review of the literature, a statement of objectives, and the organization of Part I are presented in Chapter 2.

In **Part II** a framework is proposed where data-driven and physics-based predictors are integrated within a common assessment workflow for regional operations. Chapter 7 develops the setting for these contributions in detail.

Part I

Structural Modeling

Chapter 2

Introduction to Part I

2.1 Introduction

Accurate simulation of beams and columns is central to nonlinear structural condition assessment. In framed structures, these members govern the local mechanisms by which stiffness degrades, strength is mobilized, and damage accumulates. For problems of structural assessment, the required analyses must often be performed repeatedly and at scales for which direct three-dimensional continuum discretization is seldom practical. Beam theories therefore remain the principal computational setting for nonlinear analysis of structural systems.

A beam theory is typically formulated as a dimensional reduction of the continuum field equations (Kantorovich & Krylov, 1958; Trabucho & Viano, 1996), where the body is represented by a single spatial dimension associated with the axial direction of the member. The response in the orthogonal directions is condensed into a cross section model, which serves as the constitutive model of the beam theory. Classical fiber sections based on the plane-section hypothesis reconstruct predominantly uniaxial strain fields and are often adequate for slender members under relatively simple loading (Taucer et al., 1991). Under more general loading, however, cross-sectional warping and multiaxial stress states become significant, and their neglect may lead to an overestimation of both member strength and stiffness.

The limitations of the plane-section hypothesis appear even in elementary cases. In torsion of non-circular members, the section does not remain rigid, axial warping develops, and the associated shear stress field cannot be represented by a uniaxial reconstruction. Under transverse shear the situation is more severe, since the Saint–Venant response involves both axial warping and in-plane deformation through the Poisson effect.

When warping is incorporated into a beam formulation, prescribed section shapes are ordinarily introduced and their amplitudes are resolved along the member axis. These approaches may be grouped into two classes. In the first, the effect of warping is represented internally through the classical beam deformation measures. In the second, auxiliary warping fields are introduced explicitly in the beam kinematics. The latter construction is systematic and general, but it increases the number of global unknowns and introduces boundary data whose physical interpretation becomes less transparent as the number of warping fields increases.

2.2 Objectives and Scope

A family of section constitutive models is developed that enhances standard beam elements with the following objectives:

- Inclusion of finite deformations in the element fields.
- Representation of infinitesimal-to-moderate section strains.
- Exact agreement with continuum solutions under elastic uniform warping.
- Exact satisfaction of the continuum equilibrium equations under nonuniform elastic torsion.
- Incorporation of general multiaxial material response.
- Representation of warping with a minimal number of global degrees of freedom.

An overarching objective is to achieve these capabilities through section-level constitutive modeling alone. Consequently, the proposed sections must be compatible with existing beam finite elements without modification to the element implementation.

2.3 Outline

Chapters 3 to 5 establish governing differential equations that model the features of interest. The use of these models in finite element analysis is developed in Chapter 6.

Enhanced Strain Formulation. Chapter 3 presents a novel enhanced assumed strain principle for formulating beam constitutive equations which incorporates assumed strain shapes into the section response. General conditions are imposed on the assumed fields, but specific identifications are not made until the following chapters. A general section state determination algorithm is presented.

Enhanced Internal Warping. Chapter 4 develops enhanced shapes that are suitable when warping boundary effects are insignificant. By imposing agreement with Saint Venant's linear elastic continuum solutions and requiring compatibility with standard beam elements, the space of arbitrary strain fields is reduced to a family with 16 free parameters. Section E.1 and Section E.2 present two explicit identifications of these parameters with formulae that depend on the geometry and composition of the member.

Enhanced External Warping. Chapter 5 develops enhanced strains that are suitable when auxiliary warping fields are introduced in the beam model to represent non-uniform torsional warping. In contrast with Chapter 4, continuum solutions are not available in this setting, and consistency is instead achieved by requiring point-wise equilibrium in the elastic regime. The space of strain fields is reduced to a one-parameter family which furnishes as a special case the torsion model of Armero (2022).

Implementation and Verification. Chapter 6 summarizes the developments of Part I, discusses implementation details, and presents finite element simulations that verify proposed models.

Conclusions and suggestions for future research are given in Chapter 10.

Chapter 3

A Nonlinear Beam Theory with Enhanced Section Strains

3.1 Introduction

This chapter develops a method of formulating cross-section resultant models for a class of nonlinear beam theories based on the geometrically exact Cosserat rod.

In the proposed method, assumed section strain fields are introduced to improve the representation of the underlying three-dimensional strain field, and eliminating the need for some, or all, external warping fields. The amplitudes of the assumed strains are determined locally at each cross section, and in a finite element setting do not interact with the spatial discretization or global system of equations. As a result, the beam equilibrium equations are unchanged, while the section constitutive model is enriched. This feature permits the section models that will later be formulated by the method (Chapters 4 and 5) to be used with existing finite element formulations which have been derived against beam theories in the class of interest.

The outline is as follows. The governing equations for a family of nonlinear beam theories with warping are developed in Section 3.2, where an arbitrary number n of warping fields are permitted. Section 3.3 derives the kinematic linearization of the model, and examines the response of an omitted warping shape in that linear setting. The emerging decomposition of the omitted warping into boundary restraint-driven and local strain-driven components motivates the premise of the following section, where a condensed model is sought to represent the locally determined warping without a corresponding external field. Section 3.4 introduces the family of strain-enhanced section constitutive models. A variational interpretation of the method is presented in Appendix B.

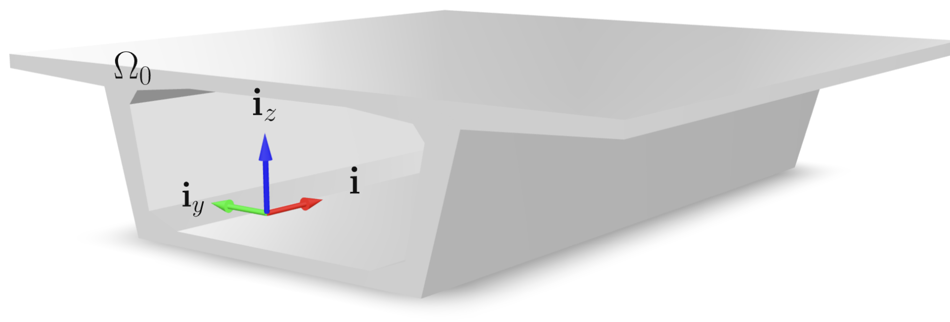

Figure 3.1: A prismatic structural member.

3.2 Nonlinear Beam Theory with General Warping

The model presented in this section is a generalization of the special Cosserat rod (Antman, 1995), where directors are parameterized by a rotation field as introduced by Simo (1984). O'Reilly (2017) provides a historical account of similar rod models. The incorporation of a torsional warping field into this model was introduced by Simo and Vu-Quoc (1991) using linear section kinematics. This formulation was later generalized to three warping fields and nonlinear section kinematics by Klinkel and Govindjee (2003). The present treatment formulates the governing equations for an arbitrary number of warping fields. Its kinematic linearization is equivalent to the model employed by Le Corvec (2012). Additional works concerning the warping of beams that have influenced the present treatment include Brown and Burgoyne (1994), El Fatmi (2007), Armero (2021), and Montalto and Konstantinidis (2024). Additional works are cited throughout the text.

In Section 3.2.1, the body is introduced in the continuum setting. Section 3.2.2 introduces the kinematic representation of this body in terms of one-dimensional beam fields, from which the beam deformations $\boldsymbol{e}$ precipitate and resisting generalized stresses $\boldsymbol{s}$ are implied. Section 3.2.5 derives the work-conjugate section constitutive model $\boldsymbol{e} \to \boldsymbol{s}$ that is compatible with the kinematic assumptions of the theory, and that will serve as the baseline for the enhanced method presented in Section 3.4.

3.2.1 Continuum

A prismatic structural member occupies a region $B = (0, L) \times \Omega$, where $\Omega \subset \mathbb{R}^3$ is a cross-section spanned by two basis vectors $\mathbf{i}_\beta$ in the reference configuration (Figure 3.1). Together with the axial unit vector $\mathbf{i}$, the three vectors $\{\mathbf{i},\, \mathbf{i}_\beta\}$ form an orthonormal basis and the identity in $\mathbb{R}^3$ is:

$$\mathbf{1} = \mathbf{i} \otimes \mathbf{i} + \mathbf{1}_\Omega \qquad \text{with} \qquad \mathbf{1}_\Omega = \mathbf{i}_\beta \otimes \mathbf{i}_\beta$$

where summation over the two plane bases $\mathbf{i}_\beta$ is implied by repetition of the Greek index β. A point in B has coordinates $x\,\mathbf{i} + \boldsymbol{r}$ in the reference configuration, where $\boldsymbol{r}(x) \in \Omega_x$ is the coordinate of a point in the section at x and $\boldsymbol{r} \cdot \mathbf{i} = 0$. The boundary of B consists of the lateral surface $\partial_{\mathbf{i}} B = \Gamma \times (0, L)$ and the surfaces Ω_0, Ω_L of the sections at the ends $x \in \{0, L\}$.

3.2.2 Kinematics

The deformation is represented by the deflection $\boldsymbol{x}(x) \in \mathbb{R}^3$, rotation $\boldsymbol{\Lambda}(x) \in \mathrm{SO}(3)$, and warping fields $\boldsymbol{\alpha}(x) \in \mathbb{R}^{n_w}$:

$$\hat{\boldsymbol{x}}(x, \boldsymbol{r}) = \boldsymbol{x}(x) + \boldsymbol{\Lambda}(\boldsymbol{r} + \mathbf{i} \otimes \boldsymbol{\varphi}(\boldsymbol{r})\boldsymbol{\alpha}(x)) \tag{3.2.1}$$

where $\boldsymbol{\varphi} : \Omega \to \mathbb{R}^{n_w}$ collects n_w cross-sectional warping shapes. The deformation gradient $\boldsymbol{F}$ of the motion (3.2.1) is:

$$\boldsymbol{F} = \boldsymbol{\Lambda}\left(\mathbf{1} + \boldsymbol{\mu} \otimes \mathbf{i} \;+\; \mathbf{i} \otimes \nabla\omega\right), \qquad \text{with} \qquad \boldsymbol{\mu}(\boldsymbol{r}) := \boldsymbol{\gamma} + \boldsymbol{\kappa} \times \left(\boldsymbol{r} + \mathbf{i} \otimes \boldsymbol{\varphi}\,\boldsymbol{\alpha}\right) \tag{3.2.2}$$

where $\omega := \boldsymbol{\varphi} \cdot \boldsymbol{\alpha}$ is the magnitude of axial warping and $\boldsymbol{\gamma}$ and $\boldsymbol{\kappa}$ are the geometrically exact beam strain measures:

$$\begin{aligned} \boldsymbol{\gamma} &= \boldsymbol{\Lambda}^\top \boldsymbol{x}' - \mathbf{i} \\ &= \epsilon\mathbf{i} + \gamma_\beta \mathbf{i}_\beta \end{aligned} \qquad \text{and} \qquad \begin{aligned} \boldsymbol{\kappa} &= \left(\boldsymbol{\Lambda}^\top \boldsymbol{\Lambda}'\right)^\vee \\ &= \varkappa\mathbf{i} + \kappa_\beta \mathbf{i}_\beta \end{aligned} \tag{3.2.3}$$

The vector $\boldsymbol{\gamma}$ comprises the axial strain ϵ and the transverse shears γ_β, and $\boldsymbol{\kappa}$ comprises the twist $\varkappa$ and curvatures κ_β. The notation $(\,\cdot\,)^\vee$ in (3.2.3) furnishes the axial vector of a 3×3 skew-symmetric matrix. Likewise, the notation $(\,\cdot\,)^\times$ provides the skew-symmetric matrix:

$$\begin{pmatrix} \omega_1 \\ \omega_2 \\ \omega_3 \end{pmatrix}^\times = \begin{pmatrix} 0 & -\omega_3 & \omega_2 \\ \omega_3 & 0 & -\omega_1 \\ -\omega_2 & \omega_1 & 0 \end{pmatrix} \tag{3.2.4}$$

The Green-Lagrange strain tensor $\hat{\boldsymbol{E}} := \frac{1}{2}(\boldsymbol{F}^\top \boldsymbol{F} - \mathbf{1})$ is:

$$\hat{\boldsymbol{E}} = \boldsymbol{\mu} \overset{\mathrm{s}}{\otimes} \mathbf{i} + \nabla\omega \overset{\mathrm{s}}{\otimes} \mathbf{i} + (\boldsymbol{\mu} \cdot \mathbf{i})\, \nabla\omega \overset{\mathrm{s}}{\otimes} \mathbf{i} + \frac{1}{2}\left(\boldsymbol{\mu} \cdot \boldsymbol{\mu}\, \mathbf{i} \otimes \mathbf{i} + \nabla\omega \otimes \nabla\omega\right) \tag{3.2.5}$$

where the symmetric bun product $\boldsymbol{a} \overset{\mathrm{s}}{\otimes} \boldsymbol{b}$ is defined for vectors $\boldsymbol{a}$, $\boldsymbol{b}$, and $\boldsymbol{c}$ by

$$(\boldsymbol{a} \overset{\mathrm{s}}{\otimes} \boldsymbol{b})\boldsymbol{c} := \tfrac{1}{2}\big(\boldsymbol{a}\,(\boldsymbol{b}\cdot\boldsymbol{c}) + \boldsymbol{b}\,(\boldsymbol{a}\cdot\boldsymbol{c})\big).$$

Remark 3.2.1. The nonlinearities in the strain tensor (3.2.5) are of two origins:

- *Element geometric nonlinearity* arises from nonlinear dependence of $\boldsymbol{\gamma}$ and $\boldsymbol{\kappa}$ on $\boldsymbol{x}$, $\boldsymbol{\Lambda}$, and $\boldsymbol{\alpha}$ in (3.2.3), and must be resolved by the finite element discretization of the beam axis. This includes the finite rotation $\boldsymbol{\Lambda}$ and the strain measures (3.2.3). Finite element interpolation of the rotation along x requires particular care and has been investigated by several authors including Romero (2004) and Perez and Filippou (2024).
- *Section geometric nonlinearity* arises from nonlinear dependence of $\hat{\boldsymbol{E}}$ on $\boldsymbol{\gamma}$, $\boldsymbol{\kappa}$, $\boldsymbol{\alpha}$ and $\boldsymbol{\alpha}'$. In a finite element setting this may be resolved locally at each cross section.

This separation allows the section constitutive model to be developed independently of the frame model. All strain representations derived below may be employed in connection with either the finite deformation beam model (3.2.1) or its linearization (3.3.2).

3.2.3 Equilibrium Equations

In Section 3.2.2 the measures $\boldsymbol{\gamma}$, $\boldsymbol{\kappa}$, $\boldsymbol{\alpha}$ and $\boldsymbol{\alpha}'$ arise as natural strain measures along x. Thus, in the beam model, the state of stress and strain along x is modeled by the $6 + 2n_w$ dimensional deformation vector $\boldsymbol{e}$ and an implied vector of $6 + 2n_w$ resistance variables $\boldsymbol{s}$ referred to as stress resultants:

$$\boldsymbol{e} := \begin{pmatrix} \boldsymbol{\gamma} \\ \boldsymbol{\kappa} \\ \boldsymbol{\alpha}' \\ \boldsymbol{\alpha} \end{pmatrix} \quad \text{and} \quad \boldsymbol{s} := \begin{pmatrix} \boldsymbol{n} \\ \boldsymbol{m} \\ \boldsymbol{w} \\ \boldsymbol{v} \end{pmatrix} \tag{3.2.6}$$

The governing equations of the beam theory are obtained by requiring that the equality

$$\langle \boldsymbol{s},\, \delta\boldsymbol{e}\rangle_{\mathcal{B}} = \langle \boldsymbol{S},\, \delta\boldsymbol{E}\rangle_{\hat{\mathcal{B}}} \tag{3.2.7}$$

hold for all admissible variations $\delta\boldsymbol{e}$. The identity (3.2.7) is enforced in two steps. Integration along the beam axis $\mathbf{i}$ yields the differential equations of equilibrium in x, and, in Section 3.2.5 below, integration over the cross section will define conjugate stress resultants $\boldsymbol{s}$.

Imposing (3.2.7) by integration along x and integrating by parts furnishes the system of equilibrium equations:

$$\begin{cases} (\boldsymbol{\Lambda n})' + \boldsymbol{f}_{\mathrm{n}} = \mathbf{0} \\ (\boldsymbol{\Lambda m})' + \boldsymbol{x}' \times (\boldsymbol{\Lambda n}) + \boldsymbol{f}_{\mathrm{m}} = \mathbf{0} \\ \boldsymbol{w}' - \boldsymbol{v} + \boldsymbol{f}_{\mathrm{w}} = \mathbf{0} \end{cases} \tag{3.2.8}$$

where $\boldsymbol{f}_{\mathrm{n}}$, $\boldsymbol{f}_{\mathrm{m}}$, and $\boldsymbol{f}_{\mathrm{w}}$ are given body force and moment loadings, respectively.

3.2.4 Material Constitution

Before the conjugate stress resultants $\boldsymbol{s}$ are determined, a customary restriction is introduced regarding the continuum stress field. A general state of strain in a continuum has the representation:

$$\hat{\boldsymbol{E}} = \mathbf{i} \overset{\mathrm{s}}{\otimes} \hat{\boldsymbol{\varepsilon}} + \tilde{\boldsymbol{E}} \tag{3.2.9}$$

where $\tilde{\boldsymbol{E}} := \mathbf{1}_\Omega \hat{\boldsymbol{E}} \mathbf{1}_\Omega$ so that $\mathbf{i} \otimes \mathbf{i} \tilde{\boldsymbol{E}}\, \mathbf{i} \otimes \mathbf{i} = \mathbf{0}$ and the strain vector $\hat{\boldsymbol{\varepsilon}} \in \mathbb{R}^3$ contains the axial $\varepsilon \in \mathbb{R}$ and shear $\boldsymbol{\varepsilon}_\gamma \in \Omega$ terms:

$$\hat{\boldsymbol{\varepsilon}} = \varepsilon\, \mathbf{i} + \boldsymbol{\varepsilon}_\gamma \tag{3.2.10}$$

Note that the components $\mathbf{i}_\beta \cdot \boldsymbol{\varepsilon}_\gamma$ furnish the "engineering" shear strains, which scale the tensorial shear components $\mathbf{i} \cdot \boldsymbol{E}\, \mathbf{i}_\beta$ by a factor of 2 . It is common to restrict the material response in a beam to stress tensors $\boldsymbol{S}$ with the form:

$$\boldsymbol{S} = \sigma\, \mathbf{i} \otimes \mathbf{i} + \boldsymbol{\tau} \otimes \mathbf{i} + \mathbf{i} \otimes \boldsymbol{\tau} \qquad \text{with} \qquad \begin{array}{l} \sigma := \mathbf{i} \cdot \boldsymbol{S}\, \mathbf{i} \\ \boldsymbol{\tau} := \mathbf{i}_\beta \otimes \mathbf{i}_\beta\, \boldsymbol{S}\, \mathbf{i} \end{array} \tag{3.2.11}$$

where σ is the scalar axial stress and $\boldsymbol{\tau} \in \mathbb{R}^2$ the vector of shear stresses. Thus, the in-plane stress components $\mathbf{i}_\alpha \cdot \boldsymbol{S}\, \mathbf{i}_\beta$ are forced to vanish by imposing the constraint:

$$\mathbf{i}_\alpha \cdot \boldsymbol{S}\, \mathbf{i}_\beta = 0 \tag{3.2.12}$$

and the stress tensor (3.2.11) is entirely characterized by the stress vector $\boldsymbol{\sigma} \in \mathbb{R}^3$:

$$\boldsymbol{\sigma} := \boldsymbol{S}\, \mathbf{i} = \sigma \mathbf{i} + \boldsymbol{\tau}. \tag{3.2.13}$$

The condition (3.2.11) naturally arises in Saint Venant's continuum solutions for isotropic prismatic members with uniform Poisson's ratio ν in B (Appendix C). The section of such a member may feature a nonuniform material composition, but Young's E and the shear modulus G will exhibit the dependence:

$$E(\boldsymbol{r}) = 2G(\boldsymbol{r})(1 + \nu) \tag{3.2.14}$$

where independence in x is understood under the present restriction to prismatic members. This is representative of common structural members like reinforced concrete where material inhomogeneity presents strongly through the Young E and shear moduli G, but exhibits little variation in Poisson's ratio.

Although the assumption (3.2.11) is motivated by the special case of linear elasticity with Poisson uniformity (3.2.14), it is routinely retained in more general beam formulations. Klinkel and Govindjee (2003) adopted the assumption in a geometrically exact warping beam and demonstrated excellent agreement with numerical continuum simulations of anisotropic elastic members undergoing finite rotations. Similarly, Gruttmann et al. (2000) adopted the assumption in a geometrically exact warping beam and demonstrated excellent agreement with inelastic shell simulations of members undergoing finite deformations.

Under the condition (3.2.11), the compatible in-plane strain $\tilde{\boldsymbol{E}}$ is orthogonal to the residual (3.2.7), furnishing the simplification:

$$\left\langle \boldsymbol{S},\, \delta\hat{\boldsymbol{E}} \right\rangle = \langle \boldsymbol{\sigma},\, \delta\hat{\boldsymbol{\varepsilon}} \rangle\,. \tag{3.2.15}$$

The in-plane strains are determined implicitly by enforcing $\mathbf{i}_\alpha \cdot \boldsymbol{S}\,\mathbf{i}_\beta = 0$ at each material point through a local condensation procedure outlined in Box 3.1 (Klinkel & Govindjee, 2002).

Box 3.1: Material State Determination

Objective. Given a strain vector $\boldsymbol{\varepsilon} \in \mathbb{R}^3$ and tensorial stress-strain material model $\mathcal{M}\colon \mathrm{Sym}(\mathbb{R}^3, \mathbb{R}^3) \to \mathrm{Sym}(\mathbb{R}^3, \mathbb{R}^3)$, return the stress vector $\boldsymbol{\sigma} \in \mathbb{R}^3$ representing the constrained stress tensor.
Procedure. Perform Newton-Raphson iterations solving for the strain tensor $\tilde{\boldsymbol{E}}$ that satisfies the constraints

$$\mathbf{i}_\alpha \cdot \boldsymbol{S}(\boldsymbol{\varepsilon} \overset{\mathrm{s}}{\otimes} \mathbf{i} + \tilde{\boldsymbol{E}})\,\mathbf{i}_\beta = 0 \tag{3.2.16}$$

3.2.5 Section Constitution

By the virtual work simplification (3.2.15), the section constitutive relation requires only the strain vector $\hat{\boldsymbol{\varepsilon}}$ defined by (3.2.10). This may be truncated at various orders of section-level nonlinearity; two cases of interest are:

Moderate (Wagner) strain. A truncation of (3.2.5) which retains prominent effects under torsion is:

$$\hat{\boldsymbol{\varepsilon}} := \boldsymbol{\gamma} + \boldsymbol{\kappa} \times \boldsymbol{r} + \mathbf{i} \otimes \boldsymbol{\varphi}\,\boldsymbol{\alpha}' + \nabla_\Omega(\boldsymbol{\varphi} \cdot \boldsymbol{\alpha}) + \tfrac{1}{2}\varkappa^2\, \boldsymbol{r} \cdot \boldsymbol{r}\,\mathbf{i} \tag{3.2.17}$$

where $\varkappa := \mathbf{i} \cdot \boldsymbol{\kappa}$ is the rate of twist, or torsional curvature, and ∇_Ω acts with respect to the section coordinates $\boldsymbol{r}$ (Wagner, 1936).

Linear strain. The complete linearization of (3.2.5) furnishes the linear strain:

$$\hat{\boldsymbol{\varepsilon}} := \boldsymbol{\gamma} + \boldsymbol{\kappa} \times \boldsymbol{r} + \mathbf{i} \otimes \boldsymbol{\varphi}\,\boldsymbol{\alpha}' + \nabla_\Omega(\boldsymbol{\varphi} \cdot \boldsymbol{\alpha}) \tag{3.2.18}$$

The variation of the strain vector takes the form $\delta\hat{\boldsymbol{\varepsilon}} = \boldsymbol{A}_\varepsilon\,\delta\boldsymbol{e}$, where $\boldsymbol{A}_\varepsilon(\boldsymbol{r})$ is the *section kinematic matrix*. The moderate strain model (3.2.17) furnishes:

$$\boldsymbol{A}_\varepsilon = \begin{bmatrix} \mathbf{1} & -\boldsymbol{r}^\times + \varkappa r^2 \mathbf{i} \otimes \mathbf{i} & \mathbf{i} \otimes \boldsymbol{\varphi} & \mathbf{i}_\beta \otimes \nabla_\beta \boldsymbol{\varphi} \end{bmatrix}, \tag{3.2.19}$$

where $r^2 := \boldsymbol{r} \cdot \boldsymbol{r}$. The linear form (3.2.18) gives:

$$\boldsymbol{A}_\varepsilon = \begin{bmatrix} \mathbf{1} & -\boldsymbol{r}^\times & \mathbf{i} \otimes \boldsymbol{\varphi} & \mathbf{i}_\beta \otimes \nabla_\beta \boldsymbol{\varphi} \end{bmatrix}. \tag{3.2.20}$$

Resultants. Recall the Frobenius inner product $\boldsymbol{A} \cdot \boldsymbol{B} := \operatorname{tr} \boldsymbol{A}\boldsymbol{B}^\top$ for two linear operators $\boldsymbol{A}$ and $\boldsymbol{B}$. Under the stress constraint (3.2.12), variations $\delta\hat{\boldsymbol{E}}$ take the form $(\boldsymbol{A}_\varepsilon \delta\boldsymbol{e}) \overset{\mathrm{s}}{\otimes} \mathbf{i}$, which furnishes in (3.2.7):

$$\langle \boldsymbol{S},\, \delta\boldsymbol{E} \rangle_\Omega = \int \operatorname{tr}\left[\boldsymbol{S}\, \tfrac{1}{2}\left(\boldsymbol{A}_\varepsilon \delta\boldsymbol{e} \otimes \mathbf{i} + \mathbf{i} \otimes \boldsymbol{A}_\varepsilon \delta\boldsymbol{e}\right)\right]\, \mathrm{d}A.$$

Exploiting linearity of the trace together with the identity $\operatorname{tr}(\boldsymbol{a} \otimes \boldsymbol{b}) = \boldsymbol{a} \cdot \boldsymbol{b}$ for arbitrary vectors $\boldsymbol{a}$ and $\boldsymbol{b}$ yields

$$\langle \boldsymbol{S},\, \delta\boldsymbol{E} \rangle_\Omega = \delta\boldsymbol{e} \cdot \int \boldsymbol{A}_\varepsilon^\top\, \tfrac{1}{2}\left(\boldsymbol{S}\,\mathbf{i} + \boldsymbol{S}^\top \mathbf{i}\right)\, \mathrm{d}A,$$

and consequently, requiring (3.2.7) section-wise, the conjugate resultants $\boldsymbol{s}$ are:

$$\boldsymbol{s} = \int \boldsymbol{A}_\varepsilon^\top \boldsymbol{\sigma}\, \mathrm{d}A \tag{3.2.21}$$

where the last equality uses symmetry of $\boldsymbol{S}$ and the definition (3.2.13) of the stress vector. Linearizing the stress resultant relation (3.2.21) about $\boldsymbol{e}$ furnishes the section tangent:

$$\boldsymbol{K}_s := \int \boldsymbol{A}_\varepsilon^\top \mathbb{C} \boldsymbol{A}_\varepsilon\, \mathrm{d}A + \boldsymbol{K}_\sigma = \boldsymbol{K}_\ell + \boldsymbol{K}_\sigma \tag{3.2.22}$$

where $\mathbb{C}$ is the 3×3 tangent of the condensed material response,

$$\boldsymbol{K}_\ell = \int \begin{bmatrix} \mathbb{C} & -\mathbb{C}\boldsymbol{r}^\times & \mathbb{C}\mathbf{i} \otimes \boldsymbol{\varphi} & \mathbb{C}\mathbf{i}_\beta \otimes \nabla_\beta \boldsymbol{\varphi} \\ & -\boldsymbol{r}^\times \mathbb{C} \boldsymbol{r}^\times & \boldsymbol{r}^\times \mathbb{C}\mathbf{i} \otimes \boldsymbol{\varphi} & \boldsymbol{r}^\times \mathbb{C}\mathbf{i}_\beta \otimes \nabla_\beta \boldsymbol{\varphi} \\ & & \boldsymbol{\varphi} \otimes \mathbf{i}\mathbb{C}\mathbf{i} \otimes \boldsymbol{\varphi} & \boldsymbol{\varphi} \otimes \mathbf{i}\mathbb{C}\mathbf{i}_\beta \otimes \nabla_\beta \boldsymbol{\varphi} \\ \text{sym.} & & & \nabla_\beta \boldsymbol{\varphi} \otimes \mathbf{i}_\beta \mathbb{C}\mathbf{i}_\beta \otimes \nabla_\beta \boldsymbol{\varphi} \end{bmatrix} \mathrm{d}A \tag{3.2.23}$$

and $\boldsymbol{K}_\sigma$ is obtained by linearizing the Wagner term (3.2.17):

$$\boldsymbol{K}_\sigma = \varkappa \int \begin{bmatrix} \mathbf{0} & r^2 \mathbb{C}\mathbf{i} \otimes \mathbf{i} & \mathbf{0} & \mathbf{0} \\ & r^2 \left(\boldsymbol{r}^\times \mathbb{C}\mathbf{i} \otimes \mathbf{i} - \mathbf{i} \otimes \mathbf{i} \mathbb{C} \boldsymbol{r}^\times \right) & r^2 \mathbf{i} \otimes \mathbf{i} \mathbb{C}\mathbf{i} \otimes \boldsymbol{\varphi} & r^2 \mathbf{i} \otimes \mathbf{i} \mathbb{C}\mathbf{i}_\beta \otimes \nabla_\beta \boldsymbol{\varphi} \\ & & \mathbf{0} & \mathbf{0} \\ \text{sym.} & & & \mathbf{0} \end{bmatrix} \mathrm{d}A$$

$$+ \varkappa^2 \int \begin{bmatrix} \mathbf{0} & \mathbf{0} & \mathbf{0} & \mathbf{0} \\ & r^4 \mathbf{i} \otimes \mathbf{i} \mathbb{C}\mathbf{i} \otimes \mathbf{i} & \mathbf{0} & \mathbf{0} \\ & & \mathbf{0} & \mathbf{0} \\ \text{sym.} & & & \mathbf{0} \end{bmatrix} \mathrm{d}A \tag{3.2.24}$$

$$+ \int \begin{bmatrix} \mathbf{0} & \mathbf{0} & \mathbf{0} & \mathbf{0} \\ & r^2 \sigma & \mathbf{0} & \mathbf{0} \\ & & \mathbf{0} & \mathbf{0} \\ \text{sym.} & & & \mathbf{0} \end{bmatrix} \mathrm{d}A$$

3.2.6 Summary and Remarks

Box 3.2 summarizes the model developed in this section, with notation collected in Table 3.1.

Warping Variables. Each warping field α describes how much a warping shape φ is excited. Because each shape φ enters with an independent amplitude α, warping restraints against a given shape may be modeled by fixing boundary conditions in the amplitude field α. For certain cross sectional shapes, physical warping restraints significantly alter the behavior of the member, and the possibility to model this by fixing the field α proves valuable for accurate simulation. However, it is often the case that these boundary conditions produce little discernible effect, despite the warping still producing a significant impact in the overall response. This is investigated in the following section.

Section Kinematics. In Section 3.2.2 three compatibility relations have been derived relating the beam deformations $\boldsymbol{e}$ to a material strain tensor $\boldsymbol{E}$: the exact form (3.2.5), the partial truncation (3.2.17), and the total linearization (3.2.18). All three representations of the material strains may be employed in connection with a finite deformation beam theory (3.2.1), or the linearization (3.3.2). In the remainder of this work attention will be limited to the moderate-strain Wagner model (3.2.17), and the linearized model (3.2.18). These results specialize to several notable works in the literature:

- Simo and Vu-Quoc (1991) employed the linearized material kinematics (3.2.18) in connection with the geometrically exact model (Box 3.2) with one warping mode associated to the Saint-Venant torsion function. Gruttmann et al. (2000) generalized Simo and Vu-Quoc (1991) to consider sections in arbitrary coordinate systems and elasto-plastic material response. The present treatment supports an arbitrary number of warping shapes, and allows for accurate incorporation of the Wagner effect in the geometrically exact setting (3.2.1) by switching the cross-sectional model.

- The higher-order strain field (3.2.17) was considered by Battini (2002) and Le Corvec (2012) with specializations of the linearized beam model (Box 3.3). However, these works tightly coupled the effect of nonlinear section strains to the expression of the frame model. In the work by Battini (2002) this resulted in a dedicated finite element implementation to incorporate the effect. Du and Hajjar (2021) employed a similar approach. Le Corvec (2012) achieved a modular implementation by averaging out the Wagner effect and incorporating it into a geometric transformation. However, this approach was found to be less accurate, and remains coupled to the element implementation. In the present approach the effect is encapsulated in the section resultant model and is compatible with any finite element formulation in the family presented in Section 3.2 without loss of accuracy as demonstrated in Example 6.5.

Box 3.2: Geometrically Exact Frame Model

Equilibrium (3.2.8)

$$\left\{\begin{aligned} (\boldsymbol{\Lambda n})' + \boldsymbol{f}_n &= \mathbf{0} \\ (\boldsymbol{\Lambda m})' + \boldsymbol{x}' \times (\boldsymbol{\Lambda n}) + \boldsymbol{f}_m &= \mathbf{0} \\ \boldsymbol{w}' - \boldsymbol{v} + \boldsymbol{f}_{\mathrm{w}} &= \mathbf{0} \end{aligned}\right.$$

Kinematics (3.2.1)

$$\boldsymbol{\gamma} = \boldsymbol{\Lambda}^{\top}\boldsymbol{x}' - \mathbf{i} \qquad \text{and} \qquad \boldsymbol{\kappa} = \left(\boldsymbol{\Lambda}^{\top}\boldsymbol{\Lambda}'\right)^{\vee}$$

Table 3.1: Summary of symbols for Chapter 3

Symbol	Equation	Description
		Kinematics
x		Beam coordinate normalized by reference arc length
$\{\mathbf{i}, \mathbf{i}_\beta\}$		Beam directors in the reference configuration
$\boldsymbol{x}$	(3.2.1)	Position of a cross section
$\boldsymbol{\Lambda}$	(3.2.1)	Rotation of a cross section
n_w		Number of warping fields
$\boldsymbol{\alpha}$		Warping fields
$\boldsymbol{\varphi}$	(3.2.1)	Axial warping shapes.
$\boldsymbol{\gamma}$	(3.2.3) or (3.3.3)	Beam shear deformation vector along x
$\boldsymbol{\kappa}$	(3.2.3) or (3.3.3)	Beam curvature vector
$\varkappa$	(3.2.3)	Rate of twist, defined as $\mathbf{i} \cdot \boldsymbol{\kappa}$
		Material
$\hat{\boldsymbol{E}}$		Compatible strain tensor
$\boldsymbol{S}$		Material stress tensor
$\boldsymbol{\sigma}$	(3.2.13)	Saint Venant stress vector
$\hat{\varepsilon}$	(3.2.9)	Compatible strain vector
		Section
$\boldsymbol{A}_\varepsilon$	(3.2.19) or (3.2.20)	Compatible section kinematic matrix
$\boldsymbol{e}$		Strain resultant vector
$\boldsymbol{s}$	(3.2.21)	Stress resultant vector

3.3 Linearized Beam Theory and Internal Warping

The present section temporarily departs from the nonlinear setting to investigate properties of warping solutions $\boldsymbol{\alpha}$ and their contribution to the model's response. The results of this investigation will motivate the subsequent development of a local condensation procedure in the nonlinear setting.

3.3.1 Kinematic Linearization

In the linear setting the rotation $\boldsymbol{\Lambda}$ is most naturally expressed by a vector $\boldsymbol{\theta} \in \mathbb{R}^3$ defined as:

$$\boldsymbol{\theta} \coloneqq \operatorname{Log} \boldsymbol{\Lambda}$$

where the logarithm Log is introduced in Section G.2.2. Linearizing (3.2.1) produces:

$$\hat{\boldsymbol{x}}(x, \boldsymbol{r}) = (x\mathbf{i} + \boldsymbol{r}) + \boldsymbol{u} + \boldsymbol{\theta}(x) \times \boldsymbol{r} + \mathbf{i} \otimes \boldsymbol{\varphi}(\boldsymbol{r})\, \boldsymbol{\alpha}(x) \tag{3.3.1}$$

and the linearized displacement $\hat{\boldsymbol{u}} \coloneqq \hat{\boldsymbol{x}} - (x\mathbf{i} + \boldsymbol{r})$ is

$$\hat{\boldsymbol{u}}(x, \boldsymbol{r}) = \boldsymbol{u}(x) + \boldsymbol{\theta}(x) \times \boldsymbol{r} + \mathbf{i} \otimes \boldsymbol{\varphi}(\boldsymbol{r})\, \boldsymbol{\alpha}(x) \tag{3.3.2}$$

In terms of the linearized deflection $\boldsymbol{u} \coloneqq \boldsymbol{x} - x\,\mathbf{i}$ the linearized strains (3.2.1) are:

$$\boldsymbol{\gamma} = \boldsymbol{u}' + \mathbf{i} \times \boldsymbol{\theta}, \qquad \boldsymbol{\kappa} = \boldsymbol{\theta}'. \tag{3.3.3}$$

Linearizing the rotation $\boldsymbol{\Lambda}$ and position $\boldsymbol{x}$ in the equilibrium balance produces the model with governing equations summarized in Box 3.3.

Box 3.3: Linearized Frame Model

Equilibrium

$$\begin{cases} \boldsymbol{n}' + \boldsymbol{f}_n = \mathbf{0} \\ \boldsymbol{m}' + \mathbf{i} \times \boldsymbol{n} + \boldsymbol{f}_m = \mathbf{0} \\ \boldsymbol{w}' - \boldsymbol{v} + \boldsymbol{f}_{\mathrm{w}} = \mathbf{0} \end{cases} \tag{3.3.4}$$

Kinematics. (3.3.3)

$$\boldsymbol{\gamma} = \boldsymbol{u}' + \mathbf{i} \times \boldsymbol{\theta} \qquad \text{and} \qquad \boldsymbol{\kappa} = \boldsymbol{\theta}'$$

3.3.2 Uniform Warping

Consider a baseline model with n shapes $\boldsymbol{\varphi}$ and a second model that incorporates an additional warping shape $\varphi_{n+1} : \Omega \to \mathbb{R}$ that is not represented in the first basis $\boldsymbol{\varphi}$. The objective is to characterize the part of the response arising from this omitted shape that can be represented through the retained beam state $\boldsymbol{e}$ of model with only n shapes. The investigation extends classical characterizations of single-field warping torsion to the setting of multiple warping shapes (Trahair, 1993). A similar investigation was undertaken by Hjelmstad (1987) for planar shear warping.

The model with $n+1$ fields appends φ_{n+1} to $\boldsymbol{\varphi}$ and appends a new field α_{n+1} to $\boldsymbol{\alpha}$:

$$\boldsymbol{\varphi} \to \begin{pmatrix} \boldsymbol{\varphi} \\ \varphi_{n+1} \end{pmatrix}, \qquad \boldsymbol{\alpha} \to \begin{pmatrix} \boldsymbol{\alpha} \\ \alpha_{n+1} \end{pmatrix}.$$

This introduces the equilibrium equation:

$$w'_{n+1} - v_{n+1} + f_{\mathrm{w},n+1} = 0, \tag{3.3.5}$$

The resultant constitutive equations are expressed by the $(6+2n+2)\times(6+2n+2)$ stiffness matrix with blocks determined by (3.2.23):

$$\begin{pmatrix} \boldsymbol{s} \\ w_{n+1} \\ v_{n+1} \end{pmatrix} = \begin{bmatrix} \mathbf{K}_n & \boldsymbol{k}_{ew} & \boldsymbol{k}_{ev} \\ & k_{ww} & k_{wv} \\ \text{sym.} & & k_{vv} \end{bmatrix} \begin{pmatrix} \boldsymbol{e} \\ \alpha'_{n+1} \\ \alpha_{n+1} \end{pmatrix}. \tag{3.3.6}$$

where $\mathbf{K}_n$ is the stiffness of the baseline model. Substitution of (3.3.6) into (3.3.5) gives the differential equation governing the additional amplitude:

$$k_{ww}\, \alpha''_{n+1} - k_{vv}\, \alpha_{n+1} = -\boldsymbol{k}_{ew} \cdot \boldsymbol{e}' + \boldsymbol{k}_{ev} \cdot \boldsymbol{e} - f_{\mathrm{w},n+1}. \tag{3.3.7}$$

It is assumed that the member is not subjected to distributed loading $\boldsymbol{f}$. The solution to (3.3.7) has the decomposition

$$\alpha_{n+1} = \alpha_{\mathrm{h}} + \alpha_{\mathrm{p}}, \tag{3.3.8}$$

where α_{h} and α_{p} solve the homogeneous and particular problems:

$$\mathrm{L}\, \alpha_{\mathrm{h}} = 0, \tag{3.3.9a}$$
$$\mathrm{L}\, \alpha_{\mathrm{p}} = -\boldsymbol{k}_{\mathrm{ew}} \cdot \boldsymbol{e}' + \boldsymbol{k}_{\mathrm{ev}} \cdot \boldsymbol{e} \tag{3.3.9b}$$

with $\mathrm{L}\, \alpha := k_{\mathrm{ww}}\, \alpha'' - k_{\mathrm{vv}}\, \alpha$. The homogeneous problem (3.3.9a) has the solution:

$$\alpha_{\mathrm{h}}(x) = A_+ e^{x/\ell_{n+1}} + A_- e^{-x/\ell_{n+1}}, \qquad \ell_{n+1} := \sqrt{k_{\mathrm{ww}}/k_{\mathrm{vv}}}, \tag{3.3.10}$$

with constants A_+ and A_- fixed by the warping boundary data of the $(n+1)$ model. A particular solution is sought in terms of constant vectors $\boldsymbol{c}_{\mathrm{v}}$ and $\boldsymbol{c}_{\mathrm{w}}$ such that

$$\alpha_{\mathrm{p}} = \boldsymbol{c}_{\mathrm{v}} \cdot \boldsymbol{e}, \qquad \alpha'_{\mathrm{p}} = \boldsymbol{c}_{\mathrm{w}} \cdot \boldsymbol{e}. \tag{3.3.11}$$

In the absence of body loads, the linear model admits a closed form solution where the strains $\boldsymbol{e}$ are given by (A.0.2) in terms of a matrix $\boldsymbol{G}$. Substituting (3.3.11) and (A.0.2) into (3.3.9b) gives

$$\boldsymbol{c}_{\mathrm{v}} = \left(k_{ww}\,(\boldsymbol{G}^\top)^2 - k_{vv}\mathbf{1}\right)^{-1} \left(\boldsymbol{k}_{\mathrm{ev}} - \boldsymbol{G}^\top \boldsymbol{k}_{ew}\right), \qquad \text{and} \qquad \boldsymbol{c}_{\mathrm{w}} = \boldsymbol{G}^\top \boldsymbol{c}_{\mathrm{v}}. \tag{3.3.12}$$

As long as the inverted matrix in (3.3.12) is not singular, (3.3.11) identifies the particular solution of the $(n+1)$-global model. The particular solution (3.3.11) contributes a local constitutive correction

$$\Delta \boldsymbol{K}_s = \boldsymbol{k}_{ew} \otimes \boldsymbol{c}_{\mathrm{w}} + \boldsymbol{k}_{ev} \otimes \boldsymbol{c}_{\mathrm{v}}. \tag{3.3.13}$$

and the corresponding strain induced by φ_{n+1} is

$$\Delta\hat{\boldsymbol{\varepsilon}}_{n+1} = \mathbf{i}\,\varphi_{n+1}\,(\boldsymbol{c}_{\mathrm{w}} \cdot \boldsymbol{e}) + \nabla_\Omega \varphi_{n+1}\,(\boldsymbol{c}_{\mathrm{v}} \cdot \boldsymbol{e}), \tag{3.3.14}$$

which is independent of the homogeneous external amplitude field α_{h}.

The homogeneous solution (3.3.10) carries the effects of restraints on the warping shape φ_{n+1}, which decay with a rate of ℓ_{n+1}. Warping of this nature is referred to as *nonuniform* warping, and cannot be represented by the baseline state $\boldsymbol{e}$ alone. In contrast, the contribution by the particular solution is referred to as *uniform* warping.

For a member of length L, the significance of this effect is measured by the dimensionless length:

$$\rho_{n+1} := \ell_{n+1}/L. \tag{3.3.15}$$

When $\ell_{n+1}/L \ll 1$, the homogeneous solution is confined to thin layers near the restrained ends and the section-local particular solution reproduces the $(n+1)$-global response over the bulk of the member.

3.4 Nonlinear Enhanced Strain Section Formulation

Section 3.3 demonstrates that in the linear elastic setting with vanishing body loads, the n-field warping model retains several salient characteristics of the classical torsion problem. In particular, for a field α_{n+1} appended to a baseline model:

- There exists[1] a particular warping solution that is resolvable pointwise along x in terms of only the baseline model's strains $\boldsymbol{e}$,
- Boundary effects on the warping shape φ_{n+1} enter through the homogeneous solution (3.3.10), which does not follow the baseline strains $\boldsymbol{e}$, and necessitates the external field α_{n+1},
- The potential significance of the homogeneous solution for a particular member is measured in part by the characteristic length scale ℓ_{n+1} of the warping mode.

[1] Assuming invertibility in (3.3.12).

In the literature these results are typically extrapolated to model uniform torsion in geometrically exact beams. This is viable because torsion introduces several simplifications to the general equations of Section 3.3. Under the fully nonlinear model of Box 3.2 with multiple warping fields complications arise:

- The construction of the evolution operator $\boldsymbol{G}$ is not generally possible. Under pure isotropic torsion the model of Box 3.2 degenerates to exactly the linear model of Box 3.3.
- When general warping shapes are admitted, the reduced tangent (3.3.13) is not symmetric in general and thus the reduced constitutive model is not necessarily variational. Torsion is a special case for which this can be made variational.
- It is a reasonable expectation that introducing an unrestrained deformation mode to a structural model would produce a softer model. However, in general (3.3.13) may produce either a stiffened or softened response relative to the baseline model.

Thus an assumed strain procedure is proposed that incorporates boundary-insensitive warping modes into the section response, that avoids these issues in the geometrically exact setting.

3.4.1 Enhanced Strain Field

The compatible strain vector $\hat{\boldsymbol{\varepsilon}}$ of Section 3.2.5 is regarded as the action of a section operator on the beam strain measures,

$$\mathrm{A}[\boldsymbol{e}] \;:=\; \hat{\boldsymbol{\varepsilon}}(\boldsymbol{e}) \in L_2(\Omega; \mathbb{R}^3),$$

so that $\hat{\boldsymbol{\varepsilon}}(\boldsymbol{e})(\boldsymbol{r})$ is the compatible point-wise strain vector at a point $\boldsymbol{r}$ in the section Ω_x at x. The enhanced strain ansatz augments this field by a finite set of section modes with the form:

$$\bar{\boldsymbol{\varepsilon}}(x, \boldsymbol{r}) = \hat{\boldsymbol{\varepsilon}}(\boldsymbol{e}) + \bar{\boldsymbol{A}}(\boldsymbol{r})\boldsymbol{\eta}(x) \tag{3.4.1}$$

where $\bar{\boldsymbol{A}}(\boldsymbol{r}) \in \mathbb{R}^{3\times n_L}$ is a matrix of prescribed linearly independent shape functions and $\boldsymbol{\eta}(x) \in \mathbb{R}^{n_L}$ is a vector of *local* section parameters. The ansatz (3.4.1) is analogous to the classical enhanced/assumed strain formulation of solid mechanics which derives from a three-field variational statement of elasticity (Simo & Hughes, 1986; Simo & Rifai, 1990; Simo & Armero, 1992).

The enhanced modes generate the finite-dimensional subspace $\tilde{\mathcal{E}}$, consisting of strain tensors of the form $(\bar{\boldsymbol{A}}(\boldsymbol{r})\boldsymbol{\eta}) \overset{s}{\otimes} \mathbf{i}$. Two restrictions on $\tilde{\mathcal{E}}$ naturally arise.

3.4.2 Stability

The enhanced modes must be linearly independent of strains already representable by admissible beam fields. This requires:

$$\tilde{\mathcal{E}} \cap \mathrm{A}[\mathcal{E}] = \{0\}, \tag{3.4.2}$$

where $\mathcal{E}$ is the space of admissible frame strain fields $\boldsymbol{e}(x)$. Equation (3.4.2) ensures identifiability of the split in (3.4.1) and prevents rank deficiency in the local condensation.

3.4.3 Consistency

A second consideration is that the enhanced strain space is L_2-orthogonal to the space of admissible stresses $\mathcal{S}^h$. This is equivalent to requiring:

$$\tilde{\boldsymbol{g}}(\boldsymbol{\eta}) = \boldsymbol{0} \tag{3.4.3}$$

where the residual $\tilde{\boldsymbol{g}}$ is:

$$\tilde{\boldsymbol{g}}(\boldsymbol{\eta}) := \int \bar{\boldsymbol{A}}^\top \boldsymbol{\sigma}\left(\hat{\boldsymbol{\varepsilon}}(\boldsymbol{e}) + \bar{\boldsymbol{A}}\boldsymbol{\eta}\right)\, \mathrm{d}A \tag{3.4.4}$$

When (3.4.3) holds, virtual work contributions associated with variations $\delta\boldsymbol{\eta}$ vanish, so the beam-level balance laws remain those of Section 3.2 and only the section constitutive mapping $\boldsymbol{e} \mapsto \boldsymbol{s}$ is modified through the enhanced stress response.

Remark 3.4.1. The condition (3.4.3) is ideal, but it is not strictly required for the objective of Chapter 4 which seeks to represent Saint-Venant solutions exactly in the linear elastic regime. In contrast, the stability condition (3.4.2) is always required. This is investigated further below in Appendix B and Chapter 4.

3.4.4 Implementation

For a given strain state $\boldsymbol{e}(x)$, the enhanced parameters $\boldsymbol{\eta}(x)$ are obtained locally by solving (3.4.4) at the section. This local solve is performed concurrently with the material-point condensation implied by (3.2.11). At each section quadrature point one evaluates $\bar{\boldsymbol{\varepsilon}} = \mathrm{A}[\boldsymbol{e}] + \bar{\boldsymbol{A}}\boldsymbol{\eta}$, computes the constrained stress vector $\boldsymbol{\sigma}(\bar{\boldsymbol{\varepsilon}})$, and assembles $\tilde{\boldsymbol{g}}(\boldsymbol{\eta})$. A Newton iteration in $\boldsymbol{\eta}$ then furnishes the unique section value. The corresponding beam resultants are computed exactly as in (3.2.21), using the stress vector associated with the enhanced strain state (3.4.1).

The consistent linearization follows by differentiating the resultant map and the local residual. Linearizing (3.2.21) furnishes:

$$\mathcal{L}\boldsymbol{s} = \boldsymbol{K}_n \mathrm{d}\boldsymbol{e} + \boldsymbol{K}_{e\eta}\mathrm{d}\boldsymbol{\eta} \tag{3.4.5}$$

where $\boldsymbol{K}_n$ is defined by (3.2.22) and:

$$\boldsymbol{K}_{e\eta} := \int \boldsymbol{A}_\varepsilon^\top \mathbb{C} \bar{\boldsymbol{A}} \, \mathrm{d}A \tag{3.4.6a}$$

Linear independence in $\boldsymbol{A}_\varepsilon$ ensures $\boldsymbol{K}_n$ inherits symmetry and positivity in $\mathbb{C}$:

$$\mathbb{C} \succ 0 \qquad \Longrightarrow \qquad \boldsymbol{K}_n \succ 0$$

Linearizing (3.4.4) furnishes:

$$\mathcal{L}\tilde{\boldsymbol{g}} = \mathbf{K}_{e\eta}^\top \mathrm{d}\boldsymbol{e} + \mathbf{K}_{\eta\eta} \mathrm{d}\boldsymbol{\eta} \qquad \text{so} \qquad \mathrm{d}\boldsymbol{\eta} = \widetilde{\mathbf{K}} \mathrm{d}\boldsymbol{e} \tag{3.4.7}$$

with

$$\boldsymbol{K}_{\eta\eta} := \int \bar{\boldsymbol{A}}^\top \mathbb{C} \bar{\boldsymbol{A}} \, \mathrm{d}A \tag{3.4.8a}$$

$$\tag{3.4.8b}$$

where $\boldsymbol{K}_{\eta\eta}$ similarly inherits the variational structure in $\mathbb{C}$. Substitution in (3.4.5) produces the condensed section tangent:

$$\boldsymbol{K}_s = \boldsymbol{K}_n - \mathbf{K}_{\eta e}^\top \boldsymbol{K}_{\eta\eta}^{-1} \boldsymbol{K}_{e\eta}^\top \tag{3.4.9}$$

where invertibility of $\boldsymbol{K}_s$ is ensured by (3.4.2). The complete procedure is summarized by Box 3.4.

The general algorithm for the state determination of the section is summarized by Box 3.4.

Chapter 4 pertains to beam models without auxiliary warping fields and results in a family of section models with 16 free parameters. These parameters, collected in Table 4.2, determine the kinematic association between the beam fields $\boldsymbol{u}, \boldsymbol{\theta}$ and the continuum motion $\hat{\boldsymbol{u}}$. Two distinct resolutions for these parameters are developed in Section E.1 and Section E.2. These models are generally appropriate when cross sectional warping is expected to vary uniformly in x and the effects of warping restraints can be neglected.

Chapter 5 pertains to beams with an auxiliary torsional warping field α. This model is suitable for thin-walled sections where the effect of warping restraints is significant.

The enhanced shapes of Chapter 4 and Chapter 5 require warping functions that are defined by boundary value problems in the section. The point-wise values of these functions and their gradients at integration points in the section (i.e., fibers) are supplied as input data for the cross section model. The process is summarized by Box 3.5.

Box 3.4: Section State Determination

Objective. Given deformations $\boldsymbol{e}$, compute resultants $\boldsymbol{s}$ (3.2.21), enhanced parameters $\boldsymbol{\eta}$, and the tangent $\boldsymbol{K}_s$ (3.4.9) by solving (3.4.4) over a cross section discretization as described in Box 3.5:

$$\{\boldsymbol{r}_\ell,\, \mathrm{d}A_\ell,\, \boldsymbol{A}_\varepsilon(\boldsymbol{r}_\ell),\, \bar{\boldsymbol{A}}(\boldsymbol{r}_\ell),\, \mid \boldsymbol{r}_\ell \in \Omega^h\}$$

Procedure.

1. Retrieve the section state variable $\boldsymbol{\eta} \in \mathbb{R}^{n_L}$ from the prior evaluation

2. Find $\boldsymbol{\eta}$, $\boldsymbol{K}_{e\eta}$ (3.4.6a), and $\boldsymbol{K}_{\eta\eta}$ by solving the residual equation (3.4.4):

$$\tilde{\boldsymbol{g}}(\boldsymbol{\eta}) := \int \bar{\boldsymbol{A}}^\top \boldsymbol{\sigma}\left(\hat{\boldsymbol{\varepsilon}}(\boldsymbol{e}) + \bar{\boldsymbol{A}}\boldsymbol{\eta}\right)\, \mathrm{d}A \tag{3.4.4}$$

   where at each Newton-Raphson iteration k:

$$\boldsymbol{\eta}^{k+1} = \boldsymbol{\eta}^k - \boldsymbol{K}_{\eta\eta}^{-1}\tilde{\boldsymbol{g}}(\boldsymbol{\eta}^k) \qquad \text{and} \qquad \boldsymbol{K}_{\mathrm{ae}} = \int \bar{\boldsymbol{A}}^\top \mathbb{C}^k \boldsymbol{A}_\varepsilon\, \mathrm{d}A$$

   and the stress vector $\boldsymbol{\sigma}$ and tangent $\mathbb{C}$ are evaluated using the procedure of Box 3.1 with $\boldsymbol{\varepsilon} = \hat{\boldsymbol{\varepsilon}}(\boldsymbol{e}) + \bar{\boldsymbol{A}}\boldsymbol{\eta}$.

3. Integrate the section resultant vector $\boldsymbol{s}$ (3.2.21) and tangent $\boldsymbol{K}_n$ (3.2.22):

$$\boldsymbol{s} = \int \boldsymbol{A}_\varepsilon^\top \boldsymbol{\sigma}(\hat{\boldsymbol{\varepsilon}} + \bar{\boldsymbol{A}}\boldsymbol{\eta})\, \mathrm{d}A \qquad \text{and} \qquad \boldsymbol{K}_s = \int \boldsymbol{A}_\varepsilon^\top \mathbb{C} \boldsymbol{A}_\varepsilon\, \mathrm{d}A + \boldsymbol{K}_\sigma$$

   with $\boldsymbol{K}_\sigma$ given by (3.2.24).

4. Form the tangent $\boldsymbol{K}_s$ (3.4.9):

$$\boldsymbol{K}_s = \boldsymbol{K}_n - \mathbf{K}_{\eta e}^\top \boldsymbol{K}_{\eta\eta}^{-1} \boldsymbol{K}_{e\eta}^\top \tag{3.4.9}$$

Box 3.5: Section Preprocessing

Objective. Given a cross section $\Omega \subset \mathbb{R}^2$ where each point is assigned a tensorial stress-strain material $\mathcal{M} : \boldsymbol{E} \mapsto \boldsymbol{S}$, define a *cross section discretization* Ω^h. **Procedure.**

1. Discretize the section Ω into quadrature points $\{\boldsymbol{r}_\ell\}$ and weights $\{\mathrm{d}A_\ell\}$
2. Compute the relevant warping shapes for $\bar{\boldsymbol{A}}$ over Ω^h:
   - $\bar{\varphi}_{\mathrm{I}}$ via Equation (C.3.3) for Chapter 4 and Chapter 5
   - $\bar{\boldsymbol{\varphi}}_{\mathrm{II}}$ via Equation (C.4.5) for Chapter 4
   - ψ via Equation (5.4.3) for Chapter 5
3. Supply the constants of Table 4.2 (Chapter 4) or (5.4.11) (Chapter 5).
4. For each point ℓ in the section discretization supply
   - The coordinates $\boldsymbol{r}_\ell$ and weight $\mathrm{d}A_\ell$.
   - The value $\varphi(\boldsymbol{r}_\ell)$ and section gradients $\nabla_\beta \varphi(\boldsymbol{r}_\ell)$ for each relevant warping shape.

Chapter 4

Enhanced Section for Uniform Warping

4.1 Introduction

The previous section established a general method for resolving enhanced strain fields in cross sectional constitutive models for a class of nonlinear beam models. The present section builds on these developments by seeking enhanced fields $\bar{\boldsymbol{A}}$ such that the response of the linearized model Box 3.3 will exactly reproduce the linear continuum solutions to Saint Venant's problems without the incorporation of external warping fields.

4.1.1 Motivation

Saint Venant's continuum problems offer closed form solutions for a prismatic member that is loaded at its end by resultant forces and moments. In the solutions to these problems, recalled in Appendix C, cross sections undergo deformations in a combination of six warping modes: three in the cross section plane, and three along the axis of the member. Since their initial resolution, these problems have served as targets for formulating beam theories. The first of the axial deformation modes, Saint Venant's torsion function, furnishes the canonical torsion constant J_{φ}, and the latter two are often employed to resolve the shear correction coefficient that arises in Timoshenko beam theory. However, associating these deformations with the kinematic model of a beam involves several complications:

1. Shear response couples to in-plane deformations through the Poisson effect.

2. When warping occurs in flexure, a "cross sectional rotation" $\boldsymbol{\Lambda}$ is fundamentally undefined, and consequently neither are the strain measures $\boldsymbol{\kappa}, \boldsymbol{\gamma}$.

3. The Saint Venant solutions for a prescribed body and load system are not unique.

4. In general, directly injecting warping strains in proportion to beam strains will not produce a variational model.

The effect of 1 cannot be represented by the kinematic model of the warping beam (3.2.1), which incorporates only axial warping. In the literature this is commonly accepted as an approximation with vanishing Poisson's ratio. The effect is recovered exactly in the present approach by incorporating an "incompatible" field in the assumed strain shapes of Section 3.4.

When attention is restricted to plane motions, 4 is avoided. An example of such a treatment is the investigation by Simo (1982) which employed Cowper's construction (Cowper, 1966) for the plane rotation to produce a condensed warping beam theory for elastomeric bearings. However, this approach cannot be made variationally consistent in the three-dimensional setting. A similar approach was taken by Saritas and Filippou (2009) to formulate a planar beam model for shear-yielding structural steel members where Poisson's ratio was assumed to vanish.

4.1.2 Outline

The presentation proceeds as follows. Section 4.2 establishes the setting of the Saint Venant continuum problems. Section 4.3 systematically characterizes the ambiguity inherent in a beam representation of these solutions. Finally, Section 4.4 constructs explicit enhanced section shapes in the setting of Chapter 3.

4.2 Problem Setting

Saint Venant's solutions pertain to a prismatic member in the following setting:

(ii) The cross section is heterogeneously composed of an initially isotropic material with homogeneous Poisson ratio ν. Consequently, Young's modulus E is given by:

$$E(\boldsymbol{r}) = 2G(\boldsymbol{r})(1+\nu)$$

where the shear modulus $G(\boldsymbol{r})$ is constant in the axial coordinate x but may vary in the section coordinate $\boldsymbol{r} \in \Omega$.

(ii) Loads are only applied at the terminal sections Ω_0 and Ω_L as axial N, transverse $\boldsymbol{F}$, torsional T, and bending $\boldsymbol{M}$ resultants.

(ii) Loads are proportioned to produce only infinitesimal deformations.

The conditions (i)-(iii) only limit the extent to which the following developments can be said to be in exact correspondence with Saint Venant's solutions. However, the developments remain useful in problems where any of these are relaxed, as demonstrated in Chapter 6.

The restriction (i) limits attention to bodies where Saint Venant's solution exactly reproduces the stress condition (3.2.11):

$$\boldsymbol{S} = \sigma\,\mathbf{i}\otimes\mathbf{i} + \boldsymbol{\tau}\otimes\mathbf{i} + \mathbf{i}\otimes\boldsymbol{\tau} \qquad \text{with} \qquad \begin{aligned}\sigma &:= \mathbf{i}\cdot\boldsymbol{S}\,\mathbf{i}\\ \boldsymbol{\tau} &:= \mathbf{i}_\beta\otimes\mathbf{i}_\beta\,\boldsymbol{S}\,\mathbf{i}\end{aligned} \tag{3.2.11}$$

This ensures that constitutive response in the elastic regime is exactly represented through the reduced relations:

$$\boldsymbol{\sigma} = \mathbb{C}\boldsymbol{\varepsilon} \qquad \text{with} \qquad \mathbb{C} = E(\boldsymbol{r})\,\mathbf{i}\otimes\mathbf{i} + G(\boldsymbol{r})\,\mathbf{1}_\Omega \tag{4.2.1}$$

where the stress $\boldsymbol{\sigma}$ and strain $\boldsymbol{\varepsilon}$ vectors are defined by (3.2.13) and (3.2.9), respectively. This is a reasonable condition for typical composite sections like reinforced concrete, where Poisson's ratio of each material is typically in the range 0.23–0.27.

Under the condition (3.2.11), the continuum equilibrium equations admit the representation:

$$\boldsymbol{\tau}' = \mathbf{0} \qquad \text{in } B, \tag{4.2.2a}$$
$$\operatorname{div}_\Omega \boldsymbol{\tau} + \sigma' = 0 \qquad \text{in } B, \tag{4.2.2b}$$
$$\boldsymbol{\tau}\cdot\boldsymbol{\nu} = 0 \qquad \text{on } \Gamma. \tag{4.2.2c}$$

The classical stress resultants $\boldsymbol{s}_o := (N, \boldsymbol{F}, T, \boldsymbol{M})$ [1] are defined by

$$N := \int_\Omega \sigma\,\mathrm{d}A, \quad \boldsymbol{F} := \int_\Omega \boldsymbol{\tau}\,\mathrm{d}A, \quad T := \int_\Omega (\mathbf{i}\times\boldsymbol{r})\cdot\boldsymbol{\tau}\,\mathrm{d}A, \quad \boldsymbol{M} := \int_\Omega \boldsymbol{r}\times\boldsymbol{\sigma}\,\mathrm{d}A, \tag{4.2.3}$$

These form a first-order initial value problem:

$$\begin{cases}\boldsymbol{s}_o'(x) = \mathbb{J}\,\boldsymbol{s}_o(x),\\ \boldsymbol{s}_o(0) = \boldsymbol{s}_0\end{cases} \tag{4.2.4}$$

where $\mathbb{J}$ is the 6×6 equilibrium generator:

$$\mathbb{J} := \begin{bmatrix}\mathbf{0} & \mathbf{0}\\ -\mathbf{i}^\times & \mathbf{0}\end{bmatrix} \tag{4.2.5}$$

[1] The deformation gradient denoted by $\boldsymbol{F}$ in Section 3.2 will not arise in the remainder of this work and henceforth $\boldsymbol{F}$ is understood in connection with (4.2.3).

Integrating (4.2.4) in view of the nilpotency $\mathbb{J}^2 = \mathbf{0}$ furnishes:

$$\boldsymbol{s}_o(x) = (\mathbf{1} + x\mathbb{J})\, \boldsymbol{s}_o(0). \tag{4.2.6}$$

The resultants at $x = 0$ are parameterized by the six kinematic constants of the Saint Venant particular solution (C.5.2), furnishing the expression:

$$\boldsymbol{s}_o(0) = \widehat{\mathbf{K}}_{\mathrm{p}} \boldsymbol{p} \tag{4.2.7}$$

where $\boldsymbol{p} \in \mathbb{R}^6$ collects the six kinematic parameters of the particular solution:

$$\boldsymbol{p} := (a_\varepsilon,\, \boldsymbol{a}_\Omega,\, a_\vartheta,\, \boldsymbol{b}_\Omega) \tag{4.2.8}$$

and in view of (C.3.5) and (C.4.8):

$$\widehat{\mathbf{K}}_{\mathrm{p}} = \begin{bmatrix} \widehat{EA} & \boldsymbol{c}_\varepsilon^\top & 0 & \mathbf{0} \\ \mathbf{0} & \mathbf{0} & \mathbf{0} & \widehat{E\boldsymbol{J}}_\gamma \\ 0 & \mathbf{0} & \widehat{GJ}_\vartheta & \mathbf{0} \\ -\mathbf{i} \times \boldsymbol{c}_\varepsilon & -\mathbf{i}^\times \widehat{E\boldsymbol{J}}_\kappa & \mathbf{0} & \mathbf{0} \end{bmatrix}. \tag{4.2.9}$$

where the centroidal flexural rigidity $\widehat{E\boldsymbol{J}}_\gamma$ is defined:

$$\widehat{E\boldsymbol{J}}_\gamma := \widehat{E\boldsymbol{J}}_\kappa - \boldsymbol{c}_\varepsilon \otimes \bar{\boldsymbol{\rho}} \tag{4.2.10}$$

The constants figuring in $\widehat{\mathbf{K}}_{\mathrm{p}}$ are summarized by Table 4.1.

Table 4.1: Rigid cross sectional properties

Symbol	Units	Equation	Description
$\widehat{EA}$	SL^2	(C.3.6)	Axial rigidity.
$\boldsymbol{c}_\varepsilon$	SL^3	(C.3.6)	First moment vector.
$\widehat{E\boldsymbol{J}}_\kappa$	SL^4	(C.3.7)	Second moment tensor.
$\widehat{GJ}_\vartheta$	SL^4	(C.3.7)	Saint Venant torsional rigidity
$\bar{\boldsymbol{\rho}}$	L	(C.4.4)	Location of the centroid.
$\boldsymbol{\rho}_{\mathrm{II}}$	L	(C.4.10)	Torsion-flexure center
$\widehat{E\boldsymbol{J}}_\gamma$	SL^4	(4.2.10)	Centroidal plane inertia tensor

Note. S indicates dimensions of stress and L is a dimension of length.

4.3 Characterization of Continuum Motions through Beam Fields

The ambiguities outlined above are investigated in this work by introducing the concept of a trace. A trace $\mathcal{T}$ identifies an association between one-dimensional fields and a given continuum displacement $\hat{\boldsymbol{u}}(x, \boldsymbol{r})$:

$$\mathcal{T} : \hat{\boldsymbol{u}}(x, \boldsymbol{r}) \longmapsto \Big(\boldsymbol{u}_{\mathcal{T}}(x),\, \boldsymbol{\theta}_{\mathcal{T}}(x),\, \boldsymbol{\alpha}(x) \Big) \tag{4.3.1}$$

There are infinitely many traces that may exactly represent a given particular solution $\hat{\boldsymbol{u}}_{\mathrm{P}}$ to a Saint-Venant problem, and each imparts a distinct physical meaning to boundary conditions like $\boldsymbol{\theta}_{\mathcal{T}}(x_0) = \mathbf{0}$ in a finite element simulation with displacements differing by the rigid homogeneous solution $\hat{\boldsymbol{u}}_{\mathrm{R}}$ (C.5.4).

In general a trace $\mathcal{T}$ may be represented by a functional which operates on continuum fields, as for example the geometric representation (E.1.1). However, because the present objective only concerns exact consistency in the finite dimensional space of Saint Venant solutions, traces may be identified by membership in the following equivalence class[2]:

Definition 4.3.1 (Saint Venant Equivalence)**.** *Two traces $\mathcal{T}_1, \mathcal{T}_2$ are Saint Venant-equivalent if $\mathcal{T}_1[\hat{\boldsymbol{u}}] = \mathcal{T}_2[\hat{\boldsymbol{u}}]$ for all $\hat{\boldsymbol{u}} \in \mathcal{U}_{\mathrm{SV}}$, where $\mathcal{U}_{\mathrm{SV}}$ is the finite dimensional space of Saint–Venant solutions.*

4.3.1 Class I: Kinematic Consistency

It is natural to restrict attention to traces which exhibit the following properties:

1. Strain measures $\boldsymbol{e}_{\mathcal{T}}$ generated under Saint-Venant loading are at most linear in the axial coordinate x.
2. Any Saint-Venant strain field is exactly reconstructed from only the plane section strains $\boldsymbol{\gamma}, \boldsymbol{\kappa}$ (3.3.3).
3. Continuum plane-section deformations are preserved.

The first two properties ensure that continuum strains can be exactly represented by typical beam finite elements. The final property serves as a *patch test*. These considerations are formalized as follows.

[2] Equivalence classes are expounded on, for example, by Halmos (1974).

Definition 4.3.2 (Class I). *A trace $\mathcal{T}$ is called a* ***Class I*** *trace if:*

(ii) For all $\hat{\boldsymbol{u}} \in \mathbb{P} \oplus \mathbb{Q}$ the following relations are furnished by x-independent linear operators $\mathbf{G}_T$, $\mathbf{H}_T$, and $\mathbf{K}_s \in \mathrm{GL}(6)$:

$$\boldsymbol{e}'_{\mathcal{T}}(x) =: \mathbf{G}_T \boldsymbol{e}_{\mathcal{T}}(0) \tag{4.3.2a}$$

$$\partial_{\boldsymbol{p}} \boldsymbol{e}'_{\mathcal{T}}(x) =: \mathbf{H}_T \tag{4.3.2b}$$

$$\partial_{\boldsymbol{e}_{\mathcal{T}}} \boldsymbol{s}_o(x) =: \mathbf{K}_s \tag{4.3.2c}$$

(ii) For all section-rigid motions $\hat{\boldsymbol{u}} = \boldsymbol{v}(x) + \boldsymbol{\omega}(x) \times \boldsymbol{r} \in \mathcal{R}$, the trace fields $\boldsymbol{u}, \boldsymbol{\theta} = \mathcal{T}[\hat{\boldsymbol{u}}]$ are:

$$\boldsymbol{u}(x) = \hat{\boldsymbol{u}}(x, \mathbf{0}) \tag{4.3.3a}$$

$$\boldsymbol{\theta}(x) = \boldsymbol{\omega}(x) \tag{4.3.3b}$$

Class I is not a Saint–Venant equivalence class itself, but defines a family of Saint–Venant equivalence classes. An equivalence class of traces with the properties (4.3.2) is uniquely represented in the Saint Venant class by a matrix $\mathbf{T} \in \mathrm{GL}(6)$, such that:

$$\mathbf{G}_T = \mathbf{T}^{-1} \mathbb{G} \mathbf{T} \tag{4.3.4a}$$

$$\mathbf{H}_T = \mathbf{T}^{-1} \mathbb{G} \tag{4.3.4b}$$

$$\mathbf{K}_s = \widehat{\mathbf{K}}_{\mathrm{p}} \mathbf{T} \tag{4.3.4c}$$

where $\widehat{\mathbf{K}}_{\mathrm{p}}$ is given by (4.2.9) and $\mathbb{G}$ is given by:

$$\mathbb{G} := \widehat{\mathbf{K}}_{\mathrm{p}}^{-1} \mathbb{J} \widehat{\mathbf{K}}_{\mathrm{p}} = \begin{bmatrix} 0 & \mathbf{0} & 0 & -\bar{\boldsymbol{\rho}}^{\top} \\ \mathbf{0} & \mathbf{0} & \mathbf{0} & \mathbf{1}_{\Omega} \\ 0 & \mathbf{0} & 0 & \mathbf{0} \\ \mathbf{0} & \mathbf{0} & \mathbf{0} & \mathbf{0} \end{bmatrix} \tag{4.3.5}$$

Beam strains $\boldsymbol{e}_{\mathcal{T}}$ generated from a trace with the property (4.3.2) can be written in the form:

$$\boldsymbol{e}_{\mathcal{T}}(x) = (\mathbf{1} + x\mathbf{G}_T)\mathbf{T}^{-1}\boldsymbol{p} \tag{4.3.6}$$

Furthermore, if $\mathcal{T}$ is Class I, then the trace matrix $\mathbf{T}^{-1}$ must have the block form:

$$\mathbf{T}^{-1} = \begin{bmatrix} 1 & \mathbf{0} & 0 & \bar{\boldsymbol{\varsigma}}_{\epsilon}^{\top} \\ \mathbf{0} & \mathbf{0} & \bar{\boldsymbol{\rho}}_{\gamma} & \bar{\boldsymbol{\Xi}}_{\gamma} \\ 0 & \mathbf{0}^{\top} & 1 & \bar{\boldsymbol{\rho}}_{\varkappa}^{\top} \\ \mathbf{0} & -\mathbf{i}^{\times} & \bar{\boldsymbol{\varsigma}}_{\kappa} & \bar{\boldsymbol{\Xi}}_{\kappa} \end{bmatrix} \qquad \text{with} \qquad \det \mathbf{T}^{-1} = \det\left(\bar{\boldsymbol{\Xi}}_{\gamma} - \bar{\boldsymbol{\rho}}_{\gamma} \otimes \bar{\boldsymbol{\rho}}_{\varkappa}\right) \tag{4.3.7}$$

where partitions correspond to $\boldsymbol{e} = (\epsilon, \mathbf{1}_\Omega\boldsymbol{\gamma}, \varkappa, \mathbf{1}_\Omega\boldsymbol{\kappa})$, and the entries in $\mathbf{T}^{-1}$ are free parameters with $\mathbf{i}\cdot\bar{\boldsymbol{\varsigma}}_\epsilon = \mathbf{i}\cdot\bar{\boldsymbol{\rho}}_\gamma = \mathbf{i}\cdot\bar{\boldsymbol{\varsigma}}_\kappa = \mathbf{i}\cdot\bar{\boldsymbol{\rho}}_\varkappa = 0$. The free parameters comprise a 16-dimensional family[3].

The necessity of (4.3.7) under Definition 4.3.2 is demonstrated as follows. The property (4.3.3) constrains how $\mathbf{T}^{-1}$ acts on the section-rigid part of each Saint Venant solution:

Extension (a_ε): The section-rigid displacement is $x\,a_\varepsilon\mathbf{i}$, giving $\boldsymbol{\theta} = \mathbf{0}$ and $\boldsymbol{u} = x\,a_\varepsilon\mathbf{i}$. The strains are $\epsilon = a_\varepsilon$ with all other components zero. This fixes column 1 of $\mathbf{T}^{-1}$ to $(1, \mathbf{0}, 0, \mathbf{0})^\top$.

Bending ($\boldsymbol{a}_\Omega$): The section-rigid rotation is $\boldsymbol{\theta} = -x\,\mathbf{i}\times\boldsymbol{a}_\Omega$, giving curvature $\mathbf{1}_\Omega\boldsymbol{\kappa} = -\mathbf{i}\times\boldsymbol{a}_\Omega$.

The shear strain $\mathbf{1}_\Omega\boldsymbol{\gamma}$ receives no section-rigid contribution. This fixes columns 2–3: entries $(2\text{–}3, 2\text{–}3) = \mathbf{0}$, $(4, 2\text{–}3) = 0$, and $(5\text{–}6, 2\text{–}3) = -\mathbf{i}^\times$.

Torsion (a_ϑ): The section-rigid rotation is $\boldsymbol{\theta} = x\,a_\vartheta\mathbf{i}$, giving twist $\varkappa = a_\vartheta$. This fixes column 4 entries $(1,4) = 0$, $(4,4) = 1$, $(5\text{–}6, 4) = \mathbf{0}$. The shear–torsion coupling $\bar{\boldsymbol{\rho}}_\gamma$ and curvature–torsion coupling $\bar{\boldsymbol{\varsigma}}_\kappa$ arise from warping and remain free.

Flexure ($\boldsymbol{b}_\Omega$): The section-rigid part contributes to ϵ and κ_β through the x-dependent terms, but these enter only in $\mathbf{H}_T = \mathbf{T}^{-1}\mathbb{G}$. All entries in columns 5–6 arise from warping contributions and remain free parameters: $\bar{\boldsymbol{\varsigma}}_\epsilon$ (axial–flexure), $\bar{\boldsymbol{\Xi}}_\gamma$ (shear–flexure), $\bar{\boldsymbol{\rho}}_\varkappa$ (twist–flexure), and $\bar{\boldsymbol{\Xi}}_\kappa$ (curvature–flexure).

Using (4.3.4b) and (4.3.7) furnishes the following universal form for $\mathbf{H}_T$:

$$\mathbf{H}_T = \mathbf{T}^{-1}\mathbb{G} = \begin{bmatrix} 0 & \mathbf{0} & 0 & -\bar{\boldsymbol{\rho}}^\top \\ \mathbf{0} & \mathbf{0} & \mathbf{0} & \mathbf{0} \\ 0 & \mathbf{0} & 0 & \mathbf{0} \\ \mathbf{0} & \mathbf{0} & \mathbf{0} & -\mathbf{i}^\times \end{bmatrix} \tag{4.3.8}$$

Inverting (4.3.7) furnishes for $\mathbf{T}$:

$$\mathbf{T} = \left[\begin{array}{cc|cc} 1 & \boldsymbol{\varsigma}_\epsilon^\top & \mu_\epsilon & \mathbf{0} \\ \mathbf{0} & \boldsymbol{\Xi}_\kappa & \boldsymbol{\varsigma}_\kappa & \mathbf{i}^\times \\ \hline 0 & \boldsymbol{\varsigma}_\varkappa^\top & \lambda_\varkappa & \mathbf{0} \\ \mathbf{0} & \boldsymbol{\Xi}_\gamma & \boldsymbol{\varsigma}_\gamma & \mathbf{0} \end{array}\right] \tag{4.3.9}$$

with entries given in terms of the entries in (4.3.7) by:

[3]These parameters must satisfy the additional restriction that $\mathbf{T}^{-1}$ be invertible.

$$
\begin{aligned}
\boldsymbol{\Xi}_\gamma &= \left(\bar{\boldsymbol{\Xi}}_\gamma - \bar{\boldsymbol{\rho}}_\gamma \otimes \bar{\boldsymbol{\rho}}_\varkappa\right)^{-1} && \text{(4.3.10a)}\\
\boldsymbol{\Xi}_\kappa &= \mathbf{i}^\times \left(\bar{\boldsymbol{\varsigma}}_\kappa \otimes \bar{\boldsymbol{\rho}}_\varkappa - \bar{\boldsymbol{\Xi}}_\kappa\right) \boldsymbol{\Xi}_\gamma && \text{(4.3.10b)}\\
\boldsymbol{\varsigma}_\gamma &= -\boldsymbol{\Xi}_\gamma \bar{\boldsymbol{\rho}}_\gamma && \text{(4.3.10c)}\\
\boldsymbol{\varsigma}_\varkappa &= -\boldsymbol{\Xi}_\gamma^\top \bar{\boldsymbol{\rho}}_\varkappa && \text{(4.3.10d)}\\
\boldsymbol{\varsigma}_\epsilon &= -\boldsymbol{\Xi}_\gamma^\top \bar{\boldsymbol{\varsigma}}_\epsilon && \text{(4.3.10e)}\\
\boldsymbol{\varsigma}_\kappa &= \mathbf{i} \times \Big(-\bar{\boldsymbol{\varsigma}}_\kappa + \left(\bar{\boldsymbol{\Xi}}_\kappa - \bar{\boldsymbol{\varsigma}}_\kappa \otimes \bar{\boldsymbol{\rho}}_\varkappa\right) \boldsymbol{\Xi}_\gamma \bar{\boldsymbol{\rho}}_\gamma\Big) && \text{(4.3.10f)}\\
\mu_\epsilon &= \bar{\boldsymbol{\varsigma}}_\epsilon \cdot \boldsymbol{\Xi}_\gamma \bar{\boldsymbol{\rho}}_\gamma && \text{(4.3.10g)}\\
\lambda_\varkappa &= 1 - \bar{\boldsymbol{\rho}}_\varkappa \cdot \boldsymbol{\varsigma}_\gamma && \text{(4.3.10h)}
\end{aligned}
$$

In view of (4.3.9) with $\widehat{\mathbf{K}}_\mathrm{p}$ given by (4.2.9), the section stiffness $\mathbf{K}_s = \widehat{\mathbf{K}}_\mathrm{p}\mathbf{T}$ takes the general form:

$$
\mathbf{K}_s = \left[\begin{array}{cc|cc}
\widehat{EA} & \left(\widehat{EA}\boldsymbol{\varsigma}_\epsilon + \boldsymbol{\Xi}_\kappa^\top \boldsymbol{c}_\varepsilon\right)^\top & \left(\widehat{EA}\mu_\epsilon + \boldsymbol{c}_\varepsilon \cdot \boldsymbol{\varsigma}_\kappa\right) & \boldsymbol{c}_\varepsilon^\top \mathbf{i}^\times \\
\mathbf{0} & \widehat{G\mathbf{A}}_\gamma & \widehat{G\mathbf{A}}_\gamma \boldsymbol{\rho}_\gamma & \mathbf{0} \\
\hline
0 & \widehat{GJ}_\vartheta \left(\boldsymbol{\varsigma}_\varkappa\right)^\top & \widehat{GJ}_\vartheta\, \lambda_\varkappa & \mathbf{0} \\
-\mathbf{i} \times \boldsymbol{c}_\varepsilon & -(\mathbf{i} \times \boldsymbol{c}_\varepsilon) \otimes \boldsymbol{\varsigma}_\epsilon - \mathbf{i}^\times E\mathbf{J}_o\, \boldsymbol{\Xi}_\kappa & -\mathbf{i} \times \boldsymbol{c}_\varepsilon\, \mu_\epsilon - \mathbf{i} \times E\mathbf{J}_o\, \boldsymbol{\varsigma}_\kappa & -\mathbf{i}^\times E\mathbf{J}_o\, \mathbf{i}^\times
\end{array}\right]_{6\times 6} \tag{4.3.11}
$$

where:

$$
\begin{aligned}
\widehat{G\mathbf{A}}_\gamma &:= \widehat{E\boldsymbol{J}}_\gamma \boldsymbol{\Xi}_\gamma && \text{(4.3.12)}\\
\boldsymbol{\rho}_\gamma &:= -\bar{\boldsymbol{\rho}}_\gamma && \text{(4.3.13)}\\
\boldsymbol{\rho}_\varkappa &:= -\widehat{GJ}_\vartheta (\widehat{G\mathbf{A}}_\gamma)^{-1} \boldsymbol{\Xi}_\gamma \bar{\boldsymbol{\rho}}_\varkappa && \text{(4.3.14)}
\end{aligned}
$$

Remark 4.3.1. For a linear isotropic material with shear modulus G, the displacement field (3.3.2) with warping neglected generates shear resultants $\boldsymbol{F}$ in terms of the shear deformations $\bar{\boldsymbol{\gamma}} := \mathbf{i}_\beta \gamma_\beta \in \mathbb{R}^2$ in the form

$$
\boldsymbol{F} = GA\,\bar{\boldsymbol{\gamma}} \tag{4.3.15}
$$

In the classical literature on shear-flexible elastic beams, the shear correction factor k augments (4.3.15) to incorporate the effect of uniform warping:

$$
\boldsymbol{F} = k\,GA\bar{\boldsymbol{\gamma}} \tag{4.3.16}
$$

In the present setting the (2,2) block of (4.3.11) offers the analogous relation:

$$\boldsymbol{F} = \widehat{G\mathbf{A}}_\gamma \bar{\boldsymbol{\gamma}} \tag{4.3.17}$$

This may be expressed alternatively by defining a generalized shear correction matrix:

$$\boldsymbol{K} := (\widehat{GA})^{-1}\widehat{E\boldsymbol{J}}_\gamma \boldsymbol{\Xi}_\gamma \qquad \text{with} \qquad \widehat{GA} := \int G \,\mathrm{d}A \tag{4.3.18}$$

so that $\boldsymbol{F} = \boldsymbol{K}\widehat{GA}\,\bar{\boldsymbol{\gamma}}$. The eigenvalues k_β of the normalized matrix (4.3.18) may be compared to shear correction factor k of (4.3.16), and similarly represent the shear stiffness relative to the warping-free stiffness (4.3.15). When $\widehat{G\mathbf{A}}_\gamma$ is isotropic, (4.3.17) recovers (4.3.16).

Remark 4.3.2. The (4,4) block of (4.3.11) is independent of the trace and therefore unambiguous.

Remark 4.3.3. (4.3.11) is not generally symmetric. This is addressed in Section 4.3.4.

4.3.2 Class I: Summary

The Class I traces represent a family of beam theories parameterized by 16 constants (Table 4.2) which are all capable of exactly representing Saint Venant solutions through the linear beam model of Box 3.3 without auxiliary warping fields $\boldsymbol{\alpha}$.

Table 4.2: Parameters identifying a trace in the Saint Venant class.

Block	Size	Units[a]	Description
$\widehat{G\mathbf{A}}_\gamma$	$\mathbb{R}^{2\times 2}$	L^2	Trace-consistent shear rigidity.
$\boldsymbol{\Xi}_\kappa$	$\mathbb{R}^{2\times 2}$	L^1	Curvature–flexure coupling
$\boldsymbol{\rho}_\gamma$	$\mathbb{R}^2$	L	Shear–torsion coupling
$\boldsymbol{\rho}_\varkappa$	$\mathbb{R}^2$	L	Twist–flexure coupling
$\boldsymbol{\varsigma}_\kappa$	$\mathbb{R}^2$	$\sim$	Curvature–torsion coupling
$\boldsymbol{\varsigma}_\epsilon$	$\mathbb{R}^2$	$\sim$	Axial–flexure coupling

[a] L indicates a unit of length, and $\sim$ indicates a dimensionless quantity.

In terms of the independent constants of Table 4.2 the remaining blocks of the trace matrix (4.3.9) are:

$$\boldsymbol{\Xi}_\gamma = (\widehat{E\boldsymbol{J}_\gamma})^{-1}\widehat{G\mathbf{A}_\gamma} \tag{4.3.19}$$

$$\varsigma_\gamma = (\widehat{E\boldsymbol{J}_\gamma})^{-1}\widehat{G\mathbf{A}_\gamma}\boldsymbol{\rho}_\gamma \tag{4.3.20}$$

$$\varsigma_\varkappa = (\widehat{GJ_\vartheta})^{-1}\widehat{G\mathbf{A}_\gamma}\boldsymbol{\rho}_\varkappa \tag{4.3.21}$$

$$\mu_\epsilon = \bar{\varsigma}_\epsilon \cdot \boldsymbol{\Xi}_\gamma \bar{\boldsymbol{\rho}}_\gamma \tag{4.3.22}$$

$$\lambda_\varkappa = 1 - \bar{\boldsymbol{\rho}}_\varkappa \cdot \varsigma_\gamma \tag{4.3.23}$$

A general procedure for implementing the Class I traces parameterized by Table 4.2 in the setting of Section 3.2 will be developed in Section 4.4. Before this, two special cases of the Class I traces are investigated.

4.3.3 Class II: Equilibrium Consistency

The traces that fall under Class I are capable of exactly representing Saint Venant's continuum solutions in a standard finite element context, but without further restriction they may still exhibit certain undesirable properties.

The strain measures $\boldsymbol{e}_{\mathcal{T}}$ associated to a trace $\mathcal{T}$ define work conjugate resultants $\bar{\boldsymbol{s}}_{\mathcal{T}}$ through the relation (3.2.7)

$$\langle \bar{\boldsymbol{s}}_{\mathcal{T}},\, \delta \boldsymbol{e}_{\mathcal{T}} \rangle = \langle \boldsymbol{\sigma},\, \delta \boldsymbol{\varepsilon} \rangle \tag{4.3.24}$$

Thus the conjugate resultants $\bar{\boldsymbol{s}}_{\mathcal{T}}$ are generally distinct from the classical resultants $\boldsymbol{s}_o$ of (4.2.3) and do not necessarily follow the evolution (4.2.6). Thus a section constitutive model that returns $\boldsymbol{s}_o$ in the setting of Box 3.3 may be variationally incompatible, but one returning $\bar{\boldsymbol{s}}_{\mathcal{T}}$ may violate continuum consistency. The former is not ideal, but nonetheless may produce a continuum exact representation as demonstrated in Example 6.2. The latter would appear unjustifiable unless it can be shown that the conjugate resultants of the trace $\bar{\boldsymbol{s}}_{\mathcal{T}}$ satisfy the evolution (4.2.4). Thus define Class II as the subset of Class I traces for which this holds.

Definition 4.3.3 (Class II)**.** *A Class I trace $\mathcal{T}$ is a **Class II** trace if the energy-conjugate resultants $\bar{\boldsymbol{s}}_{\mathcal{T}}$ from* (4.3.24) *satisfy the same equilibrium as the classical resultants* (4.2.4)*:*

$$\bar{\boldsymbol{s}}'_{\mathcal{T}} = \mathbb{J}\, \bar{\boldsymbol{s}}_{\mathcal{T}}. \tag{4.3.25}$$

Evidently the conjugate resultants $\bar{\boldsymbol{s}}_{\mathcal{T}}$ will depend linearly on the trace deformations $\boldsymbol{e}_{\mathcal{T}}$ through a linear operator $\bar{\mathbf{C}}_T(x)$ defined by:

$$\mathcal{U}(x) := \tfrac{1}{2}\int_\Omega \boldsymbol{\varepsilon} \cdot \mathbb{C}\, \boldsymbol{\varepsilon}\; \mathrm{d}A = \tfrac{1}{2}\boldsymbol{e}_{\mathcal{T}} \cdot \bar{\mathbf{C}}_T(x)\, \boldsymbol{e}_{\mathcal{T}}, \tag{4.3.26}$$

Remark 4.3.4. The *conjugate resultant stiffness* $\bar{\mathbf{C}}_T(x)$ is called *prismatic* if it is independent of x. Evidently, through inheritance of the Class I property (4.3.2c), every $\bar{\mathbf{C}}_T(x)$ in Class II is prismatic. Thus prismatic $\mathbf{K}_s$ implies prismatic $\bar{\mathbf{C}}_T$ but the converse does not hold.

Proposition 4.3.4 (Equilibrium compatibility)**.** *Let $\mathcal{T}$ be a Class I trace, let $\mathbf{C}_T := \mathbf{K}_s$, and assume that $\bar{\mathbf{C}}_T$ is prismatic. Then* (4.3.25) *holds for every Saint Venant solution if and only if*

$$[\bar{\mathbf{G}}, \mathbb{J}] = \mathbf{0}, \qquad \bar{\mathbf{G}} := \bar{\mathbf{C}}_T \mathbf{C}_T^{-1}. \tag{4.3.27}$$

Proof. For a Class I trace the classical resultants satisfy

$$\boldsymbol{s}_o = \mathbf{C}_T \boldsymbol{e}_{\mathcal{T}}, \qquad \boldsymbol{s}_o' = \mathbb{J}\boldsymbol{s}_o. \tag{4.3.28}$$

Moreover, $\mathbf{C}_T$ is invertible since $\mathbf{C}_T = \widehat{\mathbf{K}}_\mathrm{p}\mathbf{T}$ and both factors are invertible. Thus

$$\boldsymbol{e}_{\mathcal{T}} = \mathbf{C}_T^{-1}\boldsymbol{s}_o. \tag{4.3.29}$$

By the definition of the conjugate stiffness,

$$\bar{\boldsymbol{s}}_{\mathcal{T}} = \bar{\mathbf{C}}_T \boldsymbol{e}_{\mathcal{T}} = \bar{\mathbf{C}}_T \mathbf{C}_T^{-1}\boldsymbol{s}_o = \bar{\mathbf{G}}\boldsymbol{s}_o. \tag{4.3.30}$$

Since $\bar{\mathbf{C}}_T$ and $\mathbf{C}_T$ are prismatic, $\bar{\mathbf{G}}' = \mathbf{0}$. Differentiating the preceding identity gives

$$\bar{\boldsymbol{s}}_{\mathcal{T}}' = \bar{\mathbf{G}}\boldsymbol{s}_o' = \bar{\mathbf{G}}\mathbb{J}\boldsymbol{s}_o. \tag{4.3.31}$$

On the other hand,

$$\mathbb{J}\bar{\boldsymbol{s}}_{\mathcal{T}} = \mathbb{J}\bar{\mathbf{G}}\boldsymbol{s}_o. \tag{4.3.32}$$

Therefore (4.3.25) holds for every Saint Venant solution if and only if

$$(\bar{\mathbf{G}}\mathbb{J} - \mathbb{J}\bar{\mathbf{G}})\boldsymbol{s}_o(x) = \mathbf{0} \tag{4.3.33}$$

for every admissible resultant field $\boldsymbol{s}_o$.

It remains only to remove the dependence on a particular loading. From (4.2.6) and (4.2.7),

$$\boldsymbol{s}_o(x) = (\mathbf{1} + x\mathbb{J})\widehat{\mathbf{K}}_\mathrm{p}\boldsymbol{p}. \tag{4.3.34}$$

The matrix $\widehat{\mathbf{K}}_\mathrm{p}$ is invertible, and $\mathbf{1} + x\mathbb{J}$ is invertible with inverse $\mathbf{1} - x\mathbb{J}$ because $\mathbb{J}^2 = \mathbf{0}$. Hence, for each fixed x, the set of attainable values of $\boldsymbol{s}_o(x)$ is all of $\mathbb{R}^6$. Consequently

$$(\bar{\mathbf{G}}\mathbb{J} - \mathbb{J}\bar{\mathbf{G}})\boldsymbol{s}_o(x) = \mathbf{0} \quad \text{for all Saint–Venant solutions} \tag{4.3.35}$$

if and only if

$$\bar{\mathbf{G}}\mathbb{J} - \mathbb{J}\bar{\mathbf{G}} = \mathbf{0}. \tag{4.3.36}$$

□

The set of all matrices satisfying (4.3.27) comprise the equilibrium invariance group G:

$$G := \{\, \mathbf{K} \in \mathrm{GL}(6) \;\big|\; [\mathbf{K}, \mathbb{J}] = 0 \,\}.$$

This restricts the space of Class II trace matrices $\mathbf{T}^{-1}$ to a nonlinear sub-manifold, for which a simple parameterization like that of Table 4.2 does not exist. Nonetheless, any Class II trace may be represented by the parameters of Table 4.2 provided (4.3.27) is satisfied. It is possible to conveniently parameterize a subset of Class II traces, by first identifying a reference trace $\mathcal{T}_R$ in the class. The Class III trace developed in the following section provides such a reference.

4.3.4 Class III: Variational Consistency

A final restriction is now considered which eliminates all remaining free parameters, and furnishes a unique trace matrix called the *energetic* trace.

Definition 4.3.5 (Class III)**.** *A Class I trace is a* ***Class III*** *trace if the conjugate resultants* $\bar{\boldsymbol{s}}_{\mathcal{T}}$ *are exactly the classical rigid-section resultants* $\boldsymbol{s}_o$ (4.2.3)*:*

$$\bar{\boldsymbol{s}}_{\mathcal{T}} \equiv \boldsymbol{s}_o. \tag{4.3.37}$$

All Class III traces are equivalent in the Saint Venant class, with trace matrix determined by the consistency condition:

$$\mathbf{T}^{-1} = \widehat{\mathbf{K}}_{\mathrm{p}}^{-\top} \bar{\mathbf{C}}_p \tag{4.3.38}$$

where $\bar{\mathbf{C}}_p$ is furnished by (E.2.1). The demonstration is as follows. For a Class I trace with $\boldsymbol{e}_{\mathcal{T}}(x)$ following (4.3.6), the conjugate stiffness (4.3.26) is:

$$\delta\boldsymbol{p} \cdot (\mathbf{1} + x\mathbf{Q}_T^\top)\, \mathbf{T}^{-1^\top} \boldsymbol{s}(x) = \delta\boldsymbol{p} \cdot (\mathbf{1} + x\mathbf{Q}_T^\top)\, \bar{\mathbf{C}}_p\, (\mathbf{1} + x\mathbf{Q}_T)\, \boldsymbol{p}.$$

Since this must hold for all $\boldsymbol{p}$, the class requires:

$$\mathbf{T}^{-1^\top} \widehat{\mathbf{K}}_{\mathrm{p}} (1 + x\mathbb{G}) = \bar{\mathbf{C}}_p\, (\mathbf{1} + x\mathbf{Q}_T)\,.$$

Expanding both sides using $(\mathbf{1} + x\mathbf{Q}_T) = \mathbf{1} + x\mathbb{G}$ and matching powers of x produces:

$$\begin{aligned} x^0 : &\qquad \mathbf{T}^{-1^\top} \widehat{\mathbf{K}}_{\mathrm{p}} = \bar{\mathbf{C}}_p, \\ x^1 : &\qquad \mathbf{T}^{-1^\top} \mathbf{K}_s \mathbf{H}_T = \bar{\mathbf{C}}_p\, \mathbb{G}. \end{aligned}$$

Consistency in x^0 furnishes the identification of $\mathbf{T}^{-1}$:

$$\mathbf{T}^{-1} = \widehat{\mathbf{K}}_{\mathrm{p}}^{-\top} \bar{\mathbf{C}}_p$$

The linear evolution x^1 yields the consistency condition:

$$\bar{\mathbf{C}}_p \, \widehat{\mathbf{K}}_\mathrm{p}^{-1} \mathbf{K}_s \mathbf{H}_T = \bar{\mathbf{C}}_p \, \mathbb{G} \qquad \Longrightarrow \qquad \widehat{\mathbf{K}}_\mathrm{p}^{-1} \mathbf{K}_s \mathbf{H}_T = \mathbb{G} \tag{4.3.39}$$

Explicit expressions for the parameters (Table 4.2) identifying the Class III trace matrix $\mathbf{T}$ for a given cross section and material composition are derived in Section E.2 and collected in (E.2.6).

4.4 Enhanced Strains

In view of the developments in Section 4.3, any Class I (including Class II and Class III as subsets) trace is representable without any auxiliary fields by a finite element that models the system of Box 3.3. However, the consistency condition (3.4.3) is only meaningful for Class II (with Class III as a subset). Thus, in the following developments enhanced strain shapes $\bar{\boldsymbol{A}}$ are derived for the general Class I family parameterized by Table 4.2 by setting the local amplitudes $\boldsymbol{\eta} = \boldsymbol{e}$. For Class II and III traces the resulting shapes may be used in the procedure of Box 3.4, which will converge to $\boldsymbol{\eta} = \boldsymbol{e}$ in one iteration for an elastic isotropic material. If the trace is not Class I or II, then the iterative procedure of Box 3.4 is not performed. The resulting section model is generally non-variational for any trace outside of Class II.

In the absence of auxiliary warping fields, the linearized compatible section kinematic operator (3.2.20) is

$$\hat{\boldsymbol{\varepsilon}}(\boldsymbol{e}) = \boldsymbol{A}_\mathrm{r} \boldsymbol{e} \qquad \text{with} \qquad \boldsymbol{A}_\mathrm{r}(\boldsymbol{r}) := \begin{bmatrix} \mathbf{1} & -\boldsymbol{r}^\times \end{bmatrix}_{3\times 6}$$

Enhanced shapes $\bar{\boldsymbol{A}}$ are sought to inject strains with the form:

$$\bar{\boldsymbol{\varepsilon}}(x, \boldsymbol{r}) = \hat{\boldsymbol{\varepsilon}}(\boldsymbol{e}) + \bar{\boldsymbol{A}}(\boldsymbol{r}) \boldsymbol{\eta}(x) \tag{3.4.1}$$

In view of the Saint Venant strain field (C.5.5), the enhanced shapes must take the form:

$$\bar{\boldsymbol{A}} = \boldsymbol{A}_\mathrm{r} \boldsymbol{\Gamma}_\mathrm{r} + \boldsymbol{A}_\mathrm{w} \boldsymbol{\Gamma}_\mathrm{w} \qquad \text{with} \qquad \boldsymbol{A}_\mathrm{w}(\boldsymbol{r}) := \begin{bmatrix} \nabla \bar{\varphi}_\mathrm{I} & \mathbf{i}_\beta \otimes \nabla_\beta \bar{\boldsymbol{\varphi}}_\mathrm{II} + \widetilde{\boldsymbol{\Pi}} \end{bmatrix}_{3\times 3} \tag{4.4.1}$$

where $\boldsymbol{\Gamma}_\mathrm{r}$ and $\boldsymbol{\Gamma}_\mathrm{w}$ are constant matrices, and the warping functions $\bar{\varphi}_\mathrm{I}$, $\bar{\boldsymbol{\varphi}}_\mathrm{II}$ and $\widetilde{\boldsymbol{\Pi}}$ are defined by (C.3.3), (C.4.5), and (C.4.3), respectively. Because all Class I traces generate deformations $\boldsymbol{e}_\mathcal{T}$ that evolve with the form (4.3.6), it is sufficient to match the x-constant strain field represented by $\boldsymbol{\varepsilon}(0, \boldsymbol{r})$:

$$\boldsymbol{\varepsilon}(0, \boldsymbol{r}) = \Big(\boldsymbol{A}_\mathrm{r}(\boldsymbol{r})(\mathbf{1} + \boldsymbol{\Gamma}_\mathrm{r}) + \boldsymbol{A}_\mathrm{w}(\boldsymbol{r}) \boldsymbol{\Gamma}_\mathrm{w} \Big) \, \mathbf{T}^{-1} \boldsymbol{p} \tag{4.4.2}$$

Equating the x-constant strains in (C.5.5) with (4.4.2) and exploiting the block structure of $\mathbf{T}$ (4.3.9) furnishes after a lengthy but otherwise straightforward manipulation:

$$\mathbf{\Gamma}_{\mathrm{r}} = \begin{bmatrix} \mathbf{i}\otimes\boldsymbol{\varsigma}_\epsilon - \mathbf{1}_\Omega & \mu_\epsilon \mathbf{i}\otimes\mathbf{i} \\ -\mathbf{i}^\times \boldsymbol{\Xi}_\kappa + \mathbf{i}\otimes\boldsymbol{\Xi}_\gamma^\top(\boldsymbol{\rho}_{\mathrm{II}} + \boldsymbol{\varsigma}_\varkappa) & (\lambda_\varkappa + \boldsymbol{\varsigma}_\gamma\cdot\boldsymbol{\rho}_{\mathrm{II}} - 1)\mathbf{i}\otimes\mathbf{i} + (\boldsymbol{\varsigma}_\kappa\times\mathbf{i})\otimes\mathbf{i} \end{bmatrix}_{6\times 6} \tag{4.4.3}$$

and

$$\mathbf{\Gamma}_{\mathrm{w}} = \begin{bmatrix} (\boldsymbol{\Xi}_\gamma^\top\boldsymbol{\rho}_{\mathrm{II}} + \boldsymbol{\varsigma}_\varkappa)^\top & (\boldsymbol{\rho}_{\mathrm{II}}\cdot\boldsymbol{\varsigma}_\gamma + \lambda_\varkappa)\mathbf{i}^\top \\ \boldsymbol{\Xi}_\gamma & \boldsymbol{\varsigma}_\gamma\otimes\mathbf{i} \end{bmatrix}_{3\times 6} \tag{4.4.4}$$

where $\boldsymbol{\rho}_{\mathrm{II}} \in \mathbb{R}^2$ is the constant vector defined by (C.4.10) that arises from Saint Venant's flexure solution.

4.5 Summary and Remarks

There are infinitely many distinct warping free beam models in the family of Chapter 3 that exactly trace solutions to Saint Venant's continuum problems. Under the Saint Venant equivalence class (Definition 4.3.1) one has the results:

- Traces are physically distinguished by how they manifest boundary fixities on the beam displacement $\boldsymbol{u}$ and rotation $\boldsymbol{\theta}$ fields.
- Any Class I trace (Definition 4.3.2) is compatible with the linearized beam model of Box 3.3 and is represented through the enhanced strain section of Section 3.4 and relaxation of the consistency condition (3.4.3). However, most Class I traces are not variational and produce an asymmetric tangent stiffness.
- The geometric (Cowper, 1966) and energetic (Renton, 1991) treatments of shear both lead to exact continuum solutions in the present framework, and are included in the Class I family of traces.
- Class II traces (Definition 4.3.3) are the subset of Class I traces which support the variational condition (3.4.3) and furnish a symmetric tangent stiffness.
- Class III traces (Definition 4.3.5) are the subset of Class II traces that produce the classical stress resultants $(N, \boldsymbol{F}, T, \boldsymbol{M})$ under variational condition (3.4.3).
- All Class III traces are equivalent under the Saint Venant class , and their trace matrix is given uniquely by (E.2.6).

Chapter 5

Enhanced Section for Nonuniform Torsion Warping

5.1 Introduction

The present chapter applies the method of Chapter 3 to develop an improved model of nonuniform torsion. The objective is to rectify the violation of equilibrium that is induced by the single-field torsion warping beam model. In this setting, general continuum solutions are no longer available in closed form to identify appropriate section fields. Consistency is instead sought by enforcing the section equilibrium equations in the elastic regime.

The approach developed here represents the equilibrium defect of the single-field model as a residual functional on the cross section and determines an appropriate strain shape that cancels it under linear isotropy. The residual is shown to involve two functionals, which leads to a minimal compatible space generated by two gradient fields. In the absence of distributed warping loads, this two-dimensional space reduces to a one-parameter family of one-dimensional section-local corrections.

The presentation proceeds as follows. Section 5.2 establishes notation, recalls the baseline beam model with a single torsional warping field, and sets up the problem of pure nonuniform torsion. Section 5.3 derives the equilibrium defect that arises in the baseline model. Section 5.4 constructs the space of correcting enhanced strains. Section 5.5 derives the condensed torsional response and the corresponding general solution of the enhanced strain model under pure torsion.

5.2 Baseline Model

The model that will be enhanced is the warping beam theory with one external field α and warping shape $\boldsymbol{\varphi} = \bar{\varphi}_{\mathrm{I}}$ determined by Saint Venant's torsion problem (C.3.3) (Reissner, 1952; Simo & Vu-Quoc, 1991; Gruttmann et al., 2000).

The material is isotropic and furnishes, under the stress constraint (3.2.11):

$$\boldsymbol{\sigma} = \mathbb{C}\boldsymbol{\varepsilon} \qquad \text{with} \qquad \mathbb{C} = E\,\mathbf{i}\otimes\mathbf{i} + G\,\mathbf{1}_{\Omega}$$

where E and G are Young's and the shear modulus, respectively, and the notation of Section 3.2.1 is employed. The shear G and Young's modulus E define smooth, positive differential 2-forms μ_G and μ_E, respectively, on the cross-section Ω:

$$\mu_G = G(\boldsymbol{r})\ \mathrm{d}A \qquad\qquad \mu_E = E(\boldsymbol{r})\ \mathrm{d}A$$

where $\mathrm{d}A$ is the Euclidean area form in the cross section plane Ω. Define the E-inner product, G-energy inner product, and G-Poisson bracket:

$$\langle u,\, v\rangle_E := \int_\Omega u\, v\, \mu_E, \qquad (u,\, v)_G := \int_\Omega \nabla u\cdot\nabla v\, \mu_G, \quad \text{and} \quad \{u,\, v\}_G := \int_\Omega \nabla u\cdot \mathbf{i}\times\nabla v\, \mu_G \tag{5.2.1}$$

of functions u, v on Ω. The bracket $(5.2.1)_3$ integrates the scalar triple product $[\nabla\phi,\, \mathbf{i},\, \boldsymbol{r}] := \nabla\phi\cdot\mathbf{i}\times\boldsymbol{r}$

$$\tfrac{1}{2}\left\{\phi, r^2\right\}_G = \int [\nabla\phi,\, \mathbf{i},\, \boldsymbol{r}]\, \mu_G$$

For a symmetric section with coordinates $\boldsymbol{r}$ originating at the centroid the section constitutive relation is linear with $\boldsymbol{K}_s$ determined by (3.2.22) (Simo & Vu-Quoc, 1991):

$$\boldsymbol{s} = \boldsymbol{K}_s\boldsymbol{e} \qquad \text{with} \qquad \boldsymbol{K}_s = \left[\begin{array}{ccc|ccc|cc} EA & 0 & 0 & 0 & 0 & 0 & 0 & 0 \\ & GA & 0 & 0 & 0 & 0 & 0 & 0 \\ & & GA & 0 & 0 & 0 & 0 & 0 \\ \hline & & & \widetilde{GI}_{\mathrm{o}} & 0 & 0 & 0 & -\widetilde{GJ}_{\mathrm{v}} \\ & & & & EI_{yy} & 0 & 0 & 0 \\ & & & & & EI_{zz} & 0 & 0 \\ \cline{4-8} & & & & & & \widetilde{EJ}_{\mathrm{w}} & 0 \\ & \text{sym.} & & & & & & \widetilde{GJ}_{\mathrm{v}} \end{array}\right] \tag{5.2.2}$$

with :

$$\widetilde{GI}_{\mathrm{o}} := \left(\tfrac{1}{2}r^2,\, \tfrac{1}{2}r^2\right) \tag{5.2.3a}$$

$$\widetilde{EJ}_{\mathrm{w}} := \langle\bar{\varphi}_{\mathrm{I}}, \bar{\varphi}_{\mathrm{I}}\rangle_E \tag{5.2.3b}$$

$$\widetilde{GJ}_{\mathrm{v}} := (\bar{\varphi}_{\mathrm{I}}, \bar{\varphi}_{\mathrm{I}})_G, \tag{5.2.3c}$$

$$\widetilde{GJ}_{\vartheta} := \left(\bar{\varphi}_{\mathrm{I}}, \tfrac{1}{2}r^2\right)_G + \left(\tfrac{1}{2}r^2, \tfrac{1}{2}r^2\right)_G \equiv \widetilde{GI}_{\mathrm{o}} - \widetilde{GJ}_{\mathrm{v}}. \tag{5.2.3d}$$

and $r^2 := \boldsymbol{r}\cdot\boldsymbol{r}$ Under pure torsion the finite rotation $\boldsymbol{\Lambda}$ is represented with only a single parameter ϑ such that:

$$\begin{aligned} \boldsymbol{\Lambda} &= \operatorname{Exp}\vartheta\mathbf{i} \\ &= \cos\vartheta\mathbf{1} + \sin\vartheta\,\mathbf{i}^{\times} + (1-\cos\vartheta)\mathbf{i}\otimes\mathbf{i} \end{aligned} \qquad \text{and} \qquad \begin{aligned} \boldsymbol{\kappa}^{\times} &= \boldsymbol{\Lambda}'\boldsymbol{\Lambda}^{\top} \\ &= \vartheta'\,\mathbf{i}^{\times} \end{aligned} \tag{5.2.4}$$

from which the torsional curvature is $\varkappa = \vartheta'$. The notation $\mathbf{v}^{\times}$ in (5.2.4) indicates a skew symmetric matrix with axial vector $\mathbf{v}$. Under this motion the deformed (spatial) axial director $\hat{\mathbf{i}}$ remains equivalent to the reference axial director $\mathbf{i}$ (that is, $\hat{\mathbf{i}} = \boldsymbol{\Lambda}\mathbf{i} \equiv \mathbf{i}$). The compatible linearized strain tensor $\hat{\boldsymbol{E}}$ is characterized by the strain vector $\hat{\boldsymbol{\varepsilon}}$ of (3.2.18) which, under pure torsion, is:

$$\hat{\boldsymbol{\varepsilon}} = \alpha'\bar{\varphi}_{\mathrm{I}}\,\mathbf{i} + \varkappa\,\mathbf{i}\times\boldsymbol{r} + \alpha\nabla\bar{\varphi}_{\mathrm{I}} \tag{5.2.5}$$

5.3 Equilibrium Residual

For any stress field satisfying (3.2.11) and the traction-free condition $\boldsymbol{S}\boldsymbol{\nu} = \mathbf{0}$ on $\partial_{\mathbf{i}}B$, the field equations reduce on each section to

$$\begin{aligned} \boldsymbol{\tau}' &= \mathbf{0} && \text{in } B, && (5.3.1\text{a}) \\ \operatorname{div}_{\Omega}\boldsymbol{\tau} + \sigma' &= 0 && \text{in } B, && (5.3.1\text{b}) \\ \boldsymbol{\tau}\cdot\boldsymbol{\nu} &= 0 && \text{on } \Gamma. && (5.3.1\text{c}) \end{aligned}$$

Using the constitutive relations (5.2.2), weighting (5.3.1) against an arbitrary function v and integrating by parts in $\boldsymbol{r}$ gives the equilibrium residual projection

$$\int_{\Omega} G\,\boldsymbol{\varepsilon}_{\gamma}\cdot\nabla v\;\mathrm{d}A \;=\; -\int_{\Omega}(E\,\alpha'\bar{\varphi}_{\mathrm{I}})'\,v\;\mathrm{d}A \qquad \forall v. \tag{5.3.2}$$

The equilibrium condition requires the mapping $v \mapsto \int_{\Omega} G\,\boldsymbol{\varepsilon}_{\gamma}\cdot\nabla v$ to reproduce the mapping $v \mapsto -\alpha''\int_{\Omega} E\bar{\varphi}_{\mathrm{I}}v$.

Recall the Saint Venant function $\bar{\varphi}_{\mathrm{I}}$ with respect to a point $\boldsymbol{\pi} \in \Omega$ is defined up to a constant as the solution to the standard Neumann Laplace problem (C.3.3):

$$\begin{cases} \operatorname{div}_G\left(\nabla\bar{\varphi}_{\mathrm{I}} + \mathbf{i}\times(\boldsymbol{r}-\boldsymbol{\pi})\right) & = 0 \qquad \text{in } \Omega, \\ \nabla_{\boldsymbol{\nu}}\bar{\varphi}_{\mathrm{I}} & = -\mathbf{i}\times(\boldsymbol{r}-\boldsymbol{\pi})\cdot\boldsymbol{\nu} \qquad \text{on } \Gamma, \\ \int_\Omega \bar{\varphi}_{\mathrm{I}}\mu_E & = 0 \end{cases} \tag{5.3.3}$$

where div_G is the divergence with respect to the volume form μ_G, as defined by (D.1.6) (Box D.1). The function $\tilde{\varphi}$ is equivalently defined up to a constant by (Identity D.3.1),

$$(\bar{\varphi}_{\mathrm{I}},\, v)_G = \frac{1}{2}\left\{\|\boldsymbol{r}-\boldsymbol{\pi}\|^2,\, v\right\}_G \qquad \forall v \tag{5.3.4}$$

Insert (5.2.5) into the left side of (5.3.2) and apply (5.3.4):

$$\int_\Omega G\,\hat{\boldsymbol{\varepsilon}}_\gamma\cdot\nabla v\;\mathrm{d}A = (\alpha-\varkappa)\int_\Omega G\,\nabla\bar{\varphi}_{\mathrm{I}}\cdot\nabla v\;\mathrm{d}A. \tag{5.3.5}$$

Therefore (5.3.2) becomes

$$(\alpha-\varkappa)\,L_1(v) + \alpha''\,L_2(v) = 0 \qquad \forall v\in H^1(\Omega)/\mathbb{R}, \tag{5.3.6}$$

where

$$L_1(v) := (\bar{\varphi}_{\mathrm{I}},\, v)_G \qquad \text{and} \qquad L_2(v) := \langle\bar{\varphi}_{\mathrm{I}},\, v\rangle_E\,. \tag{5.3.7}$$

5.4 Enhanced Strain Shape

The enhanced strain fields $\tilde{\boldsymbol{\varepsilon}}_\gamma$ are sought to derive from a scalar potential χ:

$$\delta\tilde{\boldsymbol{\varepsilon}}_\gamma = \nabla\chi$$

Elimination of the residual (5.3.6) requires the potential χ to satisfy:

$$\int_\Omega G\,\nabla\chi\cdot\nabla v = -(\alpha-\varkappa)L_1(v) - \alpha'' L_2(v) \quad \forall v. \tag{5.4.1}$$

In view of (5.4.1), define the function ψ by the Riesz representation (Oden & Reddy, 1976):

$$(\psi,\, v)_G = -\left\langle\bar{\varphi}_{\mathrm{I}},\, v\right\rangle_E \qquad \forall v \tag{5.4.2}$$

This implies the boundary value problem (Identity D.3.2)

$$\begin{cases} (\operatorname{div}_G\nabla\psi)\mu_G = \bar{\varphi}_{\mathrm{I}}\,\mu_E. & \text{in } \Omega, \\ \nabla_\nu\psi = 0 & \text{on } \Gamma \\ \displaystyle\int_\Omega \psi\mu_E = 0 \end{cases} \tag{5.4.3}$$

where the final integral condition is the standard normalization required for uniqueness of the solution. This function was considered by Reissner (1952), Genoese et al. (2013), and Armero (2021).

In view of (5.3.4), the strain potential χ that satisfies (5.4.1) is defined up to a constant by

$$\chi = -(\alpha - \varkappa)\bar{\varphi}_{\mathrm{I}} + \alpha'' \psi, \tag{5.4.4}$$

and thus

$$\delta\tilde{\boldsymbol{\varepsilon}}_{\gamma} = -(\alpha - \varkappa)\nabla\bar{\varphi}_{\mathrm{I}} + \alpha'' \,\nabla\psi. \tag{5.4.5}$$

The residual strain (5.4.5) can be injected by introducing an additional warping field α_{n_w+1} with the shape ψ. However, in the absence of distributed warping loads $\boldsymbol{f}_{\mathrm{w}}$, $\alpha'' \propto \alpha - \varkappa$, in which case, the correction can be supplied within the section-local framework of Section 3.4. To this end, introduce the $n_{L} = 1$ enhanced shape with a free parameter c_η:

$$\bar{\boldsymbol{A}} = \nabla\bar{\varphi}_{\mathrm{I}} + c_\eta \,\nabla\psi \tag{5.4.6}$$

where $c_\eta \neq 0$ is required by the stability condition (3.4.2). The enhanced potential is

$$\chi_c \coloneqq \bar{\varphi}_{\mathrm{I}} + c_\eta \,\psi.$$

The consistency condition (3.4.4) is

$$0 = -(\varkappa - \alpha)\,\tilde{J}(c_\eta) + \|\chi_c\|_G^2 \,\eta, \tag{5.4.7}$$

where

$$\tilde{J}(c_\eta) \coloneqq (\bar{\varphi}_{\mathrm{I}}, \chi_c)_G, \qquad \text{and} \qquad \|\chi_c\|_G^2 \coloneqq (\chi_c, \chi_c)_G. \tag{5.4.8}$$

Solving (5.4.7) gives the local warping amplitude η in terms of the free parameter c_η:

$$\eta = (\varkappa - \alpha)\,\bar{\eta}(c_\eta), \qquad \text{with} \qquad \bar{\eta}(c_\eta) = \frac{\tilde{J}(c_\eta)}{\|\chi_c\|_G^2}. \tag{5.4.9}$$

A practical condition that eliminates the free parameter c_η is to require that the shear-norm $\|\chi_c\|_G^2$ of the potential χ_c is minimized. Using the definitions (5.2.3) the norm is:

$$\|\chi_c\|_G^2 = \widetilde{GJ}_{\mathrm{v}} - 2c_\eta\widetilde{EJ}_{\mathrm{w}} + c_\eta^2 J_\eta$$

where

$$J_\eta \coloneqq (\psi, \psi)_G \equiv -\left\langle \bar{\varphi}_{\mathrm{I}}, \psi \right\rangle_E, \tag{5.4.10}$$

The minimum is attained at

$$\frac{\mathrm{d}}{\mathrm{d}c_\eta}\|\chi_c\|_G^2 = -2\widetilde{EJ}_{\mathrm{w}} + 2c_\eta J_\eta = 0$$

furnishing

$$c_\eta = -\frac{(\psi, \bar{\varphi}_{\mathrm{I}})_G}{(\psi, \psi)_G} = \frac{\widetilde{EJ}_{\mathrm{w}}}{J_\eta}. \tag{5.4.11}$$

With the choice (5.4.11),

$$\tilde{J}(c_\eta) = \widetilde{GJ}_{\mathrm{v}} - \frac{\widetilde{EJ}_{\mathrm{w}}^2}{J_\eta}, \qquad \text{and} \qquad \|\chi_c\|_G^2 = \widetilde{GJ}_{\mathrm{v}} - \frac{\widetilde{EJ}_{\mathrm{w}}^2}{J_\eta},$$

This furnishes $\bar{\eta} = 1$ in (5.4.9) and the condensed amplitude is

$$\eta = \varkappa - \alpha. \tag{5.4.12}$$

5.5 General Solution

Under pure torsion, the geometrically exact model (Box 3.2) produces the same response as the linearized model (Box 3.3). A general solution for this case is derived in closed form.

Constitution. Substitution of (5.4.11) and (5.4.12) into the enhanced strain ansatz (3.4.1) produces:

$$\boldsymbol{\varepsilon} = \alpha' \bar{\varphi}_{\mathrm{I}}\, \mathbf{i} + \varkappa(\mathbf{i} \times \boldsymbol{r} + \nabla \bar{\varphi}_{\mathrm{I}}) + \frac{\widetilde{EJ}_{\mathrm{w}}}{J_\eta}(\varkappa - \alpha)\nabla\psi. \tag{5.5.1}$$

Under pure torsion $\boldsymbol{\gamma} = 0$, $\boldsymbol{n} = N\mathbf{i}$ and the moment is $T = \boldsymbol{m} \cdot \mathbf{i}$, which from (3.2.21):

$$\begin{aligned} T &= \mathbf{i} \cdot \int \boldsymbol{r} \times \boldsymbol{\sigma}\ \mathrm{d}A \\ &= \widetilde{GI}_{\mathrm{o}}\varkappa + \tfrac{1}{2}\left\{\bar{\varphi}_{\mathrm{I}},\, r^2\right\}_G \alpha + \tfrac{1}{2}\left\{\bar{\varphi}_{\mathrm{I}} + \frac{\widetilde{EJ}_{\mathrm{w}}}{J_\eta}\psi,\, r^2\right\}_G (\varkappa - \alpha) \\ &= \widetilde{GI}_{\mathrm{o}}\varkappa - \widetilde{GJ}_{\mathrm{v}}\alpha - \left(\widetilde{GJ}_{\mathrm{v}} - \frac{\widetilde{EJ}_{\mathrm{w}}^2}{J_\eta}\right)(\varkappa - \alpha) \\ &= \widehat{GJ}_\vartheta\, \varkappa + \frac{\widetilde{EJ}_{\mathrm{w}}^2}{J_\eta}(\varkappa - \alpha). \end{aligned} \tag{5.5.2}$$

Similarly from (3.2.21) the bi-moment is

$$W = \int \bar{\varphi}_{\mathrm{I}} \mathbf{i} \cdot \boldsymbol{\sigma}\, \mathrm{d}A = \widetilde{EJ}_{\mathrm{w}}\alpha' \tag{5.5.3}$$

and the bi-shear is

$$V = \int \nabla \bar{\varphi}_{\mathrm{I}} \cdot \boldsymbol{\tau} \, \mathrm{d}A = \frac{\widetilde{EJ}_{\mathrm{w}}^{2}}{J_\eta}(\alpha - \varkappa). \tag{5.5.4}$$

Equilibrium.

The moment equilibrium equation $(3.2.8)_2$ is stated in terms of the spatial moment $(\boldsymbol{\Lambda m})'$. However, for the rotation field (5.2.4), $\boldsymbol{\Lambda}\mathbf{i} = \mathbf{i}$ and the resulting equation exactly matches the linear theory:

$$\begin{aligned} \mathbf{i} \cdot (\boldsymbol{\Lambda m})' &= \left(\widehat{GJ}_\vartheta \, \varkappa + \tfrac{\widetilde{EJ}_{\mathrm{w}}^{2}}{J_\eta}(\varkappa - \alpha)\right)' = 0, \\ W' - V &= (\widetilde{EJ}_{\mathrm{w}} \, \alpha')' + \tfrac{\widetilde{EJ}_{\mathrm{w}}^{2}}{J_\eta}(\varkappa - \alpha) = 0. \end{aligned} \tag{5.5.5}$$

Note that $\boldsymbol{x}' = \mathbf{i}$ so that $\mathbf{i} \cdot \boldsymbol{x}' \times (\boldsymbol{\Lambda n}) = 0$.

Solution. Integrating $(5.5.5)_1$ gives

$$\widehat{GJ}_\vartheta \, \varkappa + \frac{\widetilde{EJ}_{\mathrm{w}}^{2}}{J_\eta}(\varkappa - \alpha) = T_0, \tag{5.5.6}$$

where T_0 is a constant. Hence

$$\alpha(x) = \left(1 + \frac{\widehat{GJ}_\vartheta \, J_\eta}{\widetilde{EJ}_{\mathrm{w}}^{2}}\right) \varkappa(x) - \frac{T_0 J_\eta}{\widetilde{EJ}_{\mathrm{w}}^{2}}. \tag{5.5.7}$$

Substitution into $(5.5.5)_2$ yields

$$\widetilde{EJ}_{\mathrm{w}} \left(1 + \frac{\widehat{GJ}_\vartheta \, J_\eta}{\widetilde{EJ}_{\mathrm{w}}^{2}}\right) \varkappa'' - \widehat{GJ}_\vartheta \, \varkappa + T_0 = 0.$$

Equivalently,

$$\varkappa'' - \lambda^2 \left(\varkappa - \frac{T_0}{\widehat{GJ}_\vartheta}\right) = 0, \qquad \lambda^2 := \frac{\widehat{GJ}_\vartheta}{\widetilde{EJ}_{\mathrm{w}} \left(1 + \frac{\widehat{GJ}_\vartheta \, J_\eta}{\widetilde{EJ}_{\mathrm{w}}^{2}}\right)}. \tag{5.5.8}$$

The general solution to (5.5.8) is

$$\varkappa(x) = \frac{T_0}{\widehat{GJ}_\vartheta} + c_1 \cosh(\lambda x) + c_2 \sinh(\lambda x). \tag{5.5.9}$$

Using (5.5.7),

$$\alpha(x) = \frac{T_0}{\widehat{GJ}_\vartheta} + \left(1 + \frac{\widehat{GJ}_\vartheta \, J_\eta}{\widetilde{EJ}_{\mathrm{w}}^{2}}\right)\left(c_1 \cosh(\lambda x) + c_2 \sinh(\lambda x)\right). \tag{5.5.10}$$

Using $\varkappa = \vartheta'$, integration gives the final twist ϑ, bimoment W and bishear V:

$$\vartheta(x) = \frac{T_0}{\widehat{GJ}_\vartheta}\, x + \frac{c_1}{\lambda} \sinh(\lambda x) + \frac{c_2}{\lambda} \cosh(\lambda x) + c_3. \tag{5.5.11}$$

$$W(x) = \widetilde{EJ}_\mathrm{w} \left(1 + \frac{\widehat{GJ}_\vartheta \, J_\eta}{\widetilde{EJ}_\mathrm{w}^2} \right) \lambda \left[c_1 \sinh(\lambda x) + c_2 \cosh(\lambda x) \right], \tag{5.5.12}$$

$$V(x) = -\widehat{GJ}_\vartheta \left[c_1 \cosh(\lambda x) + c_2 \sinh(\lambda x) \right]. \tag{5.5.13}$$

Chapter 6

Finite Element Simulations

6.1 Overview

This chapter presents finite element simulations that demonstrate the formulations that were developed in the previous chapters. Before turning to the examples, the underlying element architecture is summarized.

The developments of Part I separate modeling assumptions into three components (Box 6.1). The *element* model determines the representation of the spatial kinematics and produces a one-dimensional boundary value problem of equilibrium. The *section* model provides the constitutive relation supplied to the frame model and incorporates further kinematic and constitutive assumptions. The *material* model represents the point-wise response of a classical Cauchy continuum, for which an general multiaxial material law may be assigned. This structure facilitates a finite element implementation with the architecture developed by F. C. Filippou (2004b) and Scott et al. (2008).

The following finite elements are employed, where the subscript $n = \dim \boldsymbol{\alpha}$ indicates the number of warping fields incorporated in the model:

- The EF_n element is a displacement interpolation of the geometrically exact model in Box 3.2. The formulation is due to Simo and Vu-Quoc (1991) and follows the implementation described by Perez and Filippou (2024). The element employs a uniformly reduced Gauss-Legendre quadrature of order $m = n_e - 1$, where n_e is the number of element nodes in order to prevent shear locking.

- The MF_n element is a mixed interpolation of the linearized model in Box 3.3. The formulation is in the lineage of Taylor et al. (2003). The element uses Gauss-Legendre quadrature with 5 integration points, unless otherwise stated. In the setting of finite deformations the element is employed in connection with a corotational formulation.

Box 6.1: Summary of Frame Models

1. Element Kinematics

   ◦ **Finite** (Box 3.2)

$$\hat{\boldsymbol{x}}(x,\boldsymbol{r}) = \boldsymbol{x}(x) + \boldsymbol{\Lambda}(\boldsymbol{r} + \mathbf{i} \otimes \boldsymbol{\varphi}(\boldsymbol{r})\boldsymbol{\alpha}(x)) \tag{3.2.1}$$

   ◦ **Linear** (Box 3.3)

$$\hat{\boldsymbol{u}}(x,\boldsymbol{r}) = \boldsymbol{u}(x) + \boldsymbol{\theta}(x) \times \boldsymbol{r} + \mathbf{i} \otimes \boldsymbol{\varphi}(\boldsymbol{r})\,\boldsymbol{\alpha}(x) \tag{3.3.2}$$

2. Section Kinematics

$$\bar{\boldsymbol{\varepsilon}}(x,\boldsymbol{r}) = \hat{\boldsymbol{\varepsilon}}(\boldsymbol{e}) + \bar{\boldsymbol{A}}(\boldsymbol{r})\boldsymbol{\eta}(x) \tag{3.4.1}$$

   with

   ◦ **Wagner**

$$\hat{\boldsymbol{\varepsilon}} := \boldsymbol{\gamma} + \boldsymbol{\kappa} \times \boldsymbol{r} + \mathbf{i} \otimes \boldsymbol{\varphi}\,\boldsymbol{\alpha}' + \nabla_{\Omega}(\boldsymbol{\varphi} \cdot \boldsymbol{\alpha}) + \tfrac{1}{2}\varkappa^2\,\boldsymbol{r} \cdot \boldsymbol{r}\,\mathbf{i} \tag{3.2.17}$$

   ◦ **Linear**

$$\hat{\boldsymbol{\varepsilon}} := \boldsymbol{\gamma} + \boldsymbol{\kappa} \times \boldsymbol{r} + \mathbf{i} \otimes \boldsymbol{\varphi}\,\boldsymbol{\alpha}' + \nabla_{\Omega}(\boldsymbol{\varphi} \cdot \boldsymbol{\alpha}) \tag{3.2.18}$$

3. Enhanced Strains

   ◦ **Chapter 4**

$$\bar{\boldsymbol{A}} = \boldsymbol{A}_{\mathrm{r}}\boldsymbol{\Gamma}_{\mathrm{r}} + \boldsymbol{A}_{\mathrm{w}}\boldsymbol{\Gamma}_{\mathrm{w}} \qquad \text{with} \qquad \boldsymbol{A}_{\mathrm{w}}(\boldsymbol{r}) := \begin{bmatrix} \nabla\bar{\varphi}_{\mathrm{I}} & \mathbf{i}_{\beta} \otimes \nabla_{\beta}\bar{\boldsymbol{\varphi}}_{\mathrm{II}} + \widetilde{\boldsymbol{\Pi}} \end{bmatrix}_{3\times 3} \tag{4.4.1}$$

   ◦ **Chapter 5**

$$\bar{\boldsymbol{A}} = \nabla\bar{\varphi}_{\mathrm{I}} + c_{\eta}\,\nabla\psi \tag{5.4.6}$$

An element with n warping fields requires $6 + n$ degrees of freedom at each node.

Cross sectional warping shapes are evaluated using quadratic triangle finite elements in an automated pre-processing step. Fibers in the section are defined at the Gauss points of these elements.

Inelastic simulations employ a condensed J_2 plasticity model with linear kinematic and isotropic hardening, implemented by the backward Euler discretization:

$$\begin{cases} \boldsymbol{\xi}^{\mathrm{tr}}_{n+1} \coloneqq \mathbb{C}^{\mathrm{e}}\boldsymbol{\varepsilon}_{n+1} - (\mathbb{C}^{\mathrm{e}} + \mathbf{B})\boldsymbol{\varepsilon}^{p}_{n}, \\ \boldsymbol{\xi}_{n+1} \coloneqq \boldsymbol{\xi}^{\mathrm{tr}}_{n+1} - \Delta\gamma(\mathbb{C}^{\mathrm{e}} + \mathbf{B})\mathbf{M}\boldsymbol{\xi}_{n+1}, \\ q_{n+1} \coloneqq \sqrt{\boldsymbol{\xi}_{n+1} \cdot \mathbf{M}\boldsymbol{\xi}_{n+1}}, \\ f_{n+1} \coloneqq q_{n+1} - \sqrt{\tfrac{2}{3}}\left(F_y + H_{\mathrm{iso}}\alpha_{n+1}\right) \leq 0, \\ \boldsymbol{\varepsilon}^{p}_{n+1} \coloneqq \boldsymbol{\varepsilon}^{p}_{n} + \Delta\gamma\mathbf{M}\boldsymbol{\xi}_{n+1}, \\ \alpha_{n+1} \coloneqq \alpha_n + \Delta\gamma\sqrt{\tfrac{2}{3}}\, q_{n+1}, \\ \boldsymbol{\sigma}_{n+1} \coloneqq \boldsymbol{\xi}_{n+1} + \mathbf{B}\boldsymbol{\varepsilon}^{p}_{n+1}, \\ \quad \Delta\gamma \geq 0, \qquad \Delta\gamma f_{n+1} = 0. \end{cases} \tag{6.1.1}$$

where the yield stress F_y and hardening moduli H_{iso}, H_{kin} are material parameters, $\mathbb{C}^{\mathrm{e}}$ is the constrained isotropic material tangent (4.2.1) given by the Young E and shear G moduli, and the operators $\mathbf{B}$ and $\mathbf{M}$ are defined by

$$\mathbf{B} \coloneqq H_{\mathrm{kin}}\mathbf{M}^{-1}, \qquad \mathbf{M} \coloneqq \mathsf{R}^{*}\mathbb{I}^{\mathrm{dev}}\mathsf{R} = \tfrac{2}{3}\mathbf{i}\otimes\mathbf{i} + 2\mathbf{1}_{\Omega}$$

with

$$\mathsf{R} \coloneqq (\mathbf{i}\otimes\mathbf{i})\otimes\mathbf{i} + \left(\mathbf{i}\otimes\mathbf{i}_{\beta} + \mathbf{i}_{\beta}\otimes\mathbf{i}\right)\otimes\mathbf{i}_{\beta}.$$

The formulations were developed using the FEDEASLab framework (F. C. Filippou, 2004a). The simulations are implemented in and performed with the Xara simulation engine (Perez et al., 2024; "Xara Documentation", n.d.). Renderings are generated with the Veux Python package (Perez & Vouvakis Manousakis, 2024; Perez, n.d.).

The source code implementing these simulations is available at https://github.com/claudioperez/thesis.

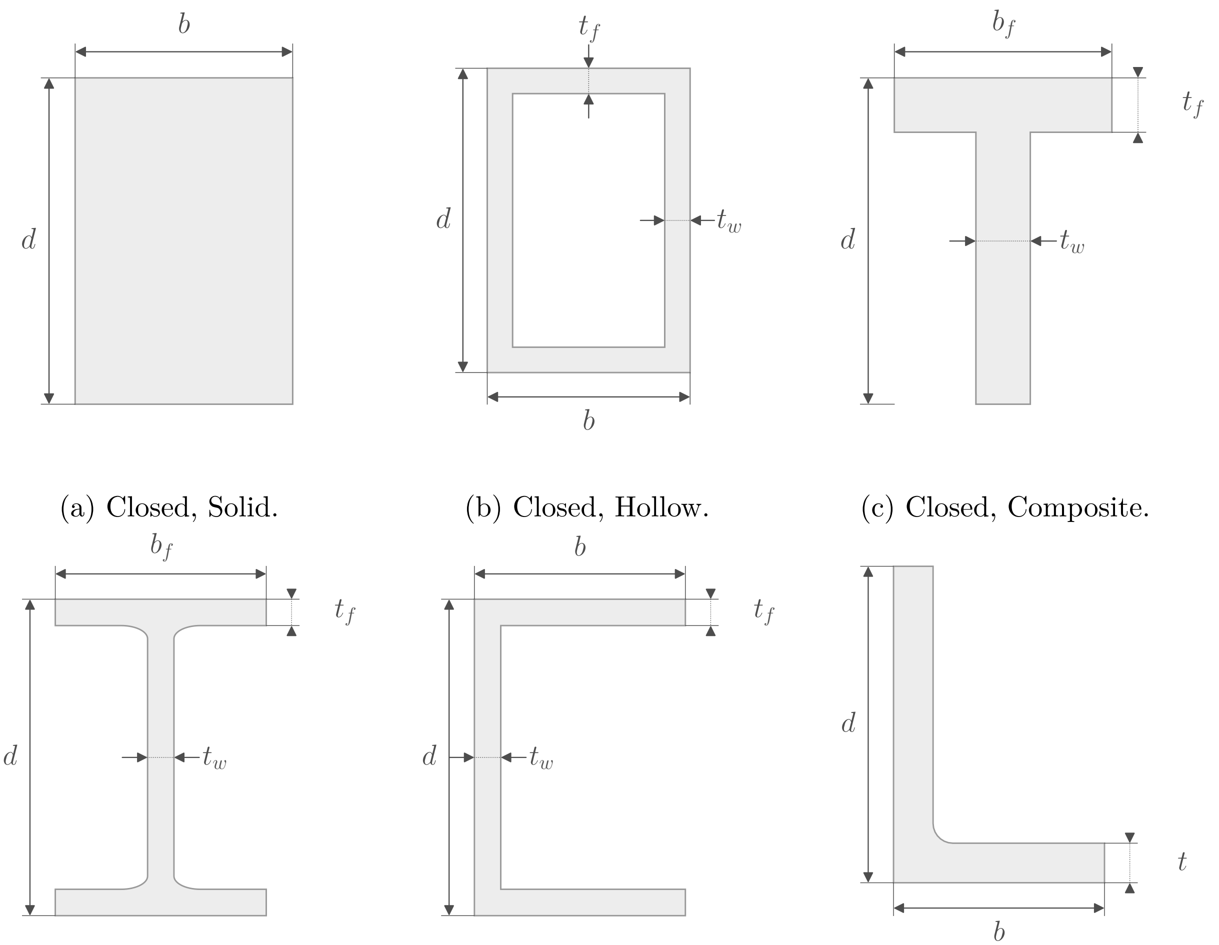

(a) Closed, Solid. (b) Closed, Hollow. (c) Closed, Composite.

(d) Open, Double Sym. (e) Open, Single Sym. (f) Asymmetric.

Figure 6.1: Representative cross sectional shapes employed by examples.

6.2 Saint-Venant Flexure

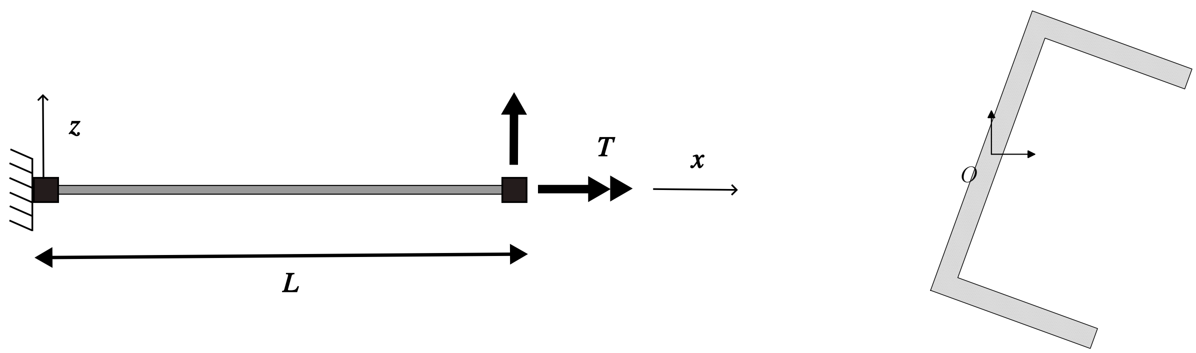

Figure 6.2: Model for Example 6.2.

Motivation. This example demonstrates consistency with Saint Venant's continuum solutions for two specializations of the section model of Chapter 4. The reference continuum solution is derived in Appendix C.

Setup. A cantilever beam fixed at $x = 0$ is loaded with a transverse force $\bar{F}\,\mathbf{i}_z$ and torque $\bar{T}\,\mathbf{i}$ at the free end $x = L$ (Figure 6.2).

The length-depth ratio is $L/d = 3/2$. The cross section of the beam is rotated off the principal axes by an angle of $\pi/8$ as depicted in Figure 6.2. All problems are solved using one MF_n element with $n = 0$ external warping fields. The cross sectional parameters of the section are collected in Box 6.1 for $\nu = 0$ and Box 6.2 for $\nu = 0.3$.

Results. Table 6.2 compares the fiber stresses $\sigma_{1k} := \mathbf{i}_k \cdot \boldsymbol{\sigma}(\xi_i, \boldsymbol{r}_i)$ obtained by the two traces against the continuum solution at three quadrature points $\boldsymbol{r}_i$ in each cross section. Stresses are evaluated at the first Gauss point along the element length. For traces, the axial stress σ_{11} is recovered to machine precision. The shear stresses σ_{12} and σ_{13} agree with the continuum solution to five or more significant figures, with the small residual attributable to the finite fiber discretization of the warping field. Notably, the energetic and geometric traces produce essentially identical stress values at every monitoring point, confirming that both formulations represent the same continuum stress field.

The tip deflections in Table 6.1, by contrast, differ between the two traces despite this shared stress field. This outcome is consistent with the development in Chapter 4, where the two traces were shown to correspond to continuum solutions that differ by a rigid body motion.

The relative errors in Table 6.1 confirm that each set of tip deflections agrees with its own corresponding continuum solution to at least five significant figures.

Table 6.1: Tip displacements at $x = L$ for Example 6.2. Relative errors against the respective continuum displacements are below 6.4×10^{-6} for all components.

ν	Displacement	Energetic Trace	Geometric Trace
0	u_y	$36.5476{\times}10^{-3}$	$36.5472{\times}10^{-3}$
	u_z	$266.935{\times}10^{-3}$	$266.934{\times}10^{-3}$
3/10	u_y	$58.8232{\times}10^{-3}$	$59.4932{\times}10^{-3}$
	u_z	$333.682{\times}10^{-3}$	$333.570{\times}10^{-3}$

Table 6.2: Fiber stresses at monitoring points for Example 6.2.

$\boldsymbol{r}$	Component	Reference	Energetic Error	Geometric Error
(0.17, 1.61)	σ_{11}	-180×10^{-3}	5.3×10^{-15}	5.4×10^{-15}
	σ_{12}	-88×10^{-3}	5.5×10^{-6}	5.5×10^{-6}
	σ_{13}	-220×10^{-3}	5.5×10^{-6}	5.5×10^{-6}
(1.22, 2.14)	σ_{11}	-170×10^{-3}	5.0×10^{-15}	5.2×10^{-15}
	σ_{12}	140×10^{-3}	5.0×10^{-6}	5.0×10^{-6}
	σ_{13}	380×10^{-3}	5.1×10^{-6}	5.1×10^{-6}
(−0.10, −1.48)	σ_{11}	-43×10^{-3}	16×10^{-15}	16×10^{-15}
	σ_{12}	140×10^{-3}	6.1×10^{-6}	6.1×10^{-6}
	σ_{13}	390×10^{-3}	6.1×10^{-6}	6.1×10^{-6}

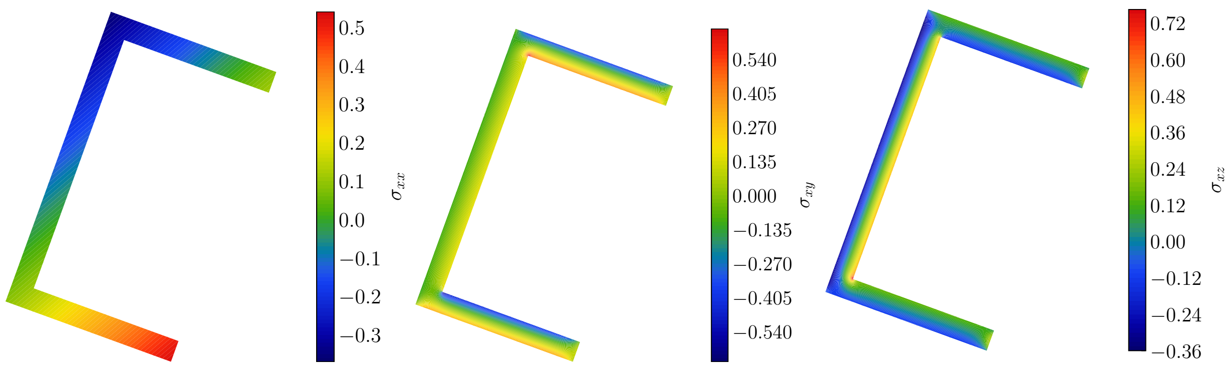

Figure 6.3: Element stress field at $x = 0$ with $\nu = 0.3$ for Example 6.2.

Box 6.1. Properties for Example 6.2

Material

$$E = 29 \times 10^3 \text{ ksi}$$
$$G = 15 \times 10^3 \text{ ksi}$$

Shape (Figure 6.1e)

$$d = 14 \text{ in}$$
$$b = 8 \text{ in}$$
$$t = 1 \text{ in}$$

Table 4.1

$$\widehat{EA} = 28\ E \text{ ksi in}^2$$
$$\widehat{GJ}_\vartheta = 9.3\ G \text{ ksi in}^4$$

Warping Shape Parameters (Table 4.2)

Energetic (E.2.6)

$$\widehat{GA}_y = 380 \times 10^{-3}\ \widehat{GA} \text{ ksi in}^2$$
$$\widehat{GA}_z = 390 \times 10^{-3}\ \widehat{GA} \text{ ksi in}^2$$
$$(\bar{\boldsymbol{\rho}}_\gamma)_y = 970 \times 10^{-3} \text{ in}^2$$
$$(\bar{\boldsymbol{\rho}}_\gamma)_z = 2.7 \text{ in}^2$$
$$(\bar{\boldsymbol{\rho}}_\varkappa)_y = 170 \text{ in}^2$$
$$(\bar{\boldsymbol{\rho}}_\varkappa)_z = 470 \text{ in}^2$$

Geometric (E.1.9)

$$\widehat{GA}_y = 380 \times 10^{-3}\ \widehat{GA} \text{ ksi in}^2$$
$$\widehat{GA}_z = 390 \times 10^{-3}\ \widehat{GA} \text{ ksi in}^2$$
$$(\bar{\boldsymbol{\rho}}_\gamma)_y = 970 \times 10^{-3} \text{ in}^2$$
$$(\bar{\boldsymbol{\rho}}_\gamma)_z = 2.7 \text{ in}^2$$
$$(\bar{\boldsymbol{\rho}}_\varkappa)_y = 170 \text{ in}^2$$
$$(\bar{\boldsymbol{\rho}}_\varkappa)_z = 470 \text{ in}^2$$

Box 6.2. Properties for Example 6.2

Material

$$E = 29 \times 10^3 \text{ ksi}$$
$$G = 11 \times 10^3 \text{ ksi}$$

Shape (Figure 6.1e)

$$d = 14 \text{ in}$$
$$b = 8 \text{ in}$$
$$t = 1 \text{ in}$$

Table 4.1

$$\widehat{EA} = 28\ E \text{ ksi in}^2$$
$$\widehat{GJ}_\vartheta = 9.3\ G \text{ ksi in}^4$$

Warping Shape Parameters (Table 4.2)

Energetic (E.2.6)

$$\widehat{GA}_y = 380 \times 10^{-3}\ \widehat{GA} \text{ ksi in}^2$$
$$\widehat{GA}_z = 390 \times 10^{-3}\ \widehat{GA} \text{ ksi in}^2$$
$$(\bar{\boldsymbol{\rho}}_\gamma)_y = 970 \times 10^{-3} \text{ in}^2$$
$$(\bar{\boldsymbol{\rho}}_\gamma)_z = 2.7 \text{ in}^2$$
$$(\bar{\boldsymbol{\rho}}_\varkappa)_y = 220 \text{ in}^2$$
$$(\bar{\boldsymbol{\rho}}_\varkappa)_z = 620 \text{ in}^2$$

Geometric (E.1.9)

$$\widehat{GA}_y = 410 \times 10^{-3}\ \widehat{GA} \text{ ksi in}^2$$
$$\widehat{GA}_z = 390 \times 10^{-3}\ \widehat{GA} \text{ ksi in}^2$$
$$(\bar{\boldsymbol{\rho}}_\gamma)_y = 970 \times 10^{-3} \text{ in}^2$$
$$(\bar{\boldsymbol{\rho}}_\gamma)_z = 2.7 \text{ in}^2$$
$$(\bar{\boldsymbol{\rho}}_\varkappa)_y = 220 \text{ in}^2$$
$$(\bar{\boldsymbol{\rho}}_\varkappa)_z = 620 \text{ in}^2$$

6.3 Steel Shear Link

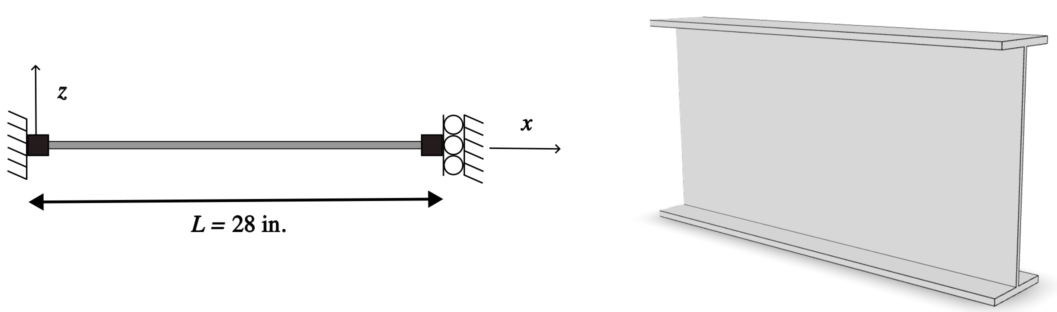

Figure 6.4: Model of the shear link from Example 6.3.

Motivation. This example demonstrates the effectiveness of the formulation from Chapter 4 under inelastic material response. The benchmark solution is a shell finite element model.

Setup. The built-in span in Figure 6.4 represents a shear link with a steel wide-flange W18x40 section (American Institute of Steel Construction, 2017). Properties of the cross section and material parameters are collected in Box 6.3.

The setting is consistent with the assumptions of Chapter 4 with the exception of inelastic material response. Thus no auxiliary warping fields are employed and displacements and strains are assumed linear.

The span is discretized by 1 element. A displacement cycle is imposed at the end $x = L$.

Results. Figure 6.5 reports the transverse (z) shear force – displacement response at the point of imposed displacement $x = L$. Both variants (Section E.1 and Section E.2) of the Chapter 4 formulation significantly improve the response both in the elastic and inelastic range.

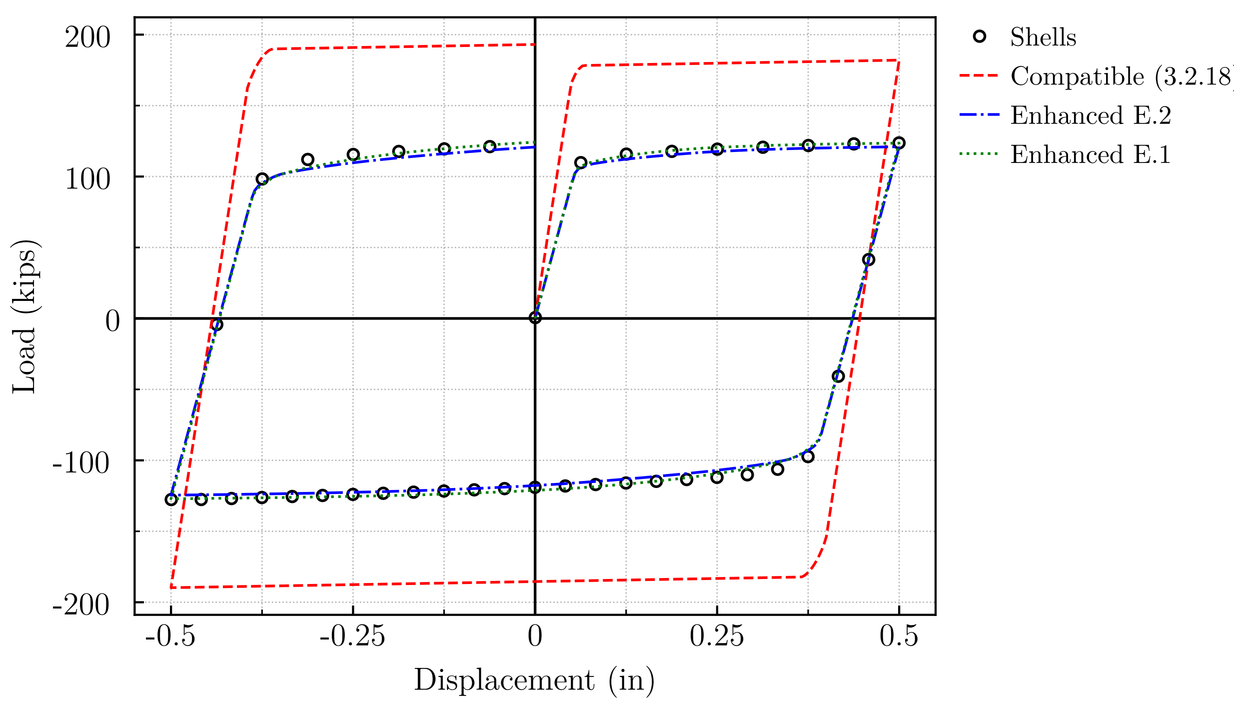

Figure 6.5: Shear force F_z vs. displacement u_z at $x = L$.

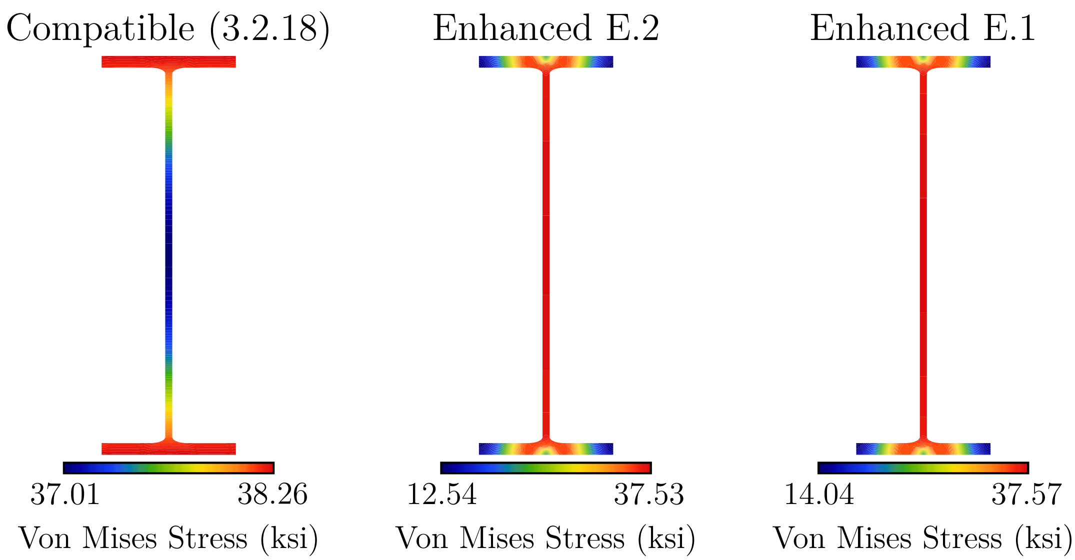

Figure 6.6: J_2 stress in section 1 at the end of the simulation.

Box 6.3. Properties for Example 6.3

Material (6.1.1)

E	$=$	30×10^3 ksi
G	$=$	12×10^3 ksi
H_{iso}	$=$	$0.002\ E$ ksi
F_y	$=$	35 ksi

Shape (Figure 6.1d)

d	$=$	17.9 in
b_f	$=$	6.02 in
t_f	$=$	0.525 in
t_w	$=$	0.315 in

Table 4.1

$\widehat{EA}$	$=$	$12\ E$ ksi in^2
$\widehat{GJ}_\vartheta$	$=$	$870 \times 10^{-3}\ G$ ksi in^4

Warping Shape Parameters (Table 4.2)

Energetic (E.2.6)

$\widehat{GA}_y$	$=$	$470 \times 10^{-3}\ \widehat{GA}$ ksi in^2
$\widehat{GA}_z$	$=$	$460 \times 10^{-3}\ \widehat{GA}$ ksi in^2
$(\bar{\boldsymbol{\rho}}_\gamma)_y$	$=$	4.5×10^{-6} in^2
$(\bar{\boldsymbol{\rho}}_\gamma)_z$	$=$	-7.3×10^{-6} in^2
$(\bar{\boldsymbol{\rho}}_\varkappa)_y$	$=$	250×10^{-6} in^2
$(\bar{\boldsymbol{\rho}}_\varkappa)_z$	$=$	-13×10^{-3} in^2

Geometric (E.1.9)

$\widehat{GA}_y$	$=$	$710 \times 10^{-3}\ \widehat{GA}$ ksi in^2
$\widehat{GA}_z$	$=$	$470 \times 10^{-3}\ \widehat{GA}$ ksi in^2
$(\bar{\boldsymbol{\rho}}_\gamma)_y$	$=$	2.6×10^{-6} in^2
$(\bar{\boldsymbol{\rho}}_\gamma)_z$	$=$	-7.3×10^{-6} in^2
$(\bar{\boldsymbol{\rho}}_\varkappa)_y$	$=$	360×10^{-6} in^2
$(\bar{\boldsymbol{\rho}}_\varkappa)_z$	$=$	-13×10^{-3} in^2

6.4 Inelastic Nonuniform Torsion

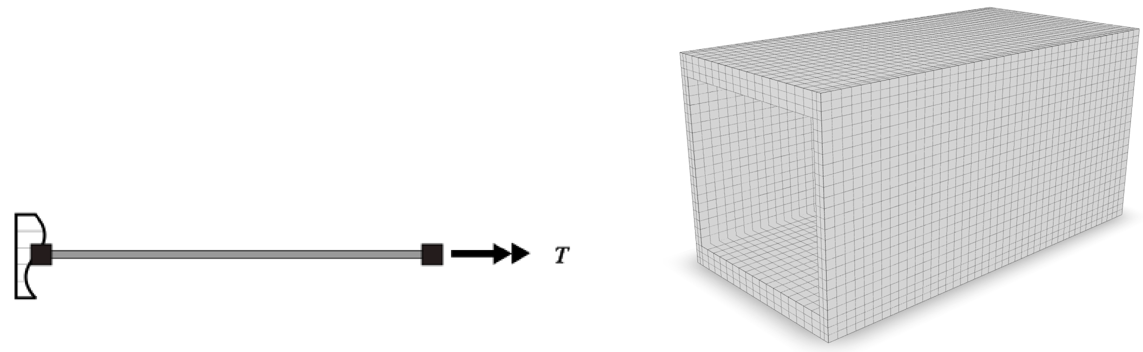

Figure 6.7: Model for Example 6.4.

Motivation. This example demonstrates accuracy of the enhanced formulation of Chapter 5 under inelastic material response. The reference solution is a finite element simulation of the continuum problem.

Setup. The cantilever of Figure 6.7 is subjected to a torque at the free end $x = L$. Material response is modeled by J_2 plasticity with linear hardening. Two warping conditions are considered:

1. Warping is restrained only at the root
2. Warping is prevented at both ends

The solid model is composed of linear mean dilation hexahedron elements. All nodes at $x = 0$ are fully restrained. For boundary condition 2, axial displacements are restrained at $x = L$. A rotation is imposed at $x = L$ by setting the displacements to

$$\mathbf{u}_i = \mathbf{x}_i \times \mathbf{i}\,\vartheta$$

for each node i at $x = L$, where $\mathbf{x}_i$ is the position of the node and the twist angle ϑ is scaled with time.

The problem is modeled using four EF_n elements with $n = 1$ warping field. The enhanced section formulation of Chapter 5 is employed and a comparison is drawn against the continuum finite element model of Figure 6.7 and the torsion warping model of Simo and Vu-Quoc (1991). Properties of the cross section and material parameters are collected in Box 6.4.

Results. Results are displayed in Figure 6.8 with the torque normalized by:

$$T_o := \frac{F_y}{\sqrt{3}} \int r \, \mathrm{d}A$$

The enhanced model of Chapter 5 shows closer agreement with the reference finite element solution. Identical results are obtained using the MF_n element.

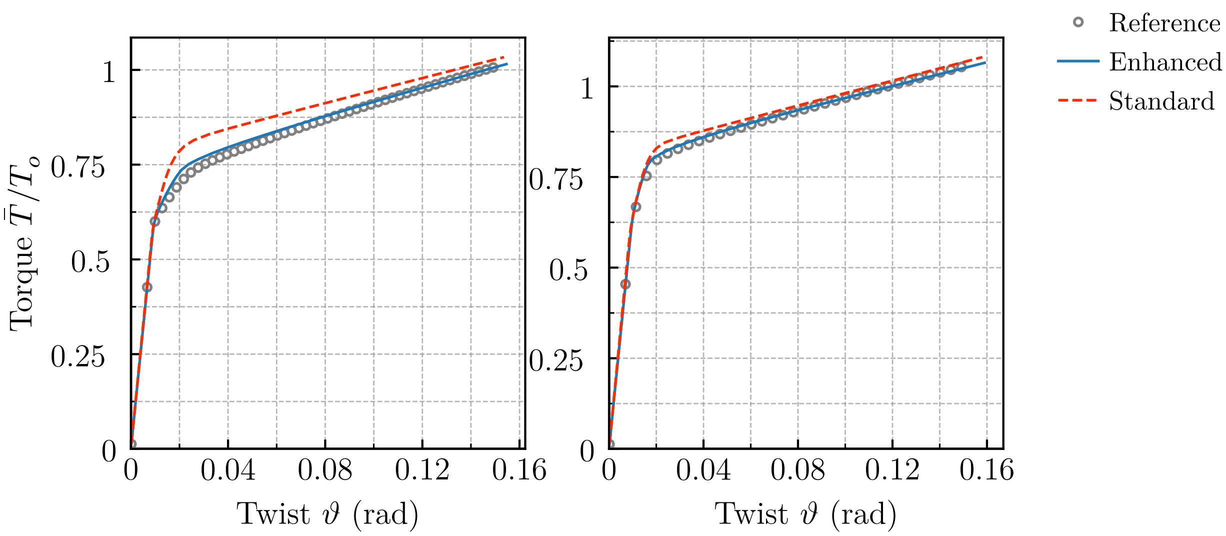

(a) Tip warping restrained.

(b) Tip warping free.

Figure 6.8: Results for Example 6.4 with $L = 2d$.

Box 6.4. Properties for Example 6.4

Material (6.1.1)			*Shape* (Figure 6.1b)			Table 4.1		
E	$=$	29×10^3 ksi	d	$=$	20 in	$\widehat{EA}$	$=$	$110\ E$ ksi in^2
G	$=$	11×10^3 ksi	b	$=$	20 in	$\widehat{GJ}_\vartheta$	$=$	$9.0 \times 10^3\ G$ ksi in^4
H_{iso}	$=$	$0.03\ E$ ksi	t_f	$=$	2 in			
F_y	$=$	60 ksi	t_w	$=$	1 in			

6.5 Inelastic Nonlinear Nonuniform Torsion

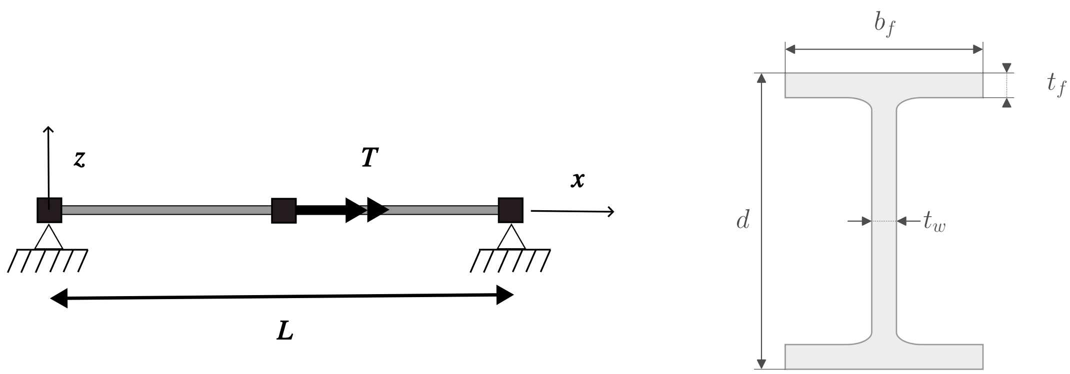

Figure 6.9: Model for Example 6.5.

Motivation. This example demonstrates the section-local evaluation of the Wagner term (3.2.17) proposed by Chapter 3. The benchmark solution is the experiment by Farwell and Galambos (1969)[1].

Setup. The span in Figure 6.9 is subjected to a concentrated torque $\bar{T}$ at midspan ($x = L/2$). Ten EF_1 elements are used to model the span with $n = 1$ auxiliary torsional warping field. The enhanced section of Chapter 5 is used. The section is a wide flange shape with properties collected in Box 6.5.

Results. Results are displayed in Figure 6.10 where the torque is normalized by T_o (Dinno & Merchant, 1965):

$$T_o := \left[\frac{d}{L}\frac{1}{4}t_f b_f^2 + \frac{1}{2}\left(2b_f t_f^2 + (d/2 - t_f)t_w^2\right)\right]\frac{F_y}{\sqrt{3}}$$

The formulation proposed by Le Corvec (2012) successfully represented the Wagner term in problems where the axial force was restrained. However, in a problem that was similar to the present (Le Corvec, 2012, Figure 5.13 (b)), where axial forces were unrestrained, the Wagner effect vanished so the model produced the linear strain response of Figure 6.10.

[1] See also the discussion by Pandit (1970).

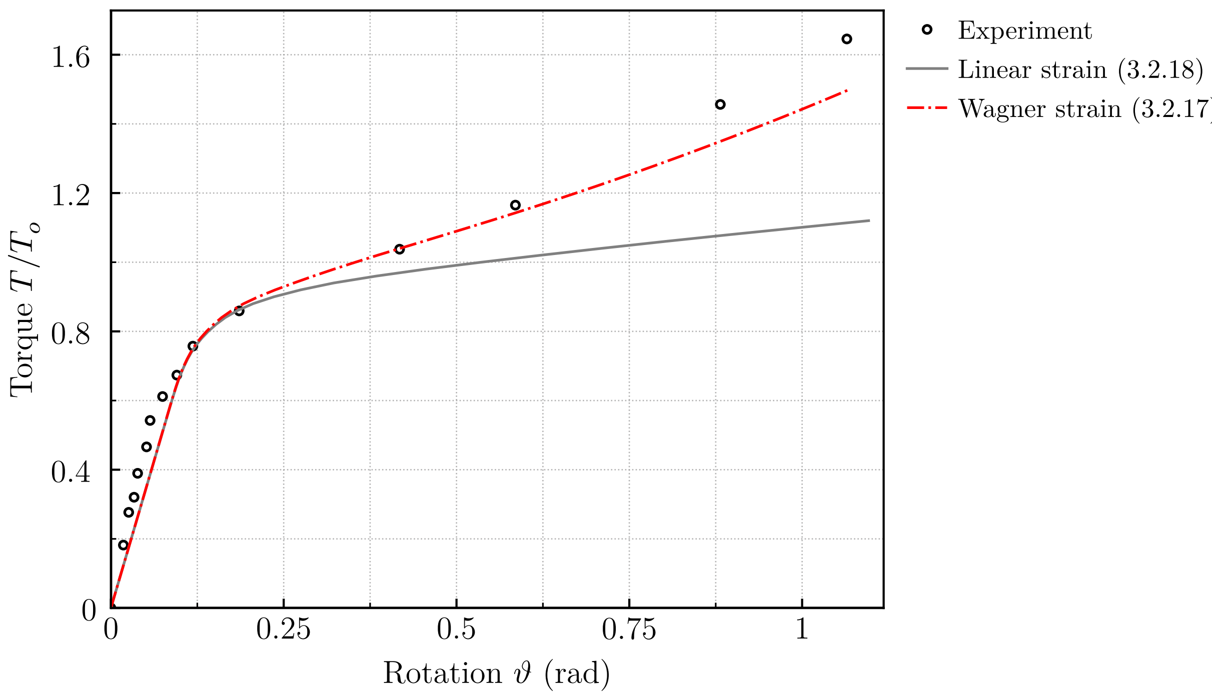

Figure 6.10: Normalized torque-rotation response of Example 6.5.

Box 6.5. Properties for Example 6.5

Material (6.1.1)

E	=	29×10^3 ksi
G	=	11×10^3 ksi
H_{iso}	=	$0.03\ E$ ksi
F_y	=	41 ksi

Shape (Figure 6.1d)

d	=	6 in
b	=	5.94 in
t_f	=	0.481 in
t_w	=	0.313 in

Table 4.1

$\widehat{EA}$	=	$7.3\ E$ ksi in^2
$\widehat{GJ}_\vartheta$	=	$0.484\ G$ ksi in^4

6.6 Finite Deformation of a Cantilever with Channel Section

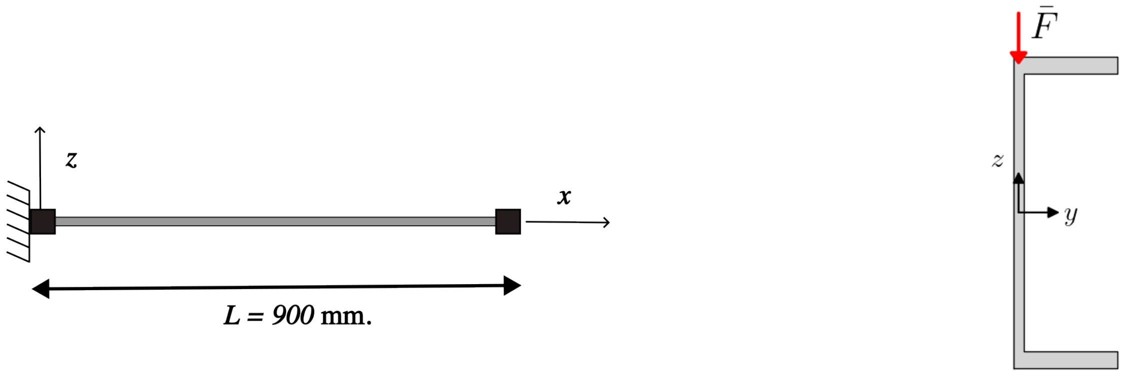

Figure 6.11: Model for Example 6.6.

Motivation. This example demonstrates the proposed formulation under finite deformations.

Setup. A cantilever with a channel section is loaded by an eccentric transverse force into the finite deformation range. The model depicted in Figure 6.13 with 4,320 shell elements is used to obtain the reference solution.

The problem is simulated using 20 EF_0 beam finite elements with the enhanced formulation of Chapter 4 and the energetic trace of Section E.2. The Wagner term (3.2.17) is not considered. The relevant cross sectional properties are collected in Box 6.6

Results. The deformed shape is depicted in Figure 6.14 and load-displacement curves are plotted in Figure 6.12, where excellent agreement with the shell model is observed.

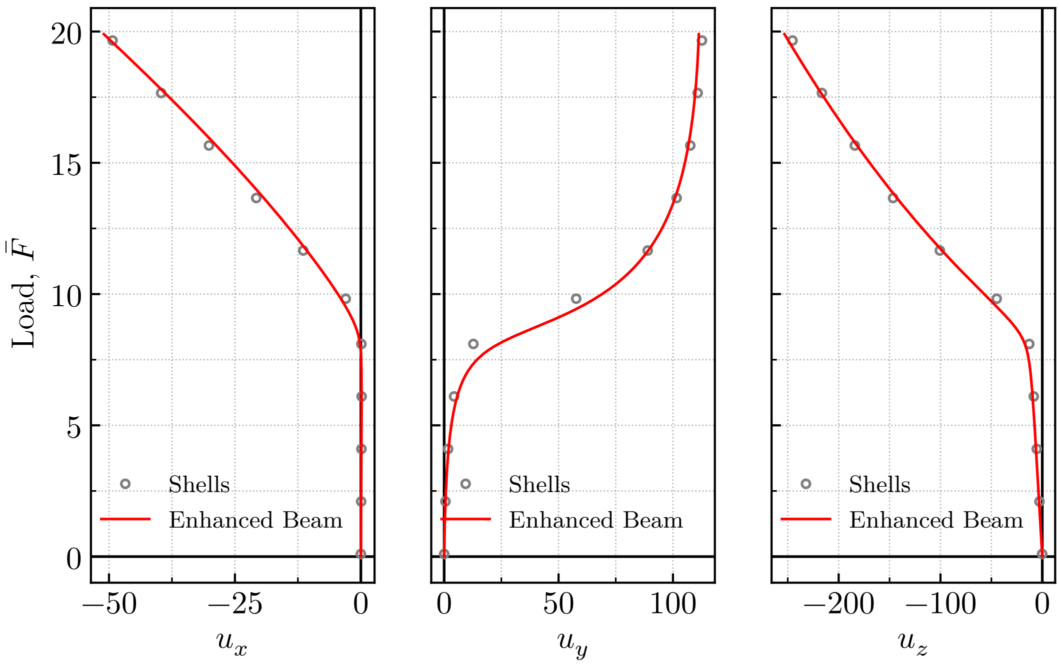

Figure 6.12: Displacements vs load $\bar{F}$ for Example 6.6.

Box 6.6. Properties for Example 6.6

Material

$$E = 210 \text{ GPa}$$
$$G = 81 \text{ GPa}$$

Shape (Figure 6.1e)

$$d = 30 \text{ cm}$$
$$b = 10 \text{ cm}$$
$$t_f = 1.6 \text{ cm}$$
$$t_w = 1 \text{ cm}$$

Table 4.1

$$\widehat{EA} = 59\ E \text{ GPa cm}^2$$
$$\widehat{GJ}_\vartheta = 35\ G \text{ GPa cm}^4$$

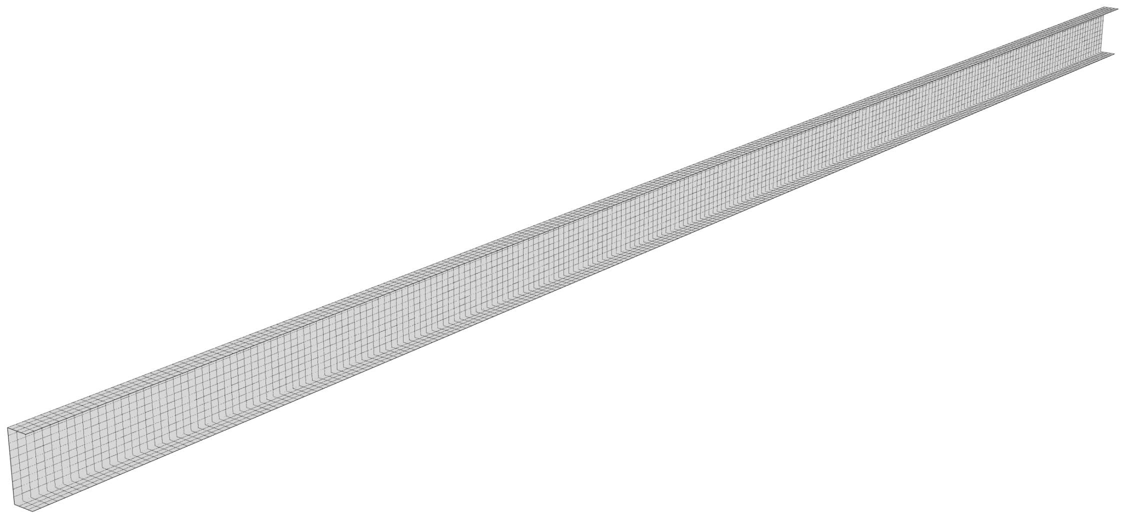

Figure 6.13: Shell model for Example 6.6.

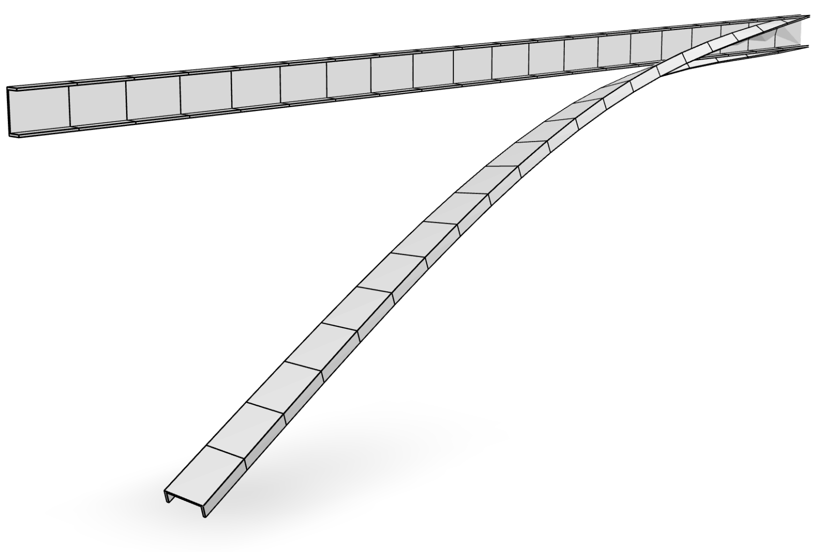

Figure 6.14: Deformed shape of the enhanced beam model for Example 6.6.

Part II

Structural Assessment

Chapter 7

Introduction to Part II

7.1 Motivation

Part II of this dissertation develops a framework for structural health monitoring that integrates physics-based simulation and data-driven inference within a common operational environment. The setting is motivated by the need to transform recorded structural motions into quantitative assessments of condition at the speed and scale required for post-earthquake decision-making. Accelerometer records may be available within seconds of an event, yet their translation into actionable guidance for closure, inspection, and follow-up analysis remains difficult for regional transportation systems. Recent work on digital twins and structural health monitoring has underscored both the promise of this setting and the absence of a stable framework in which simulation, sensing, inference, and reporting may be made to cooperate coherently (Kapteyn et al., 2021; Alibrandi, 2022; Torzoni et al., 2024; Chern et al., 2025).

Two complementary strategies are available for this task. In physics-based assessment, a structural model is subjected to recorded or simulated motions and the resulting response quantities are interpreted through condition metrics. In data-driven assessment, recorded motions are used to identify dynamic characteristics whose variation over time serves as an indicator of damage. Both strategies have demonstrated value, but their integration in an operational setting poses architectural demands that are not addressed by either class of method in isolation. A practical platform must admit heterogeneous predictors, preserve the provenance of their outputs, and remain sufficiently modular to accommodate new analysis procedures, including those arising from machine learning, without repeated reformulation of the surrounding software (Mosalam & Gao, 2024).

The present work develops such a framework. Structural assessment is organized around five abstractions, *Asset*, *Event*, *Predictor*, *Metric*, and *Evaluation*, which together furnish a stable basis for scalable monitoring platforms. The framework is implemented as the Bridge

Rapid Assessment Center for Extreme Events (BRACE^2), developed in collaboration with the California Department of Transportation (Caltrans) to provide real-time post-earthquake assessments for instrumented bridges in California. The developments of Part I furnish the primary simulation engine for the physics-based predictors on this platform.

A further requirement of this setting is the calibration of simulation models against identified response descriptors. In practice, the parameters of interest often enter through geometry generation, section discretization, constitutive preprocessing, or load parameterization, rather than directly through the finite element kernel. This motivates the development of analytic response gradients in a form that respects the layered structure of the modeling workflow and supports interaction with automatic-differentiation toolchains.

7.2 Outline

The presentation is organized as follows. Chapter 8 develops the architecture of the BRACE^2 platform. Structural assessment is organized around the abstractions of *Asset*, *Event*, *Predictor*, *Metric*, and *Evaluation*, and the corresponding implementation is realized through a layered software architecture separating presentation, orchestration, domain, and infrastructure concerns. This organization permits physics-based simulation and data-driven identification procedures to operate within a common event-evaluation workflow and to report their results through a unified metric interface.

Chapter 9 develops a compositional system for computing analytic parameter gradients of finite element simulations. The approach extends the work of HAUKAAS (2003) and SCOTT (2004) by embedding a solver supported by direct differentiation within a differentiable pipeline that chains gradients through transformations of arbitrary depth, including those computed by algorithmic differentiation of host-language code. A host-level parameterization constructs the core parameter vector required by the analysis kernel, the finite element kernel supplies reduced-response derivatives with respect to that core vector, and full sensitivities with respect to the original user variables are recovered by the chain rule. This provides critical functionality for the model updating and reliability workflows under development on the BRACE^2 platform.

Chapter 8

A Platform for Structural Health Monitoring

8.1 Introduction

Over the past two decades, performance-based assessment has increased the demand for computational procedures capable of predicting bridge response under extreme actions. Earthquake loading remains the principal motivation, but similar demands arise in blast, vehicular impact, scour, and progressive-collapse scenarios. In each case the analysis procedures of interest must accommodate nonlinear material response, finite-displacements, and numerically stable solution algorithms. Simultaneously, the expansion of structural monitoring networks has increased the importance of data-driven identification procedures that transform ambient or event-recorded vibrations into quantitative indicators of structural condition. Physics-based simulation and data-driven inference therefore address the same assessment problem from complementary directions.

The practical realization of these capabilities requires a software framework that is both operationally reliable and sufficiently modular to accommodate continued changes in numerical methods and computing technology. Earlier work has shown that simulation environments can remain useful over long periods when their responsibilities are organized through careful separation of concerns and composition-oriented design (McKenna, 1997; Scott, 2004). The present chapter develops such a framework for structural health monitoring. The framework is implemented as the Bridge Rapid Assessment Center for Extreme Events (Brace^2), and structural assessment is organized around five abstractions, *Asset*, *Event*, *Predictor*, *Metric*, and *Evaluation*. This organization permits physics-based and data-driven procedures to operate within a common event-assessment workflow while preserving the independence of the underlying numerical engines.

Each abstraction is realized through a narrow interface that exposes only the behavior required for coordination with the remainder of the platform. Predictor outputs are reduced to a common metric representation with explicit provenance and are subsequently assembled into evaluations by structure-specific policies. In this way, nonlinear response-history analysis, system-identification procedures, and emerging surrogate models may be incorporated within the same operational environment without repeated reformulation of the surrounding software. The resulting architecture is intended to support continued development in material modeling, solution algorithms, machine learning, and computing infrastructure.

Section 8.2 describes the architectural layers. Section 8.3 describes the predictor-scheduling workflow. Section 8.4 describes the policy mechanism through which metrics are assembled into actionable structural health evaluations.

8.2 Architectural Overview

The framework is organized as a four-layer interface stack that flows from user-facing web pages down to operating-system resources. The implementation has four layers: presentation, orchestration, domain, and infrastructure. Each layer holds a distinct responsibility and communicates with its neighbors solely through deliberately thin, technology-neutral interfaces. This partitioning both localizes change and establishes clear trust boundaries for security and audit.

8.2.1 Presentation Layer

The topmost layer delivers HTML dashboards, REST endpoints, and programmatic client libraries (Richardson & Amundsen, 2015). Its single obligation is to translate internal domain concepts into artifacts that humans or external services can consume. All interaction with the analysis core is mediated through type-checked view models; raw database cursors or solver handles never cross this boundary. The separation prevents tightly coupled dependencies and allows rapid evolution of the interface without risking regressions in numerical behavior.

8.2.2 Orchestration Layer

Beneath the presentation tier sits a scheduler that governs the life-cycle of monitoring workflows. It listens for *Event* notifications, allocates compute resources, dispatches *Predictor* instances, and reconciles their outputs into an *Evaluation*. Orchestration is intentionally stateless between jobs. Every mutable artifact is persisted by the Domain Layer so that workflows can be replayed verbatim for audit or research replication. Because the scheduler interacts with predictors only through a minimal launch protocol, additional numerical engines can be registered without changes to scheduling code.

8.2.3 Domain Layer

The Domain Layer captures the five abstractions that underpin the monitoring logic. These objects expose behavior through stable interfaces while hiding implementation details such as schema migration, file-system layout, or communication middleware. Two design decisions reinforce the layer's modularity:

- **Composition over specialization.** New predictor capabilities are introduced by assembling existing behavior blocks rather than by extending deep inheritance hierarchies. This approach limits cross-cutting side-effects and keeps object graphs shallow.
- **Strict data immutability at workflow boundaries.** An *Event* record is never modified after creation; an *Evaluation* becomes read-only once published. Immutability simplifies concurrent access, supports content-addressable caching, and eliminates entire classes of race conditions.

8.2.4 Infrastructure Layer

The bottom layer abstracts operating-system concerns: database connectivity, object storage, job queues, and low-level telemetry. These services are accessed through narrow gateway classes so that the remainder of the codebase remains indifferent to whether the platform runs on a developer laptop or a cloud cluster. Changes in deployment target therefore require only the replacement of gateway adapters, not a refactor of business logic.

8.2.5 Layer Collaboration

Communication proceeds strictly downward. For example, when the Presentation Layer receives a request for the latest bridge health report it calls the Orchestration Layer, which in turn queries the Domain Layer for immutable *Evaluation* objects. Only the Infrastructure Layer is permitted to reach outside the codebase. Upward calls are prohibited; infrastructure code does not emit direct UI updates, and domain objects have no knowledge of HTTP[1] semantics. The unidirectional rule guards against hidden coupling and ensures that each layer can be tested in isolation.

[1] The Hypertext Transfer Protocol (HTTP) is a standard protocol established by FIELDING et al. (2022).

8.3 Prediction Subsystem

The design objective of the Prediction Subsystem is to permit the continuous integration of new modeling techniques while shielding the rest of the platform from solver-specific details. To this end, each concrete predictor is packaged behind a **Strategy** object (GAMMA, 2011) that realizes a simplified four-phase template: *initialize*, *execute*, *harvest*, and *summarize*. A lightweight **Factory Registry** maps protocol identifiers to concrete strategy instances at runtime. Adding a novel predictor therefore requires no modification to orchestration code, only the registration of a new strategy class and, if desired, the definition of new metric types to reflect its particular output.

During execution a predictor writes its raw results to a unique run directory and emits a structured summary describing the provenance of every number that ultimately appears on a dashboard. This provenance trail is critical to after-action audits and mirrors the reproducibility guarantees advocated in earlier software for finite-element research. The same provenance mechanism underpins a run-level caching scheme: if an identical event–predictor combination is encountered twice, the second request can be satisfied by replaying the cached results instead of performing a new analysis.

8.3.1 Metrics

Health metrics are immutable value objects (FOWLER, 2013) that bind three pieces of information: a *label* that identifies the physical quantity (e.g., fundamental period, peak deck acceleration, column strain state), a compact payload containing the numerical value(s), and a *verdict* that classifies the value against user-defined thresholds. Metrics understand how to render themselves in the web interface, how to serialize into archival formats, and how to participate in evaluation-level aggregation. Because all predictors emit metrics rather than solver-specific artifacts, downstream consumers need not know whether a given metric was extracted from a finite-element response history, inferred by a statistical emulator, or read from a fragility table.

8.4 Event and Evaluation Workflow

An event enters the system through a secure web service that authenticates the request, stores raw sensor streams in object storage, and inserts a new row in the *Event* ledger. At that instant a long-lived scheduler running in the Orchestration Layer called the **Evaluation Daemon** receives a notification. The daemon queries the Asset record to discover which predictors are active and queues them for execution according to resource-aware policies. Predictors may run concurrently, and each operates in isolation within its own working directory.

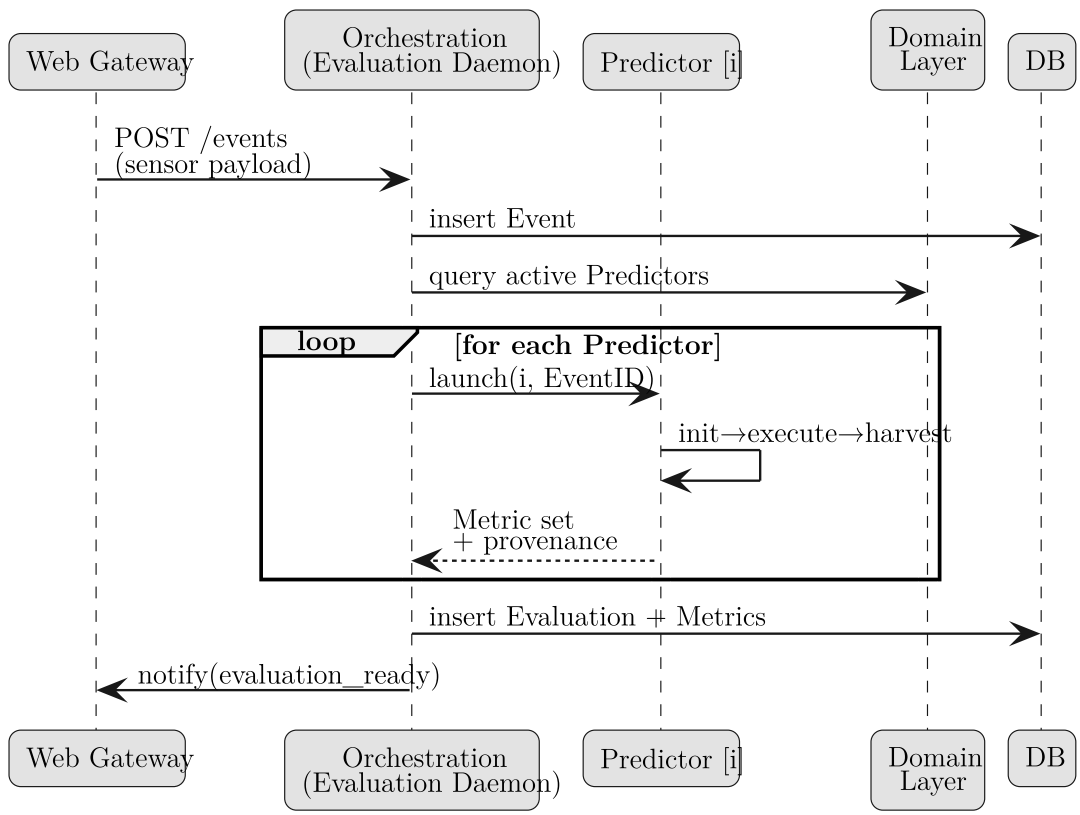

Figure 8.1: Sequence diagram illustrating the process of evaluating an event.

When a predictor finishes, the daemon collects its metrics and inserts them into the database under a new *Evaluation* record. Once all predictors for an event have reported, the daemon invokes an **Evaluation Policy** that scans the assembled metric set, assigns an overall health state, and dispatches notifications to stakeholders. The policy mechanism is again a Strategy: facilities managers can supply their own decision logic, ranging from simple threshold checks to Bayesian belief networks, without disturbing core services.

Figure 8.1 illustrates the complete event path, from acceleration time histories arriving at the web gateway to color-coded health tiles appearing on the bridge dashboard.

Algorithm 1 Top–level evaluation routine.

```
function Evaluate(event, evaluation)
    c_ok ← 0
    daemon ← LiveEvaluation(event, event.asset.predictors, evaluation)
    predictors ← AssignMetricPredictors(daemon, event)
    for all (pName, runID) ∈ RunPredictor(daemon, predictors) do
        for all m ∈ predictors[ pName ].metrics do
            data ← daemon.predictors[ pName ].getMetricData(runID, m)
            if data ≠ ∅ then
                c_ok ← c_ok + 1
                SetMetricData(daemon, m, pName, data)
            end if
        end for
    end for
    if c_ok > 0 then
        evaluation.status ← Finished
    else
        evaluation.status ← Invalid
    end if
    save(evaluation) | save(daemon)
    return evaluation
end function
```

Algorithm 2 Assigning predictors to active metrics (method of LiveEvaluation).

```
function AssignMetricPredictors(daemon, event)
    Q ← ∅                                        ▷ Map: predictor ↦ (runID, metric-list)
    for all m ∈ daemon.active_metrics do
        for all (π, s) ∈ ScorePredictors(m, daemon.predictors, event) do
            if π.active ∧ π.name ∉ dom(Q) then
                ρ ← π.newPrediction(event)
                Q[π.name] ← (ρ, [ ])
            end if
            π.activateMetric(m, Q[π.name].ρ)
        end for
    end for
    return Q
end function
```

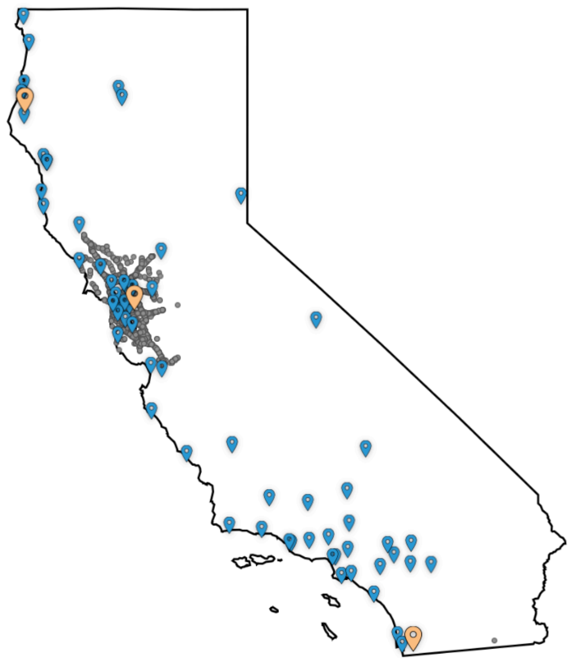

Figure 8.2: Assets in the California deployment of BRACE[2].

8.4.1 Events

Data driven methods are currently limited by data sparsity. Figure 8.3 compares the recorded data in each Caltrans district with that district's exposure to large ground motions. Figure 8.3a shows the number of recorded events normalized by the number of BRACE[2] assets in the district. Figure 8.3b shows the exposure index

$$E_D = Q_{0.90}\{s(\mathbf{x}) : \mathbf{x} \in G_D\},$$

where G_D is the set of grid points used to sample district D, $Q_{0.90}$ is the empirical 0.90 quantile, and $s(\mathbf{x})$ is the 2% in 50 year uniform-hazard value of 5%-damped $S_A(1.0\,\mathrm{s})$ at Site Class BC. The value $s(\mathbf{x})$ is obtained from the USGS hazard curve at $\mathbf{x}$ by solving

$$\nu_{\mathbf{x}}(s(\mathbf{x})) = -\frac{\log(1-0.02)}{50},$$

with interpolation performed in logarithmic coordinates.

[2]Number of events with PGA $\geq 0.1\,g$ per asset in the district.

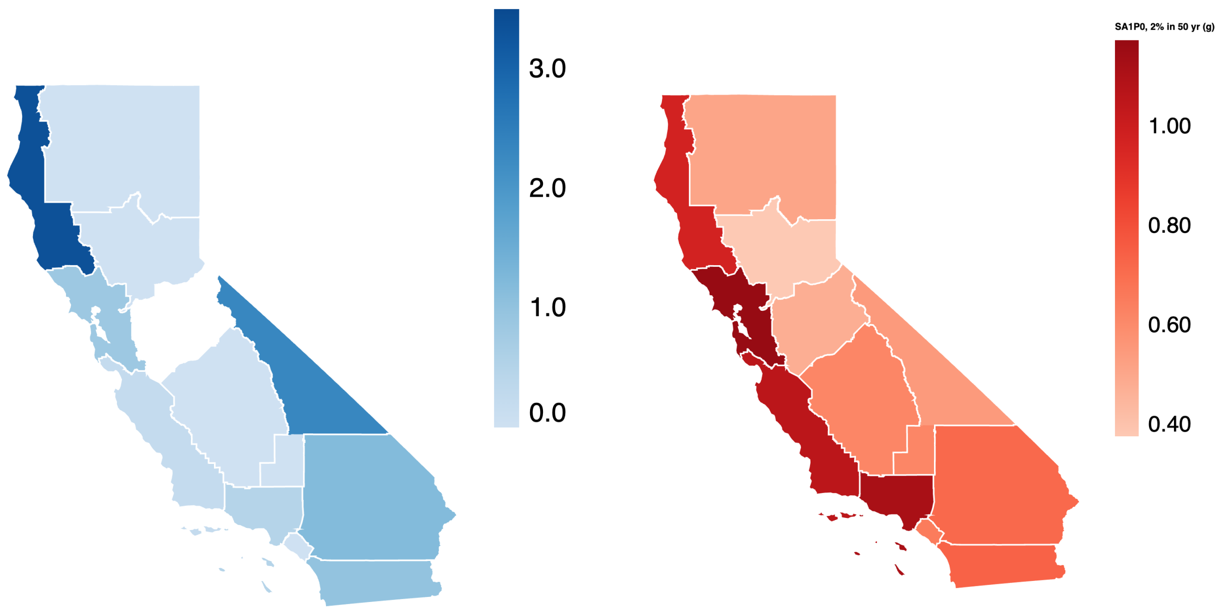

(a) Events per asset[2]

(b) District seismic exposure

Figure 8.3: District-level exposure measures.

The discrepancy illustrated by Figure 8.3 is addressed through the use of synthetic ground motion data. Recent efforts have produced extensive simulation databases over seismically active regions, with the Simulated Ground Motion Database (McCallen et al., 2025) providing high-fidelity simulations across an 80 km×120 km region of the San Francisco Bay Area (Figure 8.4[3]).

8.4.2 Inventory

The platform was initially deployed in a 6-month pilot phase, where digital twins were created for 22 instrumented bridges in the Caltrans inventory (Table 8.2). Throughout the development of the platform, real-time monitoring has centered around two pilot structures:

- The *Hayward Hwy 580-238 Interchange* (`33-0214L`)
- The *US 101/Painter St. Overcrossing* (`04-0236`)

Table 8.1 summarizes the events processed for these structures through past records (CESMD) and real time transmissions (Brace[2]).

[3]This graphic was created using *vega-lite* (Satyanarayan et al., 2017).

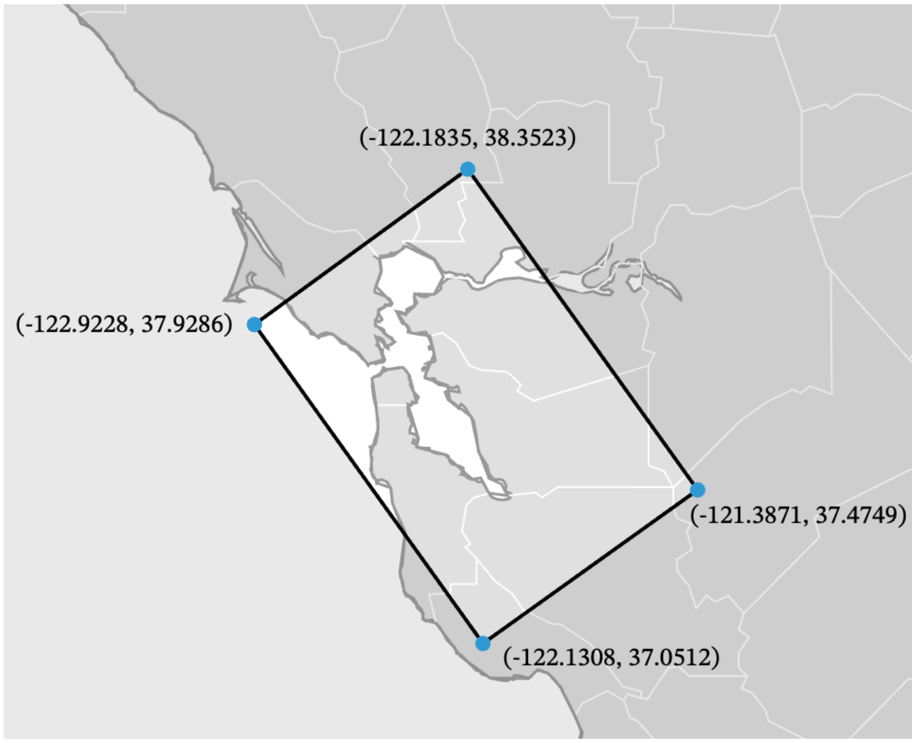

Figure 8.4: San Francisco Bay region of the SGMD.

Table 8.1: Strong motion records at BRACE^2 pilot assets as of January 9, 2026.

Asset	Station	Records	
		CESMD	BRACE^2
`33-0214L`	CE58658	16	90
	CE58486	6	20
`04-0236`	CE89324	33	3
	CE89462	45	5

The remaining 21 bridges where studied using preexisting records. Following the success of this trial deployment, development of the platform was resumed with future work expected to expand its coverage of the California highway network.

Table 8.2: Bridges included in the pilot study for the BRACE^2 platform.

ID	**Name**	**Events**	**Sensors**	**Predictors**
56-0586G	Corona - I15/Hwy91 Interchange Bridge	3	9	6
55-0225	Capistrano Beach - I5/Via Calif. Bridge	5	12	3
53-1471	Los Angeles - Vincent Thomas Bridge	7	26	4
53-2795F	Sylmar - I5/14 Interchange Bridge	2	42	2
53-2791	Los Angeles - I10/La Cienega Bridge	5	15	3
53-1794	Palmdale - Hwy 14/Barrel Springs Bridge	6	12	3
50-0271	Grapevine - I5/Lebec Rd Bridge	7	16	3
50-0340	Ridgecrest - Hwy 395/Brown Road Bridge	5	9	3
43-0031E	San Juan Bautista - Hwy 101/156 Overpass	10	15	3
23-0015R	Vallejo - Carquinez/I80 East Bridge	3	58	2
28-0352L	Vallejo - Carquinez/I80 West Bridge	5	103	5
10-0299	Leggett - Hwy 101/Confusion Hill Bridge	5	24	6
04-0228	Eureka - Samoa Channel Bridge	18	27	4
04-0170	Hwy 101/Murray Road Bridge (Arcata)	7	12	6
04-0229	Eureka - Middle Channel Bridge	14	9	3
04-0230	Eureka - Eureka Channel Bridge	13	12	4
04-0016R	Rio Dell - Hwy 101/Eel River Bridge	46	18	3
54-0823G	San Bernardino - I10/215 Interchange	9	18	4
47-0048	Hwy 395 Bridge (Lake Crowley)	5	9	6
04-0236	Hwy 101/Painter St. Overcrossing	31	20	6
58-0215	Hwy8/Meloland Overpass	13	32	7
33-0214L	Hayward Hwy 580-238 Interchange	62	20	7
Total		281	518	93

Chapter 9

Compositional Differentiation for Finite Element Analysis

9.1 Introduction

This chapter develops a compositional framework for analytic response gradients in finite element analysis. The setting of interest is one in which the variables governing model calibration, reliability analysis, and simulation-based inference are introduced through geometry generation, section discretization, constitutive preprocessing, or load parameterization, rather than directly as arguments of the discrete equilibrium equations. In such problems, the parameters that are meaningful to the analyst and the parameters native to the analysis model are generally distinct, and a useful differential formulation must therefore account for the full construction by which the latter are obtained.

The proposed treatment separates these roles. A host parameterization constructs the core parameter vector required by the finite element model, while the analysis procedure furnishes derivatives of the reduced response with respect to that core representation. Sensitivities with respect to the original modeling variables are then recovered by composition. The formulation supports both forward and reverse contractions, and introduces a parameter-binding procedure that associates host variables with the concrete locations at which they act in the assembled model. In this way, geometry generation, fiber discretization, constitutive data, and loading may be incorporated in a differentiable simulation workflow without extending the analysis model to each new user-defined construction.

The resulting framework provides the gradient capability required for the model updating and reliability procedures under development on the BRACE^2 platform and, more generally, places finite element simulation in a form suitable for interaction with automatic-differentiation toolchains.

The presentation proceeds as follows. Section 9.2 defines the state, response, and parameter maps. Section 9.3 develops the differential structure and the associated forward and reverse contractions. Section 9.4 describes the parameter-binding procedure. Section 9.5 presents verification examples.

9.2 Setting. State and Response Maps

A system that relies entirely on direct differentiation must implement differentiation rules for any parameterization of the model that may be of interest. In the proposed approach, direct differentiation is only required for a minimal parameter set that is required to perform the analysis. These parameters are referred to as *core parameters* $\boldsymbol{y} \in \mathcal{Y} \sim \mathbb{R}^n$. Typical core parameters include material properties, fiber coordinates and areas, nodal coordinates, and prescribed force magnitudes.

Any parameter set from which the core parameter may be derived is referred to as the *host parameterization* $\hat{\boldsymbol{y}} \in \hat{\mathcal{Y}} \sim \mathbb{R}^{\hat{n}}$. These generally represent quantities that the analyst wishes to differentiate with respect to and typically include cross-section dimensions, load multipliers, random-field coefficients, or any other inputs that the user controls.

A user-defined parameterization is a differentiable map

$$\Phi : \mathbb{R}^{\hat{n}} \to \mathbb{R}^n, \qquad \hat{\boldsymbol{y}} \mapsto \boldsymbol{y} = \Phi(\hat{\boldsymbol{y}}), \tag{9.2.1}$$

For each $\boldsymbol{y} \in \mathcal{Y}$, the equilibrium state $\boldsymbol{u} \in \mathcal{U}$ satisfies

$$\mathcal{G}_{\mathcal{M}}(\boldsymbol{u}, \boldsymbol{y}) = 0.$$

where $\mathcal{M}$ is a fixed discretization of the physical model. For a well posed problem this implicitly defines a differentiable solution map:

$$S_{\mathcal{M}} : \mathcal{Y} \to \mathcal{U}, \qquad \boldsymbol{u} = S_{\mathcal{M}}(\boldsymbol{y}).$$

Given a quantity of interest $Q_{\mathcal{M}} : \mathcal{U} \times \mathcal{Y} \to \mathcal{Z}$ the reduced response map is

$$R_{\mathcal{M}}(\boldsymbol{y}) = Q_{\mathcal{M}}(S_{\mathcal{M}}(\boldsymbol{y}), \boldsymbol{y}). \tag{9.2.2}$$

The user-facing response is the composite map

$$\widehat{R}_{\mathcal{M}} = R_{\mathcal{M}} \circ \Phi : \hat{\mathcal{Y}} \to \mathcal{Z}, \qquad \boldsymbol{y} = \Phi(\hat{\boldsymbol{y}}).$$

Remark 9.2.1. If the quantity of interest is the full discrete state, then one may take

$$Q_{\mathcal{M}}(\boldsymbol{u}, \boldsymbol{y}) = \boldsymbol{u},$$

in which case $R_{\mathcal{M}} = S_{\mathcal{M}}$.

9.3 Differential Structure

For any differentiable map $f : X \to Z$, define its tangent extension by

$$\mathrm{Tan}\,[\,f\,]\,(x, \dot{x}) = \big(f(x), \mathrm{D}f(x)[\dot{x}]\big).$$

For composable differentiable maps $g : X \to Y$ and $f : Y \to Z$,

$$\mathrm{Tan}\,[\,f \circ g\,] = \mathrm{Tan}\,[\,f\,] \circ \mathrm{Tan}\,[\,g\,]\,.$$

The total derivative of the reduced map (9.2.2) satisfies the chain rule

$$\mathrm{D}\widehat{R}_{\mathcal{M}}(\hat{\boldsymbol{y}}) = \mathrm{D}R_{\mathcal{M}}(\boldsymbol{y}) \circ \mathrm{D}\Phi(\hat{\boldsymbol{y}}) \in \mathcal{L}(\hat{\mathcal{Y}}, \mathcal{Z}). \tag{9.3.1}$$

After choosing coordinates on $\hat{\mathcal{Y}}$, $\mathcal{Y}$, and $\mathcal{Z}$, this becomes

$$\frac{\partial \widehat{R}_{\mathcal{M}}}{\partial \hat{\boldsymbol{y}}} = \frac{\partial R_{\mathcal{M}}}{\partial \boldsymbol{y}}\,\frac{\partial \Phi}{\partial \hat{\boldsymbol{y}}}. \tag{9.3.2}$$

Kernel Level Operators.

The finite element kernel is required to provide the tangent extension of the reduced response map

$$\mathrm{Tan}\,[\,R_{\mathcal{M}}\,] : \mathcal{Y} \times \mathcal{Y} \to \mathcal{Z} \times \mathcal{Z}.$$

If $\boldsymbol{u} = S_{\mathcal{M}}(\boldsymbol{y})$, the tangent state $\dot{\boldsymbol{u}}$ is defined by the linearized equilibrium equation

$$\mathrm{D}_1\mathcal{G}_{\mathcal{M}}(\boldsymbol{u}, \boldsymbol{y})[\dot{\boldsymbol{u}}] = -\mathrm{D}_2\mathcal{G}_{\mathcal{M}}(\boldsymbol{u}, \boldsymbol{y})[\dot{\boldsymbol{y}}].$$

The corresponding response variation is

$$\mathrm{D}R_{\mathcal{M}}(\boldsymbol{y})[\dot{\boldsymbol{y}}] = \mathrm{D}_1Q_{\mathcal{M}}(\boldsymbol{u}, \boldsymbol{y})[\dot{\boldsymbol{u}}] + \mathrm{D}_2Q_{\mathcal{M}}(\boldsymbol{u}, \boldsymbol{y})[\dot{\boldsymbol{y}}].$$

When the quantity of interest is a pure state extraction, the second term vanishes.

Host Level Operators.

The host system is required to provide the tangent extension of the parameterization map

$$\mathrm{Tan}\,[\,\Phi\,] : \hat{\mathcal{Y}} \times \hat{\mathcal{Y}} \to \mathcal{Y} \times \mathcal{Y}.$$

Equivalently, for any $(\hat{\boldsymbol{y}}, \dot{\hat{\boldsymbol{y}}})$, the host returns

$$\Phi(\hat{\boldsymbol{y}}), \qquad \mathrm{D}\Phi(\hat{\boldsymbol{y}})[\dot{\hat{\boldsymbol{y}}}].$$

This layer contains all differentiable preprocessing that is external to the finite element kernel. It includes geometry generation, section construction, discretization rules, constitutive preprocessing, and load parametrization.

The Jacobian in (9.3.2) is not formed explicitly. One evaluates its action on tangent vectors or on cotangent vectors. The forward view is encoded by

$$\operatorname{Tan}\left[\widehat{R}_{\mathcal{M}}\right] = \operatorname{Tan}\left[R_{\mathcal{M}}\right] \circ \operatorname{Tan}\left[\Phi\right],$$

and the reverse view is encoded by

$$\mathrm{D}\widehat{R}_{\mathcal{M}}(\hat{\boldsymbol{y}})^* = \mathrm{D}\Phi(\hat{\boldsymbol{y}})^* \circ \mathrm{D}R_{\mathcal{M}}(\boldsymbol{y})^*.$$

9.3.1 Forward Mode

Given a tangent direction $\dot{\hat{\boldsymbol{y}}} \in \hat{\mathcal{Y}}$, the Jacobian–vector product is

$$\dot{\boldsymbol{z}} = \mathrm{D}\widehat{R}_{\mathcal{M}}(\hat{\boldsymbol{y}})[\dot{\hat{\boldsymbol{y}}}] = \underbrace{\mathrm{D}R_{\mathcal{M}}(\boldsymbol{y})}_{\text{kernel}}\Big[\underbrace{\mathrm{D}\Phi(\hat{\boldsymbol{y}})[\dot{\hat{\boldsymbol{y}}}]}_{\text{host}}\Big], \tag{9.3.3}$$

where $\boldsymbol{z} := \widehat{R}_{\mathcal{M}}(\hat{\boldsymbol{y}})$. The computation is performed in two stages:

1. **Host forward pass.** Evaluate

$$(\boldsymbol{y}, \dot{\boldsymbol{y}}) = \operatorname{Tan}\left[\Phi\right](\hat{\boldsymbol{y}}, \dot{\hat{\boldsymbol{y}}}), \qquad \dot{\boldsymbol{y}} = \mathrm{D}\Phi(\hat{\boldsymbol{y}})[\dot{\hat{\boldsymbol{y}}}].$$

2. **Kernel forward pass.** Evaluate

$$(\boldsymbol{z}, \dot{\boldsymbol{z}}) = \operatorname{Tan}\left[R_{\mathcal{M}}\right](\boldsymbol{y}, \dot{\boldsymbol{y}}), \qquad \boldsymbol{z} = R_{\mathcal{M}}(\boldsymbol{y}).$$

When the response map is induced by the residual and observation operators,

$$\mathcal{G}_{\mathcal{M}}(\boldsymbol{u}, \boldsymbol{y}) = 0, \qquad \boldsymbol{z} = Q_{\mathcal{M}}(\boldsymbol{u}, \boldsymbol{y}),$$

the tangent variables satisfy

$$\mathrm{D}_1\mathcal{G}_{\mathcal{M}}(\boldsymbol{u}, \boldsymbol{y})[\dot{\boldsymbol{u}}] = -\mathrm{D}_2\mathcal{G}_{\mathcal{M}}(\boldsymbol{u}, \boldsymbol{y})[\dot{\boldsymbol{y}}], \tag{9.3.4}$$

$$\dot{\boldsymbol{z}} = \mathrm{D}_1 Q_{\mathcal{M}}(\boldsymbol{u}, \boldsymbol{y})[\dot{\boldsymbol{u}}] + \mathrm{D}_2 Q_{\mathcal{M}}(\boldsymbol{u}, \boldsymbol{y})[\dot{\boldsymbol{y}}]. \tag{9.3.5}$$

After choosing coordinates $\boldsymbol{y} = (y_1, \dots, y_{n_\mathrm{c}})$,

$$\dot{\boldsymbol{z}} = \sum_{i=1}^{n_\mathrm{c}} \frac{\partial R_{\mathcal{M}}}{\partial y_i}(\boldsymbol{y})\, \dot{y}_i. \tag{9.3.6}$$

Forward mode is natural when derivatives are required in only a small number of host directions.

9.3.2 Reverse Mode

Given a cotangent $\bar{\boldsymbol{z}} \in \mathcal{Z}^*$, the vector–Jacobian product is

$$\bar{\hat{\boldsymbol{y}}} = \mathrm{D}\widehat{R}_{\mathcal{M}}(\hat{\boldsymbol{y}})^*[\bar{\boldsymbol{z}}] = \underbrace{\mathrm{D}\Phi(\hat{\boldsymbol{y}})^*}_{\text{host}}\Big[\underbrace{\mathrm{D}R_{\mathcal{M}}(\boldsymbol{y})^*[\bar{\boldsymbol{z}}]}_{\text{kernel}}\Big]. \tag{9.3.7}$$

In finite-dimensional Euclidean coordinates this is

$$\bar{\hat{\boldsymbol{y}}} = \left[\mathrm{D}\Phi(\hat{\boldsymbol{y}})\right]^{\top}\bar{\boldsymbol{y}}, \qquad \bar{\boldsymbol{y}} = \left[\mathrm{D}R_{\mathcal{M}}(\boldsymbol{y})\right]^{\top}\bar{\boldsymbol{z}}. \tag{9.3.8}$$

For a scalar objective $J : \mathcal{Z} \to \mathbb{R}$, one takes

$$\bar{\boldsymbol{z}} = \mathrm{D}J(\boldsymbol{z}), \qquad \bar{\hat{\boldsymbol{y}}} = \mathrm{D}(J \circ \widehat{R}_{\mathcal{M}})(\hat{\boldsymbol{y}}),$$

so that a single reverse sweep delivers the gradient with respect to all host parameters.

The computation again separates into two stages:

1. **Kernel reverse pass.** Compute the core-parameter cotangent

$$\bar{\boldsymbol{y}} = \mathrm{D}R_{\mathcal{M}}(\boldsymbol{y})^*[\bar{\boldsymbol{z}}].$$

   After choosing coordinates $\boldsymbol{y} = (y_1, \dots, y_{n_c})$,

$$\bar{y}_i = \left(\frac{\partial R_{\mathcal{M}}}{\partial y_i}(\boldsymbol{y})\right)^{\top}\bar{\boldsymbol{z}}, \qquad i = 1, \dots, n_{\mathrm{c}}. \tag{9.3.9}$$

   If $R_{\mathcal{M}}$ is described through $\mathcal{G}_{\mathcal{M}}$ and $Q_{\mathcal{M}}$, the same quantity may be obtained from the adjoint system

$$\mathrm{D}_1\mathcal{G}_{\mathcal{M}}(\boldsymbol{u}, \boldsymbol{y})^*[\boldsymbol{\eta}] = \mathrm{D}_1 Q_{\mathcal{M}}(\boldsymbol{u}, \boldsymbol{y})^*[\bar{\boldsymbol{z}}], \tag{9.3.10}$$

$$\bar{\boldsymbol{y}} = \mathrm{D}_2 Q_{\mathcal{M}}(\boldsymbol{u}, \boldsymbol{y})^*[\bar{\boldsymbol{z}}] - \mathrm{D}_2\mathcal{G}_{\mathcal{M}}(\boldsymbol{u}, \boldsymbol{y})^*[\boldsymbol{\eta}]. \tag{9.3.11}$$

2. **Host reverse pass.** Propagate $\bar{\boldsymbol{y}}$ through the parameter map:

$$\bar{\hat{\boldsymbol{y}}} = \mathrm{D}\Phi(\hat{\boldsymbol{y}})^*[\bar{\boldsymbol{y}}].$$

Reverse mode is natural when the number of outputs, or the number of scalar objectives, is small relative to the number of host parameters.

9.4 Parameter Binding

The preceding discussion treats the core parameter vector $\boldsymbol{y}$ as if its coordinates were already known. In a typical model-building workflow this identification is not immediate. A host variable may appear at different levels of the model description and may induce perturbations at many concrete locations in the discrete model. A separate registration step is therefore needed to identify which kernel entries are controlled by each scalar coordinate.

Let

$$\hat{\boldsymbol{y}} = (\hat{y}_1, \dots, \hat{y}_{n_\mathrm{h}})$$

denote the scalar host coordinates. The model factory is evaluated as a finite sequence of elementary construction operations defining a computational graph (Frostig et al., 2018) whose nodes are the intermediate objects created during model construction.

The set of model objects $\mathcal{O}$ appearing in this trace is partitioned into materials, sections, fibers, and elements:

$$\mathcal{O} = \mathcal{O}_\mathrm{mat} \cup \mathcal{O}_\mathrm{sec} \cup \mathcal{O}_\mathrm{fib} \cup \mathcal{O}_\mathrm{ele}$$

The trace induces a directed dependency relation on $\mathcal{O}$. For example, a fiber depends on the section in which it is created, and an element depends on the section instances referenced in its definition.

Labeling and Binding. Each scalar host coordinate is treated together with an identifying label,

$$\pi_i = (i, \nu_i, \hat{y}_i), \qquad i = 1, \dots, n_\mathrm{h},$$

where i is a global differentiation index and ν_i is a symbolic name. The value $\hat{y}_i$ is used in the primal construction, while (i, ν_i) records the identity of the coordinate in the differential structure.

When a labeled coordinate π_i appears in the evaluation trace, it is bound to an object

$$a_i \in \mathcal{O},$$

called its anchor. The anchor specifies the level at which the coordinate enters the model description. A material constant may be anchored at a material object, a geometric parameter at a section object, and a fiber area at a fiber object.

The evaluation trace then propagates this dependence downstream through the computational graph. In this way, one obtains the set of all concrete parameter locations in the kernel that are controlled by coordinate i.

Kernel Addresses. Let $\mathcal{A}$ denote the set of admissible kernel addresses. An address $\alpha \in \mathcal{A}$ identifies a parameter slot in the assembled model, for example a material parameter at a given section point within a given element, or a fiber attribute within a section occurrence. The binding process determines a set-valued map

$$\mathcal{B} : \{1, \dots, n_{\mathrm{h}}\} \to 2^{\mathcal{A}},$$

where $\mathcal{B}(i)$ is the set of all kernel addresses reached by following the dependency graph outward from the anchor a_i and $2^{\mathcal{A}}$ is the power set of $\mathcal{A}$ (Halmos, 1998).

Once the binding map $\mathcal{B}$ has been resolved, the host coordinates acquire a concrete realization in the kernel. In the simplest case one identifies

$$\boldsymbol{y} = (y_1, \dots, y_{n_{\mathrm{c}}}), \qquad n_{\mathrm{c}} = n_{\mathrm{h}}, \qquad y_i = \hat{y}_i,$$

so that the host and kernel use the same scalar coordinates, but the binding map $\mathcal{B}$ specifies where each coordinate acts in the assembled model.

Forward Contraction. The forward differential therefore takes the form

$$\mathrm{D}R_{\mathcal{M}}(\boldsymbol{y})[\dot{\boldsymbol{y}}] = \sum_{i=1}^{n_{\mathrm{c}}} \frac{\partial R_{\mathcal{M}}}{\partial y_i}(\boldsymbol{y})\, \dot{y}_i,$$

where each partial derivative already accounts for all bound kernel addresses associated with coordinate i. The host layer determines the perturbation coefficients $\dot{y}_i$, while the kernel layer evaluates the corresponding directional effect on the response.

Remark 9.4.1. The preceding description assumes that the evaluation trace produces a fixed model topology. Under this assumption the binding map $\mathcal{B}$ is locally constant, and the composite response is differentiable in the usual sense. If the topology itself changes with the host parameters, then the map Φ is only piecewise smooth, and the resulting differential structure requires additional care.

9.5 Examples

The following examples illustrate the preceding developments. Examples 9.5.1 and 9.5.2 verify the procedure against simple elastic problems for which closed form solutions are readily obtained.

9.5.1 Linear Elastic Cantilever with a Solid Section

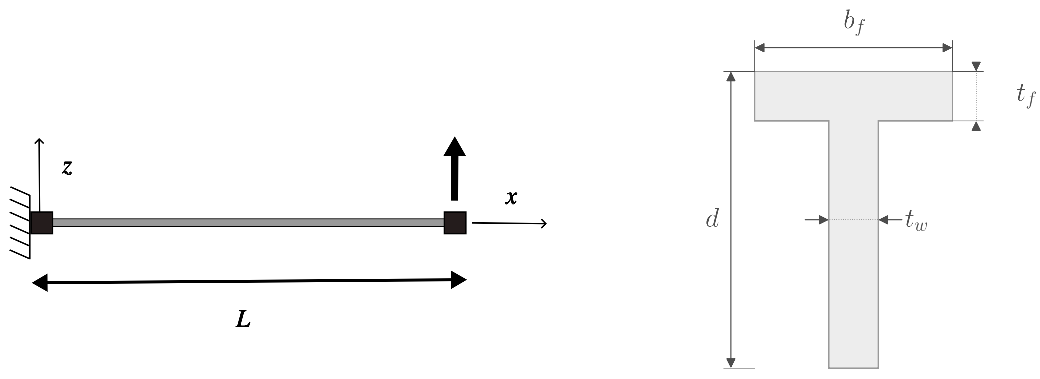

Figure 9.1: Model for Example 9.5.1.

Setup. The cantilever of Figure 9.1 is loaded by a transverse tip force $\bar{F}$. The cross-section is a single-flange "T" shape characterized by the flange width b_f, depth d, flange thickness t_f, and web thickness t_w. The simulation employs a simple elastic cross section model for which the area A, Young's modulus E, and second moment of area I, are directly supplied as input data. Thus the core parameters are

$$\boldsymbol{y} = (E, I, A)$$

In a model updating procedure, the material parameter E and section dimensions b_f, d, t_f, t_w furnish a natural parameterization for which gradients are sought. Thus the host parameters are taken as

$$\hat{\boldsymbol{y}} = (E, b_f, b_w, t_f, t_w)$$

with $b_w := d - t_f$, for which the parameter map is

$$\Phi\colon \hat{\boldsymbol{y}} \mapsto \Big(E, \Phi_I(\hat{\boldsymbol{y}}),\ \Phi_A(\hat{\boldsymbol{y}})\Big) \quad \text{with} \quad \begin{aligned} \Phi_A(\hat{\boldsymbol{y}}) &= b_w t_w + b_f t_f \\ \Phi_I(\hat{\boldsymbol{y}}) &= \tfrac{1}{3} t_w (d_w + t_f)^3 + \tfrac{1}{3}(b_f - t_w) t_f^3 - \Phi_A(\hat{\boldsymbol{y}})\, \bar{y}(\hat{\boldsymbol{y}})^2 \\ \bar{y}((\hat{\boldsymbol{y}}) &= \frac{1}{2\Phi_A(\hat{\boldsymbol{y}})} t_w (d_w + t_w)^2 + (b_f - t_w) t_f^2 \end{aligned}$$

Figure 9.2 illustrates the computational graph induced by Φ_A.

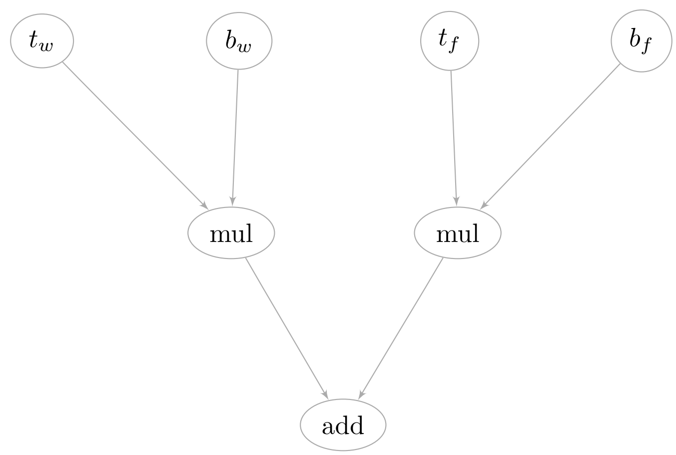

Figure 9.2: Computational graph for the area of a T-section.

9.5.2 Linear Elastic Cantilever with a Fiber Section

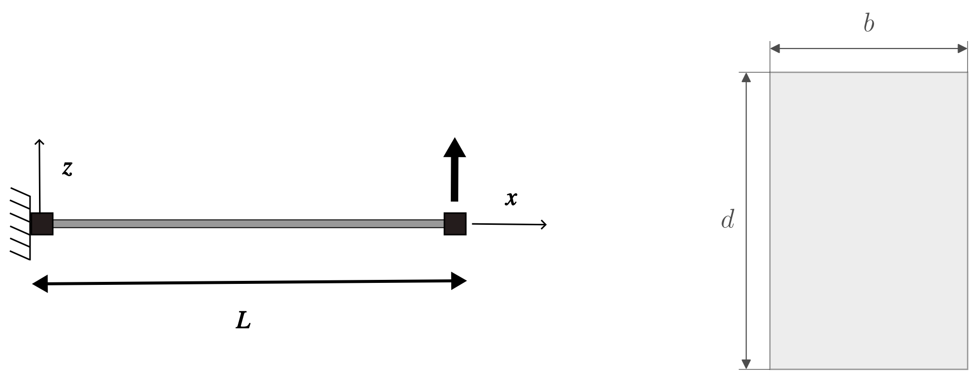

Figure 9.3: Model for Example 9.5.2.

Motivation. This example extends the analysis of Example 9.5.1 to use a section discretized by fibers. In the finite element kernel the section is not provided with any geometry-specific data apart from the general data described in Box 3.5. The proposed compositional framework is employed to compute response gradients with respect to geometric parameters of interest.

Setup. The cantilever of Figure 9.3 is loaded by a transverse tip force $\bar{F}$. The cross-section is a solid rectangle of width b and depth d.

The cross-section is represented by a grid of N integration points, each characterized by a location $\boldsymbol{r}_k \in \Omega$ and weight A_k.

The core parameters are the input data of the section (Box 3.5):

$$\boldsymbol{y} = (L,\ E,\ \boldsymbol{r}_1,\ A_1,\ \dots,\ \boldsymbol{r}_N,\ A_N)\ \in\ \mathbb{R}^{2+3N},$$

where E is Young's modulus. Direct differentiation delivers $\partial u/\partial y_i$, where u is the transverse tip displacement. The analyst, however, is interested in the dependence of u on the section geometry:

$$\hat{\boldsymbol{y}} = (L,\ E,\ b,\ d)\ \in\ \mathbb{R}^4. \tag{9.5.1}$$

Thus the parameter map Φ is

$$\Phi(\hat{\boldsymbol{y}}) = \big(L, E, \mathcal{F}(d,b)\big),$$

where $\mathcal{F}(d,b)$ generates a fiber discretization from geometric dimensions. Given a regular $n_x \times n_y$ grid over the rectangle $[-b/2,\ b/2] \times [-d/2,\ d/2]$, the fiber coordinates and areas are deterministic, differentiable functions of b and d:

$$(b,\ d)\ \overset{\mathcal{F}}{\longmapsto}\ \big\{(y_k,\ z_k,\ A_k)\big\}_{k=1}^{N}.$$

Composing $\mathcal{M}$ with Φ and applying the chain rule yields the sensitivity of the tip displacement to the section depth:

$$\frac{\partial u}{\partial d} = \sum_{k=1}^{N} \left(\frac{\partial u}{\partial y_k}\,\frac{\partial y_k}{\partial d} + \frac{\partial u}{\partial z_k}\,\frac{\partial z_k}{\partial d} + \frac{\partial u}{\partial A_k}\,\frac{\partial A_k}{\partial d} \right),$$

where the terms $\partial u/\partial y_k$, $\partial u/\partial z_k$, $\partial u/\partial A_k$ are provided by the DDM inside the kernel, and the terms $\partial y_k/\partial d$, $\partial z_k/\partial d$, $\partial A_k/\partial d$ are computed by algorithmic differentiation of the parameter map Φ.

The analytic solution is

$$u = \frac{\bar{F} L^3}{3\, E\, I_y} + \frac{\bar{F}\, L}{G\, A},$$

where the second moment of area is $I_y = b\, d^3/12$ and G is the shear modulus. The derivative with respect to the depth d is

$$\frac{\partial u}{\partial d} = -\frac{\bar{F} L^3}{3\, E\, I_y^2}\,\frac{b\, d^2}{4} - \frac{\bar{F}\, L}{G\, A^2}\, b,$$

and serves as a verification target.

Result. The composed numerical gradient $\partial u / \partial d$ computed through the framework agrees with this expression to the precision of the fiber discretization.

9.5.3 Cantilever Undergoing Finite Rotations

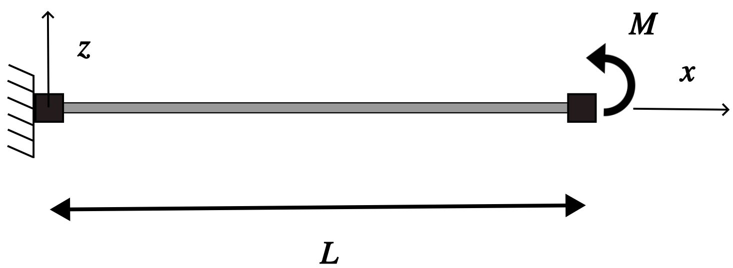

Figure 9.4: Model for Example 9.5.3.

Context. This example is selected to demonstrate the ability of the proposed formulations to accurately reproduce available analytical solutions through finite rotations.

Setup. The cantilever beam in Figure 9.4 is subjected to a point moment $\boldsymbol{M}$ at its free end $x = L$. The centerline of the reference configuration is given by $\boldsymbol{x}_0(x) = x\,\mathbf{E}_1$.

The configuration is expected to remain in the $\mathbf{E}_1 - \mathbf{E}_2$ plane. Consequently, the out-of-plane director $\mathbf{i}_3$ does not change during deformation so that $\mathbf{i}_3 \equiv \hat{\mathbf{i}}_3$. This simplification has two consequences:

- There is no distinction between a spatially applied moment $\boldsymbol{M} = M\hat{\mathbf{i}}_3$ and a materially applied moment $\boldsymbol{M} = M\mathbf{i}_3$.
- The rotation $\boldsymbol{\Lambda}$ becomes vectorial, its variations $\boldsymbol{u}_{\Lambda}^{(i)}$ at different configurations $\chi^{(i)}$ can be added, and the sum of these variations over the course of global equilibrium iterations is equivalent to the logarithmic rotation increment:

$$\sum_{i=0}^{n} \boldsymbol{u}_{\Lambda}^{(i)} \equiv \boldsymbol{\theta} = \operatorname{Log}\left(\boldsymbol{\Lambda}_{(n)} \boldsymbol{\Lambda}_{(0)}^{\top}\right).$$

In this case, the moment loading can be treated identically for all analyses by simply scaling a constant reference load vector for the node at $x = L$:

$$\mathbf{f}_{M,\mathrm{ref}} = \begin{pmatrix} 0 & 0 & M \end{pmatrix}^\top \tag{9.5.2}$$

where the reference magnitude $M = \lambda 2\pi EI/L$ varies with $\lambda = 1/8,\ 1,$ and 2 for different cases causing the cantilever to loop over itself λ times. The following parameters are used:

$$\begin{aligned} L &= 10 & A &= 1 \\ E &= 10^4 & I &= 10^{-2} \\ G &= 10^4 & J &= 10^{-2} \end{aligned}$$

The simulation uses a single load step with uniform meshes of 5 and 10 EF_n elements. The solution requires only two iterations for each formulation matching the ideal performance reported by Simo and Vu-Quoc (1986). The analytic solution of the governing boundary value problem in (3.2.8) is given by:

$$\begin{cases} \boldsymbol{x}(x) = \dfrac{EI}{M} \sin\vartheta(x)\,\mathbf{E}_1 + \dfrac{EI}{M}\left(\cos\vartheta(x) - 1\right)\,\mathbf{E}_2 \\ \vartheta(x) = x\dfrac{M}{EI} \end{cases}$$

where ϑ parameterizes the rotation $\boldsymbol{\Lambda}(x) = \operatorname{Exp}\vartheta(x)\,\mathbf{E}_3$.

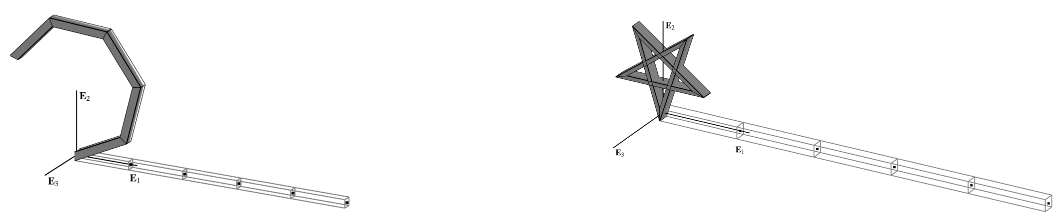

(a) $\lambda = 0.7$ (b) $\lambda = 2$

Figure 9.5: Deformed configuration of cantilever beam under two moment magnitudes.

Algorithm 3 Fiber discretization $\mathcal{F}(b, d)$.

function $\mathcal{F}(b,\, d,\, n_x,\, n_y)$

$\triangleright$ *Stage 1: Quadrilateral mesh over* $[-b/2,\, b/2] \times [-d/2,\, d/2]$

$m \leftarrow 2n_x + 1, \quad n \leftarrow 2n_y + 1$ $\triangleright$ nodes per direction

for $j = 0, \dots, n-1;\ i = 0, \dots, m-1$ **do**

$\mathbf{x}_{jm+i} \leftarrow \left(-\frac{b}{2} + \frac{i\,b}{m-1},\ -\frac{d}{2} + \frac{j\,d}{n-1}\right)$

end for

for $J = 0, \dots, n_y - 1;\ I = 0, \dots, n_x - 1$ **do**

$s \leftarrow 2Jm + 2I$ $\triangleright$ element anchor in node grid

corners: $c_1, c_2, c_3, c_4 \leftarrow s,\ s+2,\ s+2m+2,\ s+2m$

midpoints: $c_5, c_6, c_7, c_8 \leftarrow s+1,\ s+m+2,\ s+2m+1,\ s+m$

insert center node $\mathbf{x}_{\text{new}} \leftarrow \frac{1}{2}(\mathbf{x}_{c_1} + \mathbf{x}_{c_3});\quad c_9 \leftarrow$ new tag

$e_{I,J} \leftarrow (c_1, \dots, c_9)$

end for

Renumber: $\mathbf{x} \in \mathbb{R}^{n_{\text{nd}} \times 2},\ \mathbf{C} \in \mathbb{Z}^{n_x n_y \times 9}$

$\triangleright$ *Stage 2: Gauss integration*

$\xi_i \leftarrow \{-\sqrt{3/5},\ 0,\ \sqrt{3/5}\}, \quad w_i \leftarrow \{\frac{5}{9},\ \frac{8}{9},\ \frac{5}{9}\}$

$\mathcal{Q} \leftarrow \{((\xi_i, \xi_j),\ w_i w_j/4) : i, j = 1, 2, 3\}$

$\mathcal{S} \leftarrow \emptyset$

for all $e \in \mathbf{C}$ **do**

$\mathbf{p}_1,\, \mathbf{p}_2,\, \mathbf{p}_4 \leftarrow \mathbf{x}[e_1],\ \mathbf{x}[e_2],\ \mathbf{x}[e_4]$

$A_e \leftarrow |(\mathbf{p}_2 - \mathbf{p}_1) \times (\mathbf{p}_4 - \mathbf{p}_1)|$

for all $((\xi, \eta),\, w) \in \mathcal{Q}$ **do**

$(y_k,\, z_k) \leftarrow \textsc{Map}(\mathbf{p}_1,\, \mathbf{p}_2,\, \mathbf{p}_4,\, \xi,\, \eta)$

$\mathcal{S} \leftarrow \mathcal{S} \cup \{(y_k,\, z_k,\, A_e\, w)\}$

end for

end for

return $\mathcal{S} = \{(y_k,\, z_k,\, A_k)\}_{k=1}^{N}$

end function

Chapter 10

Conclusions

This dissertation investigates computational methods for the simulation and assessment of structures following natural hazards. The work is presented in two parts. Part I concerns the development of structural models for accurate and efficient structural simulations, and Part II presents a framework that integrates these models into a structural assessment workflow leveraging data-driven methods.

10.1 Closure to Part I

Part I of this dissertation develops a general framework for the constitutive modeling and finite element implementation of beam sections with cross-sectional warping. The framework is formulated for geometrically exact beams with an arbitrary number of global warping fields and remains applicable to linearizations of that model, including classical Timoshenko beam theory. Enhanced section strains are introduced with amplitudes determined locally at each cross section. Warping modes whose restraint effects are insignificant are represented through section-level condensation, while modes for which boundary restraints remain significant are retained as global unknown fields. The formulation preserves the standard one-dimensional equilibrium equations and permits the proposed section models to be used with existing beam finite element implementations without modification of the element state determination procedure. Two specializations are developed. The first pertains to members for which all warping boundary effects are insignificant and yields warping-free section models that recover Saint–Venant continuum solutions in the elastic regime. The second pertains to restrained torsion and yields a seven-field beam theory in which one torsional warping field is retained globally and an additional correction is resolved locally at the section.

A summary of the principal contributions is given below.

Chapter 3. A nonlinear beam theory with an arbitrary number of warping fields is formulated, and an enhanced strain procedure is developed for the construction of section constitutive models. The additional section parameters are resolved locally at each cross section and condensed from the global problem. In the linearized setting, the response of an omitted warping mode is shown to decompose into a boundary-restraint-driven part and a section-local part. This decomposition provides the basis for the subsequent specializations of the framework.

Chapter 4. The framework of Chapter 3 is specialized to members for which all warping boundary effects are insignificant. Enhanced section shapes are derived that recover the Saint–Venant solutions of the elastic prismatic continuum for heterogeneously composed sections with homogeneous Poisson ratio, without auxiliary global warping fields and without suppressing the Poisson-coupled in-plane warping contributions. All Saint–Venant warping modes are therefore resolved at the section level, and the resulting models are compatible with classical six-field beam elements with $n = 0$ auxiliary warping fields.

Chapter 5. The same framework is specialized to restrained torsion. In this setting one torsional warping field is retained globally to represent the restraint-driven part of the response, and an additional correction field is resolved locally through the enhanced section formulation. The resulting theory furnishes a seven-field beam model that restores pointwise equilibrium in the elastic regime, removes the equilibrium defect of the standard single-field torsion-warping theory, and contains the model of Armero (2022) as a special case extended here to geometrically exact and inelastic beam analysis.

Chapter 6. The developments of Part I are organized for finite element implementation through a separation of frame, section, and material models. The proposed sections are incorporated in both geometrically exact and mixed beam elements without alteration of the element state determination procedure. Numerical studies verify exact agreement with Saint–Venant solutions in the elastic regime addressed by Chapter 4 and demonstrate improved response in shear-dominated inelastic problems, restrained torsion, section-local evaluation of the Wagner term, and finite-deformation benchmarks.

The Chapter 4 analysis establishes that Saint–Venant consistency admits an infinite family of exact six-field beam models, within which the classical geometric and energetic treatments of shear arise as particular cases. These models are distinguished by the trace through which the continuum motion is associated with the beam displacement and rotation fields, and the distinction is expressed physically through the boundary interpretation induced on those fields. Within this family, the variational requirement identifies a restricted subclass with symmetric tangent stiffness, and the energetic requirement determines the unique representative that recovers the classical stress resultants.

These developments furnish a framework for beam modeling in which multiaxial section response, Poisson-coupled warping effects, and restrained torsion may be incorporated with only the global warping fields required by the role of boundary restraints in the problem under consideration.

Directions for future research include the development of section-level damage and coupled damage-plasticity models, extension to curved and non-prismatic members, and further study of alternative traces under inelastic response.

10.2 Closure to Part II

Part II of this dissertation develops a framework for structural health monitoring that leverages the developments of Part I, and develops a procedure for computing response gradients of physical simulations that supports integration with machine learning workflows employing automatic differentiation. The framework is implemented as the Bridge Rapid Assessment Center for Extreme Events (BRACE^2), developed in collaboration with the California Department of Transportation (Caltrans) to provide real-time post-earthquake assessments for instrumented highway bridges in California. The developments of Part I furnish the simulation engine for the physics-based predictors on this platform. Within this setting, physics-based simulation and data-driven methods cooperate through a common computational environment, and the resulting reports furnish a quantitative basis for closure and inspection decisions. Following a pilot deployment covering 22 bridges (CHERN & MOSALAM, 2024; PEREZ & MOSALAM, 2024), continued development has been approved to extend coverage across the California highway network.

A brief summary of the principal contributions is given below.

Chapter 8. The architecture of BRACE^2 is developed as a framework for operational structural health monitoring. Structural assessment is organized around the five abstractions of *Asset*, *Event*, *Predictor*, *Metric*, and *Evaluation*, and is realized through a four-layer interface stack separating presentation, orchestration, domain, and infrastructure concerns. This organization permits heterogeneous predictors, including nonlinear simulation and data-driven identification procedures, to operate through a common event-evaluation workflow, reduces their outputs to a shared metric representation with explicit provenance, and assembles those metrics into actionable reports through structure-specific evaluation policies. The pilot deployment demonstrates that historical records, real-time transmissions, and simulated motions may be incorporated within the same regional assessment environment.

Chapter 9. A compositional formulation is developed for computing analytic parameter gradients of finite element simulations. The method separates user-defined host parameterizations from the core parameter vector required by the analysis kernel, obtains reduced-response derivatives at the kernel level through direct differentiation, and recovers sensitivities with respect to the original variables by the chain rule. The formulation accommodates both forward and reverse contractions, includes a parameter-binding procedure that associates host variables with concrete locations in the assembled model, and is verified on representative linear and nonlinear examples. The resulting construction places finite element simulation in a form suitable for model updating, reliability analysis, and integration with automatic-differentiation toolchains.

These developments furnish an operational environment in which recorded motions, simulated events, nonlinear structural analysis, and differentiable calibration may be brought within a single workflow for rapid bridge assessment.

Chapter 11

References

Abraham, R., Marsden, J. E., & Ratiu, T. (1988). *Manifolds, Tensor Analysis, and Applications* (J. E. Marsden, L. Sirovich, & F. John, Eds.; Vol. 75). Springer New York. https://doi.org/10.1007/978-1-4612-1029-0

Abraham, R. H., Marsden, J. E., Ratiu, T. S., & Cushman, R. H. (1994). *Foundations of mechanics: A mathematical exposition of classical mechanics with an introduction to the qualitative theory of dynamical systems and applications to the three-body problem* (2nd ed., rev., enl., and reset). Addison-Wesley.

Alibrandi, U. (2022). Risk-Informed Digital Twin of Buildings and Infrastructures for Sustainable and Resilient Urban Communities. *ASCE-ASME Journal of Risk and Uncertainty in Engineering Systems, Part A: Civil Engineering*, *8*(3), 04022032. https://doi.org/10.1061/AJRUA6.0001238

American Institute of Steel Construction. (2017). *Steel construction manual* (15th).

Antman, S. S. (1995). *Nonlinear problems of elasticity* (2nd ed.). Springer. https://doi.org/10.1007/978-1-4612-0829-3

Armero, F. (2021, July). *On the modeling of restrained torsional warping in prismatic elastic shafts (a full report)* (SEMM-2021-03). University of California Berkeley. Berkeley, CA. https://nisee.berkeley.edu/elibrary/Text/202108192

Armero, F. (2022). A new structural model of warping torsion. I: Formulation for prismatic elastic shafts. *International Journal of Solids and Structures*, *248*, 111626. https://doi.org/10.1016/j.ijsolstr.2022.111626

Armero, F., & Romero, I. (2003). Energy-dissipative momentum-conserving time-stepping algorithms for the dynamics of nonlinear Cosserat rods. *Computational Mechanics*, *31*(1–2), 3–26. https://doi.org/10.1007/s00466-002-0389-9

Arnold, V. I. (1978). *Mathematical Methods of Classical Mechanics* (C. C. Moore, Ed.; Vol. 60). Springer New York. Retrieved February 22, 2023, from http://link.springer.com/10.1007/978-1-4757-1693-1

Artin, M. (1991). *Algebra*. Prentice Hall.

Barfoot, T. D. (2017, July 31). *State Estimation for Robotics* (1st ed.). Cambridge University Press. https://doi.org/10.1017/9781316671528

Battini, J.-M. (2002). *Co-rotational beam elements in instability problems* [Doctoral dissertation, Royal Institute of Technology].

Bauchau, O. A., & Trainelli, L. (2003). The Vectorial Parameterization of Rotation. *Nonlinear Dynamics*, *32*(1), 71–92. https://doi.org/10.1023/A:1024265401576

Brown, E., & Burgoyne, C. (1994). Nonuniform elastic torsion and flexure of members with asymmetric cross-section. *International Journal of Mechanical Sciences*, *36*(1), 39–48. https://doi.org/10.1016/0020-7403(94)90005-1

California Department of Transportation. (2017). *First Responder Bridge Assessment Guide*.

Cardona, A., & Geradin, M. (1988). A beam finite element non-linear theory with finite rotations. *International Journal for Numerical Methods in Engineering*, *26*(11), 2403–2438. https://doi.org/10.1002/nme.1620261105

Chern, C., & Mosalam, K. M. (2024). Cross-Sectional Study of Physics-Informed Bridge Health Identification.

Chern, C., Perez, C. M., & Mosalam, K. M. (2025). Response Prediction from Learned System Matrices for Structural Health Monitoring. https://doi.org/10.1007/978-3-031-96110-6_72

Cowper, G. R. (1966). The Shear Coefficient in Timoshenko's Beam Theory. *Journal of Applied Mechanics*, *33*(2), 335–340. https://doi.org/10.1115/1.3625046

Crisfield, M. A., & Jelenić, G. (1999). Objectivity of strain measures in the geometrically exact three-dimensional beam theory and its finite-element implementation. *Proceedings of the Royal Society of London. Series A: Mathematical, Physical and Engineering Sciences*, *455*(1983), 1125–1147. https://doi.org/10.1098/rspa.1999.0352

de Souza, R. M. (2000). *Force-based finite element for large displacement inelastic analysis of frames* [Doctoral dissertation, University of California, Berkeley]. https://www.proquest.com/docview/304624959/D8D738C3AC49427EPQ/1?accountid=14496

Dinno, K., & Merchant, W. (1965). A procedure for calculating the plastic collapse of i-sections under bending and torsion. *The Structural Engineer*, *43*(7), 219–221.

Du, X., & Hajjar, J. (2021). Three-dimensional nonlinear displacement-based beam element for members with angle and tee sections. *Engineering Structures*, *239*, 112239. https://doi.org/10.1016/j.engstruct.2021.112239

Du, X., & Hajjar, J. F. (2021). Three-dimensional nonlinear mixed 6-DOF beam element for thin-walled members. *Thin-Walled Structures*, *164*, 107817. https://doi.org/10.1016/j.tws.2021.107817

El Fatmi, R. (2007). Non-uniform warping including the effects of torsion and shear forces. Part II: Analytical and numerical applications. *International Journal of Solids and Structures*, *44*(18–19), 5930–5952. https://doi.org/10.1016/j.ijsolstr.2007.02.005

Eugster, S. R., & Harsch, J. (2023). A family of total Lagrangian Petrov–Galerkin Cosserat rod finite element formulations. *GAMM-Mitteilungen*, *46*(2), e202300008. https://doi.org/10.1002/gamm.202300008

Farrar, C. R., & Worden, K. (2007). An introduction to structural health monitoring. *Philosophical Transactions of the Royal Society A: Mathematical, Physical and Engineering Sciences*, *365*(1851), 303–315. Retrieved March 24, 2026, from https://royalsocietypublishing.org/rsta/article-abstract/365/1851/303/51134

Farwell, C. R., & Galambos, T. V. (1969). Nonuniform Torsion of Steel Beams in inelastic Range. *Journal of the Structural Division*, *95*(12), 2813–2830. https://doi.org/10.1061/JSDEAG.0002438

Felippa, C. A. (2005). *The Amusing History of Shear Flexible Beam Elements* (CU-CAS-05-1). Boulder, Colorado.

Fielding, R. T., Nottingham, M., & Reschke, J. (2022, June). *HTTP/1.1* (Request for Comments No. RFC 9112). Internet Engineering Task Force. https://doi.org/10.17487/RFC9112

Filippou, F., & Fenves, G. (2004, May 11). Methods of Analysisfor Earthquake- Resistant Structures. In Y. Bozorgnia & V. Bertero (Eds.), *Earthquake Engineering*. CRC Press. https://doi.org/10.1201/9780203486245.ch6

Filippou, F. C. (2004a). *FedeasLab Documentation* (UCB/SEMM 2004/01). University of California, Berkeley. Berkeley, CA.

Filippou, F. C. (2004b). *FEDEASLab: A Matlab Toolbox for Nonlinear Structural Response Simulations* (UCB/SEMM 2004/01). University of California Berkeley. Berkeley, Ca.

Fowler, M. (2013). *Patterns of Enterprise Application Architecture*. Addison-Wesley Professional.

Frostig, R., Johnson, M. J., & Leary, C. (2018). Compiling machine learning programs via high-level tracing. https://cs.stanford.edu/~rfrostig/pubs/jax-mlsys2018.pdf

Gamma, E. (Ed.). (2011). *Design patterns: Elements of reusable object-oriented software* (39. printing). Addison-Wesley.

Genoese, A., Genoese, A., Bilotta, A., & Garcea, G. (2013). A mixed beam model with non-uniform warpings derived from the Saint Venànt rod. *Computers & Structures*, *121*, 87–98. https://doi.org/10.1016/j.compstruc.2013.03.017

Goel, R. K., & Chopra, A. K. (1997). Evaluation of Bridge Abutment Capacity and Stiffness during Earthquakes. *Earthquake Spectra*, *13*(1), 1–23. https://doi.org/10/fdkchm

Gruttmann, F., Sauer, R., & Wagner, W. (2000). Theory and numerics of three-dimensional beams with elastoplastic material behaviour. *International Journal for Numerical Methods in Engineering*, *48*(12), 1675–1702. https://doi.org/10.1002/1097-0207(20000830)48:12<1675::AID-NME957>3.0.CO;2-6

Halmos, P. R. (1974). *Finite-Dimensional Vector Spaces* (S. Axler, F. W. Gehring, & K. A. Ribet, Eds.). Springer New York. https://doi.org/10.1007/978-1-4612-6387-6

Halmos, P. R. (1998). *Naive set theory*. Springer-Verlag.

Haukaas, T. (2003). *Finite element reliability and sensitivity methods for performance-based engineering*.

Heninger, R. (2023, August). The Use of Drones Following the 2022 Ferndale Earthquake and the PEQIT TEAM REPORT. Caltrans 2023 PEER Annual Meeting Presentation [https://www.youtube.com/watch?v=Nc9qg1ouW6s&list=PLh-lLpxUh0NKiKAiBkNsdEc4Vs9fX20lzf&index=6&t=968s].

Hertzberg, C. (2008). *A Framework for Sparse, Non-Linear Least Squares Problems on Manifolds*.

Hjelmstad, K. D. (1987). Warping Effects in Transverse Bending of Thin-Walled Beams. *Journal of Engineering Mechanics*, *113*(6), 907–924. https://doi.org/10.1061/(ASCE)0733-9399(1987)113:6(907)

Ibrahimbegovic, A. (1997). On the choice of finite rotation parameters. *Computer Methods in Applied Mechanics and Engineering*, *149*(1–4), 49–71. https://doi.org/10.1016/S0045-7825(97)00059-5

Ibrahimbegović, A., Frey, F., & Kožar, I. (1995). Computational aspects of vector-like parametrization of three-dimensional finite rotations. *International Journal for Numerical Methods in Engineering*, *38*(21), 3653–3673. https://doi.org/10.1002/nme.1620382107

Ieşan, D. (1976). Saint-Venant's problem for inhomogeneous bodies. *International Journal of Engineering Science*, *14*(4), 353–360. https://doi.org/10.1016/0020-7225(76)90008-2

Ieşan, D. (1986). On Saint-Venant's problem. *Archive for Rational Mechanics and Analysis*, *91*(4), 363–373. https://doi.org/10.1007/BF00282340

Ieşan, D. (1987). *Saint-Venant's Problem*. Springer Berlin / Heidelberg.

Iserles, A., Munthe-Kaas, H. Z., Nørsett, S. P., & Zanna, A. (2000). Lie-group methods. *Acta Numerica*, *9*, 215–365. https://doi.org/10.1017/S0962492900002154

Jafari, V., Vahdani, S., & Rahimian, M. (2010). Derivation of the consistent flexibility matrix for geometrically nonlinear Timoshenko frame finite element. *Finite Elements in Analysis and Design*, *46*(12), 1077–1085. https://doi.org/10.1016/j.finel.2010.07.015

Jelenić, G., & Crisfield, M. A. (1998). Interpolation of rotational variables in nonlinear dynamics of 3D beams. *International Journal for Numerical Methods in Engineering*, *43*(7), 1193–1222. https://doi.org/10.1002/(SICI)1097-0207(19981215)43:7<1193::AID-NME463>3.0.CO;2-P

Jelenić, G., & Crisfield, M. A. (1999). Geometrically exact 3D beam theory: Implementation of a strain-invariant finite element for statics and dynamics. *Computer Methods in Applied Mechanics and Engineering*, *171*(1–2), 141–171. https://doi.org/10/dj37b3

Kaba, S. A., & Mahin, S. A. (1984). *Refined modelling of reinforced concrete columns for seismic analysis* (EERC-84-03). Earthquake Engineering Research Center. https://nisee.berkeley.edu/elibrary/Text/141375

Kantorovich, L. V., & Krylov, V. I. (1958). *Approximate methods of higher analysis* (C. D. Benster, Trans.; Dover edition). Dover Publications, Inc.

Kapteyn, M. G., Pretorius, J. V. R., & Willcox, K. E. (2021, April 13). *A Probabilistic Graphical Model Foundation for Enabling Predictive Digital Twins at Scale*. arXiv: 2012.05841 `[cs, math]`. http://arxiv.org/abs/2012.05841

Klinkel, S., & Govindjee, S. (2003). Anisotropic bending-torsion coupling for warping in a non-linear beam. *Computational Mechanics*, *31*(1–2), 78–87. https://doi.org/10.1007/s00466-002-0395-y

Klinkel, S., & Govindjee, S. (2002). Using finite strain 3D-material models in beam and shell elements. *Engineering Computations*, *19*(3), 254–271. https://doi.org/10.1108/02644400210423918

Le Corvec, V. (2012). *Nonlinear 3d frame element with multi-axial coupling under consideration of local effects* [Doctoral dissertation, University of California, Berkeley]. https://www.proquest.com/dissertations-theses/nonlinear-3d-frame-element-with-multi-axial/docview/1086348470/se-2

Lee, C.-L., & Filippou, F. C. (2009). Frame elements with mixed formulation for singular section response. *International Journal for Numerical Methods in Engineering*, *78*(11), 1320–1344. https://doi.org/10.1002/nme.2531

Mäkinen, J. (2007). Total Lagrangian Reissner's geometrically exact beam element without singularities. *International Journal for Numerical Methods in Engineering*, *70*(9), 1009–1048. https://doi.org/10.1002/nme.1892

Marsden, J. E., & Hughes, T. J. R. (1994). *Mathematical foundations of elasticity*. Dover.

McAvoy, R. C. (2025). Exotic buckling patterns in fiber-reinforced materials: Numerical simulations of Cosserat elasticity. *International Journal of Solids and Structures*, *312*, 113272. https://doi.org/10.1016/j.ijsolstr.2025.113272

McCallen, D., Pitarka, A., Tang, H., Nakata, R., Mosalam, K. M., Petrone, F., Günay, S., & Perez, C. (2025). An open-access simulated earthquake ground-motion database for an M7 Hayward Fault earthquake in the San Francisco Bay Region. *Earthquake Spectra*, *41*(3), 2560–2597. https://doi.org/10.1177/87552930251340960

McKenna, F. (1997). *Object oriented finite element programming: Frameworks for analysis, algorithms, and parallel computing* [Doctoral dissertation, University of California, Berkeley]. https://opensees.berkeley.edu/OpenSees/doc/fmkdiss.pdf

Meier, C., Popp, A., & Wall, W. A. (2019). Geometrically Exact Finite Element Formulations for Slender Beams: Kirchhoff–Love Theory Versus Simo–Reissner Theory. *Archives of Computational Methods in Engineering*, *26*(1), 163–243. https://doi.org/10.1007/s11831-017-9232-5

Montalto, E. J., & Konstantinidis, D. (2024). Buckling of Short Beams Considering Shear Warping: Application to Fiber-Reinforced Elastomeric Isolators. *Journal of Engineering Mechanics*, *150*(1), 04023105. https://doi.org/10.1061/JENMDT.EMENG-7198

Mosalam, K. M., & Gao, Y. (2024). *Artificial Intelligence in Vision-Based Structural Health Monitoring*. Springer Nature Switzerland. https://doi.org/10.1007/978-3-031-52407-3

Neuenhofer, A., & Filippou, F. C. (1997). Evaluation of Nonlinear Frame Finite-Element Models. *Journal of Structural Engineering*, *123*(7), 958–966. https://doi.org/10.1061/(asce)0733-9445(1997)123:7(958)

Neuenhofer, A., & Filippou, F. C. (1998). Geometrically Nonlinear Flexibility-Based Frame Finite Element. *Journal of Structural Engineering*, *124*(6), 704–711. https://doi.org/10/d8jvb5

Nour-Omid, B., & Rankin, C. (1991). Finite rotation analysis and consistent linearization using projectors. *Computer Methods in Applied Mechanics and Engineering*, *93*(3), 353–384. https://doi.org/10.1016/0045-7825(91)90248-5

Nukala, P. K. V., & White, D. W. (2004). Variationally consistent state determination algorithms for nonlinear mixed beam finite elements. *Computer Methods in Applied Mechanics and Engineering*, *193*(33–35), 3647–3666. https://doi.org/10.1016/j.cma.2004.01.027

Oden, J. T., & Reddy, J. N. (1976). *Variational Methods in Theoretical Mechanics*. Springer Berlin Heidelberg. https://doi.org/10.1007/978-3-642-96312-4

O'Reilly, O. M. (2017). *Modeling Nonlinear Problems in the Mechanics of Strings and Rods*. Springer International Publishing. https://doi.org/10.1007/978-3-319-50598-5

Pandit, G. S. (1970). Discussion of "Nonuniform Torsion of Steel Beams in inelastic Range". *Journal of the Structural Division*, *96*(9), 1972–1973. https://doi.org/10.1061/JSDEAG.0002703

PEER & Caltrans. (2017). *Caltrans/PEER Workshop on CCLS Uncertainty*.

Perez, C. M. (n.d.). *Veux documentation*. Pacific Earthquake Engineering Research Center. Retrieved May 18, 2026, from https://veux.io

Perez, C. M., & Filippou, F. C. (2024). On nonlinear geometric transformations of finite elements. *International Journal for Numerical Methods in Engineering*, e7506. https://doi.org/10.1002/nme.7506

Perez, C. M., McKenna, F., Filippou, F. C., & Mosalam, K. M. (2024, July). *xara*. https://doi.org/10.5281/zenodo.10456866

Perez, C. M., & Mosalam, K. M. (2024). Towards Achieving Longevity In A Digital Twin Framework For Instrumented Bridges.

Perez, C. M., & Vouvakis Manousakis, J. (2024). *veux*. https://doi.org/10.5281/zenodo.13367076

Pfister, F. (1998). Bernoulli Numbers and Rotational Kinematics. *Journal of Applied Mechanics*, *65*(3), 758–763. https://doi.org/10.1115/1.2789120

Pietraszkiewicz, W., & Badur, J. (1983). Finite rotations in the description of continuum deformation. *International Journal of Engineering Science*, *21*(9), 1097–1115. https://doi.org/10.1016/0020-7225(83)90050-2

Pilkey, W. D. (2003, May 1). *Analysis and Design of Elastic Beams: Computational Methods*. Retrieved February 9, 2022, from https://asmedigitalcollection.asme.org/appliedmechanicsreviews/article/56/3/B38/446361/Analysis-and-Design-of-Elastic-Beams-Computational

REISSNER, E. (1952). On Non-Uniform Torsion of Cylindrical Rods. *Journal of Mathematics and Physics*, *31*(1–4), 214–221. https://doi.org/10.1002/sapm1952311214

RENTON, J. D. (1991). Generalized beam theory applied to shear stiffness. *International Journal of Solids and Structures*, *27*(15), 1955–1967. https://doi.org/10.1016/0020-7683(91)90188-L

RICHARDSON, L., & AMUNDSEN, M. (2015). *RESTful Web APIs* (First edition, second release). O'Reilly.

RIFAI, M. S. (1993). *Static and dynamic finite element analysis of finite deformation geometrically exact shell models* [Doctoral dissertation, Stanford University]. https://www.proquest.com/docview/304075315/abstract/F3E799DEAC2543E9PQ/7

RITTO-CORRÊA, M., & CAMOTIM, D. (2002). On the differentiation of the Rodrigues formula and its significance for the vector-like parameterization of Reissner-Simo beam theory. *International Journal for Numerical Methods in Engineering*, *55*(9), 1005–1032. https://doi.org/10.1002/nme.532

ROBLEE, C., YANG, C. W., ZHENG, Q., XIE, T., PADGETT, J., DESROCHES, R., & YEN, S. (2020, November 27). *PRELIMINARY g2F-Compatible 4-State CCLS Models for Use in Fragility Illustration in EQE-20-122*. DesignSafe-CI. https://doi.org/10.17603/ds2-pz0s-xv32

ROMANO, G., BARRETTA, A., & BARRETTA, R. (2012). On torsion and shear of Saint-Venant beams. *European Journal of Mechanics - A/Solids*, *35*, 47–60. https://doi.org/10.1016/j.euromechsol.2012.01.007

ROMANO, G., DIACO, M., & SELLITTO, C. (2005). Tangent stiffness of elastic continua on manifolds. In S. RIONERO & G. ROMANO (Eds.), *Trends and Applications of Mathematics to Mechanics* (pp. 155–184). Springer Milan. https://doi.org/10.1007/88-470-0354-7_14

ROMERO, I. (2004). The interpolation of rotations and its application to finite element models of geometrically exact rods. *Computational Mechanics*, *34*(2), 121–133. https://doi.org/10.1007/s00466-004-0559-z

ROSSMANN, W. (2006). *Lie groups: An introduction through linear groups* (1. publ. in paperback). Oxford University Press.

SARITAS, A., & FILIPPOU, F. C. (2009). Frame Element for Metallic Shear-Yielding Members under Cyclic Loading. *Journal of Structural Engineering*, *135*(9), 1115–1123. https://doi.org/10.1061/(asce)st.1943-541x.0000041

SATYANARAYAN, A., MORITZ, D., WONGSUPHASAWAT, K., & HEER, J. (2017). Vega-lite: A grammar of interactive graphics. *IEEE Transactions on Visualization & Computer Graphics (Proc. InfoVis)*. https://doi.org/10.1109/tvcg.2016.2599030

SCOTT, M. H. (2004). *Software frameworks for the computational simulation of structural systems*. https://nisee.berkeley.edu/elibrary/Text/200901293

SCOTT, M. H., FENVES, G. L., MCKENNA, F., & FILIPPOU, F. C. (2008). Software Patterns for Nonlinear Beam-Column Models. *Journal of Structural Engineering*, *134*(4), 562–571. https://doi.org/10.1061/(asce)0733-9445(2008)134:4(562)

SHILOV, G. E. (1996). *Elementary functional analysis* (R. A. SILVERMAN, Trans.). Dover Publications.

SIMO, J. C. (1985). A finite strain beam formulation. The three-dimensional dynamic problem. Part I. *Computer Methods in Applied Mechanics and Engineering*, *49*(1), 55–70. https://doi.org/10.1016/0045-7825(85)90050-7

SIMO, J. C. (1992). The (symmetric) Hessian for geometrically nonlinear models in solid mechanics: Intrinsic definition and geometric interpretation. *Computer Methods in Applied Mechanics and Engineering*, *96*(2), 189–200. https://doi.org/10.1016/0045-7825(92)90131-3

SIMO, J. C., & ARMERO, F. (1992). Geometrically non-linear enhanced strain mixed methods and the method of incompatible modes. *International Journal for Numerical Methods in Engineering*, *33*(7), 1413–1449. https://doi.org/10.1002/nme.1620330705

SIMO, J. C., FOX, D. D., & RIFAI, M. S. (1990). On a stress resultant geometrically exact shell model. Part III: Computational aspects of the nonlinear theory. *Computer Methods in Applied Mechanics and Engineering*, *79*(1), 21–70. https://doi.org/10.1016/0045-7825(90)90094-3

SIMO, J. C., & HUGHES, T. J. R. (1986). On the Variational Foundations of Assumed Strain Methods. *Journal of Applied Mechanics*, *53*(1), 51–54. https://doi.org/10.1115/1.3171737

SIMO, J. C., & RIFAI, M. S. (1990). A class of mixed assumed strain methods and the method of incompatible modes. *International Journal for Numerical Methods in Engineering*, *29*(8), 1595–1638. https://doi.org/10.1002/nme.1620290802

SIMO, J. C., & VU-QUOC, L. (1986). A three-dimensional finite-strain rod model. part II: Computational aspects. *Computer Methods in Applied Mechanics and Engineering*, *58*(1), 79–116. https://doi.org/10/b8wd4z

SIMO, J. C., & VU-QUOC, L. (1988). On the dynamics in space of rods undergoing large motions — A geometrically exact approach. *Computer Methods in Applied Mechanics and Engineering*, *66*(2), 125–161. https://doi.org/10.1016/0045-7825(88)90073-4

SIMO, J. C., & VU-QUOC, L. (1991). A Geometrically-exact rod model incorporating shear and torsion-warping deformation. *International Journal of Solids and Structures*, *27*(3), 371–393. https://doi.org/10.1016/0020-7683(91)90089-x

SIMO, J. C., & WONG, K. K. (1991). Unconditionally stable algorithms for rigid body dynamics that exactly preserve energy and momentum. *International Journal for Numerical Methods in Engineering*, *31*(1), 19–52. https://doi.org/10.1002/nme.1620310103

SIMO, J. C. (1982). *Some Bifurcation Topics in Non-Linear Elastostatics* [Doctoral dissertation, University of California, Berkeley]. https://www.proquest.com/dissertations-theses/some-bifurcation-topics-non-linear-elastostatics/docview/303215562/se-2

SIMO, J. C. (1984). *On a One-Dimensional Finite Strain Beam Theory: The Three Dimensional Dynamic Problem* (SEMM-84-02). University of California Berkeley. Berkeley, CA.

Solà, J., Deray, J., & Atchuthan, D. (2018). *A micro Lie theory for state estimation in robotics* (tech. rep. No. IRI-TR-18-01). Institut de Robòtica i Informàtica Industrial. Barcelona.

Spacone, E., Ciampi, V., & Filippou, F. C. (1996). Mixed formulation of nonlinear beam finite element. *Computers & Structures*, *58*(1), 71–83. https://doi.org/10.1016/0045-7949(95)00103-N

Spacone, E., Ciampi, V., & Filippou, F. C. (1992, August). *A beam element for seismic damage analysis* (EERC-92-07).

Spivak, M. (1965). *Calculus on manifolds: A modern approach to classical theorems of advanced calculus* (27. print). Perseus Books.

Spurrier, R. A. (1978). Comment on " Singularity-Free Extraction of a Quaternion from a Direction-Cosine Matrix". *Journal of Spacecraft and Rockets*, *15*(4), 255–255. https://doi.org/10.2514/3.57311

Synge, J. L. (1945). The problem of Saint Venant for a cylinder with free sides. *Quarterly of Applied Mathematics*, *2*(4), 307–317. https://doi.org/10.1090/qam/12037

Taucer, F., Spacone, E., & Filippou, F. C. (1991). *Fiber Beam-Column Element for Seismic Response Analysis of Reinforced Concrete Structures.* (tech. rep. No. UCB/EERC-91/17). University of California, Berkeley. https://nehrpsearch.nist.gov/article/PB94-117629/XAB

Taylor, R. L., Filippou, F. C., Saritas, A., & Auricchio, F. (2003). A mixed finite element method for beam and frame problems. *Computational Mechanics*. https://doi.org/10.1007/s00466-003-0410-y

Torzoni, M., Tezzele, M., Mariani, S., Manzoni, A., & Willcox, K. E. (2024). A digital twin framework for civil engineering structures. *Computer Methods in Applied Mechanics and Engineering*, *418*, 116584. https://doi.org/10.1016/j.cma.2023.116584

Trabucho, L., & Viano, J. M. (1996). Mathematical Modelling of Rods.

Trahair, N. S. (1993). *Flexural-torsional buckling of structures* (1. ed). E & FN Spon.

Trefftz, E. (1935). Über den Schubmittelpunkt in einem durch eine Einzellast gebogenen Balken. *ZAMM - Journal of Applied Mathematics and Mechanics / Zeitschrift für Angewandte Mathematik und Mechanik*, *15*(4), 220–225. https://doi.org/10.1002/zamm.19350150405

Wagner, H. (1936, October 1). *Torsion and buckling of open sections* (tech. rep.). Retrieved April 17, 2026, from https://ntrs.nasa.gov/citations/19930094608

Xara documentation. (n.d.). Pacific Earthquake Engineering Research Center. Retrieved May 18, 2026, from https://xara.so

Zhou, J., & Kunnath, S. (2022, February). *Capacity Limit States for Nonductile Bridge Columns* (PEER Reports). Pacific Earthquake Engineering Research Center, University of California, Berkeley, CA. https://doi.org/10.55461/FUTW2909

Zienkiewicz, O. C., Taylor, R. L., & Govindjee, S. (2025). *The finite element method: Its basis and fundamentals* (Eighth edition). Butterworth-Heinemann.

Part III

Appendices to Part I

Appendix A

Linear Solution of the Warping Beam

Restrict (3.3.4) to the load-free linear system, so that

$$\boldsymbol{f}_n = 0, \qquad \boldsymbol{f}_m = 0, \qquad \boldsymbol{f}_{\mathrm{w}} = 0.$$

Introduce

$$\boldsymbol{s}_o := \begin{pmatrix} \boldsymbol{n} \\ \boldsymbol{m} \end{pmatrix} \in \mathbb{R}^6, \qquad \mathbb{J}_o := \begin{bmatrix} \mathbf{0} & \mathbf{0} \\ -\mathbf{i}^\times & \mathbf{0} \end{bmatrix} \in \mathbb{R}^{6\times 6}.$$

Then

$$\boldsymbol{s} = \begin{pmatrix} \boldsymbol{s}_o \\ \boldsymbol{w} \\ \boldsymbol{v} \end{pmatrix} \in \mathbb{R}^{6+2n}, \qquad \boldsymbol{e} = \begin{pmatrix} \boldsymbol{\gamma} \\ \boldsymbol{\kappa} \\ \boldsymbol{\alpha}' \\ \boldsymbol{\alpha} \end{pmatrix} \in \mathbb{R}^{6+2n}, \qquad \boldsymbol{s} = \mathbf{K}_n \boldsymbol{e}.$$

The section flexibility $\boldsymbol{F}_n := \mathbf{K}_n^{-1}$, is partitioned with row and column blocks of sizes $6 + n + n$:

$$\boldsymbol{F}_n = \begin{bmatrix} \boldsymbol{F}_{oo} & \boldsymbol{F}_{\mathrm{ow}} & \boldsymbol{F}_{ov} \\ & \boldsymbol{F}_{ww} & \boldsymbol{F}_{wv} \\ \text{sym.} & & \boldsymbol{F}_{vv} \end{bmatrix}.$$

The equilibrium equations (3.3.4) are

$$\boldsymbol{s}_o' = \mathbb{J}_o \boldsymbol{s}_o, \qquad \boldsymbol{w}' = \boldsymbol{v}.$$

From $\boldsymbol{e} = \boldsymbol{F}_n \boldsymbol{s}$,

$$\boldsymbol{\alpha}' = \boldsymbol{F}_{\mathrm{wo}} \boldsymbol{s}_o + \boldsymbol{F}_{ww} \boldsymbol{w} + \boldsymbol{F}_{wv} \boldsymbol{v}, \qquad \boldsymbol{\alpha} = \boldsymbol{F}_{\mathrm{vo}} \boldsymbol{s}_o + \boldsymbol{F}_{vw} \boldsymbol{w} + \boldsymbol{F}_{vv} \boldsymbol{v}.$$

Differentiating the second relation and using $\boldsymbol{\alpha}' = (\boldsymbol{\alpha})'$ gives

$$\boldsymbol{F}_{vv} \boldsymbol{v}' = (\boldsymbol{F}_{\mathrm{wo}} - \boldsymbol{F}_{\mathrm{vo}} \mathbb{J}_o) \boldsymbol{s}_o + \boldsymbol{F}_{ww} \boldsymbol{w} + (\boldsymbol{F}_{wv} - \boldsymbol{F}_{vw}) \boldsymbol{v}.$$

which allows the equilibrium equations to be represented as a single first order system:

$$\boldsymbol{s}' = \mathbb{J}_n \boldsymbol{s}, \tag{A.0.1}$$

with

$$\mathbb{J}_n = \begin{bmatrix} \mathbb{J}_o & \mathbf{0}_{6\times n} & \mathbf{0}_{6\times n} \\ \mathbf{0}_{n\times 6} & \mathbf{0}_{n\times n} & \mathbf{1}_{n\times n} \\ \boldsymbol{F}_{vv}^{-1}(\boldsymbol{F}_{\mathrm{wo}} - \boldsymbol{F}_{\mathrm{vo}}\mathbb{J}_o) & \boldsymbol{F}_{vv}^{-1}\boldsymbol{F}_{ww} & \boldsymbol{F}_{vv}^{-1}(\boldsymbol{F}_{wv} - \boldsymbol{F}_{vw}) \end{bmatrix} \in \mathbb{R}^{(6+2n)\times(6+2n)}.$$

Finally, with $\boldsymbol{e} = \boldsymbol{F}_n \boldsymbol{s}$,

$$\boldsymbol{e}' = \boldsymbol{F}_n \boldsymbol{s}' = \boldsymbol{F}_n \mathbb{J}_n \boldsymbol{s} = \boldsymbol{F}_n \mathbb{J}_n \mathbf{K}_n \boldsymbol{e}.$$

Hence

$$\boldsymbol{e}' = \boldsymbol{G}\boldsymbol{e}, \qquad \text{with} \qquad \boldsymbol{G} \coloneqq \mathbf{K}_n^{-1} \mathbb{J}_n \mathbf{K}_n \tag{A.0.2}$$

Appendix B

Section-Local Variational Structure

When the underlying three-dimensional constitutive law derives from a strain-energy density, the enhanced section model of Box 3.4 derives from a variational statement of elasticity.

Assume that the constitutive response is hyperelastic, with strain-energy density $\Psi(\hat{\boldsymbol{E}})$. The Saint-Venant constraint (3.2.12) induces a reduced material potential

$$\psi_{\mathrm{sv}}(\boldsymbol{\varepsilon}) := \operatorname*{stat}_{\tilde{\boldsymbol{E}}} \Psi(\boldsymbol{\varepsilon} \overset{\mathrm{s}}{\otimes} \mathbf{i} + \tilde{\boldsymbol{E}}), \tag{B.0.1}$$

where the stationary point is characterized by (3.2.16). The constrained stress vector and tangent are generated by ψ_{sv} through

$$\boldsymbol{\sigma}(\boldsymbol{\varepsilon}) = \partial_{\boldsymbol{\varepsilon}} \psi_{\mathrm{sv}}(\boldsymbol{\varepsilon}), \qquad \mathbb{C}(\boldsymbol{\varepsilon}) = \partial^2_{\boldsymbol{\varepsilon}\boldsymbol{\varepsilon}} \psi_{\mathrm{sv}}(\boldsymbol{\varepsilon}). \tag{B.0.2}$$

The corresponding section internal energy is

$$W(\boldsymbol{e}, \boldsymbol{\eta}) := \int \psi_{\mathrm{sv}}\left(\hat{\boldsymbol{\varepsilon}}(\boldsymbol{e}) + \bar{\boldsymbol{A}}\,\boldsymbol{\eta}\right)\,\mathrm{d}A. \tag{B.0.3}$$

Using $\delta\hat{\boldsymbol{\varepsilon}} = \boldsymbol{A}_\varepsilon\,\delta\boldsymbol{e}$, the first variation of W is

$$\delta W = \int \boldsymbol{\sigma}(\bar{\boldsymbol{\varepsilon}}) \cdot \left(\boldsymbol{A}_\varepsilon\,\delta\boldsymbol{e} + \bar{\boldsymbol{A}}\,\delta\boldsymbol{\eta}\right)\,\mathrm{d}A. \tag{B.0.4}$$

Collecting the coefficients of $\delta\boldsymbol{e}$ and $\delta\boldsymbol{\eta}$ gives

$$\delta W = \boldsymbol{s} \cdot \delta\boldsymbol{e} + \tilde{\boldsymbol{g}}(\boldsymbol{\eta}) \cdot \delta\boldsymbol{\eta}, \tag{B.0.5}$$

with

$$\boldsymbol{s} = \int \boldsymbol{A}_\varepsilon^\top \boldsymbol{\sigma}(\bar{\boldsymbol{\varepsilon}})\,\mathrm{d}A, \qquad \tilde{\boldsymbol{g}}(\boldsymbol{\eta}) = \int \bar{\boldsymbol{A}}^\top \boldsymbol{\sigma}(\bar{\boldsymbol{\varepsilon}})\,\mathrm{d}A. \tag{B.0.6}$$

Thus (3.4.4) is the stationarity condition of the section energy with respect to the local parameters. Because $\boldsymbol{\eta}$ enters without derivatives, this stationarity problem is posed pointwise in x. The enhanced parameters are therefore internal variables that are condensed at the section level and do not introduce additional global degrees of freedom.

For conservative loading, let $\boldsymbol{\chi} = (\boldsymbol{x}, \boldsymbol{\Lambda}, \boldsymbol{\alpha})$ collect the beam kinematic fields, and write $\boldsymbol{e} = \boldsymbol{e}(\boldsymbol{\chi})$. The total potential of the beam is then

$$\Pi[\boldsymbol{\chi}, \boldsymbol{\eta}] = \int_0^L W(\boldsymbol{e}(\boldsymbol{\chi}), \boldsymbol{\eta})\,\mathrm{d}x - \Pi_{\mathrm{ext}}[\boldsymbol{\chi}]. \tag{B.0.7}$$

Stationarity with respect to $\boldsymbol{\eta}$ recovers (3.4.4) section-wise. Stationarity with respect to $\boldsymbol{\chi}$ yields the beam equilibrium equations of Section 3.2.3. No additional one-dimensional balance law appears, because the enhancement modifies only the section constitutive response.

Let $\boldsymbol{\eta}^\star(\boldsymbol{e})$ denote the local solution of

$$\tilde{\boldsymbol{g}}(\boldsymbol{\eta}^\star(\boldsymbol{e})) = \boldsymbol{0}.$$

The condensed section potential is

$$W_{\mathrm{red}}(\boldsymbol{e}) := W(\boldsymbol{e}, \boldsymbol{\eta}^\star(\boldsymbol{e})). \tag{B.0.8}$$

Applying the chain rule and using stationarity in $\boldsymbol{\eta}$ gives

$$\delta W_{\mathrm{red}} = \partial_{\boldsymbol{e}} W\,\delta\boldsymbol{e} + \partial_{\boldsymbol{\eta}} W\,\delta\boldsymbol{\eta}^\star = \boldsymbol{s}\cdot\delta\boldsymbol{e}. \tag{B.0.9}$$

Hence the section resultants remain work-conjugate to the beam strains and are generated by the reduced potential,

$$\boldsymbol{s} = \partial_{\boldsymbol{e}} W_{\mathrm{red}}(\boldsymbol{e}).$$

The stability requirement (3.4.2) excludes null directions of the joint parametrization $(\boldsymbol{e}, \boldsymbol{\eta}) \mapsto \hat{\boldsymbol{\varepsilon}}(\boldsymbol{e}) + \bar{\boldsymbol{A}}\boldsymbol{\eta}$. If the reduced material tangent $\mathbb{C}$ is positive definite, then a zero second variation requires

$$\boldsymbol{A}_\varepsilon\,\delta\boldsymbol{e} + \bar{\boldsymbol{A}}\,\delta\boldsymbol{\eta} = \boldsymbol{0} \quad \text{in } L_2(\Omega; \mathbb{R}^3).$$

Condition (3.4.2) excludes nontrivial solutions of this relation, so the mixed Hessian is nonsingular and the condensation is well posed. Consequently the condensed tangent $\mathbf{K}_s$ inherits symmetry from the Hessian of W.

This variational interpretation illuminates the role of the consistency condition (3.4.4). If this consistency condition is relaxed and the parameters $\boldsymbol{\eta}$ are prescribed directly as functions of $\boldsymbol{e}$, the map $\boldsymbol{e} \mapsto \boldsymbol{s}$ need not derive from any reduced potential, and the consistent tangent need not be symmetric.

Appendix C

Continuum Solutions for Uniform Warping

The objective of this section is to briefly recall the family of general solutions to Saint-Venant's continuum problems (Synge, 1945; Ieşan, 1987). This is used in Chapter 4 to identify a dimensionally reduced beam model that exactly represents these solutions.

The exposition follows the approach of Ieşan (1986) and Ieşan (1976), whereby the Saint Venant class is decomposed into two problems: that of torsion-bending-elongation (Section C.3), and that of flexure (Section C.4). The developments are specialized in Section C.5 to heterogeneous bodies with homogeneous Poisson ratio.

C.1 Overview

Infinitesimal motions of the body described in Section 3.2.1 are investigated, and attention is restricted to those composed heterogeneously of an isotropic material.

The resultants are the integrals of the traction $-\boldsymbol{S}\,\mathbf{i}$ on the root section Ω_0:

$$\mathcal{F}(\hat{\boldsymbol{u}}) = \int_{\Omega_0} \boldsymbol{S}(\hat{\boldsymbol{u}})\,(-\mathbf{i})\;\mathrm{d}A, \qquad \mathcal{M}(\hat{\boldsymbol{u}}) = \int_{\Omega_0} \boldsymbol{r} \times \left(\boldsymbol{S}(\hat{\boldsymbol{u}})\,(-\mathbf{i})\right)\;\mathrm{d}A. \tag{C.1.1}$$

where $\boldsymbol{S}$ is the stress tensor. Saint Venant's solutions arise from *relaxed* elastostatic problems, where end tractions are not prescribed point-wise, but rather specified through these resultants. Neglecting to specify complete point-wise boundary data in this manner produces an ill-posed boundary-value problem which consequently lacks a unique solution $\hat{\boldsymbol{u}}$:

$$\begin{cases} \operatorname{div} \boldsymbol{S} = \boldsymbol{0} & \text{in } B \\ \boldsymbol{S}\boldsymbol{n} = \boldsymbol{0} & \text{on } \partial_{\mathbf{i}} B \\ \mathcal{M}(\hat{\boldsymbol{u}}) = \bar{\boldsymbol{M}} & \text{on } \Omega_0 \\ \mathcal{F}(\hat{\boldsymbol{u}}) = \bar{\boldsymbol{N}} \end{cases} \qquad \text{with} \qquad \begin{aligned} \boldsymbol{S} &:= \lambda\,(\operatorname{tr}\boldsymbol{E})\,\mathbf{1} + 2G\,\boldsymbol{E}, \\ \boldsymbol{E} &:= \tfrac{1}{2}(\nabla\hat{\boldsymbol{u}} + \nabla\hat{\boldsymbol{u}}^{\top}), \end{aligned} \tag{C.1.2}$$

In the treatment by Ieşan (1986) the family of Saint Venant problems is decomposed into two classes, the extension-bending-torsion problem $\mathrm{P}_{\mathrm{I}}(\bar{N}, \bar{\boldsymbol{M}})$ for prescribed axial force $\bar{N}$ and moment $\bar{\boldsymbol{M}}$ resultants, and the flexure problem $\mathrm{P}_{\mathrm{II}}(\bar{\boldsymbol{F}})$ for a prescribed transverse resultant $\bar{\boldsymbol{F}} = \bar{F}_\alpha\,\mathbf{i}_\alpha$:

$$\mathrm{P}_{\mathrm{I}}(\bar{N}, \bar{\boldsymbol{M}}) \begin{cases} \operatorname{div} \boldsymbol{S} = \boldsymbol{0} & \text{in } B \\ \boldsymbol{S}\boldsymbol{n} = \boldsymbol{0} & \text{on } \partial_{\mathbf{i}} B \\ \mathcal{M}(\hat{\boldsymbol{u}}) = \bar{\boldsymbol{M}} & \text{on } \Omega_0 \\ \mathcal{F}(\hat{\boldsymbol{u}}) = \bar{N}\,\mathbf{i} \end{cases} \qquad \text{and} \qquad \mathrm{P}_{\mathrm{II}}(\bar{\boldsymbol{F}}) \begin{cases} \operatorname{div} \boldsymbol{S} = \boldsymbol{0} & \text{in } B \\ \boldsymbol{S}\boldsymbol{n} = \boldsymbol{0} & \text{on } \partial_{\mathbf{i}} B \\ \mathcal{M}(\hat{\boldsymbol{u}}) = \boldsymbol{0} & \text{on } \Omega_0 \\ \mathcal{F}(\hat{\boldsymbol{u}}) = \bar{F}_\alpha \mathbf{i}_\alpha \end{cases} \tag{C.1.3}$$

Ieşan (1986) observes that mapping $\hat{\boldsymbol{u}} \mapsto \hat{\boldsymbol{u}}'$ preserves lateral traction–free fields and transforms resultants as (Ieşan, 1986, Thm 2.1)[1]

$$\mathcal{F}(\hat{\boldsymbol{u}}') = \boldsymbol{0}, \qquad \mathcal{M}(\hat{\boldsymbol{u}}') = \mathcal{F}(\hat{\boldsymbol{u}}) \times \mathbf{i}, \qquad \mathbf{i} \cdot \mathcal{M}(\hat{\boldsymbol{u}}') = 0$$

Consequently, if a displacement $\hat{\boldsymbol{u}}_{\mathrm{II}}$ is a solution of the flexure problem $\mathrm{P}_{\mathrm{II}}(\bar{\boldsymbol{F}})$, then its axial derivative $\hat{\boldsymbol{u}}_{\mathrm{II}}'$ is a solution of the extension-bending-torsion problem $\mathrm{P}_{\mathrm{I}}(0, \mathbf{i} \times \bar{\boldsymbol{F}})$ (Ieşan, 1987). This connection motivates the program of Ieşan, whereby a particular solution to P_{I} is identified by prescribing the shape of $\hat{\boldsymbol{u}}'$, and a solution to P_{II}, identified by prescribing the shape of $\hat{\boldsymbol{u}}''$. These prescriptions select particular solutions within the relaxed class that are unique up to a rigid body field, while leaving end tractions unspecified pointwise.

C.2 Plane Warping

Deformations that do not warp the sections in the axial direction $\mathbf{i}$ must satisfy the three plane-strain boundary value problems:

$$\Pi(\mathbf{i}_k) \begin{cases} \operatorname{div} \tilde{\boldsymbol{S}}^{(k)} + \nabla\big(\lambda\,(\mathbf{i}_k \cdot (\boldsymbol{r} + \mathbf{i}))\big) = \boldsymbol{0}, & \text{in } \Omega \quad \text{(C.2.1a)} \\ \tilde{\boldsymbol{S}}^{(k)}\boldsymbol{\nu} = -\mathbf{i}_k \cdot (\boldsymbol{r} + \mathbf{i})\,\lambda\boldsymbol{\nu}, & \text{on } \Gamma \quad \text{(C.2.1b)} \end{cases}$$

[1] The units for these identities appear paradoxical, and may be understood as the follows. Because $\boldsymbol{S}(\hat{\boldsymbol{u}}') = (\boldsymbol{S}(\hat{\boldsymbol{u}}))'$, the resultants computed from $\hat{\boldsymbol{u}}'$ carry an extra factor 1/length relative to those of $\hat{\boldsymbol{u}}$. Hence

$$[\mathcal{F}(\hat{\boldsymbol{u}}')] = \text{force/length}, \qquad [\mathcal{M}(\hat{\boldsymbol{u}}')] = \text{force},$$

so $\mathcal{M}(\hat{\boldsymbol{u}}')$ indeed has the same units as $\mathbf{i} \times \mathcal{F}(\hat{\boldsymbol{u}})$ (force). Interpreting $\mathcal{M}(\hat{\boldsymbol{u}}')$ as the x-derivative of the bending/torsion resultant, the identity is the continuum analogue of the 1D balance $\mathcal{M}' = \mathbf{i} \times \mathcal{F}$.

Define

$$\boldsymbol{\Pi} := \hat{\boldsymbol{u}}_\Omega^{(\beta)} \otimes \mathbf{i}_\beta, \qquad \bar{\pi} := \operatorname{tr} \tilde{\boldsymbol{E}}^{(3)}, \qquad \boldsymbol{\pi} := \mathbf{i}_\beta \operatorname{tr} \tilde{\boldsymbol{E}}^{(\beta)}, \qquad \mathbf{i}_\beta \in \Omega, \tag{C.2.2}$$

C.3 Problem I: Extension–Bending–Torsion

Synopsis

Problem $\mathrm{P_I}$ covers extension, bending, and torsion under resultants with $F_\alpha = 0$. The identifying kinematic postulate is that the first axial derivative is a rigid body motion,

$$\hat{\boldsymbol{u}}_\mathrm{I}' = a_\varepsilon\, \mathbf{i} + (a_\vartheta\, \mathbf{i} - \mathbf{i} \times \boldsymbol{a}_\Omega) \times \hat{\boldsymbol{x}}, \qquad \boldsymbol{a}_\Omega \in \mathbb{R}^2,\ a_\varepsilon, a_\vartheta \in \mathbb{R},$$

which fixes the x-dependence of $\hat{\boldsymbol{u}}$ and reduces the equilibrium equations to planar problems on Ω.

Statement

Given a resultant axial force $\bar{N}$ and couple $\bar{\boldsymbol{M}} := \bar{T}\mathbf{i} + \bar{M}_\alpha\, \mathbf{i}_\alpha$ on Ω_{x_0}, determine $(\hat{\boldsymbol{u}}, \boldsymbol{S})$ such that:

$$\begin{cases} \hat{\boldsymbol{u}}_\mathrm{I} \in \mathrm{P_I}(\bar{N},\, \bar{\boldsymbol{M}}) \\ \hat{\boldsymbol{u}}_\mathrm{I}' = a_\varepsilon\, \mathbf{i} + (a_\vartheta\, \mathbf{i} - \mathbf{i} \times \boldsymbol{a}_\Omega) \times \boldsymbol{x}. \end{cases} \tag{C.3.1}$$

Solution

Integrating (C.3.1) furnishes the particular solution:

$$\hat{\boldsymbol{u}}_\mathrm{I}\{\boldsymbol{a}\} = \Big(- \tfrac{1}{2} x^2\, \mathbf{1} + x\, \mathbf{i} \otimes \boldsymbol{r} + \boldsymbol{\Pi} \Big) \boldsymbol{a}_\Omega + (x\, \mathbf{i} - \nu\, \boldsymbol{r})\, a_\varepsilon + (x\, \mathbf{i} \times \boldsymbol{r} + \bar{\varphi}_\mathrm{I}\, \mathbf{i}) a_\vartheta, \tag{C.3.2}$$

where $\boldsymbol{\Pi}$ is the plane warping solution (C.2.2), and the torsion warping function $\bar{\varphi}_\mathrm{I} : \Omega \to \mathbb{R}$ is determined by the Neumann problem:

$$\begin{cases} \operatorname{div}_G (\nabla \varphi_\pi + \mathbf{i} \times \boldsymbol{r}) &= 0 & \text{in } \Omega, \\ \nabla_{\boldsymbol{\nu}} \varphi_\pi &= -\mathbf{i} \times \boldsymbol{r} \cdot \boldsymbol{\nu} & \text{on } \Gamma, \\ \int_\Omega \varphi_\pi \mu_E &= 0 \end{cases} \tag{C.3.3}$$

The linearized strain tensor under (C.3.2) is:

$$\boldsymbol{E}^{(a)} = (a_\varepsilon + \boldsymbol{r} \cdot \boldsymbol{a}_\Omega)\, (\mathbf{i} \otimes \mathbf{i} - \nu\, \mathbf{1}_\Omega) + \tfrac{1}{2} (\mathbf{i} \otimes \boldsymbol{\varepsilon}_\vartheta + \boldsymbol{\varepsilon}_\vartheta \otimes \mathbf{i}), \quad \boldsymbol{\varepsilon}_\vartheta := a_\vartheta (\mathbf{i} \times \boldsymbol{r} + \nabla \bar{\varphi}_\mathrm{I}), \tag{C.3.4}$$

The integration constants $(\boldsymbol{a}_\Omega, a_\varepsilon, a_\vartheta)$ are fixed by:

$$\begin{aligned} \boldsymbol{a}_\Omega \cdot \boldsymbol{c}_\varepsilon + \widehat{EA}\, a_\varepsilon &= -\bar{N}, \\ \widehat{E\boldsymbol{J}}_\kappa\, \boldsymbol{a}_\Omega + a_\varepsilon\, \boldsymbol{c}_\varepsilon &= \bar{\boldsymbol{M}} \times \mathbf{i}, \\ \widehat{GJ}_\vartheta\, a_\vartheta &= -\bar{T}, \end{aligned} \tag{C.3.5}$$

where the axial rigidity $\widehat{EA}$ and first moment vector $\boldsymbol{c}_\varepsilon$ are defined by:

$$\widehat{EA} := \int_\Omega \Big[\lambda + 2G + \lambda\bar{\pi}\Big]\, \mathrm{d}A \qquad \text{and} \qquad \boldsymbol{c}_\varepsilon := \int_\Omega \Big[(\lambda + 2G)\, \boldsymbol{r} + \lambda\, \boldsymbol{\pi}\Big]\, \mathrm{d}A \tag{C.3.6}$$

and the torsional rigidity $\widehat{GJ}_\vartheta$ and plane moment rigidity $\widehat{E\boldsymbol{J}}_\kappa$ are defined by:

$$\widehat{E\boldsymbol{J}}_\kappa := \int_\Omega \boldsymbol{r} \otimes \Big[(\lambda + 2G)\, \boldsymbol{r} + \lambda\, \boldsymbol{\pi}\Big]\, \mathrm{d}A \qquad \text{and} \qquad \widehat{GJ}_\vartheta := \int_\Omega \Big(r^2 + (\mathbf{i} \times \boldsymbol{r}) \cdot \nabla\bar{\varphi}_{\mathrm{I}}\Big)\mu_G. \tag{C.3.7}$$

Note that these are defined with respect to the unspecified coordinate origin.

C.4 Problem II: Flexure

Synopsis

Problem P_{II} models flexure under a transverse resultant force $\bar{\boldsymbol{F}}$ with $\bar{N} = 0$ and $\bar{\boldsymbol{M}} = \mathbf{0}$. The identifying kinematic postulate requires that the second axial derivative is a rigid motion,

$$\hat{\boldsymbol{u}}''_{\mathrm{II}} = b_\varepsilon\, \mathbf{i} + \big(b_\vartheta\, \mathbf{i} - \mathbf{i} \times \boldsymbol{b}_\Omega\big) \times \boldsymbol{x}, \qquad \boldsymbol{b}_\Omega \in \mathbb{R}^2,\ b_\varepsilon, b_\vartheta \in \mathbb{R}.$$

It follows that $\hat{\boldsymbol{u}}'$ is a P_{I} Saint–Venant field with bending moments $\mathbf{i} \times \bar{\boldsymbol{F}}$, and hence $\hat{\boldsymbol{u}}_{\mathrm{II}}\{\boldsymbol{b}, \boldsymbol{c}\} = \int_0^x \boldsymbol{u}_{\mathrm{I}}\{\boldsymbol{b}\}\ \mathrm{d}x + \boldsymbol{u}_{\mathrm{I}}\{\boldsymbol{c}\} + \tilde{\boldsymbol{w}}$.

Statement

Given a transverse shear resultant $\bar{\boldsymbol{F}}$ on Ω_0, determine $(\hat{\boldsymbol{u}}\{\boldsymbol{b}, \boldsymbol{c}\},\ \boldsymbol{S})$ such that:

$$\bar{\mathrm{P}}_{\mathrm{II}} \begin{cases} \hat{\boldsymbol{u}}_{\mathrm{II}} \in \mathrm{P}_{\mathrm{II}}(\bar{\boldsymbol{F}}) & \text{(C.4.1a)} \\ \hat{\boldsymbol{u}}''_{\mathrm{II}} = b_\varepsilon\, \mathbf{i} + \big(b_\vartheta\, \mathbf{i} - \mathbf{i} \times \boldsymbol{b}_\Omega\big) \times \boldsymbol{r}, & \text{(C.4.1b)} \end{cases}$$

Solution

Integrating (C.4.1) furnishes the particular solution:

$$\begin{aligned}\mathbf{1}_\Omega \hat{\boldsymbol{u}}_{\mathrm{II}}(x,\boldsymbol{r}) &= -\tfrac{1}{6}\,x^3\,\boldsymbol{b}_\Omega + x\,\nu\Big(\tfrac{1}{2}r^2\,\boldsymbol{b}_\Omega - (\boldsymbol{b}_\Omega\cdot\boldsymbol{r})\,\boldsymbol{r}\Big) + x\,\nu\,(\bar{\boldsymbol{\rho}}\cdot\boldsymbol{b}_\Omega)\,\boldsymbol{r} + c_\vartheta\,x\,(\mathbf{i}\times\boldsymbol{r}),\\ \mathbf{i}\cdot\hat{\boldsymbol{u}}_{\mathrm{II}}(x,\boldsymbol{r}) &= \tfrac{1}{2}\,x^2\,(\boldsymbol{r}-\bar{\boldsymbol{\rho}})\cdot\boldsymbol{b}_\Omega + c_\vartheta\,\bar{\varphi}_{\mathrm{I}}(\boldsymbol{r}) + \bar{\boldsymbol{\varphi}}_{\mathrm{II}}(\boldsymbol{r})\cdot\boldsymbol{b}_\Omega,\end{aligned} \tag{C.4.2}$$

where

$$\widetilde{\boldsymbol{\Pi}}(\boldsymbol{r}) := \boldsymbol{\Pi} - \hat{\boldsymbol{u}}_{(\varepsilon)}\otimes\bar{\boldsymbol{\rho}} \qquad \text{and} \qquad \tilde{\boldsymbol{\pi}} := \boldsymbol{\pi} - \bar{\pi}\,\bar{\boldsymbol{\rho}} \tag{C.4.3}$$

with

$$\bar{\boldsymbol{\rho}} := \frac{1}{\widehat{EA}}\boldsymbol{c}_\varepsilon \tag{C.4.4}$$

and the flexural warping shape $\bar{\boldsymbol{\varphi}}_{\mathrm{II}} : \Omega \to \mathbb{R}^2$ is determined by the Poisson–Neumann problem:

$$\begin{cases} \operatorname{div}\big(G\nabla(\bar{\boldsymbol{\varphi}}_{\mathrm{II}}\cdot\boldsymbol{b}_\Omega)\big) = \boldsymbol{f}_{\mathrm{II}}\cdot\boldsymbol{b}_\Omega & \text{in } \Omega,\\ G\nabla_{\boldsymbol{\nu}}(\bar{\boldsymbol{\varphi}}_{\mathrm{II}}\cdot\boldsymbol{b}_\Omega) = -\boldsymbol{\nu}\cdot\widetilde{\boldsymbol{\Pi}}\boldsymbol{b}_\Omega & \text{on } \Gamma,\\ \displaystyle\int_\Omega \bar{\boldsymbol{\varphi}}_{\mathrm{II}}\cdot\boldsymbol{b}_\Omega\,\mu_E = 0, \end{cases} \tag{C.4.5}$$

with:

$$\boldsymbol{f}_{\mathrm{II}}(\boldsymbol{r}) := -(\lambda+2G)(\boldsymbol{r}-\bar{\boldsymbol{\rho}}) - \operatorname{div}\big(G\,\widetilde{\boldsymbol{\Pi}}\big) - \lambda\,\tilde{\boldsymbol{\pi}}$$

The strain under (C.4.2) is

$$\boldsymbol{E}(\hat{\boldsymbol{u}}) = (\varepsilon\,\mathbf{i} + \boldsymbol{\varepsilon}_\gamma)\overset{\mathrm{s}}{\otimes}\mathbf{i} + \tilde{\boldsymbol{E}} \qquad \text{with} \qquad \begin{aligned}\varepsilon &= x\,(\boldsymbol{r}-\bar{\boldsymbol{\rho}})\cdot\boldsymbol{b}_\Omega,\\ \boldsymbol{\varepsilon}_\gamma &= c_\vartheta(\nabla\bar{\varphi}_{\mathrm{I}} + \mathbf{i}\times\boldsymbol{r}) + \widetilde{\boldsymbol{\Pi}}\boldsymbol{b}_\Omega + \nabla(\bar{\boldsymbol{\varphi}}_{\mathrm{II}}\cdot\boldsymbol{b}_\Omega),\end{aligned} \tag{C.4.6}$$

and the stress is

$$\begin{aligned}\sigma(\hat{\boldsymbol{u}}) &= E\,x\,(\boldsymbol{r}-\bar{\boldsymbol{\rho}})\cdot\boldsymbol{b}_\Omega,\\ \boldsymbol{\tau}(\hat{\boldsymbol{u}}) &= G\Big[(a_\vartheta + c_\vartheta)(\nabla\bar{\varphi}_{\mathrm{I}} + \mathbf{i}\times\boldsymbol{r}) + \widetilde{\boldsymbol{\Pi}}\boldsymbol{b}_\Omega + \nabla(\bar{\boldsymbol{\varphi}}_{\mathrm{II}}\cdot\boldsymbol{b}_\Omega)\Big].\end{aligned} \tag{C.4.7}$$

The free parameters are determined from

$$\begin{aligned}\widehat{E\boldsymbol{J}}_\kappa\,\boldsymbol{b}_\Omega + \boldsymbol{c}_\varepsilon\,b_\varepsilon &= -\bar{\boldsymbol{F}},\\ \boldsymbol{b}_\Omega\cdot\bar{\boldsymbol{\rho}} + b_\varepsilon &= 0,\\ b_\vartheta &= 0,\end{aligned} \tag{C.4.8}$$

and c_ϑ is determined by the relaxed torsion boundary condition $\mathbf{i}\cdot\int\boldsymbol{r}\times\boldsymbol{\tau}\,\mathrm{d}A = 0$:

$$c_\vartheta = \boldsymbol{\rho}_{\mathrm{II}}\cdot\boldsymbol{b}_\Omega \tag{C.4.9}$$

where the *shear point* $\boldsymbol{\rho}_{\mathrm{II}} \in \Omega$ is defined by:

$$\boldsymbol{\rho}_{\mathrm{II}} := \frac{1}{\widehat{GJ}_\vartheta} \int_\Omega G(\nabla \bar{\boldsymbol{\varphi}}_{\mathrm{II}} + \widetilde{\boldsymbol{\Pi}}^\top)\, \boldsymbol{r} \times \mathbf{i} \; \mathrm{d}A. \tag{C.4.10}$$

and $\widehat{GJ}_\vartheta$ is the torsion constant defined by (C.3.7).

C.5 General Solution for Poisson-Homogeneous Bodies

When Poisson's ratio ν is uniform, the boundary value problems (C.2.1) admit the closed form solutions:

$$\hat{\boldsymbol{u}}_{(\varepsilon)} = -\nu \boldsymbol{r} \tag{C.5.1a}$$

$$\boldsymbol{\Pi} = -\,\nu \operatorname{dev} \boldsymbol{r} \otimes \boldsymbol{r} \tag{C.5.1b}$$

$$\widetilde{\boldsymbol{\Pi}} = -\,\nu\big(\operatorname{dev} \boldsymbol{r} \otimes \boldsymbol{r} - \boldsymbol{r} \otimes \bar{\boldsymbol{\rho}}\big) \tag{C.5.1c}$$

where the deviator $\operatorname{dev} \boldsymbol{r}\otimes\boldsymbol{r}$ is understood in the section plane $\operatorname{dev} \boldsymbol{r}\otimes\boldsymbol{r} = \boldsymbol{r}\otimes\boldsymbol{r} - \frac{1}{2}(\boldsymbol{r}\cdot\boldsymbol{r})\,\mathbf{1}_\Omega$. Combining (C.3.2) and (C.4.2) and using (C.5.1) furnishes the particular solution for the complete Saint-Venant class:

$$\begin{aligned} \hat{\boldsymbol{u}}_{\mathrm{P}} = {} & \Big(-\tfrac{1}{2} x^2\, \mathbf{1} - \nu \operatorname{dev} \boldsymbol{r} \otimes \boldsymbol{r} + x\, \mathbf{i} \otimes \boldsymbol{r} \Big) \boldsymbol{a}_\Omega + (x\, \mathbf{i} - \nu \boldsymbol{r})\, a_\varepsilon + (x\, \mathbf{i} \times \boldsymbol{r} + \bar{\varphi}_{\mathrm{I}}\, \mathbf{i}) a_\vartheta \\ & - \tfrac{1}{6}\, x^3\, \boldsymbol{b}_\Omega - x\, \nu \Big(\operatorname{dev} \boldsymbol{r} \otimes \boldsymbol{r} - \boldsymbol{r} \otimes \bar{\boldsymbol{\rho}} \Big) \boldsymbol{b}_\Omega + \tfrac{1}{2} x^2\, \mathbf{i} \otimes (\boldsymbol{r} - \bar{\boldsymbol{\rho}})\, \boldsymbol{b}_\Omega + \mathbf{i} \otimes \bar{\boldsymbol{\varphi}}_{\mathrm{II}}(\boldsymbol{r})\, \boldsymbol{b}_\Omega \\ & + (x\, \mathbf{i} \times \boldsymbol{r} + \bar{\varphi}_{\mathrm{I}}\, \mathbf{i}) c_\vartheta, \end{aligned} \tag{C.5.2}$$

with $\boldsymbol{a}$ fixed by (C.3.5), $\boldsymbol{b}$ by (C.4.8), $\bar{\varphi}_{\mathrm{I}}$ by (C.3.3), $\bar{\boldsymbol{\varphi}}_{\mathrm{II}}$ by (C.4.5), c_ϑ by (C.4.9).

The complete Saint-Venant solution is the sum of the particular solution (C.5.2), and a homogeneous solution $\hat{\boldsymbol{u}}_{\mathrm{R}}$:

$$\hat{\boldsymbol{u}}(x, \boldsymbol{r}) = \hat{\boldsymbol{u}}_{\mathrm{P}}(x, \boldsymbol{r}) + \hat{\boldsymbol{u}}_{\mathrm{R}}(x, \boldsymbol{r}) \tag{C.5.3}$$

and $\hat{\boldsymbol{u}}_{\mathrm{R}}$ is an arbitrary rigid body motion with six free parameters $\boldsymbol{q}_u \in \mathbb{R}^3$ and $\boldsymbol{q}_\theta \in \mathbb{R}^3$:

$$\hat{\boldsymbol{u}}_{\mathrm{R}}\{\boldsymbol{q}\} = \boldsymbol{q}_u + \boldsymbol{q}_\theta \times \hat{\boldsymbol{x}}(x, \boldsymbol{r}) \tag{C.5.4}$$

The infinitesimal strain tensor is

$$\boldsymbol{E} = \varepsilon\, \mathbf{i} \otimes \mathbf{i} \;+\; \mathbf{i} \overset{\mathrm{s}}{\otimes} \boldsymbol{\varepsilon}_\gamma \;-\; \nu \varepsilon\, \mathbf{1}_\Omega,$$

where recall $\boldsymbol{a} \overset{\mathrm{s}}{\otimes} \boldsymbol{b} := \frac{1}{2}(\boldsymbol{a} \otimes \boldsymbol{b} + \boldsymbol{b} \otimes \boldsymbol{a})$ is the symmetrized bun product and:

$$\varepsilon = a_\varepsilon + \boldsymbol{r} \cdot \boldsymbol{a}_\Omega + x\, (\boldsymbol{r} - \bar{\boldsymbol{\rho}}) \cdot \boldsymbol{b}_\Omega, \tag{C.5.5a}$$

$$\boldsymbol{\varepsilon}_\gamma = (a_\vartheta + c_\vartheta)(\mathbf{i} \times \boldsymbol{r} + \nabla \bar{\varphi}_{\mathrm{I}}) + \widetilde{\boldsymbol{\Pi}} \boldsymbol{b}_\Omega + (\nabla \bar{\boldsymbol{\varphi}}_{\mathrm{II}})^\top \boldsymbol{b}_\Omega \tag{C.5.5b}$$

C.6 Summary

Table C.1: Symbols employed for Saint Venant's solution.

Symbol	Units	Equation	Description
$a_\varepsilon \in \mathbb{R}$	$\sim$		Axial strain parameter for $\mathrm{P_I}$
$a_\vartheta \in \mathbb{R}$	L^{-1}		Saint Venant torsional parameter for $\mathrm{P_I}$
$\boldsymbol{a}_\Omega \in \Omega$	L^{-1}		Bending parameters for $\mathrm{P_I}$
$c_\vartheta \in \mathbb{R}$	L^{-1}		Torsion coupling under flexure for $\mathrm{P_{II}}$
$b_\varepsilon \in \mathbb{R}$			Saint Venant elongation parameter for $\mathrm{P_{II}}$
$\boldsymbol{b}_\Omega \in \Omega$	L^{-2}		Saint Venant flexural parameters for $\mathrm{P_{II}}$
$\boldsymbol{q}_u \in \mathbb{R}^3$	L		Rigid translation at $x = 0$
$\boldsymbol{q}_\theta \in \mathbb{R}^3$			Rigid rotation at $x = 0$
$\boldsymbol{\Pi}$		(C.2.2) or (C.5.1)	Solution matrix of the plane-strain boundary value problems (C.2.1a)
$\boldsymbol{\pi}$	$\sim$	(C.2.2)	Volumetric strain vector from the plane-strain boundary value problems (C.2.1a) with $\mathbf{i}_k = \mathbf{i}_\beta$
$\bar{\pi}$	$\sim$	(C.2.2)	Volumetric strain from the third ($\mathbf{i}_k = \mathbf{i}$) plane strain problem (C.2.1a)
$\tilde{\boldsymbol{\pi}}$		(C.4.3)	Plane shear warping functions
$\widetilde{\boldsymbol{\Pi}}$		(C.4.3) or (C.5.1)	
$\bar{\varphi}_{\mathrm{I}}$	L^2	(C.3.3)	Saint Venant torsion function
$\bar{\boldsymbol{\varphi}}_{\mathrm{II}}$	L^3	(C.4.5)	Saint Venant flexural functions

Appendix D

Integral Identities

D.1 Preliminaries

Box D.1 collects standard definitions and notation concerning integration on a Riemannian manifold M with oriented volume form μ (Spivak, 1965; R. Abraham et al., 1988; Marsden & Hughes, 1994; Shilov, 1996).

D.2 Identities

Proposition D.2.1. *Let (M, μ) be a compact oriented manifold with (possibly non-empty) boundary ∂M. If a vector field $\boldsymbol{X}$ satisfies the boundary value problem:*

$$\operatorname{div}_\mu \boldsymbol{X} = 0 \quad \textit{and} \quad \boldsymbol{X} \cdot \boldsymbol{\nu} = 0 \;\; \textit{on } \partial M,$$

then $\boldsymbol{X}$ acts as a skew–symmetric operator on $\mathcal{F}(M)$:

$$\langle \boldsymbol{X}[f],\, g\rangle_\mu \;=\; -\langle f,\, \boldsymbol{X}[g]\rangle_\mu\,, \qquad \forall\, f, g \in \mathcal{F}(M).$$

with the linear operation $\boldsymbol{X}[f] \triangleq \nabla_{\boldsymbol{X}} f$.

Proof. This is an extension of R. Abraham et al. (1988, Corollary 7.2.11). The condition $\operatorname{div}_\mu \boldsymbol{X} = 0$ implies that for any $h \in \mathcal{F}(M)$

$$\mathcal{L}_{\boldsymbol{X}}(h\,\mu) = \boldsymbol{X}[h]\,\mu.$$

Taking $h = fg$ gives

$$\boldsymbol{X}[fg]\,\mu = \mathcal{L}_{\boldsymbol{X}}(fg\,\mu).$$

Box D.1: Integration Definitions

Definitions:

1. **Interior product** $\iota_{\boldsymbol{X}} : \Omega^p(M) \to \Omega^{p-1}(M)$ with a vector field $\boldsymbol{X}$ is the unique graded derivation of degree -1 satisfying

$$\iota_{\boldsymbol{X}} f = 0, \qquad \iota_{\boldsymbol{X}} \omega = \omega(\boldsymbol{X}) \qquad f \in \Omega^0(M),\ \omega \in \Omega^1(M) \tag{D.1.1}$$

and the Leibniz rule

$$\iota_{\boldsymbol{X}}(\alpha \wedge \eta) = (\iota_{\boldsymbol{X}}\alpha) \wedge \eta + (-1)^k\, \alpha \wedge \iota_{\boldsymbol{X}}\eta, \qquad \alpha \in \Omega^k(M)$$

2. **Exterior product** $\wedge : \Omega^k(M) \times \Omega^\ell(M) \longrightarrow \Omega^{k+\ell}(M)$ is a bilinear, associative product defined by

$$\alpha \wedge \eta \;=\; (-1)^{k\ell}\, \eta \wedge \alpha, \qquad \alpha \in \Omega^k(M),\ \eta \in \Omega^\ell(M),$$

with $f \wedge \alpha = f\,\alpha$ for functions $f \in \Omega^0(M)$.

3. **Hodge operator** $\star : \Omega^k(M) \longrightarrow \Omega^{n-k}(M)$ is the unique map satisfying

$$\alpha \wedge \star\eta \;=\; \langle \alpha, \eta \rangle\, \mu, \qquad \forall\, \alpha, \eta \in \Omega^k(M) \tag{D.1.2}$$

Consequences include (with the musical isomorphism "$\flat$" lowering indices):

$$\iota_{\boldsymbol{X}} \star\omega = (-1)^k \star (\boldsymbol{X}^\flat \wedge \omega) \qquad \text{for} \qquad \omega \in \Omega^k(M)$$

and the special case when $\alpha = 1$, $\star\alpha = \mu$

$$\iota_{\boldsymbol{X}}\mu = \star\boldsymbol{X}^\flat \tag{D.1.3}$$

4. **Exterior derivative** $\mathrm{d} : \Omega^k(M) \longrightarrow \Omega^{k+1}(M)$ is the unique linear operator of degree $+1$ satisfying

$$\begin{aligned} \mathrm{d}f(X) &= X[f], & f &\in \Omega^0(M), \\ \mathrm{d}(\alpha \wedge \eta) &= \mathrm{d}\alpha \wedge \eta + (-1)^k\, \alpha \wedge \mathrm{d}\eta, & \alpha &\in \Omega^k(M),\ \eta \in \Omega^\ell(M), \end{aligned}$$

Useful relations include

$$\mathrm{d}f = (\nabla f)^\flat \tag{D.1.4}$$

5. **Lie derivative** is defined on forms as the operator:

$$\mathcal{L}_{\boldsymbol{X}} \;=\; \iota_{\boldsymbol{X}}\mathrm{d} + \mathrm{d}\iota_{\boldsymbol{X}} \tag{D.1.5}$$

6. **Divergence** $\operatorname{div}_\mu \boldsymbol{X}$ of a vector field $\boldsymbol{X}$ with respect to a volume form μ

$$(\operatorname{div}_\mu \boldsymbol{X})\mu \triangleq \mathcal{L}_{\boldsymbol{X}}\mu \tag{D.1.6}$$

This furnishes the identities (for a *positive* scalar field α)

$$(\operatorname{div}_\mu \boldsymbol{X})\mu = \mathrm{d}(\iota_{\boldsymbol{X}}\mu) \qquad \text{and} \qquad \alpha \operatorname{div}_{\alpha\mu} \boldsymbol{X} = \operatorname{div}_\mu(\alpha\boldsymbol{X})$$

Theorems:

1. **Stokes-Cartan Theorem** and the **Divergence Theorem** as a special case:

$$\int_M \mathrm{d}\alpha = \int_{\partial M} \alpha \qquad \text{and} \qquad \int_M (\operatorname{div}_\mu \boldsymbol{X})\,\mu = \int_{\partial M} \iota_{\boldsymbol{X}}\mu = \int_{\partial M} \langle \boldsymbol{X}, \boldsymbol{\nu} \rangle \eta_\mu \tag{D.1.7}$$

where $\boldsymbol{\nu}$ is the unit normal to ∂M and the identity $\iota_{\boldsymbol{X}}\mu = \langle \boldsymbol{X},\, \boldsymbol{\nu} \rangle\, \underbrace{\iota_{\boldsymbol{\nu}}\mu}_{:=\eta_\mu}$ is used.

Integrating over M and applying the divergence theorem (D.1.7) yields

$$\int_M \boldsymbol{X}[fg]\,\mu \;=\; \int_{\partial M} (fg)\,(\boldsymbol{X}\cdot\boldsymbol{\nu})\,\eta$$

Using $\boldsymbol{X}\cdot\boldsymbol{\nu} = 0$ on ∂M, the integrals vanish and

$$0 = \int_M \boldsymbol{X}[fg]\,\mu = \int_M (\boldsymbol{X}[f]\,g + f\,\boldsymbol{X}[g])\mu.$$

□

Proposition D.2.2. *(R. ABRAHAM et al., 1988, Corollary 7.2.12) If M is compact without boundary, $\boldsymbol{X} \in \mathfrak{X}(M), \alpha \in \Omega^{\mathrm{k}}(M)$ and $\beta \in \Omega^{\mathrm{n-k}}(M)$, then*

$$\int_M \mathcal{L}_{\boldsymbol{X}}\alpha \wedge \beta = -\int_M \alpha \wedge \mathcal{L}_{\boldsymbol{X}}\beta$$

Proof. Using $\alpha \wedge \beta \in \Omega^n(M)$, the formula follows by integrating both sides of the relation

$$\mathrm{d}\iota_{\boldsymbol{X}}(\alpha\wedge\beta) = \mathcal{L}_X(\alpha\wedge\beta) = \mathcal{L}_X\alpha\wedge\beta + \alpha\wedge\mathcal{L}_X\beta$$

and using Stoke's Theorem (D.1.7). □

D.3 Torsion

Proposition D.3.1. *The solution $\tilde{\varphi}$ to the boundary value problem* (C.3.3) *is the Riesz vector:*

$$(\tilde{\varphi},\,\phi)_G = \frac{1}{2}\,\{\boldsymbol{r}\cdot\boldsymbol{r},\,\phi\}_G \qquad \forall\phi\in\mathcal{F}(M) \tag{D.3.1}$$

where $\{\,\cdot,\,\cdot\}_G$ is the integrated Poisson bracket (ARNOLD, 1978) given by

$$\{\psi,\,\phi\}_G = \int_M \nabla\psi\cdot\mathbb{J}\nabla\phi\,\mu_G$$

and the symplectic operator is $\mathbb{J} = \mathbf{i}^{\times}$. This gives the special cases

$$\int [\nabla\psi,\ \mathbf{i},\ \boldsymbol{r}-\tilde{\boldsymbol{\rho}}]\,\mu_{\scriptscriptstyle G} = \int_M \tilde{\varphi}^2\,\mu_{\scriptscriptstyle E} \tag{D.3.2}$$

and

$$\int_M \nabla\tilde{\varphi}\cdot\nabla\tilde{\varphi}\;\mu_{\scriptscriptstyle G} = -\int_M [\nabla\tilde{\varphi},\mathbf{i},\boldsymbol{r}]\;\mu_{\scriptscriptstyle G} > 0 \tag{D.3.3}$$

Proof. By Identity D.2.1, taking $\boldsymbol{X} = \nabla\tilde{\varphi} + \mathbf{i} \times \boldsymbol{r}$, $f = \phi$ and $g = 1$. $\square$

Proposition D.3.2. *Armero (2021) Equation (88)*

$$(\psi,\, \phi)_G = -\left\langle \tilde{\varphi},\, \phi \right\rangle_E \qquad \forall \phi \in \mathcal{F}(M) \tag{D.3.4}$$

Proof. Multiply the PDE for ψ by ϕ, and integrate over M

$$\int_M \phi\,(\operatorname{div}_G \nabla\psi)\mu_{\scriptscriptstyle G} = \int_M \phi\,\tilde{\varphi}\mu_{\scriptscriptstyle E}$$

Thus it must be shown that the left hand side is equivalent to the (negative) G-energy inner product:

$$\int_M \phi\,(\operatorname{div}_G \nabla\psi)\mu_{\scriptscriptstyle G} = -\int_M \nabla\psi \cdot \nabla\phi\,\mu_{\scriptscriptstyle G}$$

This is equivalent to showing:

$$\int_M \phi\,(\operatorname{div}_G \nabla\psi)\mu_{\scriptscriptstyle G} + \int_M \mathrm{d}\phi \wedge \iota_{\nabla\psi}\mu_{\scriptscriptstyle G} = 0 \tag{†}$$

where the following was used:

$$\begin{aligned} \mathrm{d}\phi \wedge \iota_{\nabla\psi}\mu_{\scriptscriptstyle G} &= \mathrm{d}\phi \wedge \star(\nabla\psi)^\flat && \text{(D.1.3)} \\ &= \mathrm{d}\phi \wedge \star\mathrm{d}\psi && \text{(D.1.4)} \\ &= \left\langle \mathrm{d}\psi,\, \mathrm{d}\phi \right\rangle \mu_{\scriptscriptstyle G} && \text{(D.1.2)} \end{aligned}$$

Thus (†) is an integration by parts of the product rule for (D.1.5)

$$\mathcal{L}_{(\tilde{\varphi}\nabla\psi)}\mu_{\scriptscriptstyle G} = \tilde{\varphi}\mathcal{L}_{\nabla\psi}\mu_{\scriptscriptstyle G} + \mathrm{d}\tilde{\varphi} \wedge \iota_{\nabla\psi}\mu_{\scriptscriptstyle G}$$

where by the divergence theorem (D.1.7)

$$\int_M \mathcal{L}_{(\tilde{\varphi}\nabla\psi)}\mu_{\scriptscriptstyle G} = \int_{\partial M} \tilde{\varphi}\nabla\psi \cdot \boldsymbol{\nu}\,\eta_G$$

which vanishes due to the boundary condition $\nabla_{\boldsymbol{\nu}}\psi = 0$. Therefore:

$$-\int_M \nabla\psi \cdot \nabla\tilde{\varphi}\,\mu_{\scriptscriptstyle G} = \int_M \tilde{\varphi}^2\mu_{\scriptscriptstyle E}$$

and also

$$\int_M \iota_{\nabla\psi}\mathrm{d}\tilde{\varphi}\,\mu_{\scriptscriptstyle G} = -\int_M \tilde{\varphi}^2\ \mu_{\scriptscriptstyle E}$$

$\square$

Appendix E

Trace Derivations

E.1 The Section-Average Trace

The section-average trace of a homogeneous section extracts the L^2-optimal rigid approximation to the displacement field:

$$\bar{\boldsymbol{u}}(x) := \bar{\Omega}\left[\hat{\boldsymbol{u}}\right] - \bar{\boldsymbol{\theta}} \times \bar{\boldsymbol{\rho}}, \qquad \bar{\boldsymbol{\theta}}(x) := \bar{\Theta}\left[\hat{\boldsymbol{u}}\right], \tag{E.1.1}$$

where the linear functionals $\bar{\Omega}\left[\cdot\right]$ and $\bar{\Theta}[\cdot]$ are defined for $\boldsymbol{v} : [0, L] \times \Omega \to \mathbb{E}$:

$$\bar{\Omega}\left[\boldsymbol{u}\right] := \frac{1}{A}\int_{\Omega} \boldsymbol{u} \,\mathrm{d}A, \qquad \bar{\Theta}\left[\boldsymbol{u}\right] := \bar{\mathbf{I}}^{-1}\int_{\Omega} (\boldsymbol{r} - \bar{\boldsymbol{\rho}}) \times \boldsymbol{u} \,\mathrm{d}A, \quad \text{and} \quad \bar{\mathbf{I}} := \int_{\Omega} \left(|\bar{\boldsymbol{r}}|^2\mathbf{1} - \bar{\boldsymbol{r}} \otimes \bar{\boldsymbol{r}}\right) \mathrm{d}A. \tag{E.1.2}$$

with $\mathbf{1}$ the identity in $\mathbb{R}^3$ and $\bar{\boldsymbol{\rho}} \in \Omega$ is the centroid satisfying $\bar{\Omega}\left[\boldsymbol{r} - \bar{\boldsymbol{\rho}}\right] = \mathbf{0}$.

Proposition E.1.1 (Optimal Rigid Alignment)**.** *The plane-rigid field $\bar{\boldsymbol{u}}(x) + \bar{\boldsymbol{\theta}}(x) \times \boldsymbol{r} \in \mathcal{R}$ that best fits a 3D field $\hat{\boldsymbol{u}}(x, \boldsymbol{r}) : [0, L] \times \Omega$ in the least-squares sense is given by:*

$$\bar{\boldsymbol{u}}(x) = \bar{\Omega}\left[\hat{\boldsymbol{u}}\right] - \bar{\boldsymbol{\theta}}(x) \times \bar{\Omega}\left[\boldsymbol{r}\right], \qquad \bar{\boldsymbol{\theta}}(x) = \bar{\Theta}[\hat{\boldsymbol{u}}],$$

Proof. The section-rigid motion $\bar{\boldsymbol{u}} + \bar{\boldsymbol{\theta}} \times \boldsymbol{r}$ that best fits $\hat{\boldsymbol{u}}$ in the least-squares sense minimizes the functional:

$$\mathcal{J}(\bar{\boldsymbol{u}}, \bar{\boldsymbol{\theta}}) := \int_{\Omega} \left\|\hat{\boldsymbol{u}}(\boldsymbol{r}) - (\bar{\boldsymbol{u}} + \bar{\boldsymbol{\theta}} \times \boldsymbol{r})\right\|^2 \mathrm{d}A.$$

Stationarity of $\mathcal{J}$ with respect to $\bar{\boldsymbol{u}}$ gives

$$\int_{\Omega} \left(\hat{\boldsymbol{u}} - \bar{\boldsymbol{u}} - \bar{\boldsymbol{\theta}} \times \boldsymbol{r}\right) \mathrm{d}A = \mathbf{0} \quad \Longrightarrow \quad \bar{\boldsymbol{u}}(x) = \bar{\Omega}\left[\hat{\boldsymbol{u}}\right] - \bar{\boldsymbol{\theta}}(x) \times \bar{\Omega}\left[\boldsymbol{r}\right] \tag{E.1.3}$$

Stationarity in $\bar{\boldsymbol{\theta}}$ requires,

$$\int_\Omega \boldsymbol{r} \times (\hat{\boldsymbol{u}} - \bar{\boldsymbol{u}} - \bar{\boldsymbol{\theta}} \times \boldsymbol{r})\ \mathrm{d}A = \mathbf{0}.$$

where the identity $\boldsymbol{a}\cdot(\delta\bar{\boldsymbol{\theta}}\times\boldsymbol{r}) = (\boldsymbol{r}\times\boldsymbol{a})\cdot\delta\bar{\boldsymbol{\theta}}$ was used. Insert $\bar{\boldsymbol{u}}$ from (E.1.3) and set $\bar{\boldsymbol{r}} := \boldsymbol{r}-\bar{\boldsymbol{\rho}}$ so $\bar{\Omega}\,[\bar{\boldsymbol{r}}] = \mathbf{0}$:

$$\int_\Omega \boldsymbol{r} \times (\hat{\boldsymbol{u}} - \bar{\Omega}\,[\hat{\boldsymbol{u}}]\,)\ \mathrm{d}A\ - \int_\Omega \boldsymbol{r} \times (\bar{\boldsymbol{\theta}} \times (\boldsymbol{r} - \bar{\boldsymbol{\rho}}))\ \mathrm{d}A = \mathbf{0}.$$

Using the vector identity $\bar{\boldsymbol{\rho}} \times (\bar{\boldsymbol{\theta}} \times \bar{\boldsymbol{\rho}}) = (\|\bar{\boldsymbol{\rho}}\|^2\mathbf{1} - \bar{\boldsymbol{\rho}} \otimes \bar{\boldsymbol{\rho}})\,\bar{\boldsymbol{\theta}}$ the second term furnishes:

$$\int_\Omega \bar{\boldsymbol{r}} \times (\bar{\boldsymbol{\theta}} \times \bar{\boldsymbol{r}})\ \mathrm{d}A = \bar{\mathbf{I}}\,\bar{\boldsymbol{\theta}},$$

Hence with $\bar{\boldsymbol{\rho}} \equiv \bar{\Omega}\,[\boldsymbol{r}]$ by material homogeneity,

$$\bar{\mathbf{I}}\,\bar{\boldsymbol{\theta}} = \int_\Omega (\boldsymbol{r} - \bar{\boldsymbol{\rho}}) \times \hat{\boldsymbol{u}}\ \mathrm{d}A, \qquad \bar{\boldsymbol{\theta}} = \bar{\mathbf{I}}^{-1} \int_\Omega (\boldsymbol{r} - \bar{\boldsymbol{\rho}}) \times \hat{\boldsymbol{u}}\ \mathrm{d}A.$$

where the linear functional $\bar{\Theta}$ is:

$$\bar{\Theta}[\boldsymbol{u}] := \bar{\mathbf{I}}^{-1} \int (\boldsymbol{r} - \bar{\boldsymbol{\rho}}) \times \boldsymbol{u}\ \mathrm{d}A, \qquad \bar{\mathbf{I}} := \int_\Omega \Big(|\boldsymbol{r} - \bar{\boldsymbol{\rho}}|^2\mathbf{1} - (\boldsymbol{r} - \bar{\boldsymbol{\rho}}) \otimes (\boldsymbol{r} - \bar{\boldsymbol{\rho}})\Big)\ \mathrm{d}A$$

and $\bar{\mathbf{I}}$ is the centroidal moment of inertia tensor. □

Note the properties:

$$\bar{\Theta}[\boldsymbol{a}] = \mathbf{0} \qquad \forall \boldsymbol{a} \text{ constant in } \boldsymbol{r} \tag{E.1.4a}$$
$$\bar{\Theta}[\boldsymbol{r}] = \mathbf{0} \tag{E.1.4b}$$
$$\bar{\Theta}[\boldsymbol{a} \times \boldsymbol{r}] = \boldsymbol{a} \tag{E.1.4c}$$
$$\bar{\Theta} \circ \bar{\Theta}[\boldsymbol{v}] = \bar{\Theta}[\boldsymbol{v}] \tag{E.1.4d}$$

The trace matrix $\mathbf{T}$ is derived by evaluating the functionals (E.1.2) to each Saint Venant mode and extracting the strains at $x = 0$.

Extension Mode. The extension displacement is

$$\hat{\boldsymbol{u}}^{(\varepsilon)} = (x\,\mathbf{i} - \nu\,\boldsymbol{r})\,a_\varepsilon.$$

The section averages are:

$$\bar{\Omega}\left[\hat{\boldsymbol{u}}^{(\varepsilon)}\right] = x\,\mathbf{i}\,a_\varepsilon - \nu\,\bar{\boldsymbol{\rho}}\,a_\varepsilon,$$
$$\bar{\Theta}\left[\hat{\boldsymbol{u}}^{(\varepsilon)}\right] = \mathbf{0},$$

where use has been made of the rotation average identities (E.1.4). The extracted fields are:

$$\bar{\boldsymbol{u}}^{(\varepsilon)}(x) = x\,\mathbf{i}\,a_\varepsilon - \nu\,\bar{\boldsymbol{\rho}}\,a_\varepsilon, \qquad \bar{\boldsymbol{\theta}}^{(\varepsilon)}(x) = \mathbf{0}.$$

The strains are:

$$\bar{\boldsymbol{\gamma}}^{(\varepsilon)} = \mathbf{i}\,a_\varepsilon, \qquad \bar{\boldsymbol{\kappa}}^{(\varepsilon)} = \mathbf{0}.$$

Bending Mode. The bending displacement is

$$\hat{\boldsymbol{u}}^{(a)} = \Big(-\tfrac{1}{2}x^2\,\mathbf{1}_\Omega + x\,\mathbf{i}\otimes\boldsymbol{r} + \boldsymbol{\Pi}\Big)\boldsymbol{a}_\Omega,$$

where recall $\boldsymbol{\Pi}$ is the plane shape (C.2.2). The section averages give:

$$\bar{\boldsymbol{\theta}}^{(a)}(x) = -x\,(\mathbf{i}\times\boldsymbol{a}_\Omega) + \bar{\Theta}\left[\boldsymbol{\Pi}\right]\,\boldsymbol{a}_\Omega.$$

The curvature is:

$$\bar{\boldsymbol{\kappa}}^{(a)} = -\mathbf{i}\times\boldsymbol{a}_\Omega,$$

After simplification using the identity $\mathbf{i}\times(\mathbf{i}\times\boldsymbol{a}_\Omega) = -\boldsymbol{a}_\Omega$, the shear strain is:

$$\bar{\boldsymbol{\gamma}}^{(a)} = \mathbf{i}\times\bar{\Theta}\left[\boldsymbol{\Pi}\right]\,\boldsymbol{a}_\Omega,$$

Torsion Mode.

The torsion displacement is

$$\hat{\boldsymbol{u}}^{(\vartheta)} = \big(x\,(\mathbf{i}\times\boldsymbol{r}) + \bar{\varphi}_{\mathrm{I}}\,\mathbf{i}\big)\,a_\vartheta.$$

The rotation average extracts:

$$\bar{\boldsymbol{\theta}}^{(\vartheta)}(x) = x\,\mathbf{i}\,a_\vartheta + \boldsymbol{\rho}_{\bar{\varphi}_{\mathrm{I}}}\,a_\vartheta,$$

where the *twist center* $\boldsymbol{\rho}_{\bar{\varphi}_{\mathrm{I}}}$ is:

$$\boldsymbol{\rho}_{\bar{\varphi}_{\mathrm{I}}} := \bar{\Theta}\left[\bar{\varphi}_{\mathrm{I}}\,\mathbf{i}\right]. \tag{E.1.5}$$

The center of twist (E.1.5) has been attributed to Trefftz (1935) by Pilkey (2003) and Romano et al. (2012).

The strains are:

$$\bar{\varkappa}^{(\vartheta)} = a_\vartheta, \qquad \bar{\boldsymbol{\gamma}}^{(\vartheta)} = (\mathbf{i}\times\boldsymbol{\rho}_{\bar{\varphi}_{\mathrm{I}}})\,a_\vartheta,$$

Flexure Mode. Recall the particular solution under pure flexure (C.4.2):

$$\hat{\boldsymbol{u}}_{\mathrm{II}} = (x\,\mathbf{i}\times\boldsymbol{r} + \bar{\varphi}_{\mathrm{I}}\,\mathbf{i})\,\boldsymbol{\rho}_{\mathrm{II}}\cdot\boldsymbol{b}_{\Omega} + \Big(-\tfrac{1}{6}x^3\,\mathbf{1}_{\Omega} + x\,\widetilde{\boldsymbol{\Pi}} + \tfrac{1}{2}x^2\,\mathbf{i}\otimes(\boldsymbol{r}-\bar{\boldsymbol{\rho}}) + \mathbf{i}\otimes\bar{\boldsymbol{\varphi}}_{\mathrm{II}}\Big)\,\boldsymbol{b}_{\Omega},$$

where recall $\widetilde{\boldsymbol{\Pi}} : \Omega \to \Omega\otimes\Omega$ is the plane shear warping shape (C.4.3). The rotation average $\bar{\Theta}\,[\hat{\boldsymbol{u}}_{\mathrm{II}}]$ gives:

$$\bar{\boldsymbol{\theta}}^{(b)}(x) = -\tfrac{1}{2}x^2\,(\mathbf{i}\times\boldsymbol{b}_{\Omega}) + x\,\mathbf{i}\otimes\bar{\boldsymbol{\rho}}_{\varkappa}\,\boldsymbol{b}_{\Omega} + \bar{\boldsymbol{\Xi}}_{\kappa}\,\boldsymbol{b}_{\Omega},$$

where with $\mathbf{i}\otimes\boldsymbol{\rho}_{\pi} := \bar{\Theta}\left[\widetilde{\boldsymbol{\Pi}}\right]$:

$$\bar{\boldsymbol{\rho}}_{\varkappa} := \boldsymbol{\rho}_{\mathrm{II}} + \bar{\Theta}\left[\widetilde{\boldsymbol{\Pi}}\right]^{\top}\mathbf{i} =: \boldsymbol{\rho}_{\mathrm{II}} + \boldsymbol{\rho}_{\pi}, \tag{E.1.6a}$$

$$\boldsymbol{\Gamma}_0 := \boldsymbol{\rho}_{\bar{\varphi}_{\mathrm{I}}}\otimes\boldsymbol{\rho}_{\mathrm{II}} + \bar{\Theta}\,[\mathbf{i}\otimes\bar{\boldsymbol{\varphi}}_{\mathrm{II}}]\,. \tag{E.1.6b}$$

with the center of shear $\boldsymbol{\rho}_{\mathrm{II}}$ given by (C.4.10). The curvature is:

$$\bar{\boldsymbol{\kappa}}^{(b)}(x) = -x\,(\mathbf{i}\times\boldsymbol{b}_{\Omega}) + \mathbf{i}\otimes\bar{\boldsymbol{\rho}}_{\varkappa}\,\boldsymbol{b}_{\Omega}.$$

After computing the translation average, displacement derivative, and combining with $\mathbf{i}\times\bar{\boldsymbol{\theta}}^{(b)}$, the quadratic terms cancel, yielding:

$$\bar{\boldsymbol{\gamma}}^{(b)}(x) = -x\mathbf{i}\otimes\bar{\boldsymbol{\rho}}\,\boldsymbol{b}_{\Omega} + \bar{\boldsymbol{\Xi}}_{\gamma}\,\boldsymbol{b}_{\Omega},$$

where:

$$\bar{\boldsymbol{\Xi}}_{\gamma} := \bar{\Omega}\left[\widetilde{\boldsymbol{\Pi}}\right] - \bar{\boldsymbol{\rho}}^{\times}\bar{\Theta}\left[\widetilde{\boldsymbol{\Pi}}\right] + \mathbf{i}\times(\boldsymbol{\rho}_{\bar{\varphi}_{\mathrm{I}}}\otimes\boldsymbol{\rho}_{\mathrm{II}} + \bar{\Theta}\,[\mathbf{i}\otimes\bar{\boldsymbol{\varphi}}_{\mathrm{II}}]), \tag{E.1.7}$$

Collecting the contributions at $x = 0$, the trace matrix is:

$$\mathbf{T}^{-1} = \begin{bmatrix} 1 & \mathbf{0} & 0 & \mathbf{0} \\ \mathbf{0} & \mathbf{0} & \mathbf{i}\times\boldsymbol{\rho}_{\bar{\varphi}_{\mathrm{I}}} & \bar{\boldsymbol{\Xi}}_{\gamma} \\ 0 & \mathbf{0} & 1 & \bar{\boldsymbol{\rho}}_{\varkappa}^{\top} \\ \mathbf{0} & -\mathbf{i}^{\times} & \mathbf{0} & \mathbf{0} \end{bmatrix} \qquad \text{and} \qquad \mathbf{H}_T = \begin{bmatrix} 0 & \mathbf{0} & 0 & -\bar{\boldsymbol{\rho}}^{\top} \\ \mathbf{0} & \mathbf{0} & \mathbf{0} & \mathbf{0} \\ 0 & \mathbf{0} & 0 & 0 \\ \mathbf{0} & \mathbf{0} & \mathbf{0} & -\mathbf{i}^{\times} \end{bmatrix} \tag{E.1.8}$$

where $\bar{\boldsymbol{\varsigma}}_{\kappa} = \bar{\boldsymbol{\varsigma}}_{\epsilon} = \mathbf{0}$.

- (4.3.2b) requires $\mathbf{H}_T = \mathbf{T}^{-1}\mathbb{G}$, which in view of (4.3.8) is satisfied by (E.1.8)
- (4.3.3) requires $\mathbf{T}^{-1}$ exhibit the block form (4.3.7),

In view of (4.3.10):

$$
\begin{aligned}
\boldsymbol{\Xi}_\gamma &= \left(\bar{\Omega}\left[\widetilde{\boldsymbol{\Pi}}\right] - \bar{\boldsymbol{\rho}}^\times \bar{\Theta}\left[\widetilde{\boldsymbol{\Pi}}\right] + \mathbf{i} \times \bar{\Theta}\left[\mathbf{i} \otimes \bar{\boldsymbol{\varphi}}_{\mathrm{II}}\right] - (\mathbf{i} \times \boldsymbol{\rho}_{\bar{\varphi}_{\mathrm{I}}}) \otimes \boldsymbol{\rho}_\pi\right)^{-1} \\
\boldsymbol{\varsigma}_\gamma &= -\boldsymbol{\Xi}_\gamma \mathbf{i} \times \boldsymbol{\rho}_{\bar{\varphi}_{\mathrm{I}}} \\
\boldsymbol{\varsigma}_\varkappa &= -\boldsymbol{\Xi}_\gamma(\boldsymbol{\rho}_{\mathrm{II}} + \boldsymbol{\rho}_\pi) \\
\lambda_\varkappa &= 1 - (\boldsymbol{\rho}_{\mathrm{II}} + \boldsymbol{\rho}_\pi) \cdot \boldsymbol{\varsigma}_\gamma \\
\boldsymbol{\Xi}_\kappa &= -\mathbf{i}^\times(\boldsymbol{\rho}_{\bar{\varphi}_{\mathrm{I}}} \otimes \boldsymbol{\rho}_{\mathrm{II}} + \bar{\Theta}\left[\mathbf{i} \otimes \bar{\boldsymbol{\varphi}}_{\mathrm{II}}\right])\, \boldsymbol{\Xi}_\gamma && = \mathbf{0} \\
\boldsymbol{\varsigma}_\epsilon & && = \mathbf{0} \\
\boldsymbol{\varsigma}_\kappa &= -\boldsymbol{\Xi}_\kappa(\mathbf{i} \times \boldsymbol{\rho}_{\bar{\varphi}_{\mathrm{I}}}) && = \mathbf{0} \\
\mu_\epsilon &= \bar{\boldsymbol{\varsigma}}_\epsilon \cdot \boldsymbol{\Xi}_\gamma(\mathbf{i} \times \boldsymbol{\rho}_{\bar{\varphi}_{\mathrm{I}}}) && = 0
\end{aligned}
\tag{E.1.9}
$$

E.2 The Energy-Conjugate Trace

The energy-conjugate trace is defined by requiring that the beam strains $\boldsymbol{e} = (\epsilon, \boldsymbol{\gamma}_\perp, \varkappa, \boldsymbol{\kappa}_\perp)$ be work-conjugate to the stress resultants $\boldsymbol{s} = (N, \boldsymbol{F}, T, \boldsymbol{M})$ (4.3.26):

$$\delta \boldsymbol{e} \cdot \boldsymbol{s}_o = \int_\Omega \delta \boldsymbol{\varepsilon} \cdot \boldsymbol{\sigma} \, \mathrm{d}A$$

for all variations within the Saint-Venant class.

The energetic tangent $\bar{\mathbf{C}}_p$ is (using the prismatic character of Remark 4.3.4):

$$\bar{\mathbf{C}}_p := \int_\Omega \mathbf{S}_0^\top \mathbb{C} \, \mathbf{S}_0 \, \mathrm{d}A \tag{E.2.1}$$

where in view of (C.5.5):

$$\mathbf{S}_0(\boldsymbol{r}) = \begin{bmatrix} 1 & \boldsymbol{r}^\top & 0 & \mathbf{0}^\top \\ \mathbf{0} & \mathbf{0} & \mathbf{b}_{(\bar{\varphi}_{\mathrm{I}})}(\boldsymbol{r}) & \mathbf{b}_{(\bar{\varphi}_{\mathrm{I}})}(\boldsymbol{r}) \otimes \boldsymbol{\rho}_{\mathrm{II}} + \mathbf{B}_{(\psi)}(\boldsymbol{r}) \end{bmatrix}$$

with

$$\mathbf{b}_{(\bar{\varphi}_{\mathrm{I}})}(\boldsymbol{r}) := \mathbf{i} \times \boldsymbol{r} + \nabla \bar{\varphi}_{\mathrm{I}}(\boldsymbol{r}), \tag{E.2.2a}$$

$$\mathbf{B}_{(\psi)}(\boldsymbol{r}) := (\nabla \bar{\boldsymbol{\varphi}}_{\mathrm{II}})^\top + \widetilde{\boldsymbol{\Pi}}(\boldsymbol{r}). \tag{E.2.2b}$$

The strain energy (4.3.26) at x is quadratic in the evolved parameters $\exp(x\mathbb{G})\boldsymbol{p}$:

$$\mathcal{U}(x) = \frac{1}{2} \int_\Omega \boldsymbol{\varepsilon} \cdot \mathbb{C} \, \boldsymbol{\varepsilon} \, \mathrm{d}A = \frac{1}{2} \boldsymbol{p} \cdot (\mathbf{1} + x \mathbf{G}_{\mathcal{T}}^\top) \, \bar{\mathbf{C}}_p \, (\mathbf{1} + x \mathbf{A}_T) \, \boldsymbol{p},$$

where the energy matrix (E.2.1) becomes

$$\bar{\mathbf{C}}_p := \int_\Omega \mathbf{S}_0^\top \mathbb{C} \, \mathbf{S}_0 \, \mathrm{d}A = \begin{bmatrix} \widehat{EA} & \boldsymbol{c}_\varepsilon^\top & 0 & \mathbf{0} \\ & \widehat{E\boldsymbol{J}}_\kappa & \mathbf{0} & \mathbf{0} \\ & & \widehat{GJ}_\vartheta & (\widehat{GJ}_\vartheta \boldsymbol{\rho}_{\mathrm{II}} + G \mathbf{h}_{\bar{\varphi}_{\mathrm{I}}})^\top \\ \text{sym.} & & & G(\mathbf{H}_\psi + J_\varphi \boldsymbol{\rho}_{\mathrm{II}} \otimes \boldsymbol{\rho}_{\mathrm{II}} + \boldsymbol{\rho}_{\mathrm{II}} \otimes \mathbf{h}_{\bar{\varphi}_{\mathrm{I}}} + \mathbf{h}_{\bar{\varphi}_{\mathrm{I}}} \otimes \boldsymbol{\rho}_{\mathrm{II}}) \end{bmatrix} \tag{E.2.3}$$

and the following definitions have been introduced:

$$\mathbf{H}_\psi := \int_\Omega \mathbf{B}_{(b)}^\top \mathbf{B}_{(b)} \, \mathrm{d}A, \tag{E.2.4a}$$

$$\mathbf{h}_{\bar{\varphi}_{\mathrm{I}}} := \int_\Omega \mathbf{B}_{(b)}^\top \mathbf{b}_{(\varphi)} \, \mathrm{d}A \tag{E.2.4b}$$

The inverse of the energy matrix (E.2.3) is:

$$\bar{\mathbf{C}}_p^{-1} = \begin{bmatrix} (\widehat{EA})^{-1} + \bar{\boldsymbol{\rho}} \cdot (\widehat{E\boldsymbol{J}_\gamma})^{-1} \bar{\boldsymbol{\rho}} & & & \text{sym.} \\ -\bar{\boldsymbol{\rho}}^\top (\widehat{E\boldsymbol{J}_\gamma})^{-1} & (\widehat{E\boldsymbol{J}_\gamma})^{-1} & & \\ 0 & \mathbf{0} & (\widehat{GJ_\vartheta})^{-1} + \bar{\boldsymbol{\rho}}_\varkappa \cdot (G\tilde{\mathbf{H}}_{bb})^{-1} \bar{\boldsymbol{\rho}}_\varkappa & \\ \mathbf{0} & \mathbf{0} & -\bar{\boldsymbol{\rho}}_\varkappa^\top (G\tilde{\mathbf{H}}_{bb})^{-1} & (G\tilde{\mathbf{H}}_{bb})^{-1} \end{bmatrix}$$

with

$$\tilde{\mathbf{H}}_{bb} := \mathbf{H}_\psi - \frac{1}{J_\varphi} \mathbf{h}_{\bar{\varphi}_{\mathrm{I}}} \otimes \mathbf{h}_{\bar{\varphi}_{\mathrm{I}}}, \qquad \text{and} \qquad \bar{\boldsymbol{\rho}}_\varkappa := \frac{1}{J_\varphi} \left(J_\varphi \boldsymbol{\rho}_{\mathrm{II}} + \mathbf{h}_{\bar{\varphi}_{\mathrm{I}}} \right). \tag{E.2.5}$$

Using $\widehat{\mathbf{K}}_{\mathrm{p}}$ given by (4.2.9) in (4.3.38) furnishes the inverse trace matrix with the structure (4.3.9):

$$\mathbf{T} = \bar{\mathbf{C}}_p^{-1} \widehat{\mathbf{K}}_{\mathrm{p}}^\top = \left[\begin{array}{cc|cc} 1 & \mathbf{0} & 0 & \boldsymbol{\rho}_\epsilon \\ \mathbf{0} & \mathbf{0} & \mathbf{0} & \mathbf{i}^\times \\ \hline 0 & \boldsymbol{\varsigma}_\varkappa^\top & \lambda_\varkappa & \mathbf{0} \\ \mathbf{0} & \boldsymbol{\Xi}_\gamma & \boldsymbol{\varsigma}_\gamma & \mathbf{0} \end{array} \right]$$

where

$$\begin{aligned} \boldsymbol{\Xi}_\gamma &= (G\tilde{\mathbf{H}}_{bb})^{-1} (\widehat{E\boldsymbol{J}_\gamma})^\top \\ \boldsymbol{\Xi}_\kappa &= \mathbf{0}, \\ \bar{\boldsymbol{\rho}}_\varkappa &= \frac{1}{J_\varphi} (J_\varphi \boldsymbol{\rho}_{\mathrm{II}} + \mathbf{h}_{\bar{\varphi}_{\mathrm{I}}}) \\ \bar{\boldsymbol{\rho}}_\gamma &= \widehat{GJ}_\vartheta (\widehat{E\boldsymbol{J}_\gamma})^{-1} \bar{\boldsymbol{\rho}}_\varkappa \\ \boldsymbol{\varsigma}_\epsilon &= \mathbf{0}, \\ \boldsymbol{\rho}_\epsilon &= -\Big(1 + \boldsymbol{c}_\varepsilon \cdot (\widehat{E\boldsymbol{J}_\gamma})^{-1} \bar{\boldsymbol{\rho}} \Big) (\mathbf{i} \times \bar{\boldsymbol{\rho}}) + \mathbf{i} \times E\mathbf{J}_o \, (\widehat{E\boldsymbol{J}_\gamma})^{-1} \bar{\boldsymbol{\rho}} \\ \boldsymbol{\varsigma}_\kappa &= \mathbf{0}, \\ \hline \boldsymbol{\varsigma}_\varkappa &= -\boldsymbol{\Xi}_\gamma^\top \bar{\boldsymbol{\rho}}_\varkappa \\ \boldsymbol{\varsigma}_\gamma &= -(G\tilde{\mathbf{H}}_{bb})^{-1} \big(\widehat{GJ}_\vartheta \boldsymbol{\rho}_{\mathrm{II}} + G\mathbf{h}_{\bar{\varphi}_{\mathrm{I}}} \big) \\ \lambda_\varkappa &= 1 - \bar{\boldsymbol{\rho}}_\varkappa \cdot \boldsymbol{\varsigma}_\gamma \\ \mu_\epsilon &= 0 \end{aligned} \tag{E.2.6}$$

Appendix F

Finite Element Implementation

Several difficulties must be navigated in constructing a finite element interpolation of the beam equations, both in the exact form of Box 3.2 and its linearization in Box 3.3.

This chapter presents three finite element formulations that address these obstacles by alternative means. Section F.1 reviews the literature and Section F.2 sets up the geometrically exact equations in operator form. Section F.3 presents two Galerkin (displacement) formulations of the geometrically exact equations (Box 3.2) which employ different interpolation schemes for the finite rotation field. Section F.4 presents a mixed (force) formulation of the linearized equations.

F.1 Finite Element Obstacles and Common Remedies

Primary obstacles involved in discretizing beam models include complications arising from the interpolation of rotations, and avoiding "locking" in various modes. A comprehensive historical account of the linear shear-deformable beam element is provided by Felippa (2005). Meier et al. (2019) offers a comprehensive survey of the state of the art for geometrically exact finite elements.

F.1.1 Rotation Interpolation

The rotation field $\boldsymbol{\Lambda}$ does not admit a vectorial solution space, and consequently is not amenable to standard finite element interpolation schemes. This gives rise to several competing considerations in formulating an appropriate interpolation space:

Symmetric stiffness. A symmetric tangent stiffness can significantly speed up the linear solver for the iterative solution algorithm of the governing equations. There are two common sources for a non-symmetric consistent tangent stiffness: (i) the formulation neglects to account for a Levi-Civita connection on the configuration manifold, when such a connection exists, or (ii) the residual is represented on a different basis than the configuration increment. In the case of (i), symmetry is typically restored at equilibrium points, and a non-consistent symmetrized stiffness may not jeopardize the quadratic convergence of the solution algorithm. In the case of (ii), the lack of symmetry persists even at equilibrium points, and there is generally no way to employ a symmetric solver without jeopardizing quadratic convergence.

Natural parameters. When a configuration is modeled on a manifold, the nodal variables of the configuration may be very different from those of their increments. This can be difficult to implement in a conventional finite element platform, where current and incremental state variables are represented in vectors of the same size. Furthermore, this representation may be very different from that of the linearized theory, which may discourage practitioners or prevent the use of the element in a heterogeneous mesh.

Nonsingular parameters. Finite rotation parameterizations may introduce singularities in the parameter space. This is not a problem under moderate displacements. However, large displacement analyses require either a nonsingular representation or an incremental strategy that avoids singular configurations.

Path independence. Some rotation interpolation procedures give rise to path dependence in static problems that should behave elastically (Crisfield & Jelenić, 1999). The results of a simulation may then change simply by varying the step size with which loading is applied.

Strain objectivity. Simple interpolations on a manifold can violate the invariance of objective strain measures (Crisfield & Jelenić, 1999). This difficulty is separate from the accuracy of the interpolation itself, since an interpolation can approximate rotations well while still failing to preserve the objectivity of the strain measures.

Certain combinations of these properties are often mutually exclusive, such as path independence with nonsingular parameters, while others are difficult to achieve simultaneously, like strain invariance with a symmetric stiffness (Romero, 2004; Perez & Filippou, 2024). The principal approaches are summarized as follows.

Simo and Vu-Quoc (1986, 1991) developed computationally efficient and highly accurate formulations based on tangent interpolation of the rotation field. These formulations can exhibit minor violations of objectivity (Crisfield & Jelenić, 1999) and artificial path dependence. They also exhibit asymmetric stiffness away from equilibrium. In this setting, symmetry is typically restored at equilibrium points (Simo & Vu-Quoc, 1986), and it can often be shown that a non-consistent symmetrized stiffness does not jeopardize quadratic convergence (Nour-Omid & Rankin, 1991). Furthermore, formulations of this type may be difficult to realize in a conventionally structured finite element program.

An alternative interpolation was put forward by Cardona and Geradin (1988) and Ibrahimbegović et al. (1995), who reparameterized the model of Simo (1985) in logarithmic coordinates. This results in a linear configuration space with parameters resembling those of the linearized theory. The formulation is more involved, both computationally and in derivation, but fits more naturally within standard finite element architectures because the rotation parameters may be additively composed. This approach can remedy path dependence, but logarithmic reparameterizations generally introduce singularities in the parameter space. These singularities are not problematic under moderate displacements, but large displacement analyses require an incremental strategy to avoid them (Ibrahimbegovic, 1997). An alternative treatment of singularities is given by Mäkinen (2007). The approach of McAvoy (2025) employing Euler angles is similar.

In the formulation by Armero and Romero (2003), the directors comprising the rotation are interpolated directly. This approach does not exhibit the objectivity violations of the prior formulations, but fails to produce a truly orthogonal rotation tensor at the integration points. Related director interpolation procedures were developed by Gruttmann et al. (2000) and Klinkel and Govindjee (2003). In this formulation, orthogonality is effectively recovered through mesh refinement, but in coarse meshes accuracy may suffer. A similar procedure is commonly employed in shell elements (Rifai, 1993). This approach is not investigated further in the present work.

The procedure proposed by Crisfield and Jelenić (1999) and implemented by Jelenić and Crisfield (1999) and Eugster and Harsch (2023) uses interpolation along manifold geodesics to preserve strain objectivity. The complete element formulation of Jelenić and Crisfield (1999) employs a Petrov-Galerkin formulation, which produces simplified expressions for the element tangent, but forfeits the symmetry of the tangent stiffness (Romero, 2004). The lack of symmetry persists even at equilibrium configurations. As demonstrated in Perez and Filippou (2024), the spherical interpolation can instead be implemented in a Bubnov-Galerkin formulation as an independent procedure that wraps elements employing the tangent and logarithmic interpolations.

F.1.2 Rotation Elimination and Mixed Formulations

Formulations that interpolate the rotation field $\boldsymbol{\Lambda}$ tend to be highly accurate for large elastic deformations. However, pure Galerkin displacement formulations tend to exhibit shear locking when a full order quadrature rule is employed for integrals in x. The standard remedy is to employ uniformly reduced integration, but this approach requires h or p refinement (Zienkiewicz et al., 2025) to accurately represent inelasticity, particularly in flexure when inelastic response occurs at the ends of a member.

Mixed finite element formulations tend to be desirable when inelastic response must be represented and geometric nonlinearities are expected to be moderate (Neuenhofer & Filippou, 1997; F. Filippou & Fenves, 2004).

In the linearized setting of Box 3.3, a formulation against the Hu–Washizu functional permits kinematic interpolations to be omitted entirely (Taylor et al., 2003) in a variationally consistent manner. This recovers structure identical to the flexibility family of elements, which represent some of the earliest successful frame formulations for inelasticity (Kaba & Mahin, 1984; Spacone et al., 1992; Spacone et al., 1996). Elements employing a pure stress interpolation of the linear model in Box 3.3 have been successfully extended to model finite deformations using corotational methods. These formulations tend to improve by h-refinement when the response is predominantly flexural. However, they may converge to an incorrect solution for beams that are highly flexible in shear. Related corotational formulations based on a linear local geometry are discussed by de Souza (2000) and Le Corvec (2012).

Several mixed formulations have been proposed that attempt to reduce the need for h-refinement when modeling geometric nonlinearities. These are considered in two families. The first integrates curvatures to reconstruct displacement fields, and the second employs both force and displacement interpolations.

Moderate geometric nonlinearities ($P-\delta$) were considered without shear in two dimensions by Neuenhofer and Filippou (1998), who introduced the technique of *curvature-based displacement interpolation* (CBDI). This procedure was applied to the truncated two-dimensional equilibrium equations governing Euler buckling. It was later extended to the three-dimensional shear-free $P-\delta$ model by de Souza (2000), and shear deformations have been incorporated by Jafari et al. (2010).

Nukala and White (2004) present a mixed formulation for the geometrically exact beam under the Kirchhoff–Love hypothesis with one torsional warping field. This hypothesis permits the elimination of the rotation field in terms of the displacements, which are interpolated with C^1 Hermite polynomials. A related procedure was employed by Du and Hajjar (2021), who used governing equations with truncated kinematics that primarily retain terms related to flexural-torsional buckling.

F.2 Governing Equations in Operator Form

Recall the geometrically exact equilibrium equations (3.2.8) and strains (3.2.1)

$$\left\{\begin{aligned} (\boldsymbol{\Lambda}\boldsymbol{n})' + \boldsymbol{f}_{\mathrm{n}} &= \mathbf{0} \\ (\boldsymbol{\Lambda}\boldsymbol{m})' + \boldsymbol{x}' \times (\boldsymbol{\Lambda}\boldsymbol{n}) + \boldsymbol{f}_{\mathrm{m}} &= \mathbf{0} \\ \boldsymbol{w}' - \boldsymbol{v} + \boldsymbol{f}_{\mathrm{w}} &= \mathbf{0} \end{aligned}\right. \qquad \text{and} \qquad \begin{aligned} \boldsymbol{\gamma} &= \boldsymbol{\Lambda}^{\top}\boldsymbol{x}' - \mathbf{i} \\ \boldsymbol{\kappa} &= (\boldsymbol{\Lambda}^{\top}\boldsymbol{\Lambda}')^{\vee} \end{aligned}$$

Introduce the equilibrium operator $\mathbb{B}$ and its adjoint $\mathbb{B}^*$:

$$\mathbb{B} = -\begin{bmatrix} \mathbf{1}\,\partial_x & 0 & 0 & 0 \\ \boldsymbol{x}'^{\times} & \mathbf{1}\,\partial_x & 0 & 0 \\ 0 & 0 & \mathbf{1}\,\partial_x & -\mathbf{1} \end{bmatrix}, \qquad \mathbb{B}^* = \begin{bmatrix} \mathbf{1}\,\partial_x & \boldsymbol{x}'^{\times} & 0 \\ 0 & \mathbf{1}\,\partial_x & 0 \\ 0 & 0 & \mathbf{1}\,\partial_x \\ 0 & 0 & \mathbf{1} \end{bmatrix}.$$

The governing equations are then written as:

$$\mathbb{B}\boldsymbol{\Pi}_*\boldsymbol{s} = \boldsymbol{f}, \tag{F.2.1a}$$

$$\boldsymbol{\Pi}\mathbb{B}^*\boldsymbol{\mu} = D\boldsymbol{e}\cdot\boldsymbol{\mu} \tag{F.2.1b}$$

$$D\boldsymbol{s}\cdot\boldsymbol{\mu} = \boldsymbol{K}_s\, D\boldsymbol{e}\cdot\boldsymbol{\mu}. \tag{F.2.1c}$$

where $\boldsymbol{\mu}$ is an element of the configuration manifold tangent space,

$$\boldsymbol{e} := \begin{pmatrix} \boldsymbol{\gamma} \\ \boldsymbol{\kappa} \\ \boldsymbol{\alpha}' \\ \boldsymbol{\alpha} \end{pmatrix}, \quad \boldsymbol{s} := \begin{pmatrix} \boldsymbol{n} \\ \boldsymbol{m} \\ \boldsymbol{w} \\ \boldsymbol{v} \end{pmatrix}, \quad \text{and} \quad \boldsymbol{f} := \begin{pmatrix} \boldsymbol{f}_{\mathrm{n}} \\ \boldsymbol{f}_{\mathrm{m}} \\ \boldsymbol{f}_{\mathrm{w}} \end{pmatrix},$$

and

$$\boldsymbol{\Pi}_* = \boldsymbol{\Pi}^{\top} = \begin{bmatrix} \boldsymbol{\Lambda} & \mathbf{0} & \mathbf{0} \\ \mathbf{0} & \boldsymbol{\Lambda} & \mathbf{0} \\ \mathbf{0} & \mathbf{0} & \mathbf{1} \end{bmatrix} \tag{F.2.2}$$

so that

$$\langle \boldsymbol{\eta},\, \mathbb{B}\boldsymbol{\Pi}\boldsymbol{s}\rangle_{\chi} = \langle \mathbb{B}^*\boldsymbol{\Pi}\boldsymbol{\eta},\, \boldsymbol{s}\rangle_{\chi}. \qquad \forall \boldsymbol{s}, \boldsymbol{\eta} \tag{F.2.3}$$

F.3 Exact Displacement Formulations

F.3.1 Weighted Residuals

The Galerkin weighted residual for (F.2.1) is:

$$\mathcal{G}\,[\boldsymbol{\eta}] \triangleq \langle \boldsymbol{\eta},\, \boldsymbol{f}\rangle_{\chi} - \langle \boldsymbol{\eta},\, \mathbb{B}\boldsymbol{\Pi}_*\boldsymbol{s}\rangle_{\chi}. \tag{F.3.1}$$

In nonlinear finite element analysis, the solution algorithm searches for a configuration χ in the space $\mathcal{C}$ that satisfies the equilibrium relations in (3.2.8) by applying a sequence of small perturbations $\{\boldsymbol{\mu}^{(i)}\}$ to an initial guess $\chi^{(0)}$. Each perturbation $\boldsymbol{\mu}^{(i)}$ is determined by the linearization of (F.3.1) at the last trial configuration $\chi^{(i)}$ of the iterative process. At each iteration, the tangent space $T_{\chi^{(i)}}\mathcal{C}$ contains infinitely many modes for representing $\boldsymbol{\mu}^{(i)}$ in updating the configuration $\chi^{(i)}$. This section develops the general equations for the procedure of updating the trial configuration $\chi^{(i)}$ by first linearizing (F.3.1) in Section F.3.1 and then developing a finite-dimensional representation of the linearized residual in Section F.3.1.

Linearization

The linearization of the residual functional $\mathcal{G}$ (F.3.1) is given by:

$$\mathcal{L}\mathcal{G}\left[\boldsymbol{\eta}\right] = \mathcal{G}\left[\boldsymbol{\eta}\right] + \nabla_{\boldsymbol{\mu}}\mathcal{G}\left[\boldsymbol{\eta}\right], \tag{F.3.2}$$

where $\nabla_{\boldsymbol{\mu}}\mathcal{G}[\boldsymbol{\eta}]$ is the covariant derivative of the functional $\mathcal{G}$. This is given by the formula for the covariant differentiation of co-vectors (SIMO, 1992; ROMANO et al., 2005):

$$\nabla_{\boldsymbol{\mu}}\mathcal{G}\left[\boldsymbol{\eta}\right] = D\mathcal{G}\left[\boldsymbol{\eta}\right]\cdot\boldsymbol{\mu} - \mathcal{G}\left[\nabla_{\boldsymbol{\mu}}\boldsymbol{\eta}\right], \tag{F.3.3}$$

where $D\mathcal{G}\left[\boldsymbol{\eta}\right]\cdot\boldsymbol{\mu}$ is the Gâteaux differential of the residual component $\mathcal{G}\left[\boldsymbol{\eta}\right]$ in the direction $\boldsymbol{\mu}\in T_{\chi}\mathcal{C}$ and $\mathcal{G}\left[\nabla_{\boldsymbol{\mu}}\boldsymbol{\eta}\right]$ accounts for the nonlinearity of the configuration manifold.

Integrating (F.3.1) by parts furnishes:

$$\mathcal{G}[\boldsymbol{\eta}] = \langle\boldsymbol{\eta},\, \mathbb{B}\boldsymbol{\Pi}_*\boldsymbol{s}\rangle = \langle\boldsymbol{\Pi}\mathbb{B}^*\boldsymbol{\eta},\, \boldsymbol{s}\rangle\,. \tag{F.3.4}$$

Linearization proceeds with the application of the product rule to the last expression of (F.3.4):

$$\begin{aligned} D\mathcal{G}[\boldsymbol{\eta}]\cdot\boldsymbol{\mu} &= \left.\frac{\mathrm{d}}{\mathrm{d}\tau}\mathcal{G}_\tau[\boldsymbol{\eta}]\right|_{\tau=0} \\ &= \langle\boldsymbol{\Pi}\mathbb{B}^*\boldsymbol{\eta},\, D\boldsymbol{s}\cdot\boldsymbol{\mu}\rangle + \langle D[\boldsymbol{\Pi}\mathbb{B}^*\boldsymbol{\eta}]\cdot\boldsymbol{\mu},\, \boldsymbol{s}\rangle\,. \\ &\triangleq \mathcal{K}_M\left[\boldsymbol{\eta},\boldsymbol{\mu}\right] + \mathcal{K}_G\left[\boldsymbol{\eta},\boldsymbol{\mu}\right], \end{aligned} \tag{F.3.5}$$

where $\mathcal{K}_M$ and $\mathcal{K}_G$ are referred to as the *material* and *geometric* stiffness operators of the problem. Substitution (F.2.1c) and (F.2.1b) into (F.3.5) furnishes the final expression for the material stiffness $\mathcal{K}_M$ operator:

$$\mathcal{K}_M\left[\boldsymbol{\eta},\boldsymbol{\mu}\right] = \left\langle\boldsymbol{\Pi}^\top\mathbb{B}^*\boldsymbol{\eta},\, D\boldsymbol{s}\cdot\boldsymbol{\mu}\right\rangle = \langle\boldsymbol{\Pi}\mathbb{B}^*\boldsymbol{\eta},\, \boldsymbol{K}_s\,\boldsymbol{\Pi}\mathbb{B}^*\boldsymbol{\mu}\rangle \tag{F.3.6}$$

The geometric stiffness $\mathcal{K}_G$ is characterized by the directional derivative $D[\boldsymbol{\Pi}\mathbb{B}^*\boldsymbol{\eta}]\cdot\boldsymbol{\mu}$. Application of the product rule furnishes:

$$\mathcal{K}_G\left[\boldsymbol{\eta},\boldsymbol{\mu}\right] = \left\langle\partial_{\boldsymbol{\mu}}\left[\boldsymbol{\Pi}\right]\mathbb{B}^*\boldsymbol{\eta},\, \boldsymbol{s}\right\rangle + \left\langle\boldsymbol{\Pi}\partial_{\boldsymbol{\mu}}\left[\mathbb{B}^*\boldsymbol{\eta}\right],\, \boldsymbol{s}\right\rangle. \tag{F.3.7}$$

Discretization

Because (F.3.2) and (F.3.5) are linear in both $\boldsymbol{\eta}$ and $\boldsymbol{\mu}$, a discrete algebraic problem arises directly when the discretized vectors $\boldsymbol{\eta}^h$ and $\boldsymbol{\mu}^h$ are represented as a linear combination of *simple* basis functions that only depend on the coordinate $\boldsymbol{\xi}$. However, for problems formulated on manifolds, a simple interpolation is often inappropriate. Instead it is often desirable to apply a *configuration-dependent* interpolation, where $\boldsymbol{\eta}^h$ and $\boldsymbol{\mu}^h$ depend nonlinearly on the nodal values (CARDONA & GERADIN, 1988; SIMO et al., 1990; ROMERO, 2004).

Following the developments in PEREZ and FILIPPOU (2024), interpolation in the tangent space of the configuration manifold is represented by interpolation bases $\{\boldsymbol{\varphi}_{\eta a}\}$ and $\{\boldsymbol{\varphi}_{ub}\}$:

$$\boldsymbol{\varphi}_{\eta a}(\boldsymbol{\xi}) \triangleq \frac{\mathrm{d}}{\mathrm{d}\tau}\boldsymbol{\eta}^h(\boldsymbol{\xi};\tau\boldsymbol{\mu}_a)\Big|_{\tau=0} \qquad \text{and} \qquad \boldsymbol{\varphi}_{ub}(\boldsymbol{\xi}) \triangleq \frac{\mathrm{d}}{\mathrm{d}\tau}\boldsymbol{\mu}^h(\boldsymbol{\xi};\tau\boldsymbol{\mu}_b)\Big|_{\tau=0}. \tag{F.3.8}$$

Resisting forces. The evaluation of (F.3.1) on the linearized variation $\boldsymbol{\eta}^\ell$ furnishes a representation on the basis $\boldsymbol{\varphi}_{\eta a}$ which follows from the linearity of the inner product:

$$\mathcal{G}\left[\boldsymbol{\eta}^\ell\right] = \langle \boldsymbol{\eta}^h,\, \mathbb{B}\boldsymbol{\Pi}_*\boldsymbol{s}\rangle = \sum_a \left\langle \boldsymbol{\varphi}_{\eta a}\boldsymbol{\eta}_a,\, \mathbb{B}\boldsymbol{\Pi}_*\boldsymbol{s}\right\rangle. \tag{F.3.9}$$

Integration by parts is once again expressed by shifting from the operator $\mathbb{B}$ in the second argument to $\mathbb{B}^*$ in the first:

$$\begin{aligned}\mathcal{G}\left[\boldsymbol{\eta}^\ell\right] &= \sum_a \left\langle \mathbb{B}^*\left[\boldsymbol{\varphi}_{\eta a}\boldsymbol{\eta}_a\right],\, \boldsymbol{\sigma}\right\rangle \\ &= \sum_a \langle \boldsymbol{\eta}_a,\, \boldsymbol{B}_a\boldsymbol{\sigma}\rangle\,,\end{aligned} \qquad \text{with} \qquad \boldsymbol{B}_a^\top \triangleq \mathbb{B}^*\boldsymbol{\varphi}_{\eta a} \tag{F.3.10}$$

In an orthonormal basis $\{\mathbf{e}_k\}$ (F.3.10) is given by the resisting forces $\mathbf{p}_a$

$$\mathcal{G}\left[\boldsymbol{\eta}^\ell\right] = \sum_{a,k} \boldsymbol{\eta}_a\cdot\mathbf{e}_k\,\langle \mathbf{e}_k,\, \boldsymbol{B}_a\boldsymbol{\sigma}\rangle\,, = \sum_a \boldsymbol{\eta}_a\cdot\mathbf{p}_a \tag{F.3.11}$$

Tangent Stiffness. The material tangent $\mathcal{K}_M\left[\boldsymbol{\eta}^\ell, \boldsymbol{\mu}^\ell\right]$ depends on $\boldsymbol{\mu}^\ell$ via the operator $\mathbb{B}^*$. On account of linearity, the operation has the following representation:

$$\mathbb{B}^*\boldsymbol{\mu}^\ell = \sum_b \boldsymbol{B}_b^\star\boldsymbol{\mu}_b \qquad \text{with} \qquad \boldsymbol{B}_b^\star \triangleq \mathbb{B}^*\boldsymbol{\varphi}_{ub}. \tag{F.3.12}$$

Similarly, a discrete geometric operator $\boldsymbol{G}_{ab}[\boldsymbol{s}]$ is defined as the partial derivatives of the product $\boldsymbol{B}_a\boldsymbol{\Pi}_*\boldsymbol{s}$ with respect to the nodal parameters $\boldsymbol{\mu}_b$, with $\boldsymbol{s}$ held constant:

$$\boldsymbol{G}_{ab}[\boldsymbol{s}] = \partial_b[\boldsymbol{B}_a\boldsymbol{\Pi}_* \mid \boldsymbol{s}], \tag{F.3.13}$$

where the vertical bar indicates that the terms that follow are held constant under differentiation. In terms of $\boldsymbol{B}_a$, $\boldsymbol{B}_b^\star$, and $\boldsymbol{G}_{ab}$, the Galerkin differential $D\mathcal{G}\left[\boldsymbol{\mu}^\ell\right]\cdot\boldsymbol{\eta}^\ell$ of Equation (F.3.5) then has the representation:

$$\mathcal{K}_M\left[\boldsymbol{\eta}^\ell, \boldsymbol{\mu}^\ell\right] + \mathcal{K}_G\left[\boldsymbol{\eta}^\ell, \boldsymbol{\mu}^\ell\right] = \sum_{a,b} \boldsymbol{\eta}_a\cdot\mathbf{K}_{ab}\,\boldsymbol{\mu}_b, \tag{F.3.14}$$

where the nodal stiffness matrices $\{\mathbf{K}_{ab}\}$ are furnished by summation on i and j:

$$\mathbf{K}_{ab} \triangleq \left\langle \mathbf{e}_i,\, \boldsymbol{B}_a \boldsymbol{C}_\sigma \boldsymbol{B}_b^\star \mathbf{e}_j \right\rangle \mathbf{e}_i \otimes \mathbf{e}_j + \left\langle \mathbf{e}_i,\, \boldsymbol{G}_{ab}[\boldsymbol{s}]\mathbf{e}_j \right\rangle \mathbf{e}_i \otimes \mathbf{e}_j. \tag{F.3.15}$$

and

$$\boldsymbol{C}_\sigma := \boldsymbol{\Pi}_* \boldsymbol{K}_s \boldsymbol{\Pi}$$

The discrete geometric operator $\boldsymbol{G}_{ab}[\boldsymbol{s}]$ is formed in two parts by application of the product rule:

$$\boldsymbol{G}_{ab}[\boldsymbol{s}] = \boldsymbol{G}_\Sigma + \boldsymbol{G}_\Pi \tag{F.3.16}$$

with

$$\boldsymbol{G}_\Pi := \boldsymbol{B}_a\, \partial_{\boldsymbol{\mu}}[\boldsymbol{\Pi}_* \mid \boldsymbol{s}] \boldsymbol{\varphi}_{ub} \qquad \text{and} \qquad \boldsymbol{G}_\Sigma := \partial_b[\boldsymbol{B}_a \mid \boldsymbol{\Pi}_* \boldsymbol{s}]$$

The derivative $\partial_{\boldsymbol{\mu}}[\boldsymbol{\Pi}_* \mid \boldsymbol{s}]$ follows immediately from (G.2.14):

$$\partial_{\boldsymbol{\mu}}[\boldsymbol{\Pi}_* \mid \boldsymbol{s}] = \begin{bmatrix} \mathbf{0} & -\bar{\boldsymbol{n}}^\times & \mathbf{0} & \mathbf{0} \\ \mathbf{0} & -\bar{\boldsymbol{m}}^\times & \mathbf{0} & \mathbf{0} \\ \mathbf{0} & \mathbf{0} & \mathbf{0} & \mathbf{0} \end{bmatrix}.$$

F.3.2 Rotation Interpolation

Tangent Interpolation

In a tangent rotation interpolation, both $\boldsymbol{\eta}^h$ and $\boldsymbol{\mu}^h$ are interpolated with standard Lagrange polynomials ϕ_a so that the basis operators $\boldsymbol{\varphi}_{ub}$ and $\boldsymbol{\varphi}_{\eta a}$ are given by:

$$\boldsymbol{\varphi}_{ub} = \begin{bmatrix} \phi_b \mathbf{1} & \mathbf{0} & \mathbf{0} \\ \mathbf{0} & \phi_b \mathbf{1} & \mathbf{0} \\ \mathbf{0} & \mathbf{0} & \phi_b \mathbf{1} \end{bmatrix} \qquad \text{and} \qquad \boldsymbol{\varphi}_{\eta a} = \begin{bmatrix} \phi_a \mathbf{1} & \mathbf{0} & \mathbf{0} \\ \mathbf{0} & \phi_a \mathbf{1} & \mathbf{0} \\ \mathbf{0} & \mathbf{0} & \phi_a \mathbf{1} \end{bmatrix}.$$

Then using $\boldsymbol{B}_a^\top = \mathbb{B}^*[\boldsymbol{\varphi}_{\eta a}]$

$$\boldsymbol{B}_a = \begin{bmatrix} \phi_a' \mathbf{1} & \mathbf{0} & \mathbf{0} & \mathbf{0} \\ -\phi_a \boldsymbol{x}'^\times & \phi_a' \mathbf{1} & \mathbf{0} & \mathbf{0} \\ \mathbf{0} & \mathbf{0} & \phi_a' \mathbf{1} & \phi_a \mathbf{1} \end{bmatrix} \tag{F.3.17}$$

First term of Equation (F.3.16):

$$\boldsymbol{G}_\Pi = \begin{bmatrix} \mathbf{0} & -\phi_a' \bar{\boldsymbol{n}}^\times \phi_b & \mathbf{0} \\ \mathbf{0} & \phi_a [\boldsymbol{x}'^\times][\bar{\boldsymbol{n}}^\times]\phi_b - \phi_a' \bar{\boldsymbol{m}}^\times \phi_b & \mathbf{0} \\ \mathbf{0} & \mathbf{0} & \mathbf{0} \end{bmatrix}$$

Second term of Equation (F.3.16):

$$
\boldsymbol{G}_\Sigma = \begin{bmatrix} \mathbf{0} & \mathbf{0} & \mathbf{0} \\ \phi_a \bar{\boldsymbol{n}}^\times \phi_b' & \mathbf{0} & \mathbf{0} \\ \mathbf{0} & \mathbf{0} & \mathbf{0} \end{bmatrix} \tag{F.3.18}
$$

Logarithmic Interpolation

In the formulation by IBRAHIMBEGOVIĆ et al. (1995) the logarithm on SO(3) in Algorithm 4 gives the transformed fields $\bar{\boldsymbol{\eta}}^h$ and $\bar{\boldsymbol{\mu}}^h$ which are interpolated by the Lagrange polynomials ϕ_a giving simple basis operators $\bar{\boldsymbol{\varphi}}_{\eta a}$ and $\bar{\boldsymbol{\varphi}}_{ub}$ in the transformed space:

$$
\bar{\boldsymbol{\varphi}}_{\eta a} = \begin{bmatrix} \phi_a \mathbf{1} & \mathbf{0} & \mathbf{0} \\ \mathbf{0} & \phi_a \mathbf{1} & \mathbf{0} \\ \mathbf{0} & \mathbf{0} & \phi_b \mathbf{1} \end{bmatrix} \qquad \text{and} \qquad \bar{\boldsymbol{\varphi}}_{ub} = \begin{bmatrix} \phi_b \mathbf{1} & \mathbf{0} & \mathbf{0} \\ \mathbf{0} & \phi_b \mathbf{1} & \mathbf{0} \\ \mathbf{0} & \mathbf{0} & \phi_b \mathbf{1} \end{bmatrix}. \tag{F.3.19}
$$

The transformation map g and the pull-back g^* are:

$$
g : (\boldsymbol{x}, \boldsymbol{\Lambda}) \mapsto (\boldsymbol{x}, \operatorname{Log} \boldsymbol{\Lambda}) \qquad \text{and} \qquad g^*(\boldsymbol{\xi}) = \begin{bmatrix} \mathbf{1} & \mathbf{0} \\ \mathbf{0} & \mathrm{d}_{\mathrm{R}}\mathrm{Exp}\, \boldsymbol{\theta}^h \end{bmatrix}.
$$

where Log and $\mathrm{d}_{\mathrm{R}}\mathrm{Exp}$ are functions given by Algorithm 4 and (G.2.7), respectively. The effective interpolations are:

$$
\boldsymbol{\varphi}_{\eta a} = g^* \bar{\boldsymbol{\varphi}}_a = \begin{bmatrix} \phi_a \mathbf{1} & \mathbf{0} \\ \mathbf{0} & \phi_a \, \mathrm{d}_{\mathrm{R}}\mathrm{Exp}\, \boldsymbol{\theta}^h \end{bmatrix} \qquad \text{and} \qquad \boldsymbol{\varphi}_{ub} = g^* \bar{\boldsymbol{\varphi}}_{ub} = \begin{bmatrix} \phi_b \mathbf{1} & \mathbf{0} \\ \mathbf{0} & \phi_b \, \mathrm{d}_{\mathrm{R}}\mathrm{Exp}\, \boldsymbol{\theta}^h \end{bmatrix}.
$$

The discrete equilibrium operator $\boldsymbol{B}_a^\top \triangleq \mathbb{B}^* \boldsymbol{\varphi}_{\eta a}$ is furnished by

$$
\boldsymbol{B}_a^\top = \begin{bmatrix} \phi_a' \mathbf{1} & \phi_a \boldsymbol{x}'^\times \boldsymbol{T}_{\mathrm{R}} & \mathbf{0} & \mathbf{0} \\ \mathbf{0} & (\phi_a \boldsymbol{T}_{\mathrm{R}})' & \mathbf{0} & \mathbf{0} \\ \mathbf{0} & \mathbf{0} & \phi_a' \mathbf{1} & \\ \mathbf{0} & \mathbf{0} & \phi_a \mathbf{1} & \end{bmatrix}
$$

where the shorthand for exponential differentials is employed:

$$
\boldsymbol{T}_{\mathrm{R}} \triangleq \mathrm{d}_{\mathrm{R}}\mathrm{Exp}\, \boldsymbol{\theta}^h(x) \qquad \text{and} \qquad \boldsymbol{T}_{\mathrm{L}} \triangleq \mathrm{d}_{\mathrm{L}}\mathrm{Exp}\, \boldsymbol{\theta}^h(x).
$$

Taking the derivative $(\phi_a \boldsymbol{T}_{\mathrm{R}})'$ and transposing then furnishes:

$$
\boldsymbol{B}_a = \begin{bmatrix} \phi_a' \mathbf{1} & \mathbf{0} & \mathbf{0} & \mathbf{0} \\ -\phi_a \boldsymbol{T}_{\mathrm{L}} \boldsymbol{x}'^\times & \phi_a' \boldsymbol{T}_{\mathrm{L}} + \phi_a \boldsymbol{T}_{\mathrm{L}}' & \mathbf{0} & \mathbf{0} \\ \mathbf{0} & \mathbf{0} & \phi_a' \mathbf{1} & \phi_a \mathbf{1} \end{bmatrix}. \tag{F.3.20}
$$

The first term of (F.3.16) is:

$$\boldsymbol{G}_{\Pi} = \begin{bmatrix} \mathbf{0} & -\phi'_a \bar{\boldsymbol{n}}^{\times} \boldsymbol{T}_{R} \phi_b & \mathbf{0} \\ \mathbf{0} & \phi_a (\boldsymbol{T}_{L} \boldsymbol{x}'^{\times} \bar{\boldsymbol{n}}^{\times} \boldsymbol{T}_{R} - \boldsymbol{T}'_{L} \bar{\boldsymbol{m}}^{\times} \boldsymbol{T}_{R}) \phi_b - \phi'_a \boldsymbol{T}_{L} \bar{\boldsymbol{m}}^{\times} \boldsymbol{T}_{R} \phi_b & \mathbf{0} \\ \mathbf{0} & \mathbf{0} & \mathbf{0} \end{bmatrix}$$

The second term of (F.3.16) is:

$$\boldsymbol{G}_{\Sigma} = \begin{bmatrix} \mathbf{0} & \mathbf{0} & \mathbf{0} \\ \phi_a \partial_{bx} [\boldsymbol{T}_{L} \mid \bar{\boldsymbol{n}}^{\times}] & \phi_a \, \partial_{b\Lambda} [\boldsymbol{T}_{L} \bar{\boldsymbol{n}} \times \boldsymbol{x}'] + \phi'_a \partial_{b\Lambda} [\boldsymbol{T}_{L} \mid \bar{\boldsymbol{m}}] + \phi_a \partial_{b\Lambda} [\boldsymbol{T}'_{L} \mid \bar{\boldsymbol{m}}] & \mathbf{0} \\ \mathbf{0} & \mathbf{0} & \mathbf{0} \end{bmatrix}$$

where ∂_{bx} and $\partial_{b\Lambda}$ denote partial derivatives with respect to the translational $\boldsymbol{\mu}_{bx}$ and rotational $\boldsymbol{\mu}_{b\Lambda}$ nodal parameters, respectively, and:

$$\begin{aligned} \partial_{bx} [\boldsymbol{T}_{L} \mid \bar{\boldsymbol{n}}^{\times}] &= \mathrm{d}_{\mathrm{L}} \mathrm{Exp}_{\boldsymbol{\theta}} \, \bar{\boldsymbol{n}}^{\times} \phi'_b \\ \partial_{b\Lambda} [\boldsymbol{T}_{L} \, \bar{\boldsymbol{n}} \times \boldsymbol{x}'] &= \mathrm{d}^2_{\mathrm{L}} \mathrm{Exp} \, (\boldsymbol{\theta}; \, \bar{\boldsymbol{n}} \times \boldsymbol{x}') \, \phi_b \\ \partial_{b\Lambda} \, [\boldsymbol{T}_{L} \mid \bar{\boldsymbol{m}}] &= \mathrm{d}^2_{\mathrm{L}} \mathrm{Exp} \, (\boldsymbol{\theta}; \, \bar{\boldsymbol{m}}) \, \phi_b \end{aligned}$$

$$\partial_{b\Lambda} \, [\boldsymbol{T}'_{L} \mid \bar{\boldsymbol{m}}] = \mathrm{d}^2_{\mathrm{R}} \mathrm{Exp}(\boldsymbol{\theta}; \, \boldsymbol{m})^{\top} \phi'_b + \mathrm{d}^3_{\mathrm{L}} \mathrm{Exp}(\boldsymbol{\theta}; \boldsymbol{\theta}', \boldsymbol{m}) \phi_b + \mathrm{d}^2_{\mathrm{L}} \mathrm{Exp}(\boldsymbol{\theta}; \boldsymbol{\theta}')^{\top} \boldsymbol{\Lambda}^{\top} [\bar{\boldsymbol{m}}^{\times}] \boldsymbol{T}_{R} \phi_b$$

Expressions for the functions $\mathrm{d}^{\mathrm{i}}_{\mathrm{j}} \mathrm{Exp} \, \boldsymbol{\theta}$ are given by:

$$\begin{array}{ll} \mathrm{d}_{\mathrm{L}} \mathrm{Exp} \, \boldsymbol{\theta} & \text{(G.2.8)} \\ \mathrm{d}^2_{\mathrm{R}} \mathrm{Exp}(\boldsymbol{\theta}; \, \boldsymbol{p}) & \text{(G.2.9)} \\ \mathrm{d}^2_{\mathrm{L}} \mathrm{Exp}(\boldsymbol{\theta}; \boldsymbol{p}) & \text{(G.2.10)} \\ \mathrm{d}^3_{\mathrm{R}} \mathrm{Exp} \, (\boldsymbol{\theta}; \boldsymbol{p}, \boldsymbol{q}) & \text{(G.2.11)} \end{array}$$

These expressions are obtained using the following identities:

$$\begin{gathered} \boldsymbol{T}_{R} = \boldsymbol{T}_{L}^{\top} \\ \boldsymbol{T}_{R} = \boldsymbol{\Lambda} \boldsymbol{T}_{L} \\ \mathrm{Exp} \, \boldsymbol{\theta} = \mathbf{1} + \boldsymbol{\theta}^{\times} \boldsymbol{T}_{R} \end{gathered}$$

and:

$$\begin{aligned} \boldsymbol{T}'_{R} &= \mathrm{d}^2_{\mathrm{L}} \mathrm{Exp}(\boldsymbol{\theta}; \, \boldsymbol{\theta}') + (\boldsymbol{T}_{R} \boldsymbol{\theta}')^{\times} \, \boldsymbol{T}_{R} \\ &= \mathrm{Exp} \, \boldsymbol{\theta} \; \mathrm{d}^2_{\mathrm{L}} \mathrm{Exp}(\boldsymbol{\theta}; \boldsymbol{\theta}') \end{aligned} \qquad \text{and} \qquad \begin{aligned} \boldsymbol{T}'_{L} &= \mathrm{d}^2_{\mathrm{R}} \mathrm{Exp} \, (\boldsymbol{\theta}; \, \boldsymbol{\theta}')^{\top} - \boldsymbol{T}_{L}^{\top} \, (\boldsymbol{T}_{L} \boldsymbol{\theta}')^{\times} \\ &= \mathrm{d}^2_{\mathrm{L}} \mathrm{Exp} \, (\boldsymbol{\theta}; \, \boldsymbol{\theta}')^{\top} \, \mathrm{Exp}(\boldsymbol{\theta})^{\top} \end{aligned}$$

F.4 Linearized Mixed Formulation

F.4.1 Weighted Residuals

Recall the linear equilibrium equations (Box 3.3):

$$
\begin{aligned}
\boldsymbol{n}' &= \mathbf{0} \\
\boldsymbol{m}' + \mathbf{i} \times \boldsymbol{n} &= \mathbf{0} \\
\boldsymbol{w}' - \boldsymbol{v} &= \mathbf{0}
\end{aligned}
\tag{F.4.1}
$$

Equation (F.4.1) is written compactly as

$$
\mathbb{B}\boldsymbol{s} - \boldsymbol{f} = \mathbf{0}, \qquad \boldsymbol{e} = \mathbb{B}^* \boldsymbol{\chi}, \tag{F.4.2}
$$

where $\boldsymbol{\chi}(x) = (\boldsymbol{u},\, \boldsymbol{\theta},\, \boldsymbol{\alpha})$ collects the kinematic fields, $\boldsymbol{f}(x)$ collects the distributed element loading, and the adjoint equilibrium and strain differential operators are

$$
\mathbb{B} = -\begin{bmatrix} \mathbf{1}\,\partial_x & 0 & 0 & 0 \\ \mathbf{i}^\times & \mathbf{1}\,\partial_x & 0 & 0 \\ 0 & 0 & \mathbf{1}\,\partial_x & -\mathbf{1} \end{bmatrix}, \qquad \mathbb{B}^* = \left[\begin{array}{cc|c} \mathbf{1}\,\partial_x & \mathbf{i}^\times & 0 \\ 0 & \mathbf{1}\,\partial_x & 0 \\ \hline 0 & 0 & \mathbf{1}\,\partial_x \\ 0 & 0 & \mathbf{1} \end{array}\right].
$$

The Hu–Washizu weighted residual is (Lee & Filippou, 2009)

$$
\delta\Pi_{\mathrm{HW}} := \langle \delta\boldsymbol{e},\; \boldsymbol{s} - \boldsymbol{s}(\boldsymbol{e}) \rangle + \langle \delta\boldsymbol{s},\; \mathbb{B}^*\boldsymbol{\chi} - \boldsymbol{e} \rangle + \langle \delta\boldsymbol{\chi},\; \mathbb{B}\boldsymbol{s} - \boldsymbol{f} \rangle = 0. \tag{F.4.3}
$$

The interpolation of the resultants $\boldsymbol{s}$ is:

$$
\boldsymbol{s}_h(x) := \boldsymbol{B}_s(x)\,\mathbf{q} + \boldsymbol{s}_{\mathrm{p}}(x), \qquad \delta\boldsymbol{s}_h(x) = \boldsymbol{B}_s(x)\,\delta\mathbf{q}, \tag{F.4.4}
$$

with

$$
\mathbb{B}\left(\boldsymbol{B}_s(x)\,\mathbf{q}\right) = \mathbf{0}, \qquad \mathbb{B}\boldsymbol{s}_{\mathrm{p}}(x) - \boldsymbol{f}(x) = \mathbf{0}. \tag{F.4.5}
$$

Substituting (F.4.4) into (F.4.3) eliminates the last term identically and yields

$$
\delta\Pi_{\mathrm{HW}} = \langle \delta\boldsymbol{e},\; \boldsymbol{s}_h - \boldsymbol{s}(\boldsymbol{e}) \rangle + \langle \boldsymbol{B}_s\,\delta\mathbf{q},\; \mathbb{B}^*\boldsymbol{\chi} - \boldsymbol{e} \rangle = 0. \tag{F.4.6}
$$

By adjointness of $\mathbb{B}$ and $\mathbb{B}^*$, integration by parts furnishes:

$$
\langle \delta\boldsymbol{s},\; \mathbb{B}^*\boldsymbol{\chi} \rangle = \langle \delta\boldsymbol{s},\; \mathbf{u} \rangle_{\partial e} - \langle \mathbb{B}\,\delta\boldsymbol{s},\; \boldsymbol{\chi} \rangle. \tag{F.4.7}
$$

where $\mathbf{u}$ evaluates $\boldsymbol{\chi}$ on the boundary $\{0,\, L\}$. For $\delta\boldsymbol{s} = \boldsymbol{B}_s\,\delta\mathbf{q}$, the second term vanishes in view of (F.4.5). Hence

$$
\langle \boldsymbol{B}_s\,\delta\mathbf{q},\; \mathbb{B}^*\boldsymbol{\chi} \rangle = \langle \boldsymbol{B}_s\,\delta\mathbf{q},\; \mathbf{u} \rangle_{\partial e}. \tag{F.4.8}
$$

This boundary residual defines the conjugate deformation vector $\mathbf{v}$ through a matrix $\mathbf{A}$:

$$\delta\mathbf{q} \cdot (\mathbf{A}\,\mathbf{u}) := \langle \boldsymbol{B}_s\,\delta\mathbf{q},\ \mathbf{u}\rangle_{\partial e} \qquad \forall\,\delta\mathbf{q}, \tag{F.4.9}$$

Define

$$\mathbf{v} := \mathbf{A}\,\mathbf{u}. \tag{F.4.10}$$

where if $\mathbb{B}^*\boldsymbol{\chi} = \mathbf{0}$, then $\mathbf{v} = \mathbf{0}$. Using (F.4.8)–(F.4.10) in (F.4.6) gives

$$\delta\Pi_{HW} = \delta\mathbf{q} \cdot \left[\mathbf{v} - \int_0^L \boldsymbol{B}_s^\top(x)\,\boldsymbol{e}(x)\,\mathrm{d}x\right] + \langle \delta\boldsymbol{e},\ \boldsymbol{s}_h - \boldsymbol{s}(\boldsymbol{e})\rangle = 0. \tag{F.4.11}$$

Because $\delta\mathbf{q}$ and $\delta\boldsymbol{e}$ are independent, stationarity of (F.4.11) yields the residual equations:

$$\mathbf{v} - \int_0^L \boldsymbol{B}_s^\top(x)\,\boldsymbol{e}(x)\,\mathrm{d}x = \mathbf{0}, \tag{F.4.12a}$$

$$\boldsymbol{s}_h(\mathbf{q}; x) - \boldsymbol{s}(\boldsymbol{e}(x)) = \mathbf{0}, \qquad x \in [0, L]. \tag{F.4.12b}$$

F.4.2 State Determination

The state determination requires solving $n_q + n_{\mathrm{IP}} n_s$ nonlinear equations comprising the compatibility residual $\boldsymbol{g}_{\mathrm{v}}$ and n_{IP} point-wise equilibrium residuals $\boldsymbol{g}_{\mathrm{s}}$:

$$\boldsymbol{g}_{\mathrm{v}}[\boldsymbol{e}] := \mathbf{v} - \int_0^L \boldsymbol{B}_s^\top(x)\,\boldsymbol{e}(x)\,\mathrm{d}x = \mathbf{0} \qquad (n_q \text{ equations}) \tag{F.4.13a}$$

$$\boldsymbol{g}_{\mathrm{s}}(\mathbf{q}, \boldsymbol{e};\, x_\ell) := \boldsymbol{s}_h(\mathbf{q};\, x) - \boldsymbol{s}(\boldsymbol{e}(x_\ell)) = \mathbf{0} \qquad (n_s \text{ equations for each } x_\ell) \tag{F.4.13b}$$

for the basic forces $\mathbf{q} \in \mathbb{R}^{n_q}$ and section deformations $\boldsymbol{e}_\ell \in \mathbb{R}^{n_s}$ at each integration point x_ℓ.

An efficient algorithm for solving (F.4.13) was put forth by Taylor et al. (2003). This is generalized in the following section to support the consistent handling of element loading under nonlinear geometry. The developments are summarized in Box F.1.

F.4.3 Newton Linearization and Schur Complement

Each Newton step seeks $(\mathrm{d}\mathbf{q}, \mathrm{d}\boldsymbol{e})$ such that

$$\boldsymbol{g}_{\mathrm{v}}[\boldsymbol{e} + \mathrm{d}\boldsymbol{e}] \approx 0, \qquad \boldsymbol{g}_{\mathrm{s}}(x_\ell; \mathbf{q} + \mathrm{d}\mathbf{q},\, \boldsymbol{e} + \mathrm{d}\boldsymbol{e}) \approx 0.$$

Linearizing (F.4.13a) furnishes:

$$\boldsymbol{g}_{\mathrm{v}}[\boldsymbol{e}+\mathrm{d}\boldsymbol{e}] = \boldsymbol{g}_{\mathrm{v}}[\boldsymbol{e}] - \int_0^L \boldsymbol{B}_s^\top \,\mathrm{d}\boldsymbol{e}\,\mathrm{d}x.$$

Setting $\boldsymbol{g}_{\mathrm{v}}[\boldsymbol{e}+\mathrm{d}\boldsymbol{e}] = \mathbf{0}$ gives

$$\int_0^L \boldsymbol{B}_s^\top \,\mathrm{d}\boldsymbol{e}\,\mathrm{d}x = \boldsymbol{g}_{\mathrm{v}}[\boldsymbol{e}]. \tag{F.4.14}$$

Linearizing (F.4.13b) furnishes:

$$\boldsymbol{g}_{\mathrm{s}}(x; q+\mathrm{d}\mathbf{q}, e+\mathrm{d}\boldsymbol{e}) \approx \boldsymbol{g}_{\mathrm{s}}(x; q, e) + \boldsymbol{B}_s(x)\mathrm{d}\mathbf{q} - \boldsymbol{K}_s(x)\mathrm{d}\boldsymbol{e}(x)$$

where

$$\boldsymbol{K}_s(x) := \frac{\partial s}{\partial e}(x), \qquad \boldsymbol{F}_s(x) := \boldsymbol{K}_s^{-1}(x). \tag{F.4.15}$$

Setting the linearization to zero:

$$\boldsymbol{B}_s(x)\mathrm{d}\mathbf{q} - \boldsymbol{K}_s(x)\mathrm{d}\boldsymbol{e}(x) = -\boldsymbol{g}_{\mathrm{s}}(x; \mathbf{q}, \boldsymbol{e}). \tag{F.4.16}$$

Solve for $\mathrm{d}\boldsymbol{e}(x)$:

$$\mathrm{d}\boldsymbol{e}(x) = \boldsymbol{F}_s(x)\,\boldsymbol{B}_s(x)\,\mathrm{d}\mathbf{q} \;+\; \boldsymbol{F}_s(x)\,\boldsymbol{g}_{\mathrm{s}}(x; q, e). \tag{F.4.17}$$

Now substitute (F.4.17) into (F.4.14):

$$\int_0^L \boldsymbol{B}_s^\top \boldsymbol{F}_s \boldsymbol{B}_s \,\mathrm{d}x\;\mathrm{d}\mathbf{q} \;+\; \int_0^L \boldsymbol{B}_s^\top \boldsymbol{F}_s \boldsymbol{g}_{\mathrm{s}}\,\mathrm{d}x \;=\; \boldsymbol{g}_{\mathrm{v}}[\boldsymbol{e}].$$

Define

$$\mathbf{F}_q := \int_0^L \boldsymbol{B}_s^\top \boldsymbol{F}_s \boldsymbol{B}_s\,\mathrm{d}x, \qquad \tilde{\boldsymbol{g}}_{\mathrm{v}} := \boldsymbol{g}_{\mathrm{v}} - \int_0^L \boldsymbol{B}_s^\top \boldsymbol{F}_s \boldsymbol{g}_{\mathrm{s}}\,\mathrm{d}x \tag{F.4.18}$$

Then the staggered Newton step is

$$\mathbf{F}_q\,\mathrm{d}\mathbf{q} = \tilde{\boldsymbol{g}}_{\mathrm{v}} \tag{F.4.19}$$

The basic forces $\mathbf{q}$ are updated by scaling the Newton step furnished by (F.4.19):

$$\mathbf{q} \leftarrow \mathbf{q} + \eta\,\mathrm{d}\mathbf{q} \tag{F.4.20}$$

where η is determined by a line search algorithm. A backtracking line search is performed with

$$\phi(\eta) = \|\boldsymbol{g}_{\mathrm{v}}\| \tag{F.4.21}$$

Box F.1: State Determination of the MF$_n$ Element

Given target deformations $\mathbf{v}$, find $\mathbf{q}$:

1. Initialize $\mathrm{d}\mathbf{q} = \mathbf{0}$.
2. Perform **Update B**.
3. While $\|\boldsymbol{g}_\mathrm{v}\| > \epsilon$ repeat **Update A**.
4. Compute $\mathbf{K}_u$.

where:

- **Update A.** Given $\boldsymbol{g}_\mathrm{v}$, update basic forces $\mathbf{q}$
  1. Set $\mathrm{d}\tilde{\mathbf{q}} = -\mathbf{F}_q^{-1}\tilde{\boldsymbol{g}}_\mathrm{v}$ and $\eta = 1$.
  2. Line search: While $\phi(\eta) > \epsilon$:
     (a) Perform **Update B** with $\mathrm{d}\mathbf{q} = \eta\,\mathrm{d}\tilde{\mathbf{q}}$ and evaluate $\phi(\eta) = \|\boldsymbol{g}_\mathrm{v}\|$.
     (b) Update $\eta \leftarrow \frac{1}{2}\eta$.
  3. Update $\mathbf{q} \leftarrow \eta\,\mathrm{d}\tilde{\mathbf{q}}$.
- **Update B.** Given $\mathbf{v}$, $\mathrm{d}\mathbf{q}$ and a state $\{\mathbf{q}, \boldsymbol{e}_\ell\}$, advance $\boldsymbol{e}$ and compute $\tilde{\boldsymbol{g}}_\mathrm{v}$, $\{\boldsymbol{g}_\mathrm{s}\}$ and $\mathbf{F}_q$.
  1. Section deformation update: $\boldsymbol{e} \leftarrow \boldsymbol{e} + \mathrm{d}\boldsymbol{e}$ with $\mathrm{d}\boldsymbol{e} = \mathbf{K}_s^{-1}(\boldsymbol{B}_s\mathrm{d}\mathbf{q})$
  2. Perform section state determination (Box 3.4), get resultants $\boldsymbol{s}_e$
  3. Interpolate unbalanced forces $\boldsymbol{g}_\mathrm{s} = \boldsymbol{B}_s\mathbf{q} + \boldsymbol{s}_p - \boldsymbol{s}_e$
  4. Apply second deformation correction: $\boldsymbol{e} \leftarrow \boldsymbol{e} + \mathbf{K}_s^{-1}\boldsymbol{g}_\mathrm{s}$
  5. Integrate compatibility residual (F.4.18): $\tilde{\boldsymbol{g}}_\mathrm{v} = -\mathbf{v} + \int \boldsymbol{B}_s^\top \boldsymbol{e}\,\mathrm{d}x$

and:

Symbol	Equation	Description
$\boldsymbol{g}_\mathrm{v}$	(F.4.13a)	Compatibility residual
$\boldsymbol{g}_\mathrm{s}$	(F.4.13b)	Equilibrium residual
$\boldsymbol{s}_h$	(F.4.4)	Interpolated section forces
$\tilde{\boldsymbol{g}}_\mathrm{v}$	(F.4.18)	Staggered compatibility residual
$\mathbf{K}_\mathrm{s}$	(F.4.15)	Section stiffness.
$\mathbf{F}_\mathrm{s}$	(F.4.15)	Section flexibility.
$\mathbf{F}_q$	(F.4.18)	Element flexibility
η	(F.4.20)	Line search parameter
ϕ	(F.4.21)	Line search merit function

Appendix G

The Rotation Group

G.1 Introduction

Geometrically, a rotation is a transformation of a plane or space that causes no deformation or reflection so that distance, orientation, and the origin are preserved. Mathematically this is realized in $\mathbb{R}^3$ by considering *all* functions $\boldsymbol{\Lambda}\colon \mathbb{R}^3 \to \mathbb{R}^3$, and filtering out those which do not preserve the origin 0, the vector dot product $\boldsymbol{a} \cdot \boldsymbol{b}$, and the scalar triple product $[\boldsymbol{a}, \boldsymbol{b}, \boldsymbol{c}] = \boldsymbol{a} \cdot (\boldsymbol{b} \times \boldsymbol{c})$ for vectors $\boldsymbol{a}, \boldsymbol{b}$ and $\boldsymbol{c}$ in $\mathbb{R}^3$. The set SO(3) is defined as the collection of all functions that have these properties:

$$\mathrm{SO}(3) \triangleq \left\{ \boldsymbol{\Lambda}\colon \mathbb{R}^3 \to \mathbb{R}^3 \;\middle|\; \begin{matrix} \boldsymbol{\Lambda a} \cdot \boldsymbol{\Lambda b} = \boldsymbol{a} \cdot \boldsymbol{b}\,, \\ [\boldsymbol{\Lambda a}, \boldsymbol{\Lambda b}, \boldsymbol{\Lambda c}] = [\boldsymbol{a}, \boldsymbol{b}, \boldsymbol{c}], \quad \text{and} \quad \boldsymbol{\Lambda} 0 = 0 \text{ for all } \boldsymbol{a}, \boldsymbol{b}, \boldsymbol{c} \in \mathbb{R}^3 \end{matrix} \right\} \tag{G.1.1}$$

These properties alone ensure any such map $\boldsymbol{\Lambda}$ acts linearly on vectors[1]. The properties in (G.1.1) for any $\boldsymbol{a}, \boldsymbol{b}, \boldsymbol{c} \in \mathbb{R}^3$ imply the familiar relations:

$$\begin{matrix} \boldsymbol{\Lambda a} \cdot \boldsymbol{\Lambda b} = \boldsymbol{a} \cdot \boldsymbol{b} \\ [\boldsymbol{\Lambda a}, \boldsymbol{\Lambda b}, \boldsymbol{\Lambda c}] = [\boldsymbol{a}, \boldsymbol{b}, \boldsymbol{c}] \end{matrix} \iff \begin{matrix} \boldsymbol{\Lambda}^{\mathrm{t}} \boldsymbol{\Lambda} = \mathbf{1} \\ \det \boldsymbol{\Lambda} = 1. \end{matrix}$$

There is no useful way to combine elements of SO(3) associatively while maintaining the constraints of (G.1.1). This means that when treating problems in terms of variables in SO(3), addition is undefined, and one is left without the structure of a *vector space*.

The characterization of SO(3) as a Lie group allows operations in any tangent space $T_{\boldsymbol{R}}\mathrm{SO}(3)$ at an element $\boldsymbol{R}$ to be systematically related to the single tangent space $T_1\mathrm{SO}(3)$ at the

[1] The linearity of SO(n) is more commonly specified directly by taking it as a subgroup of the general linear group, GL(n) (see e.g. Artin, 1991). However, it is helpful to observe this implication from the rotation constraints in (G.1.1).

identity element 1, essentially representing the entire *tangent bundle* $\{T_{\Lambda}\,\mathrm{SO}(3) \mid \boldsymbol{\Lambda} \in \mathrm{SO}(3)\}$ with a single vector space. For this reason, the space $T_1\mathrm{SO}(3)$ is given the special designation $\mathfrak{so}(3)$ and is referred to as the *Lie algebra* of the group SO(3). Note that for problems in a vector space $\mathcal{V}$, this ordeal of tangent spaces is generally circumvented altogether by implicitly identifying the tangent space $T_x\mathcal{V}$ at each point x in $\mathcal{V}$ with the vector space $\mathcal{V}$ itself.

The constraints in Equation (G.1.1) require that elements $\boldsymbol{\Omega}$ of the Lie algebra $\mathfrak{so}(3)$ behave like skew-symmetric linear operators. This immediately furnishes two convenient representations for these objects using either (1) vectors in $\mathbb{R}^3$, or (2) the skew symmetric matrices in $\mathbb{R}^{3\times 3}$. Any vector $\boldsymbol{\omega}$ in $\mathbb{R}^3$ is associated with a skew-symmetric matrix $\boldsymbol{\Omega}$ using the *hat* isomorphism $(\,\cdot\,)^{\times}$. This is defined by the relation $\boldsymbol{\Omega a} = \boldsymbol{\omega}^{\times}\boldsymbol{a} = \boldsymbol{\omega} \times \boldsymbol{a}$ for any vector $\boldsymbol{a}$ in $\mathbb{R}^3$ and expressed in coordinates as

$$\boldsymbol{\omega}^{\times} = \begin{pmatrix} \omega_1 \\ \omega_2 \\ \omega_3 \end{pmatrix}^{\times} = \begin{pmatrix} 0 & -\omega_3 & \omega_2 \\ \omega_3 & 0 & -\omega_1 \\ -\omega_2 & \omega_1 & 0 \end{pmatrix} = \boldsymbol{\Omega}. \tag{G.1.2}$$

Similarly, given a skew-symmetric matrix $\boldsymbol{\Omega} = \boldsymbol{\omega}^{\times}$, the *vee* isomorphism $(\,\cdot\,)^{\vee}$ is defined such that $\boldsymbol{\Omega}^{\vee} = \boldsymbol{\omega}$, which is expressed in coordinates as:

$$\boldsymbol{\Omega}^{\vee} = \begin{pmatrix} 0 & -\omega_3 & \omega_2 \\ \omega_3 & 0 & -\omega_1 \\ -\omega_2 & \omega_1 & 0 \end{pmatrix}^{\vee} = \begin{pmatrix} \omega_1 \\ \omega_2 \\ \omega_3 \end{pmatrix} = \boldsymbol{\omega}. \tag{G.1.3}$$

The inner product $\langle \cdot, \cdot \rangle \colon T_{\Lambda}\mathrm{SO}(3) \times T_{\Lambda}\mathrm{SO}(3) \to \mathbb{R}$ is defined by (R. H. Abraham et al., 1994)

$$\langle \boldsymbol{\Omega}_{\boldsymbol{\Lambda}}, \boldsymbol{W}_{\boldsymbol{\Lambda}} \rangle \triangleq \frac{1}{2}\,\mathrm{tr}\,[\boldsymbol{\Omega}_{\Lambda}^{\mathrm{t}}\boldsymbol{W}_{\Lambda}]\,. \tag{G.1.4}$$

G.2 Parameterizations

In this section, several formulas are presented that facilitate the use of calculus on the rotation manifold SO(3). Resources for this material include Barfoot (2017), Hertzberg (2008), Iserles et al. (2000).

G.2.1 Exp: The Exponential on SO(3)

Definition.

The *exponential* map $\exp\colon \mathfrak{so}(3) \to \mathrm{SO}(3)$ associates an element of the Lie algebra to a rotation. The exponential of $\boldsymbol{\Omega} \in \mathfrak{so}(3)$ is defined as $\exp \boldsymbol{\Omega} = \gamma(1)$ where $\gamma : \mathbb{R} \to \mathrm{SO}(3)$ solves the initial-value problem:

$$\begin{cases} \dot{\gamma} - \boldsymbol{\Omega}\gamma = 0 \\ \gamma(0) = \mathbf{1} \end{cases}$$

This definition implies the alternative functional definition which requires the following identities hold:

$$\begin{aligned} \exp((\xi + \varepsilon)\boldsymbol{\Omega}) &= \exp(\xi\boldsymbol{\Omega})\ \exp(\varepsilon\boldsymbol{\Omega}), \\ \frac{\mathrm{d}}{\mathrm{d}\varepsilon} \exp(\varepsilon\boldsymbol{\Omega})\bigg|_{\varepsilon=0} &= \boldsymbol{\Omega}. \end{aligned}$$

for any $\xi, \varepsilon \in \mathbb{R}$ and $\boldsymbol{\Omega} \in \mathfrak{so}(3)$. The following capitalized notation is used to express this as a function of vectors in $\mathbb{R}^3$:

$$\operatorname{Exp} \boldsymbol{\theta} := \exp \boldsymbol{\theta}^{\times}$$

Expression.

A closed-form expression for the exponential in SO(3) is furnished by the Rodrigues formula:

$$\operatorname{Exp} \boldsymbol{\theta} \ = \ \cos\theta \mathbf{1} + \frac{\sin\theta}{\theta}\boldsymbol{\theta}^{\times} + \frac{1 - \cos\theta}{\theta^2}\boldsymbol{\theta} \otimes \boldsymbol{\theta}$$

where $\theta := \|\boldsymbol{\theta}\|$. In terms of the coefficients a_i defined below (G.2.4) one has the following equivalent expressions:

$$\begin{aligned} \operatorname{Exp} \boldsymbol{\theta} &= \cos\theta \mathbf{1} + \frac{\sin\theta}{\theta}\boldsymbol{\theta}^{\times} + \frac{1 - \cos\theta}{\theta^2}\boldsymbol{\theta} \otimes \boldsymbol{\theta} \\ &= \mathbf{1} + a_1 \boldsymbol{\theta}^{\times} + a_2 \left(\boldsymbol{\theta}^{\times}\right)^2 \\ &= a_0 \mathbf{1} + a_1 \boldsymbol{\theta}^{\times} + a_2 \boldsymbol{\theta} \otimes \boldsymbol{\theta} \end{aligned} \tag{G.2.1}$$

G.2.2 Log: The Logarithm on SO(3)

Definition. The *logarithm* $\log\colon \mathrm{SO}(3) \to \mathfrak{so}(3)$ associates a rotation to a trajectory through the identity. When restricted to the open ball $\|\boldsymbol{\theta}\| < \pi$, the exponential is a bijection and the logarithm is its inverse. However, if one does not restrict the domain, the exponential becomes non-injective as every vector $(\|\boldsymbol{\theta}\| + 2k\pi)\boldsymbol{\theta}$ will map to the same $\boldsymbol{\Lambda}$ for any integer k. The logarithm may be defined in terms of the infinite series:

$$\log \boldsymbol{\Lambda} = \sum_{k=1}^{\infty} (-1)^{k+1} \frac{(\boldsymbol{\Lambda} - \mathbf{1})^k}{k}$$

The following capitalized notation is used to express the logarithm as a function of vectors in $\mathbb{R}^3$ representing element of $\mathfrak{so}(3)$:

$$\operatorname{Log} \boldsymbol{\Lambda} := (\log \boldsymbol{\Lambda})^{\vee}$$

where the notation $(\,\cdot\,)^{\vee}$ of (G.1.3) is employed.

Expression. A common formula for the logarithm in SO(3) is:

$$\log \boldsymbol{\Lambda} = \frac{\vartheta\left(\boldsymbol{\Lambda} - \boldsymbol{\Lambda}^{\top}\right)}{2\sin\vartheta} \qquad \text{with} \qquad \vartheta = \cos^{-1}\left(\frac{\operatorname{tr}\boldsymbol{\Lambda} - 1}{2}\right).$$

which holds for $\vartheta \neq 0$ and $\vartheta \in (-\pi, \pi)$. However, this expression is problematic when ϑ is small and should not be used in practice. An ideal procedure to compute the logarithm is the algorithm proposed by SPURRIER (1978), which is summarized in Algorithm 4.

G.2.3 Exponential Differentials

The differential or push-forward $\operatorname{dexp}_{\boldsymbol{\Omega}}$ of the exponential exp at $\boldsymbol{\Omega}$ is defined by:

$$\operatorname{dexp}_{\boldsymbol{\Omega}} \boldsymbol{W} = \frac{\mathrm{d}}{\mathrm{d}\varepsilon} \exp \gamma_{\varepsilon}\bigg|_{\varepsilon=0} \qquad \text{with} \qquad \begin{aligned} &\gamma(0) = \boldsymbol{\Omega}, \text{ and} \\ &\dot{\gamma}(0) = \boldsymbol{W}. \end{aligned}$$

Note that this furnishes a function with the signature:

$$\operatorname{dexp}_{\boldsymbol{\Omega}} : T_{\boldsymbol{\Omega}}\mathfrak{so}(3) \to T_{\exp(\boldsymbol{\Omega})}\mathrm{SO}(3).$$

However, as indicated earlier, it is preferable to identify each space $T_{\exp(\boldsymbol{\Omega})}\mathrm{SO}(3)$ with the single Lie algebra $\mathfrak{so}(3)$. That is, for any rotation $\boldsymbol{\Lambda}$, we seek a systematic way to associate a tangent $\dot{\boldsymbol{\Lambda}} \in T_{\Lambda}\mathrm{SO}(3)$ with an element $\boldsymbol{\Omega}$ of the Lie algebra $\mathfrak{so}(3) \equiv T_{1}\mathrm{SO}(3)$. There are two standard ways to make this association:

1. *Left representation*:

$$T^r_\Lambda \mathrm{SO}(3) := \Big\{ \boldsymbol{\Psi} \text{ with } \dot{\boldsymbol{\Lambda}} := \boldsymbol{\Lambda}\boldsymbol{\Psi} \mid \boldsymbol{\Lambda} \in \mathrm{SO}(3), \boldsymbol{\Psi} \in \mathfrak{so}(3) \Big\}$$

2. *Right representation*:

$$T^\ell_\Lambda \mathrm{SO}(3) := \Big\{ \boldsymbol{\Theta} \text{ with } \dot{\boldsymbol{\Lambda}} := \boldsymbol{\Theta}\boldsymbol{\Lambda} \mid \boldsymbol{\Lambda} \in \mathrm{SO}(3), \boldsymbol{\Theta} \in \mathfrak{so}(3) \Big\} \tag{G.2.2}$$

For each of these representations, a *trivialized* differential may be constructed. Furthermore, when $\mathfrak{so}(3)$ is identified with $\mathbb{R}^3$, these are denoted by $\mathrm{d_R Exp}$ and $\mathrm{d_L Exp}$ for the right and left representations, respectively, and each carries the signature $\mathbb{R}^3 \times \mathbb{R}^3 \to \mathbb{R}^3$. For a curve $\gamma : \mathbb{R} \to \mathfrak{so}(3)$ these are defined by the relations:

$$\begin{aligned} \frac{\mathrm{d}}{\mathrm{d}\varepsilon} \operatorname{Exp} \gamma_\varepsilon &= \mathrm{d_R Exp}(\gamma_\varepsilon)\, \dot{\gamma}(\varepsilon)\ \operatorname{Exp} \gamma_\varepsilon \\ &= \operatorname{Exp}(\gamma_\varepsilon)\ \mathrm{d_L Exp}(\gamma_\varepsilon)\, \dot{\gamma}(\varepsilon). \end{aligned} \tag{G.2.3}$$

Remarks

- In the literature on geometrically exact rods, Ibrahimbegović et al. (1995) and Ritto-Corrêa and Camotim (2002) use the notation $\boldsymbol{T}$ for $\mathrm{d_R Exp}\,\boldsymbol{\theta}$. Alternatively, Simo and Vu-Quoc (1988) and Jelenić and Crisfield (1999) used $\boldsymbol{T}$ to refer to $(\mathrm{d_R Exp}\,\boldsymbol{\theta})^{-1}$ and Simo and Wong (1991) uses the symbol for $(\mathrm{d_L Exp}\,\boldsymbol{\theta})^{-1}$. Cardona and Geradin (1988) used the same symbol for $\mathrm{d_L Exp}\,\boldsymbol{\theta}$.
- The notation dexp employed in this work is consistent with Rossmann (2006) and differs slightly from of Iserles et al. (2000), who use the symbol to denote a *trivialized* differential. That is, in the adopted notation, the expression in terms of the adjoint action ad is given by:

$$\operatorname{dexp}_X Y = \exp X \frac{1 - \exp(-\operatorname{ad} X)}{\operatorname{ad} X} Y.$$

Before proceeding to the expressions for these functions, some definitions are necessary. Define coefficients b_i and c_i:

$$\begin{aligned} b_i &:= \frac{1}{\theta}\frac{\mathrm{d}a_i}{\mathrm{d}\theta} \qquad \text{so} \qquad \delta a_i = b_i\, \boldsymbol{\theta} \cdot \delta\boldsymbol{\theta}, \quad \text{and} \\ c_i &:= \frac{1}{\theta}\frac{\mathrm{d}b_i}{\mathrm{d}\theta} \qquad \text{so} \qquad \delta b_i = c_i\, \boldsymbol{\theta} \cdot \delta\boldsymbol{\theta}. \end{aligned}$$

where a_i are the coefficients in (G.2.1) for the exponential map, $\boldsymbol{\theta}$ its argument, and $\theta := \|\boldsymbol{\theta}\|$. In closed form the coefficients b_i and c_i are:

$$
\begin{array}{cccc}
i & a_i & b_i & c_i \\
\hline
0 & \cos\theta & -\dfrac{\sin\theta}{\theta} & \dfrac{\sin\theta-\theta\cos\theta}{\theta^3} \\
1 & \dfrac{\sin\theta}{\theta} & \dfrac{\theta\cos\theta-\sin\theta}{\theta^3} & \dfrac{3\sin\theta-\theta^2\sin\theta-3\theta\cos\theta}{\theta^5} \\
2 & \dfrac{1-\cos\theta}{\theta^2} & \dfrac{\theta\sin\theta-2+2\cos\theta}{\theta^4} & \dfrac{8-8\cos\theta-5\theta\sin\theta+\theta^2\cos\theta}{\theta^6} \\
3 & \dfrac{\theta-\sin\theta}{\theta^3} & \dfrac{3\sin\theta-2\theta-\theta\cos\theta}{\theta^5} & \dfrac{8\theta+7\theta\cos\theta+\theta^2\sin\theta-15\sin\theta}{\theta^7}
\end{array}
\tag{G.2.4}
$$

Many of these equations are singular at $\theta = 0$. Near this condition, the following series expression should be used (Ritto-Corrêa & Camotim, 2002).

$$
z_{ji} = \sum_{k=0}^{\infty} \frac{2^j (j+k)!(-1)^{k+j}\theta^{2k}}{k!(i+2j+2k)!} = \begin{cases} a_i(\theta) & \text{if } j=0 \\ b_i(\theta) & \text{if } j=1 \\ c_i(\theta) & \text{if } j=2 \end{cases}
\tag{G.2.5}
$$

Remarkably, this expression contains every coefficient in (G.2.4). It is useful to define a similar table for the coefficients of the inverse exponential differential:

$$
\begin{array}{ccc}
i & \alpha_i & \beta_i \\
\hline
0 & 1+\dfrac{1}{2}\theta^2 & \\
1 & \dfrac{\theta/2}{\tan(\theta/2)} & \\
2 & -\dfrac{1}{2} & \\
3 & \dfrac{1}{\theta^2}\left(1-\dfrac{\theta/2}{\tan(\theta/2)}\right) & \dfrac{\theta(\theta+\sin\theta)-8\sin\left(\frac{\theta}{2}\right)^2}{4\theta^4\sin^2\frac{\theta}{2}}
\end{array}
\tag{G.2.6}
$$

$\mathrm{d_R Exp}$: Right Differential of the Exponential

Definition. The *right-trivialized differential* of the exponential $\mathrm{d_R Exp}\,\boldsymbol{\theta}$ is a function that maps variations of the argument $\boldsymbol{\theta}$ into right-represented vectors in the tangent space. An extensive discussion is provided by Ibrahimbegović et al. (1995). Interesting treatments from alternative perspectives can be found in Pietraszkiewicz and Badur (1983), Simo and Vu-Quoc (1986), and Pfister (1998). Note that this function is sometimes referred to as the "left Jacobian" of SO(3). The right-trivialized differential is defined by (G.2.3), and has been expressed by the limit (Solà et al., 2018):

$$\begin{aligned}\mathrm{d}_{\mathrm{R}}\mathrm{Exp}(\boldsymbol{\theta})\,\boldsymbol{u} &:= \lim_{\varepsilon\to 0}\frac{\mathrm{Log}\left(\mathrm{Exp}(\boldsymbol{\theta}+\varepsilon\boldsymbol{u})\ \mathrm{Exp}(\boldsymbol{\theta})^{-1}\right)}{\varepsilon}\\ &= \frac{\mathrm{d}}{\mathrm{d}\varepsilon}\,\mathrm{Exp}(\boldsymbol{\theta}+\varepsilon\boldsymbol{u})\,\mathrm{Exp}(-\boldsymbol{\theta})\Big|_{\varepsilon=0}^{\vee}\end{aligned}$$

Expression. In terms of the coefficients a_i in (G.2.4) the function has the expression:

$$\mathrm{d}_{\mathrm{R}}\mathrm{Exp}\,\boldsymbol{\theta} = \mathbf{1} + a_2\boldsymbol{\theta}^{\times} + a_3\left(\boldsymbol{\theta}^{\times}\right)^2 \tag{G.2.7}$$

In Simo and Vu-Quoc (1986) the notation $\boldsymbol{\beta} = (\mathrm{d}_{\mathrm{R}}\mathrm{Exp}\,\boldsymbol{\theta})\,\dot{\boldsymbol{\theta}}$ is used.

$\mathrm{d}_{\mathrm{L}}\mathrm{Exp}$: Left Differential of the Exponential

Definition. The *left-trivialized differential of the exponential* is defined by (G.2.3), and has been expressed by the limit (Solà et al., 2018):

$$\begin{aligned}\mathrm{d}_{\mathrm{L}}\mathrm{Exp}(\boldsymbol{\theta})\,\boldsymbol{u} &:= \lim_{\varepsilon\to 0}\frac{\mathrm{Log}\left(\mathrm{Exp}(\boldsymbol{\theta})^{-1}\ \mathrm{Exp}(\boldsymbol{\theta}+\varepsilon\boldsymbol{u})\right)}{\varepsilon}\\ &= \frac{\mathrm{d}}{\mathrm{d}\varepsilon}\,\mathrm{Exp}(-\boldsymbol{\theta})\,\mathrm{Exp}(\boldsymbol{\theta}+\varepsilon\boldsymbol{u})\Big|_{\varepsilon=0}^{\vee}\end{aligned}$$

Expression. In terms of the coefficients a_i in (G.2.4) the function takes the following form:

$$\mathrm{d}_{\mathrm{L}}\mathrm{Exp}\,\boldsymbol{\theta} = \mathbf{1} - a_2\boldsymbol{\theta}^{\times} + a_3\left(\boldsymbol{\theta}^{\times}\right)^2 \tag{G.2.8}$$

This expression is well-known and may be derived from (G.2.7) using the identity $\mathrm{d}_{\mathrm{R}}\mathrm{Exp}\,(\boldsymbol{\theta}) = \mathrm{d}_{\mathrm{L}}\mathrm{Exp}\,(-\boldsymbol{\theta})$.

$\mathrm{d}^2_{\mathrm{R}}\mathrm{Exp}$: Derivative of the Right Exponential Differential

Definition. The *derivative of the right exponential differential* arises by linearizing expressions containing the right differential (G.2.7). It is defined as the directional derivative of the vector-valued function $\boldsymbol{\theta} \mapsto \mathrm{d}_{\mathrm{R}}\mathrm{Exp}(\boldsymbol{\theta})\,\boldsymbol{p}$ for some constant vector $\boldsymbol{p}$:

$$\mathrm{d}^2_{\mathrm{R}}\mathrm{Exp}(\boldsymbol{\theta};\,\boldsymbol{p})\,\boldsymbol{u} := \frac{\mathrm{d}}{\mathrm{d}\varepsilon}\,\mathrm{d}_{\mathrm{R}}\mathrm{Exp}(\gamma_\varepsilon)\ \boldsymbol{p}\Big|_{\varepsilon=0} \qquad \text{with} \qquad \begin{aligned}\gamma_\varepsilon &= \boldsymbol{\theta}+\varepsilon\boldsymbol{u}\\ \dot{\gamma}(0) &= \boldsymbol{u}\end{aligned}$$

Expression. In terms of the coefficients a_i and b_i in (G.2.4) the function takes the following form:

$$\mathrm{d}^2_{\mathrm{R}}\mathrm{Exp}(\boldsymbol{\theta};\,\boldsymbol{p}) = -a_2\boldsymbol{p}^{\times} + a_3\,(\boldsymbol{p}\cdot\boldsymbol{\theta})\,\mathbf{1} + a_3\boldsymbol{\theta}\otimes\boldsymbol{p} + b_1\boldsymbol{p}\otimes\boldsymbol{\theta} + b_2\,(\boldsymbol{\theta}\times\boldsymbol{p})\otimes\boldsymbol{\theta} + b_3\,(\boldsymbol{p}\cdot\boldsymbol{\theta})\,\boldsymbol{\theta}\otimes\boldsymbol{\theta} \tag{G.2.9}$$

This expression has previously been derived by Cardona and Geradin (1988).

$\mathrm{d}^2_{\mathrm{L}}\mathrm{Exp}$: Derivative of the Left Exponential Differential

Definition. The *derivative of the left exponential differential* arises by linearizing expressions containing the left differential (G.2.7). It is defined as the directional derivative of the vector-valued function $\boldsymbol{\theta}\mapsto \mathrm{d}_{\mathrm{L}}\mathrm{Exp}(\boldsymbol{\theta})\,\boldsymbol{p}$ for some constant vector $\boldsymbol{p}$:

$$\mathrm{d}^2_{\mathrm{L}}\mathrm{Exp}(\boldsymbol{\theta};\,\boldsymbol{p})\,\boldsymbol{u} := \frac{\mathrm{d}}{\mathrm{d}\varepsilon}\,\mathrm{d}_{\mathrm{L}}\mathrm{Exp}(\gamma_\varepsilon)\,\boldsymbol{p}\bigg|_{\varepsilon=0}, \qquad \text{with} \qquad \begin{aligned}\gamma_\varepsilon &= \boldsymbol{\theta}+\varepsilon\boldsymbol{u}\\ \dot\gamma(0) &= \boldsymbol{u}\end{aligned}$$

Expression. In terms of the coefficients a_i and b_i in (G.2.4) the function takes the following form:

$$\begin{aligned}\mathrm{d}^2_{\mathrm{L}}\mathrm{Exp}(\boldsymbol{\theta};\boldsymbol{p}) &= a_2\boldsymbol{p}^{\times} + a_3\,(\boldsymbol{p}\cdot\boldsymbol{\theta})\,\mathbf{1} + a_3\,\boldsymbol{\theta}\otimes\boldsymbol{p}\\ &\quad + b_1\,\boldsymbol{p}\otimes\boldsymbol{\theta} - b_2\,(\boldsymbol{\theta}\times\boldsymbol{p})\otimes\boldsymbol{\theta} + b_3\,(\boldsymbol{p}\cdot\boldsymbol{\theta})\,\boldsymbol{\theta}\otimes\boldsymbol{\theta}\end{aligned} \tag{G.2.10}$$

This formula has been derived by Jelenić and Crisfield (1998) and Ritto-Corrêa and Camotim (2002).

$\mathrm{d}^3\mathrm{Exp}$: Second Derivative of the Left Exponential Differential

Definition. The *second derivative of the left exponential differential* arises from the linearization of products with the first derivative of the left differential.

$$\mathrm{d}^3_{\mathrm{R}}\mathrm{Exp}\,(\boldsymbol{\theta};\,\boldsymbol{p},\boldsymbol{q})\;\boldsymbol{u} := \frac{\mathrm{d}}{\mathrm{d}\varepsilon}\,\mathrm{d}^2_{\mathrm{R}}\mathrm{Exp}\,(\gamma_\varepsilon;\,\boldsymbol{p})\;\boldsymbol{q}\bigg|_{\varepsilon=0}, \qquad \text{with} \qquad \begin{aligned}\gamma_\varepsilon &= \boldsymbol{\theta}+\varepsilon\boldsymbol{u}\\ \dot\gamma(0) &= \boldsymbol{u}\end{aligned}$$

Expression.

In terms of the coefficients a_i, b_i and c_i in (G.2.4) the function takes the form:

$$
\begin{aligned}
\mathrm{d}_{\mathrm{R}}^{3}\mathrm{Exp}\,(\boldsymbol{\theta};\boldsymbol{p},\boldsymbol{q}) = & a_3(\boldsymbol{p}\otimes\boldsymbol{q}+\boldsymbol{q}\otimes\boldsymbol{p}) + b_1(\boldsymbol{p}\cdot\boldsymbol{q})\mathbf{1} + b_2(\boldsymbol{p}\times\boldsymbol{q}\otimes\boldsymbol{\theta}+\boldsymbol{\theta}\otimes\boldsymbol{p}\times\boldsymbol{q}+(\boldsymbol{\theta}\times\boldsymbol{p}\cdot\boldsymbol{q})\mathbf{1}) \\
& + b_3(\boldsymbol{p}\cdot\boldsymbol{\theta}(\boldsymbol{q}\otimes\boldsymbol{\theta}+\boldsymbol{\theta}\otimes\boldsymbol{q}) + \boldsymbol{q}\cdot\boldsymbol{\theta}(\boldsymbol{p}\otimes\boldsymbol{\theta}+\boldsymbol{\theta}\otimes\boldsymbol{p}) + (\boldsymbol{p}\cdot\boldsymbol{\theta})\,(\boldsymbol{\theta}\cdot\boldsymbol{q})\mathbf{1}) \\
& + (c_1\;\boldsymbol{p}\cdot\boldsymbol{q} + c_2(\boldsymbol{q}\times\boldsymbol{p})\cdot\boldsymbol{\theta} + c_3\,(\boldsymbol{p}\cdot\boldsymbol{\theta})\,(\boldsymbol{\theta}\cdot\boldsymbol{q}))\boldsymbol{\theta}\otimes\boldsymbol{\theta}
\end{aligned} \tag{G.2.11}
$$

This expression has been derived by Ibrahimbegović et al. (1995) and Ritto-Corrêa and Camotim (2002).

$\mathrm{d}_{\mathrm{R}}\mathrm{Log}$: Right Differential of the Logarithm

Definition. The *right differential of the logarithm* inverts the right exponential differential (G.2.7) and has been expressed as:

$$\mathrm{d}_{\mathrm{R}}\mathrm{Log}\,(\boldsymbol{\theta})\;\boldsymbol{u} = \frac{\mathrm{d}}{\mathrm{d}\varepsilon}\,\mathrm{Log}(\mathrm{Exp}(\varepsilon\boldsymbol{u})\,\mathrm{Exp}\,\boldsymbol{\theta})\Big|_{\varepsilon=0}$$

Expression. In terms of the coefficients α_i in (G.2.6) the function takes the following form:

$$\mathrm{d}_{\mathrm{R}}\mathrm{Log}\,\boldsymbol{\theta} = \alpha_1\mathbf{1} + \alpha_2\,\boldsymbol{\theta}^{\times} + \alpha_3\,\boldsymbol{\theta}\otimes\boldsymbol{\theta} \tag{G.2.12}$$

Derivations of this function can be found in Simo and Vu-Quoc (1988), Nour-Omid and Rankin (1991), Ibrahimbegović et al. (1995), and Bauchau and Trainelli (2003).

$\mathrm{d}_{\mathrm{L}}\mathrm{Log}$: Left Differential of the Logarithm

Definition. The *left differential of the logarithm* is adjoint to the right differential of the logarithm (G.2.12), and has been expressed as:

$$\mathrm{d}_{\mathrm{L}}\mathrm{Log}\,(\boldsymbol{\theta})\;\boldsymbol{u} = \frac{\mathrm{d}}{\mathrm{d}\varepsilon}\,\mathrm{Log}(\mathrm{Exp}\,\boldsymbol{\theta}\,\mathrm{Exp}(\varepsilon\boldsymbol{u}))\Big|_{\varepsilon=0}$$

Expression. In terms of the coefficients α_i in (G.2.6) the function takes the following form:

$$\mathrm{d}_{\mathrm{L}}\mathrm{Log}\,\boldsymbol{\theta} = \alpha_1\mathbf{1} - \alpha_2\boldsymbol{\theta}^{\times} + \alpha_3\boldsymbol{\theta}\otimes\boldsymbol{\theta}$$

This formula has previously been derived by Cardona and Geradin (1988).

$\mathrm{d}^2_{\mathrm{LR}}\mathrm{Log}$**: Derivative of the Left Differential of the Logarithm**

Definition. The derivative $\mathrm{d}^2_{\mathrm{LR}}\mathrm{Log}\,(\boldsymbol{\theta};\, \boldsymbol{p})$ arises when a logarithmic parameterization is linearized:

$$
\begin{aligned}
\mathrm{d}^2_{\mathrm{LR}}\mathrm{Log}\,(\boldsymbol{\theta};\, \boldsymbol{p})\, \boldsymbol{u} &= \frac{\mathrm{d}}{\mathrm{d}\varepsilon}\, \mathrm{d}_{\mathrm{L}}\mathrm{Log}\,(\mathrm{Log}\,(\mathrm{Exp}(\varepsilon \boldsymbol{u})\,\mathrm{Exp}(\boldsymbol{\theta})))\, \boldsymbol{p}\Big|_{\varepsilon=0} \\
&= \partial_{\boldsymbol{\theta}}\, \mathrm{d}_{\mathrm{L}}\mathrm{Log}\,(\boldsymbol{\theta};\, \boldsymbol{p})\ \frac{\mathrm{d}}{\mathrm{d}\varepsilon}\, \mathrm{Log}\,(\mathrm{Exp}(\varepsilon \boldsymbol{u})\,\mathrm{Exp}\,\boldsymbol{\theta})\Big|_{\varepsilon=0} \\
&= \partial_{\boldsymbol{\theta}}\, \mathrm{d}_{\mathrm{L}}\mathrm{Log}\,(\boldsymbol{\theta};\, \boldsymbol{p})\ \mathrm{d}_{\mathrm{R}}\mathrm{Log}\,(\boldsymbol{\theta})\, \boldsymbol{u}
\end{aligned}
$$

where $\mathrm{d}_{\mathrm{R}}\mathrm{Log}\,\boldsymbol{\theta}$ is given by (G.2.12) and :

$$
\partial_{\boldsymbol{\theta}}\, \mathrm{d}_{\mathrm{L}}\mathrm{Log}\,(\boldsymbol{\theta};\, \boldsymbol{p})\ \boldsymbol{u} = \frac{\mathrm{d}}{\mathrm{d}\varepsilon}\, \mathrm{d}_{\mathrm{L}}\mathrm{Log}\,(\boldsymbol{\theta} + \varepsilon \boldsymbol{u};\, \boldsymbol{p})\Big|_{\varepsilon=0}
$$

Expression. In terms of the coefficients α_i and β_i in (G.2.6) the function takes the following form:

$$
\mathrm{d}^2_{\mathrm{LR}}\mathrm{Log}(\boldsymbol{\theta};\, \boldsymbol{p}) = \left(\alpha_2 \boldsymbol{p}^{\times} + \alpha_3((\boldsymbol{\theta}\cdot\boldsymbol{p})\mathbf{1} + \boldsymbol{\theta}\otimes\boldsymbol{p} - 2\boldsymbol{p}\otimes\boldsymbol{\theta}) + \beta_2\,(\boldsymbol{\theta}^{\times})^2\,\boldsymbol{p}\otimes\boldsymbol{\theta}\right) \mathrm{d}_{\mathrm{R}}\mathrm{Log}\,\boldsymbol{\theta} \tag{G.2.13}
$$

where $\mathrm{d}_{\mathrm{R}}\mathrm{Log}\,\boldsymbol{\theta}$ is given by (G.2.12). This formula has been derived in Nour-Omid and Rankin (1991).

G.2.4 Rotation Tangents

Consider a vector function $\boldsymbol{q}$ that follows a vector $\boldsymbol{p}$ as it is rotated by a time-varying rotation $\boldsymbol{\Lambda}_{\varepsilon}$:

$$
\boldsymbol{q} \coloneqq \boldsymbol{\Lambda}_{\varepsilon}\, \boldsymbol{p}.
$$

A tangent in the right representation is furnished by:

$$
\begin{aligned}
\mathrm{d}_{\mathrm{L}}(\boldsymbol{\Lambda p})\cdot\boldsymbol{u} &= \lim_{\varepsilon\to 0} \frac{\mathrm{Exp}\,(\varepsilon\boldsymbol{u})\,\boldsymbol{\Lambda p} - \boldsymbol{\Lambda p}}{\varepsilon} \\
&= -(\boldsymbol{\Lambda p})^{\times}\boldsymbol{u}.
\end{aligned} \tag{G.2.14}
$$

Algorithm 4 Algorithm from SPURRIER (1978) for computing the logarithm Log on SO(3).

function LOGSO3($\boldsymbol{\Lambda}$)
▷ Form quaternion $(q_0 + \boldsymbol{q})$
  $a = \max\{\operatorname{tr}\boldsymbol{\Lambda},\, \Lambda_{11},\, \Lambda_{22},\, \Lambda_{33}\}$
  if $a \equiv \operatorname{tr}\boldsymbol{\Lambda}$ **then**
    $q_0 = \frac{1}{2}\sqrt{1+a}$
    for i = 0:2 **do**
      $j = (i+1)\%3$
      $k = (i+2)\%3$
      $q_i = (\Lambda_{kj} - \Lambda_{jk})/(4q_0)$
    end for
  else
    $i = \operatorname{argmax}\{\operatorname{tr}\boldsymbol{\Lambda},\, \Lambda_{11},\, \Lambda_{22},\, \Lambda_{33}\}$
    $j = (i+1)\%3$
    $k = (i+2)\%3$
    $q_i = \sqrt{a/2 + (1-\operatorname{tr}\boldsymbol{\Lambda})/4}$
    $q_j = (\Lambda_{ji} + \Lambda_{ij})/(4q_i)$
    $q_k = (\Lambda_{ki} + \Lambda_{ik})/(4q_i)$
    $q_0 = (\Lambda_{kj} - \Lambda_{jk})/(4q_i)$
  end if
  $\boldsymbol{q} = q_1\mathbf{i} + q_2\mathbf{j} + q_3\mathbf{k}$
▷ Form vector $\boldsymbol{\theta}$
  $q = \|\boldsymbol{q}\|$
  if $q_0 < 0$ **then**
    $q_0 = -q_0$
    $\boldsymbol{q} = -\boldsymbol{q}$
  end if
  if $q \equiv 0$ **then**
    $\boldsymbol{\theta} = 0$
  else if $q < q_0$ **then**
    $\boldsymbol{\theta} = (\boldsymbol{q}/q)2\sin^{-1} q$
  else
    $\boldsymbol{\theta} = (\boldsymbol{q}/q)2\cos^{-1} q_0$
  end if
  return $\boldsymbol{\theta}$
end function

Part IV

Appendices to Part II

Appendix H

Gradients of the Enhanced Section Formulation

H.1 Section Formulation

After the primal section state has been converged (Box 3.4), one differentiates the enhanced equilibrium equation at fixed generalized deformation $\boldsymbol{e}$ to recover the enhanced sensitivity $\boldsymbol{\eta}_{,\hat{y}}$. The strain and stress sensitivities at each integration point then follow from the differentiated kinematic map and the material sensitivity relation. The section sensitivity is obtained by integrating the differentiated generalized stress-resultant operator.

$$\boldsymbol{K}_{\eta\eta}\boldsymbol{\eta}_{,\hat{y}} = -\tilde{\boldsymbol{g}}^{\mathrm{dir}}_{,\hat{y}} \tag{H.1.1}$$

where $\tilde{\boldsymbol{g}}^{\mathrm{dir}}_{,\hat{y}}$ is the derivative of the enhanced residual (3.4.4) with respect to the active host parameter $\hat{y}$ while holding $\boldsymbol{\eta}$ fixed.

Differentiating the enhanced residual (3.4.4) furnishes:

$$\tilde{\boldsymbol{g}}_{,\hat{y}} = \int_{\Omega} \left(\bar{\boldsymbol{A}}^{\top}_{,\hat{y}}\boldsymbol{\sigma} + \bar{\boldsymbol{A}}^{\top}\boldsymbol{\sigma}_{,\hat{y}} + a_h\, \bar{\boldsymbol{A}}^{\top}\boldsymbol{\sigma} \right)\, \mathrm{d}A. \tag{H.1.2}$$

where

$$a_h := \frac{(\,\mathrm{d}A)_{,\hat{y}}}{\mathrm{d}A}$$

is the relative sensitivity of the section measure and the stress sensitivity $\boldsymbol{\sigma}_{,\hat{y}}$ at each integration point $\boldsymbol{r}_{\ell}$ is

$$\boldsymbol{\sigma}_{,\hat{y}} = \boldsymbol{\sigma}^{\mathrm{mat}}_{,\hat{y}} + \mathbb{C}\boldsymbol{\varepsilon}_{,\hat{y}}. \tag{H.1.3}$$

with

$$\boldsymbol{\varepsilon}_{,\hat{y}} = \hat{\boldsymbol{\varepsilon}}_{,\hat{y}} + \bar{\boldsymbol{A}}_{,\hat{y}}\boldsymbol{\eta} + \bar{\boldsymbol{A}}\,\boldsymbol{\eta}_{,\hat{y}} \tag{H.1.4}$$

Using (H.1.4) and (H.1.3) one obtains

$$\tilde{\boldsymbol{g}}_{,\hat{y}} = \boldsymbol{K}_{\eta\eta}\boldsymbol{\eta}_{,\hat{y}} + \tilde{\boldsymbol{g}}^{\mathrm{dir}}_{,\hat{y}},$$

with $\boldsymbol{K}_{\eta\eta}$ furnished by (3.4.8a) and

$$\tilde{\boldsymbol{g}}^{\mathrm{dir}}_{,\hat{y}} = \int_{\Omega} \Big[\bar{\boldsymbol{A}}^{\top}_{,\hat{y}}\boldsymbol{\sigma} + \bar{\boldsymbol{A}}^{\top}(\boldsymbol{\sigma}^{\mathrm{mat}}_{,\hat{y}} + \mathbb{C}(\boldsymbol{A}_{\varepsilon}{}_{,\hat{y}}\boldsymbol{e} + \bar{\boldsymbol{A}}_{,\hat{y}}\boldsymbol{\eta})) + a_h\, \bar{\boldsymbol{A}}^{\top}\boldsymbol{\sigma}\Big]\, \mathrm{d}A. \tag{H.1.5}$$

Hence the condensed sensitivity equation is

$$\boldsymbol{K}_{\eta\eta}\boldsymbol{\eta}_{,\hat{y}} = -\tilde{\boldsymbol{g}}^{\mathrm{dir}}_{,\hat{y}}.$$

The full resultant derivative is then:

$$\boldsymbol{s}_{,\hat{y}} = \int_{\Omega} \Big(\boldsymbol{A}_{\varepsilon}{}^{\top}_{,\hat{y}}\boldsymbol{\sigma} + \boldsymbol{A}_{\varepsilon}^{\top}\boldsymbol{\sigma}_{,\hat{y}} + a_h\, \boldsymbol{A}_{\varepsilon}^{\top}\boldsymbol{\sigma}\Big)\, \mathrm{d}A.$$

Box H.1: Section Sensitivity Determination

Objective. Given generalized deformations $\boldsymbol{e}$, the converged section state $\boldsymbol{\eta}$, and an active parameter $\hat{y}$, compute the conditional sensitivities $\boldsymbol{\eta}_{,\hat{y}}$ and $\boldsymbol{s}_{,\hat{y}}$ over the cross-section discretization.
Procedure.

1. Retrieve the converged section state $\boldsymbol{\eta}$, together with the stresses $\boldsymbol{\sigma}_\ell$ and material tangents $\mathbb{C}_\ell$ at the quadrature points of the section discretization.

2. Solve for $\boldsymbol{\eta}_{,\hat{y}}$:
$$\boldsymbol{K}_{\eta\eta}\boldsymbol{\eta}_{,\hat{y}} = -\tilde{\boldsymbol{g}}^{\mathrm{dir}}_{,\hat{y}}$$
where
$$\tilde{\boldsymbol{g}}^{\mathrm{dir}}_{,\hat{y}} = \int_\Omega \left[\bar{\boldsymbol{A}}^\top_{,\hat{y}}\boldsymbol{\sigma} + \bar{\boldsymbol{A}}^\top(\boldsymbol{\sigma}^{\mathrm{mat}}_{,\hat{y}} + \mathbb{C}(\boldsymbol{A}_{\varepsilon\,,\hat{y}}\boldsymbol{e} + \bar{\boldsymbol{A}}_{,\hat{y}}\boldsymbol{\eta})) + a_h\,\bar{\boldsymbol{A}}^\top\boldsymbol{\sigma}\right] \mathrm{d}A. \tag{H.1.5}$$

3. Integrate the section resultant sensitivity:
$$\boldsymbol{s}_{,\hat{y}} = \int_\Omega \boldsymbol{A}_\varepsilon^\top\boldsymbol{\sigma}_{,\hat{y}}\ \mathrm{d}A + \boldsymbol{s}^{\mathrm{geom}}_{,\hat{y}},$$
   - At each quadrature point, evaluate the strain sensitivity from the differentiated kinematic relation:
$$\boldsymbol{\varepsilon}_{,\hat{y}} = \hat{\boldsymbol{\varepsilon}}_{,\hat{y}} + \bar{\boldsymbol{A}}_{,\hat{y}}\boldsymbol{\eta} + \bar{\boldsymbol{A}}\,\boldsymbol{\eta}_{,\hat{y}}.$$
   - Evaluate the stress sensitivity with the material sensitivity relation:
$$\boldsymbol{\sigma}_{,\hat{y}} = \boldsymbol{\sigma}^{\mathrm{mat}}_{,\hat{y}} + \mathbb{C}\boldsymbol{\varepsilon}_{,\hat{y}}.$$

H.2 Geometrically Exact Frame Element

To accommodate parameters that may affect the element length, reference geometry, or interpolation data, it is convenient to express the element resisting forces (F.3.11) on a fixed parent domain $\hat{e}$:

$$\boldsymbol{p}_a(\boldsymbol{u},\hat{y}) = \int_{\hat{e}} J(\hat{x},\hat{y})\,\boldsymbol{B}_a(\boldsymbol{u},\hat{y})\,\boldsymbol{\sigma}(\boldsymbol{u},\hat{y})\,\mathrm{d}\hat{x} = \int_{\hat{e}} J\boldsymbol{B}_a\,\boldsymbol{A}_*\,\boldsymbol{s}\,\mathrm{d}\hat{x}. \tag{H.2.1}$$

Here $\boldsymbol{u}$ denotes the vector of discrete configuration variables in the chosen chart, J is the parent-to-element Jacobian, and $\boldsymbol{\sigma} = \boldsymbol{A}_* \boldsymbol{s}$. Define

$$(\,\cdot\,)_{,\hat{y}} := \frac{\mathrm{d}}{\mathrm{d}\hat{y}}(\,\cdot\,), \qquad (\,\cdot\,)_{;\hat{y}} := \frac{\partial}{\partial \hat{y}}(\,\cdot\,)\Big|_{\boldsymbol{u}}, \tag{H.2.2}$$

so that $(\,\cdot\,)_{;\hat{y}}$ denotes the explicit parameter derivative at fixed discrete state. Differentiating (H.2.1) along the equilibrium path gives

$$\boldsymbol{p}_{a,\hat{y}} = \int_{\hat{e}} \Big[D_\chi[\boldsymbol{B}_a \boldsymbol{A}_* \mid \boldsymbol{s}] \cdot \boldsymbol{u}_h + J \boldsymbol{B}_a \boldsymbol{A}_* \, \boldsymbol{s}_{,\hat{y}} + \big(J \boldsymbol{B}_a \boldsymbol{A}_* \mid \boldsymbol{s} \big)_{;\hat{y}} \Big] \, \mathrm{d}\hat{x}, \tag{H.2.3}$$

where $\boldsymbol{u}_h$ is the configuration sensitivity field induced by the nodal sensitivities,

$$\boldsymbol{u}_h^h = \sum_b \boldsymbol{\varphi}_{ub} \, \boldsymbol{u}_{b,h}. \tag{H.2.4}$$

The first term in (H.2.3) is the state-induced geometric contribution. By definition of the discrete geometric operator,

$$D_\chi[\boldsymbol{B}_a \boldsymbol{A}_* \mid \boldsymbol{s}] \cdot \boldsymbol{u}_h = \sum_b \boldsymbol{G}_{ab}[\boldsymbol{s}] \, \boldsymbol{u}_{b,h}. \tag{H.2.5}$$

The constitutive term is treated by differentiating the section response. The strain sensitivity admits the decomposition

$$\boldsymbol{e}_{,\hat{y}} = D\boldsymbol{e} \cdot \boldsymbol{u}_h + \boldsymbol{e}_{;\hat{y}} = \sum_b \boldsymbol{B}_b^\star \boldsymbol{u}_{b,h} + \boldsymbol{e}_{;\hat{y}}, \tag{H.2.6}$$

and therefore

$$\boldsymbol{s}_{,\hat{y}} = \boldsymbol{C}_s \, \boldsymbol{e}_{,\hat{y}} + \boldsymbol{s}_{;\hat{y}} = \boldsymbol{C}_s \sum_b \boldsymbol{B}_b^\star \boldsymbol{u}_{b,h} + \boldsymbol{C}_s \, \boldsymbol{e}_{;\hat{y}} + \boldsymbol{s}_{;\hat{y}}. \tag{H.2.7}$$

Substituting (H.2.5) and (H.2.7) into (H.2.3) yields

$$\boldsymbol{p}_{a,\hat{y}} = \sum_b \left[\int_{\hat{e}} J\Big(\boldsymbol{B}_a \, \boldsymbol{C}_\sigma \, \boldsymbol{B}_b^\star + \boldsymbol{G}_{ab}[\boldsymbol{s}] \Big) \, \mathrm{d}\hat{x} \right] \boldsymbol{u}_{b,h} + \boldsymbol{p}_{a;\hat{y}}, \tag{H.2.8}$$

with

$$\boldsymbol{p}_{a;\hat{y}} = \int_{\hat{e}} \Big[\big(J \boldsymbol{B}_a \boldsymbol{A}_* \mid \boldsymbol{s} \big)_{;\hat{y}} + J \boldsymbol{B}_a \boldsymbol{A}_* \Big(\boldsymbol{C}_s \, \boldsymbol{e}_{;\hat{y}} + \boldsymbol{s}_{;\hat{y}} \Big) \Big] \, \mathrm{d}\hat{x}. \tag{H.2.9}$$

The first term in (H.2.9) expands to

$$\big(J \boldsymbol{B}_a \boldsymbol{A}_* \mid \boldsymbol{s} \big)_{;\hat{y}} = J_{,\hat{y}} \, \boldsymbol{B}_a \boldsymbol{\sigma} + J \, (\boldsymbol{B}_a \boldsymbol{A}_*)_{;\hat{y}} \, \boldsymbol{s}. \tag{H.2.10}$$

Equation (H.2.8) gives the component sensitivity of the resisting force vector. In matrix form,

$$\boldsymbol{p}_{,\hat{y}} = \boldsymbol{k}\,\boldsymbol{u}_{,\hat{y}} + \boldsymbol{p}_{;\hat{y}}, \tag{H.2.11}$$

with element tangent

$$\boldsymbol{k}_{ab} = \int_{\hat{e}} J\Big(\boldsymbol{B}_a\,\boldsymbol{C}_\sigma\,\boldsymbol{B}_b^\star + \boldsymbol{G}_{ab}[\boldsymbol{s}]\Big)\,\mathrm{d}\hat{x}. \tag{H.2.12}$$

Thus the force sensitivity splits into a state-induced term, obtained by applying the consistent tangent to the nodal sensitivity vector, and a direct term that collects all explicit parameter dependence of the element geometry, interpolation, and constitutive response.

At the assembled level, if the equilibrium residual is written as

$$\boldsymbol{g}(\boldsymbol{u}, \hat{y}) = \boldsymbol{p}(\boldsymbol{u}, \hat{y}) - \boldsymbol{f}(\boldsymbol{u}, \hat{y}), \tag{H.2.13}$$

then differentiation gives

$$\boldsymbol{g}_{,\hat{y}} = \boldsymbol{K}\,\boldsymbol{u}_{,\hat{y}} + \boldsymbol{p}_{;\hat{y}} - \boldsymbol{f}_{,\hat{y}}, \tag{H.2.14}$$

where $\boldsymbol{K}$ is the assembled consistent tangent formed from (H.2.12). This is the form required in direct differentiation procedures for nonlinear static and dynamic sensitivity analysis.

Appendix I

Structural Condition Metrics

I.1 Introduction

I.1.1 Objective

Limit state mappings are developed for bridge columns that link computed response quantities to observable phenomena such as cover cracking, spalling, and bar buckling. In the present framework, columns are modeled with distributed-inelasticity frame elements and fiber-discretized sections. For each column, strains and stresses are available at section integration points (fibers).

I.1.2 Literature

Zhou and Kunnath (2022) show that ductility can be a reasonable indicator for minor to moderate damage under cyclic loading, but that it becomes inconsistent for severe damage under earthquake loading as peak ductility can occur before bar buckling and severe strength deterioration. Their work motivates an explicit strain-based mapping, which provides a direct link between simulated response and operational guidance. The report synthesizes an experimental database of non-ductile columns to ground the taxonomy in observable damage mechanisms, and documents both the scarcity of data at the most severe states and the sensitivity of ductility-based thresholds under earthquake loading.

I.2 Limit State Taxonomy

The seven-state taxonomy of Table I.1 for non-ductile bridge columns associates health conditions with consequences that range from no action and patching at low damage to jacketing, column replacement, and bridge replacement at the highest damage states (PEER & Caltrans, 2017; Roblee et al., 2020; Zhou & Kunnath, 2022). This classification relates recognizable damage mechanisms, including cover cracking and spalling, exposure of the confined core, bar buckling, and loss of lateral or vertical capacity, to outcomes that can be operationalized in a post-event workflow.

Zhou and Kunnath (2022) notes that data supporting some transition thresholds are sparse, particularly at the highest damage states, since many experiments terminate once lateral strength has degraded by roughly 20%. This motivates a cautious interpretation of collapse states and underscores the need for calibration as more observed event data are accumulated.

Table I.1: Limit state taxonomy for nonductile bridge columns.

Label	**Description**	**Consequences**
LS_0	No damage	None
LS_1	Cracking of concrete cover	Patch and paint
LS_2	Minor spalling of concrete cover	Concrete removal, minor epoxy injection, patch and paint
LS_3	Major spalling of concrete cover	Concrete removal, major epoxy injection
LS_4	Exposed concrete core	Strengthening through column jacketing
LS_5	Bar buckling, loss of confinement	Column replacement
LS_6	Multi bar rupture, core crushing, large residual drift	Column replacement and/or bridge replacement
LS_7	Column collapse or near total loss of axial capacity	Bridge replacement

I.3 Strain-Based Labeling

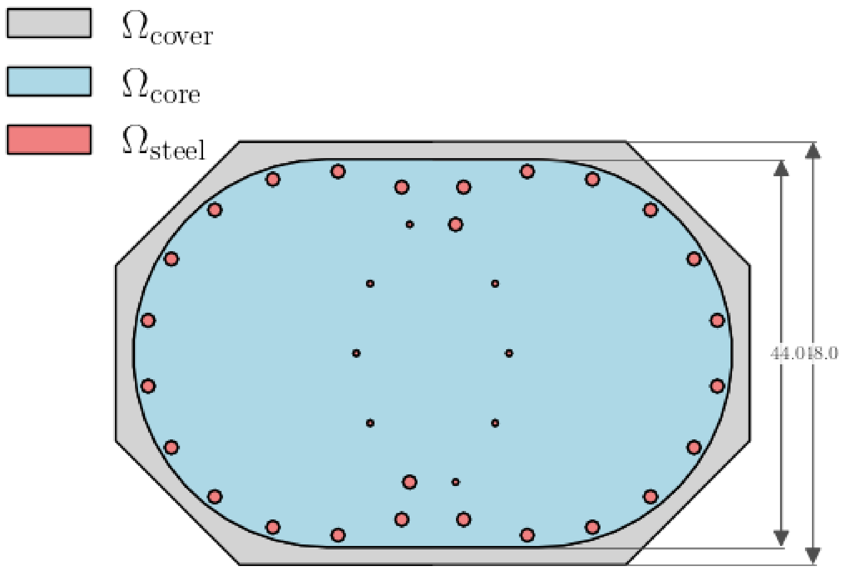

Figure I.1: Irregular column cross section from structure `33-0214L`.

Zhou and Kunnath (2022) propose a mapping from cross sectional axial strains to the states of Table I.1 for circular and rectangular columns. The following developments extend this work to consider general cross sections like that of Figure I.1.

Consider sections that admit the geometric decomposition:

$$\Omega = \Omega_{\text{c}} \cup \Omega_{\text{steel}}, \qquad \Omega_{\text{c}} := \Omega_{\text{core}} \cup \Omega_{\text{cover}}, \qquad \operatorname{int}(\Omega_{\text{core}}) \cap \operatorname{int}(\Omega_{\text{cover}}) = \emptyset.$$

Define the outer concrete boundary and the core boundary:

$$\Gamma_o := \partial\Omega_{\text{c}}, \qquad \Gamma_i := \partial\Omega_{\text{core}}.$$

so the cover boundary $\partial\Omega_{\text{cover}}$ is

$$\partial\Omega_{\text{cover}} = \Gamma_o \cup \Gamma_i,$$

For $\boldsymbol{r} \in \Omega_{\text{cover}}$, define

$$d_o(\boldsymbol{r}) := \operatorname{dist}(\boldsymbol{r}, \Gamma_o), \qquad d_i(\boldsymbol{r}) := \operatorname{dist}(\boldsymbol{r}, \Gamma_i), \qquad \delta_{\text{cov}}(\boldsymbol{r}) := \frac{d_o(\boldsymbol{r})}{d_o(\boldsymbol{r}) + d_i(\boldsymbol{r})}.$$

For $0 \le a \le b \le 1$, define the cover band

$$\Omega_{\text{cover}}[a,b] := \{\boldsymbol{r} \in \Omega_{\text{cover}} : a \le \delta_{\text{cov}}(\boldsymbol{r}) \le b\}.$$

Hence

$$\Omega_{\text{cover}}[0,0] = \Gamma_o, \qquad \Omega_{\text{cover}}[1,1] = \Gamma_i,$$

and $\Omega_{\text{cover}}[\frac{1}{2},\frac{3}{4}]$ is the mid-to-inner cover band.

In terms of these definitions, the strain-based mapping of ZHOU and KUNNATH (2022) is generalized by Table I.2 where the limit strains ε_c, ε_s,ε_c and ε_u are defined by Table I.3.

Table I.2: Strain-based labeling criteria.

State	Geometric region	Activation criterion
LS_0	—	None of LS_1–LS_6 is active.
LS_1	Outer cover boundary Γ_o	$\max_{\boldsymbol{r}\in\Gamma_o} \varepsilon(\boldsymbol{r}) \ge \varepsilon_r$.
LS_2	Outer cover boundary Γ_o	$\min_{\boldsymbol{r}\in\Gamma_o} \varepsilon(\boldsymbol{r}) \le -\varepsilon_s$.
LS_3	Cover band $\Omega_{\text{cover}}[\frac{1}{2},\frac{3}{4}]$	$\min_{\boldsymbol{r}\in\Omega_{\text{cover}}[\frac{1}{2},\frac{3}{4}]} \varepsilon(\boldsymbol{r}) \le -\varepsilon_s$.
LS_4	Inner cover boundary Γ_i	$\min_{\boldsymbol{r}\in\Gamma_i} \varepsilon_c(\boldsymbol{r}) \le -\varepsilon_s$.
LS_5	Γ_i for concrete and $\mathcal{B}$ for steel	Either $\min_{\boldsymbol{r}\in\Omega_{\text{cover}}[1,1]} \varepsilon_c(\boldsymbol{r}) \le -\varepsilon_c$ or $\max_{b\in\mathcal{B}} \varepsilon_s \ge \varepsilon_u$.
LS_6	Core failure set $\mathcal{F}_c \subset \Omega_{\text{core}}$	$\dfrac{\text{area}(\mathcal{F}_c)}{\text{area}(\Omega_{\text{core}})} \ge \eta_{\text{col}}$,

Table I.3: Monotonic axial limit strains for confined concrete columns.

Strain	Description
ε_r	Cover concrete tensile cracking strain
ε_u	steel strain at peak stress
ε_s	Unconfined concrete crushing (spalling) strain
ε_c	Core concrete crushing strain

I.4 Discussion. Implications and Limitations

The strain-based mapping provides a direct, physically interpretable link between nonlinear simulation and actionable reporting, but it also exposes several limitations. First, the damage state boundaries in Table I.2 remain sensitive to uncertainty in material properties, detailing, and confinement, and therefore must be calibrated as additional events are captured. Second, the mapping is local by construction; it captures member-level damage but does not directly encode system-level redundancy or load redistribution. Finally, the reliance on fiber strains means that model form errors in section kinematics can propagate directly into the reported damage state. The enhanced section formulations of Part I mitigate this by improving the underlying strain field, but continued validation against observed event data remains essential as the platform scales.

The damage state metric can be used to further extend the decision-making process for operational actions with standard practices by Caltrans' Structures Maintenance and Investigations group, such as those outlined in California Department of Transportation (2017).

Appendix J

Example: Caltrans Bridge No. 04-0236

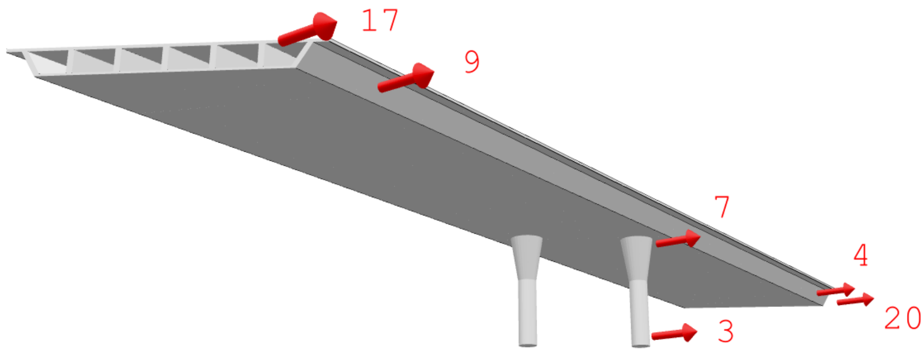

Figure J.1: Accelerometer placement on the Painter St. Overcrossing. Adapted from Chern et al. (2025).

J.1 Introduction

J.1.1 Description

The Painter St. Overcrossing is a continuous reinforced concrete box-girder bridge. The skewed 265-foot-long deck consists of two unequal spans which meet at a two-column bent. The 40-foot-wide roadway accommodates one traffic lane in each direction, each with a comfortable shoulder. There is no horizontal or vertical curvature to the structure. The structure rests on two skewed integral abutments and two column footings supported by 20 piles each.

The east abutment is monolithic with the superstructure and is supported by 14 driven 45-ton concrete friction piles. The west abutment has a thermal expansion joint and rests on a neoprene bearing strip. The foundation of this abutment consists of 16 driven 45-ton concrete friction piles.

J.2 Instrumentation and System Identification

The Painter St. Overcrossing was instrumented in 1977 with accelerometers placed as shown in Figure J.1. These are categorized as follows:

Direction	**Bridge Channels**	**Ground Channels**
Longitudinal	`1, 11`	`12, 15, 18`
Transverse	`3, 4, 7, 9`	`17, 20`
Vertical	`2, 5, 6, 8, 10`	`13, 16, 19`

The bridge has recorded accelerations from a total of 22 strong motion events. The details of these events, including dates and times are listed in Table J.1.

Event `nc73821036`, with a *peak station acceleration* (PSA)[1] of 1.38 g, is notable for its intensity. Following this event, Caltrans conducted an on-site inspection, augmented by unmanned aerial vehicles, and identified the following damage (Heninger, 2023):

- minor concrete cover spalling,
- shear key cracking, and
- a vertical displacement of approximately 1 inch at the south (acute) corner of the east abutment.

No additional significant displacement or damage was observed.

Goel and Chopra (1997) identified the following abutment stiffness parameters for two excitation intensities:

Excitation	**Lower bound (kips/ft)**	**Upper bound (kips/ft)**
Longitudinal (low intensity)	11,000	13,115
Transverse (high intensity)	7,500	12,000

[1]the maximum acceleration recorded at any accelerometer

J.3 Structural Modeling

The sole bent is modeled as a stiff beam framing into the superstructure.

Framing of the columns into the bent is modeled using a rigid joint offset to account for the rigidity of both the box girder, and column flares which are notably built-in.

The abutments are modeled by a collection of parameterized linear springs. Initial stiffness values can be selected from those reported in the literature.

Mass is assigned to the structure using consistent mass distribution in the frame elements.

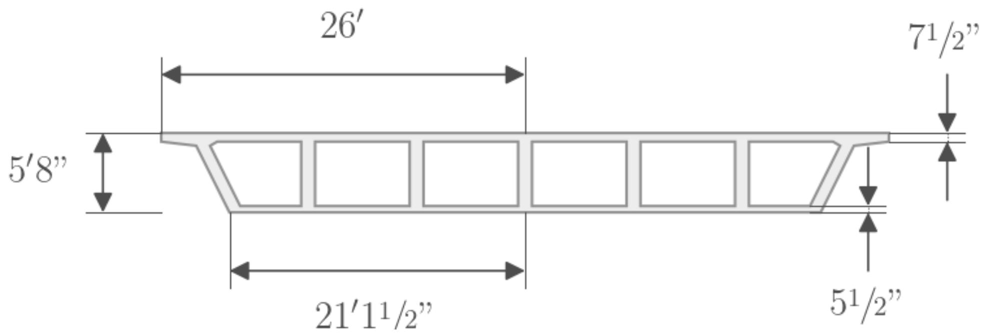

Figure J.2: Girder from the Painter Street Overcrossing.

Girders are modeled using elastic beam elements with cross sectional properties:

Girder section properties for `04-0236`

Material		
E	$=$	3.6×10^3 ksi
G	$=$	1.5×10^3 ksi

Shape

Table 4.1		
$\widehat{EA}$	$=$	$12 \times 10^3 \; E$ ksi in^2
$\widehat{GJ}_\vartheta$	$=$	$25 \times 10^6 \; G$ ksi in^4

Warping Shape Parameters (Table 4.2)

Energetic (E.2.6)		
$\widehat{GA}_y$	$=$	$550 \times 10^{-3} \; GA$ ksi in^2
$\widehat{GA}_z$	$=$	$240 \times 10^{-3} \; GA$ ksi in^2
$(\bar{\boldsymbol{\rho}}_\gamma)_y$	$=$	35 in^2
$(\bar{\boldsymbol{\rho}}_\gamma)_z$	$=$	5.9×10^{-3} in^2
$(\bar{\boldsymbol{\rho}}_\varkappa)_y$	$=$	1.3×10^3 in^2
$(\bar{\boldsymbol{\rho}}_\varkappa)_z$	$=$	-98×10^{-3} in^2

Geometric (E.1.9)		
$\widehat{GA}_y$	$=$	$560 \times 10^{-3} \; GA$ ksi in^2
$\widehat{GA}_z$	$=$	$310 \times 10^{-3} \; GA$ ksi in^2
$(\bar{\boldsymbol{\rho}}_\gamma)_y$	$=$	0.0 in^2
$(\bar{\boldsymbol{\rho}}_\gamma)_z$	$=$	0.0 in^2
$(\bar{\boldsymbol{\rho}}_\varkappa)_y$	$=$	1.3×10^3 in^2
$(\bar{\boldsymbol{\rho}}_\varkappa)_z$	$=$	3.1×10^{-3} in^2

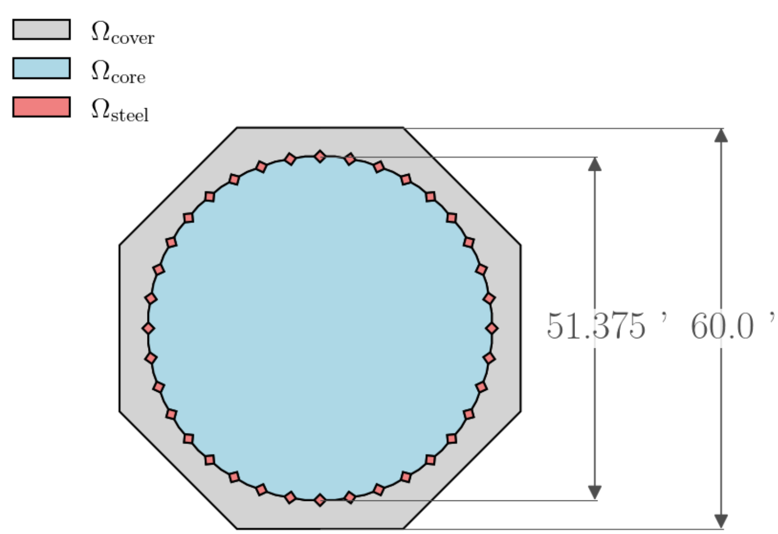

Figure J.3: Column section model.

Columns are modeled using MF_n elements. Strain regions for the limit state metrics of Appendix I are depicted in Figure J.3 and the warping shapes of Appendix C are depicted in Figure J.4. The cross sectional properties of Chapter 4 are:

Column section properties for `04-0236`

Material		*Shape*	Table 4.1	
E	$= 3.6 \times 10^3$ ksi		$\widehat{EA}$	$= 3.4 \times 10^3\ E$ ksi in^2
G	$= 1.5 \times 10^3$ ksi		$\widehat{GJ}_\vartheta$	$= 1.5 \times 10^6\ G$ ksi in^4

Warping Shape Parameters (Table 4.2)

Energetic (E.2.6)		*Geometric* (E.1.9)	
$\widehat{GA}_y$	$= 780 \times 10^{-3}\ GA$ ksi in^2	$\widehat{GA}_y$	$= 810 \times 10^{-3}\ GA$ ksi in^2
$\widehat{GA}_z$	$= 780 \times 10^{-3}\ GA$ ksi in^2	$\widehat{GA}_z$	$= 810 \times 10^{-3}\ GA$ ksi in^2
$(\bar{\boldsymbol{\rho}}_\gamma)_y$	$= 1.9 \times 10^{-3}$ in^2	$(\bar{\boldsymbol{\rho}}_\gamma)_y$	$= 0.0$ in^2
$(\bar{\boldsymbol{\rho}}_\gamma)_z$	$= -5.7 \times 10^{-3}$ in^2	$(\bar{\boldsymbol{\rho}}_\gamma)_z$	$= 0.0$ in^2
$(\bar{\boldsymbol{\rho}}_\varkappa)_y$	$= 2.6 \times 10^{-3}$ in^2	$(\bar{\boldsymbol{\rho}}_\varkappa)_y$	$= 2.4 \times 10^{-3}$ in^2
$(\bar{\boldsymbol{\rho}}_\varkappa)_z$	$= -8.0 \times 10^{-3}$ in^2	$(\bar{\boldsymbol{\rho}}_\varkappa)_z$	$= -7.9 \times 10^{-3}$ in^2

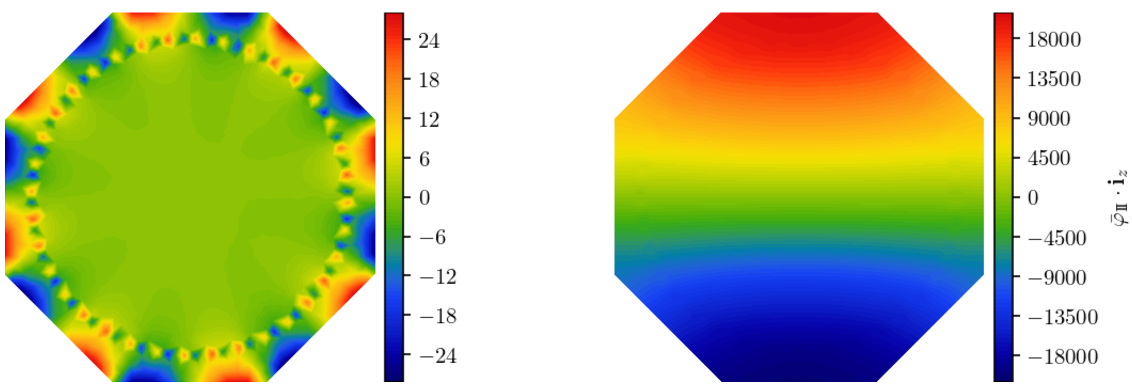

Figure J.4: Warping shapes.

J.4 Appendix: Events at Painter Street.

Table J.1: Events recorded at the Painter St. Overcrossing (04-0236).

NCEI ID	Record	Date/Time	Event ID	Source
	401	1980-11-08 10:27:00	usp0001aq1	CESMD
	399	1982-12-16T06:53:00	nc1083151	CESMD
	396	1983-08-24T13:36:00	nc1100970	
	394	1986-11-21T23:33:00	nc88508	
	393	1986-11-21T23:34:00	nc88509	
	395	1987-07-31T23:56:00	nc10083966	
		2012-09-14T11:53:00	nc71842075	
		2012-09-14T18:19:00		
	402	2013-10-11T23:05:00	nc72086051	
		2014-10-19T14:23:00		
		2015-01-28T21:08:00		
		2016-12-05T18:32:00	nc72733405	
		2016-12-08T14:50:00	us20007z6r	
		2019-06-23T03:52:00		
		2020-03-09T02:59:00	nc73351710	
		2021-12-20T21:53:00		
		2021-12-23T03:28:00		
		2022-12-20T15:08:00		
		2022-04-04T15:16:00		
		2022-12-20T10:38:00		
		2022-12-20T10:34:00		
		2023-01-01T18:34:00		
		2023-05-21T18:44:00		
		2023-09-30T17:16:00		
		2023-08-17T21:07:00		
		2023-09-30T15:26:00		
	422	2023-10-16T10:20:00	nc73947830	CESMD
10762	423	2024-12-05T18:44:00	nc75095651	CESMD
		2025-01-10T21:57:00	-	BRACE[2]
		2025-05-21T16:47:00	-	BRACE[2]
		2025-05-21T18:04:00	-	BRACE[2]